Non-aqueous dispersions of particles and their applications

Dissertation
Zur Erlangung des Grades
“Doktor der Naturwissenschaften”
im Promotionsfach Polymer Chemie

am Fachbereich Chemie, Pharmazie und Geowissenschaften
der Johannes Gutenberg-Universität Mainz

Yi Gerkmann
(Yi Zhao)
geb. in China

Mainz 2015

Abbreviations

AFM	Atomic force microscopy
BDAEE	Bis[2-(N,N-dimethylamino)ethyl] ether
BHC	1,4-bis(hydroxymethyl) cyclohexane
Cp	Cyclopentadienyl
DLS	Dynamic Light Scattering
DMAO	Dried Methylaluminoxan
DMF	Dimethylformamide
DSC	Differential Scanning Calorimeter
EDX	Energiedispersive Röntgenspektrokopie
FI	Phenoxy-Imin
wt%	Weight%
GPC	Gel Permeation Chromatography
HD-PE	High Density Polyethylen, niedrig verzweigtes Polyethylen
HMDI	1,6-hexane diisocyanate
ICP-OES	Inductively Coupled Plasma-Optical Emission Spectrometry
IR spectroscopy	Infrared spectroscopy
ISC	Intersystem crossing
Kat	Katalysatorsystem
LD-PE	Low Density Polyethylen, hoch verzweigtes Polyethylen
LLD-PE	Linear Low Density Polyethylen, niedrig verzweigtes Polyethylen mit geringer Dichte
LSCFM	laser scanning confocal fluorescent microscopy
MAO	Methylaluminoxan
MDI	4,4'-methylene diphenyl diisocyanate
2-Me-Benz[e]Ind	2-Methyl-4,5-Benzoindenyl
NMR	nuclear magnetic resonance
$NaAlEt_4$	Natriumaliminiumtetraethyl
P_c,	Percolation threshold
PE	Polyethylen
PDI	Perylenediimide derivative
PI-b-PMMA	Polyisoprene-block-polymethylmethacrylate
PP	Polypropylen

PS	Polystyrene
PU	Polyurethane
RT	Raumtemperatur
SEM	Scanning Electron Microscopy
SMFD	Single Molecule Fluorescence Detection
TEA	Triethylaluminium
TEDA	Triethylene diamine
TEM	Transmission Electron Microscopy
TIBA	Triisobutylaluminium
TGA	Thermal gravimetric analysis
THF	Tetrahydrofuran
TMA	Trimethylaluminium
TOA	Trioctylaluminium
UV-Spectroscopy	Ultraviolet-Visible Spectroscopy
XRD	X-ray Diffraction

Index

Chapter 1. Introduction

1.1 Dispersions of particles

Dispersions of particles are broadly used in industries for rubber, paints, adhesives, additives in paper and textiles, impact modifiers for plastic matrices and additives for construction materials [1]. In biomedical and pharmaceutical applications dispersions also have exceeding significance, such as for diagnostic tests and drug delivery systems [2]. The advantages of dispersion are good heat exchange and decrease of the viscosity during the production. Dispersion is a finely subdivided system of a dispersed phase in another medium (continuous phase) [3]. The dispersed phase can be solid (dispersion of polymer or inorganic particles), liquid (macroemulsion and miniemulsion), gaseous (fogging and mist) or association macromolecule (dispersion of micelle). The continuous phase can be liquid (emulsion) or solid (polymer composites).

1.2 Preparation of dispersions of particles

There are two general approaches to prepare dispersions of particles (polymer and inorganic particles). In the first approach, particles are directly prepared in dispersions. One of the important methods is polymerization in emulsion [4]. In another approach, the particles are synthesized beforehand and dispersed afterwards in a continuous phase.

1.2.1 Polymerizations in emulsions

Polymerization in emulsion can be classified into three strategies: suspension, macroemulsion and miniemulsion. The difference of suspension to other ones is no emulsifier used. Such dispersion has a lowest stability. Without strongly stirring, particles can precipitate during the polymerization. The dispersions of particles from macroemulsion and miniemulsion show high stability where emulsifier anchors on the surface of the particles and force them apart. In the following the mechanism of polymerization in macroemulsion and miniemulsion will be descript.

1.2.1.1 Polymerizations in macroemulsions

The process of polymerization in macroemulsion is divided into three intervals. Figure 1 shows a radical polymerization as a basic model [5]: In Interval I (Figure 1), radicals are generated from initiator molecules and react with few monomers that are dissoluble in dispersion phase. The new-built oligomer radicals diffuse into small monomer micelles at beginning of the polymerization, but not into large monomer droplets. Because the small monomer micelles have a much higher surface area than larger monomer droplets, they have higher probability to be attacked by oligomer radicals than monomer droplets. As the attacked monomer micelles begin polymerization, monomer micelles get larger and need more surfactant molecules to stabilize their surface. Surfactant molecules are continuously diffused from surfactant micelles to the surface of the growing monomer micelles. About 5% of the monomers are polymerized at the end of Interval I and the polymerization rate reaches a maximum (Figure 2) [5].

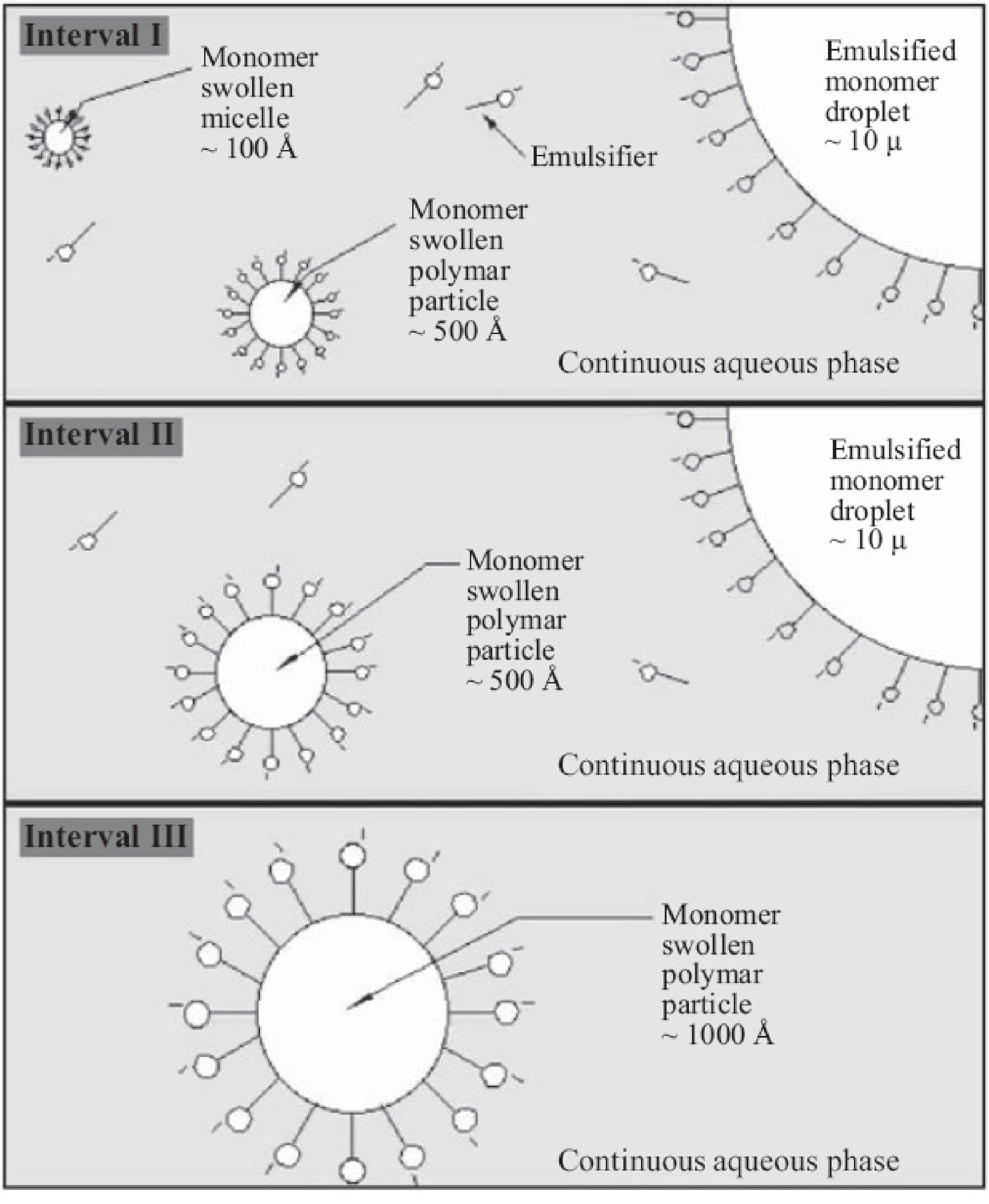

Figure 1 The process of polymerization in a macroemulsion (1-3) [6].

In interval II (Figure 1), all monomer micelles have been attacked by oligomer radicals. Therefore the number of polymerizing micelles does not increase any more. For these reasons, the polymerization rate during Interval II remains constant. Monomer molecules continuously diffuse from monomer droplets to the micelles. At the end of Interval II, the conversion of the monomers reaches 50 % (Figure 2).

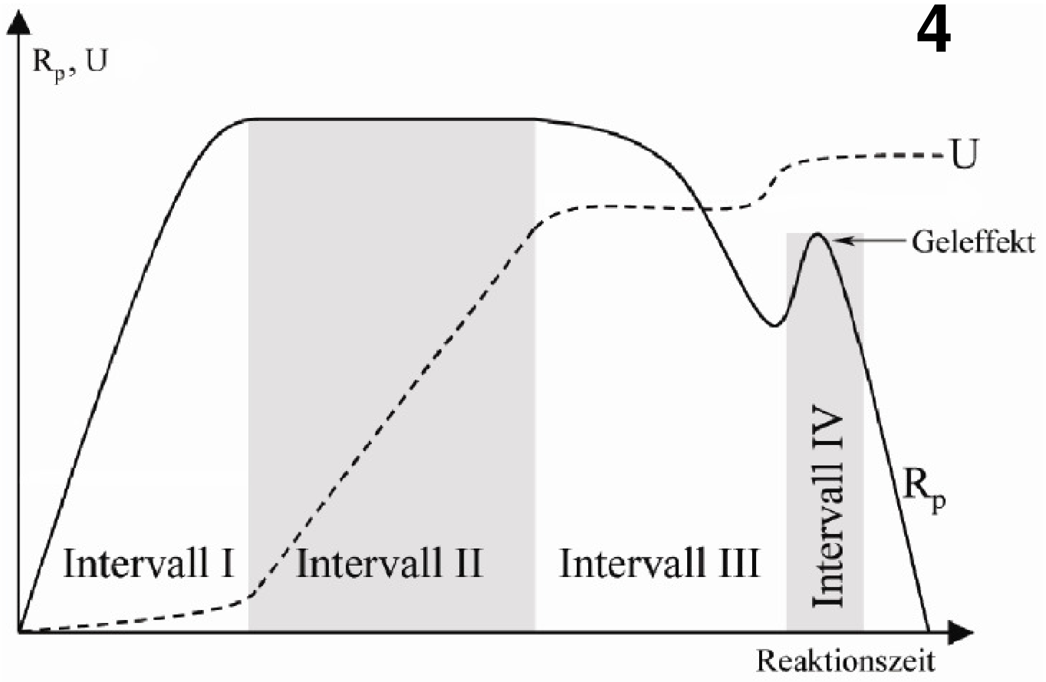

Figure 2. The dependence of the polymerization rate Rp and the conversion U of monomers on the reaction time in the radical polymerizations [5].

In Interval III, there are no more monomer droplets available in the continuous phase. Thus no additional monomers can be transported into polymerizing micelles. The polymerization is carried out only with the monomers that still remain in the polymerizing micelles. The concentration of monomers in these micelles strongly decreases. It leads to an exponential decline of the polymerization rate (Figure 2) [5]. At the end of polymerization, the polymerization rate Rp and the conversion U of monomers show a small increase. It is caused by the high viscosity of polymer, so called Geleffect (Figure 2).

1.2.1.2 Polymerizations in miniemulsions

The transport of monomers from the droplets to the polymerizing micelles through continuous phase can be limited, when the monomers are hardly soluble in the continuous phase [6]. For such polymerization, a miniemulsion is used instead. radicals are directly dispersed in the monomer droplets (Figure 3) [7]. Every monomer droplet is as nanoreactor where polymerization takes place.

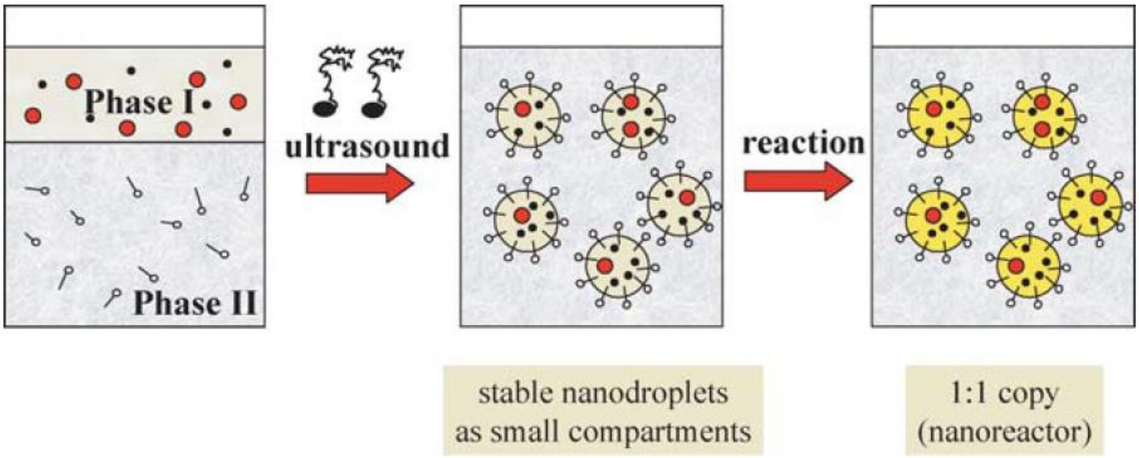

Figure 3 The principle of miniemulsion polymerizations [7]

In miniemulsion, monomer droplets with a size between 100 nm to 500 nm have a strong tendency to combine into large ones [8]. To stabilize such small droplets, a high shearing force (ultrasound or mechanical shearing) and surfactant/costabilizer are required: the first one is to fissure large droplets to small ones and the second one to protect the small droplets against Ostwald ripening. Usually a costabilizer, which has high solubility in the dispersed phase and is hardly soluble in the continuous phase, is extra used to prevent monomer diffusing from small droplets into large ones.

1.2.2 Surface modification of particles

Surface modification is another method to prepare dispersion of particles beside emulsion, where synthesized particles are stabilized in one continues phase by adsorption of one stabilizer on the surface of particles. In general there are two kinds of methods: the first one is chemisorption: adsorption through covalence forces between particles and the stabilizer. This process is also called as chemical functionalization: at first step, a precursor reacts on the surface of particles; at second step, stabilizing polymer chains grow from the precursor [9]. The second one is physisorption where the interaction involves only van der Waals force, for example, charge-charge attractions, hydrogen bonding or hydrophobic interactions [10].

1.3 Non-aqueous dispersions of particles

In the last decades, non-aqueous dispersions have attached an increasing interest in various industries. They are broadly used for the production of polymer particles where catalysts or monomers are sensitive to water, for example polyurethane particles where monomer diisocyanate and catalyst react with water very quickly [11]. Another advantage is that these dispersions have lower viscosity and lower boiling vaporization temperature compared to aqueous dispersions, particularly suitable for spraying applications of paints [12]. Non-aqueous emulsion and surface modification are two methods to prepare non-aqueous dispersions.

1.3.1 Non-aqueous emulsions

1.3.1.1 Formation of non-aqueous emulsions

A non-aqueous emulsion consists of two immiscible organic solvents as dispersed and continuous phase, for example cyclohexane/acetonitrile or hexane/DMF. The miscibility of solvents can be described by a solubility parameter δ_t [13]. The solubility parameter is computed from three other parameters: dispersion force δ_d, polar interactions δ_p, and hydrogen bonding δ_H.

$$\delta_t^2 = \delta_d^{\ 2} + \delta_p^{\ 2} + \delta_H^{\ 2}$$

Figure 4 shows the solubility scale for the main solvents used in non-aqueous emulsions. When the solubility parameters of two solvents are far apart, they are immiscible, such as hexane/DMF and cyclohexane/acetonitrile. With this solubility scale, various solvents can be selected to form a non-aqueous emulsion [13].

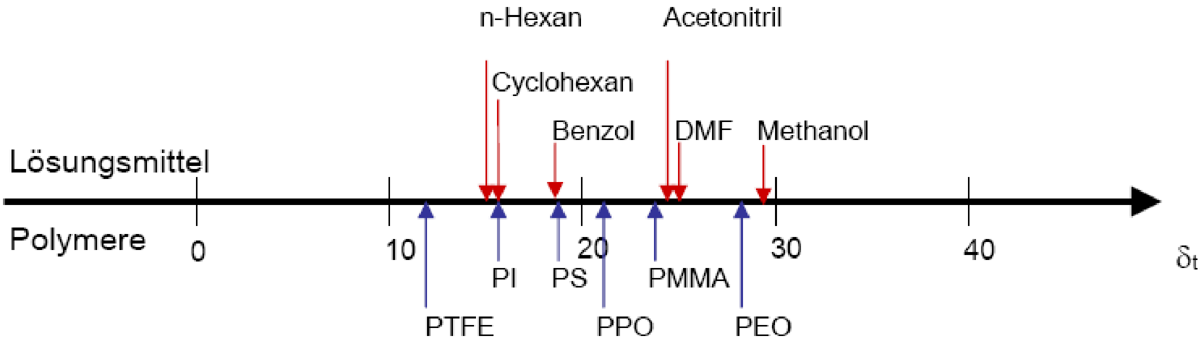

Figure 4. Solubility parameters for typical solvents and polymers [14].

1.3.1.2 Stabilizing mechanism of non-aqueous emulsions

To stabilize non-aqueous emulsions, amphiphilic block copolymers with high molecular weight are usually used. The stabilizing mechanism was established on the basis of the Flory treatment of the thermodynamics of polymer solutions [12] (Figure 5). One of the amphiphilic blocks has high solubility in the continuous phase and can form a steric hindrance to prevent aggregation of particles: When particles approach each another, the steric stabilizing blocks interpenetrate or are compressed. It results a higher concentration of polymer chains in the interpenetrated zone, generating an osmotic pressure. To counteract the high concentration, solvent diffuse into this zone, forcing the particles apart until the concentration there is no longer higher [12].

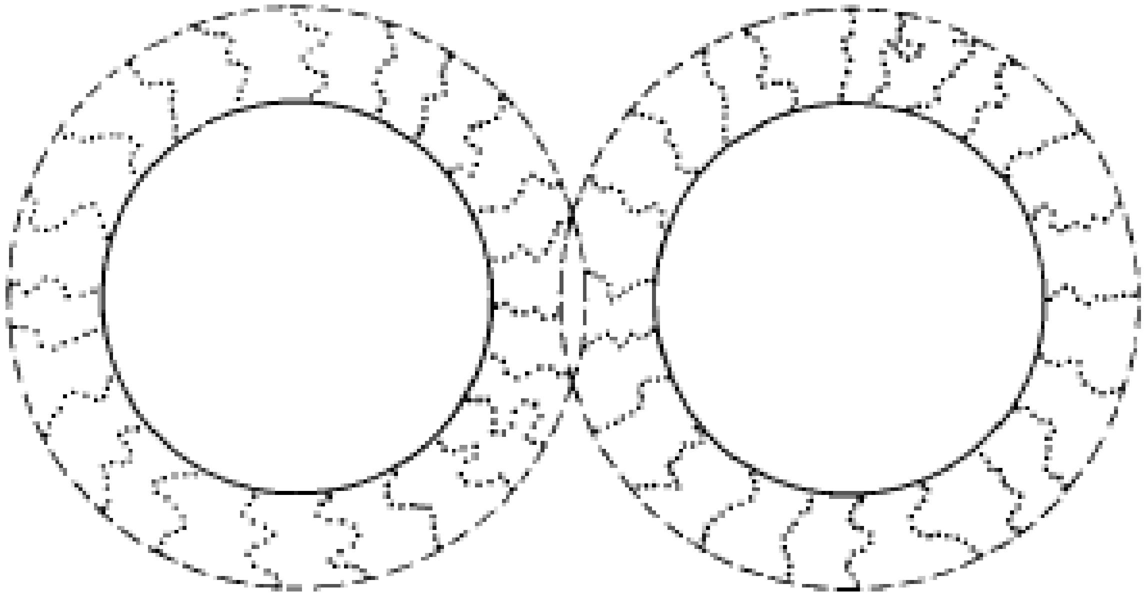

Figure 5. Schematic representation of steric stabilization of amphiphilic block copolymer in organic dispersions [12].

1.3.1.3 Amphiphilic block copolymers

Amphiphilic copolymers as stabilizer attach a lot of interest for non-aqueous emulsion because of their well defined compositions, molecular weights and structures with very elaborate architectures, for example, block, graft, random, star, multi-block [4] [15]. Specially, block amphiphilic copolymers have excellent stabilization function [3]. There are two classical synthetic routes for block copolymers [3, 16-19]: In the first one, a polymer from monomer A is synthesized with active sites, which are then used to initiate the polymerization of the second monomer B. Such polymerization can be of free radical, anionic or cationic type. In figure 6 it is shown the synthesis process of amphiphilic block copolymer poly(isoprene)-b-poly(methyl methacrylate) (PI-b-PMMA) by using this route. In the second one, which is usually called condensation or coupling, copolymers are prepared by reaction of two kinds of polymers.

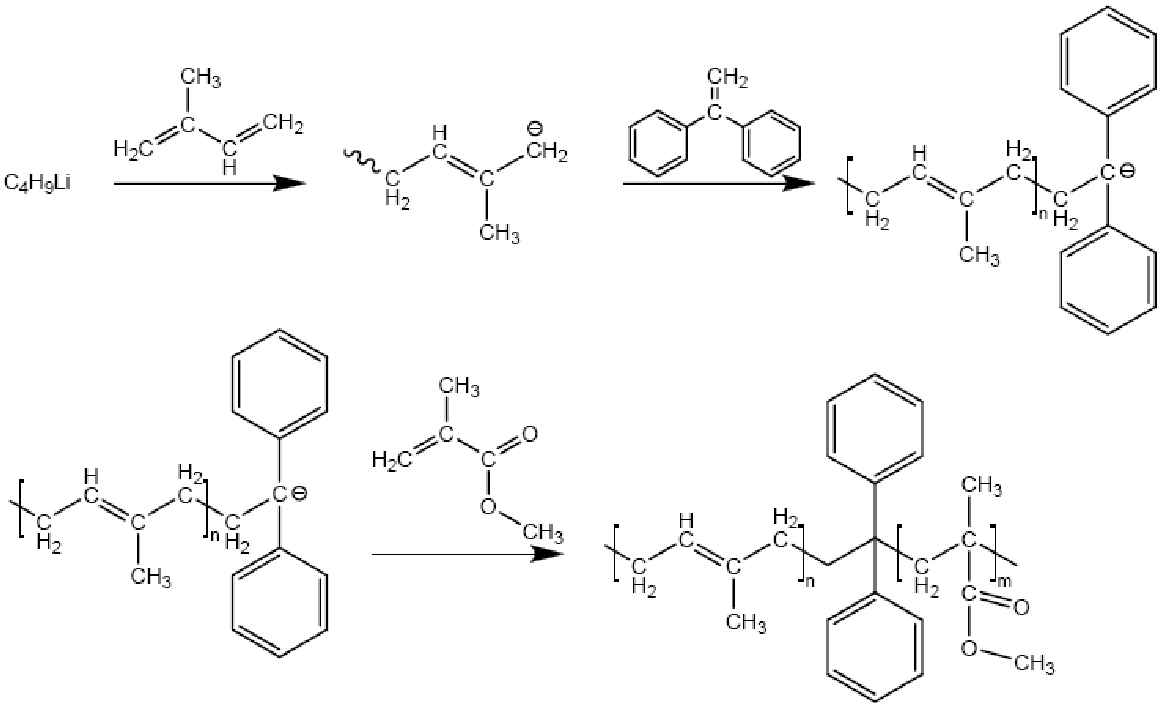

Figure 6. The synthesis of the amphiphilic block copolymer PI-b-PMMA [20].

Systematic and detailed study on amphiphilic block copolymers has been reviewed in the literature [21-25]. Poly(styrene)-b-poly(polyethylene oxide) (PS-PEO), poly(styrene)-b-poly(propylene oxide) (PS-PPO) and poly(methyl methacrylate)-b-poly(t-butylacrylate) (PMMA-PBA) are usually used for dispersions with polar continues phase, for example ethanol and polyether glycol, because of high polarity of PEO, PPO and PBA blocks. On the other hand, Poly(styrene)-b-poly(dimethyl methacrylate) (PS-PDMS), poly(styrene)-b-poly(methyl methacrylate) (PS-PMMA), poly(styrene)-b-poly(ethylene propylene) (PS-PEP), poly(styrene)-b-poly(isoprene) (PS-b-PI) and poly(isoprene)-b-poly(methyl methacrylate) (PI-b-PMMA) are used to prepare dispersions with non-polar continuous phase, for example aliphatic hydrocarbons and silicone oil.

1.3.1.4 Polymerizations in non-aqueous emulsions

In non-aqueous emulsions, various polymerizations like free radical, ionic polymerization, polycondensation and polyaddition can be carried out. It is especially significant for polycondensation and polyaddition, because most of the catalysts and monomers in these polymerizations are sensitive to water. The first attempts to carry out those polymerizations in non-aqueous emulsion were rather unsuccessful and the dispersions didn’t show good stability [24].

Recently a few of studies on polyurethane particles via non-aqueous emulsions showed interesting results. In a study, polyurethane particles with the size ranging from 0,2 to 2,0 µm were prepared by using poly(1,4-isoprene)-block-poly(ethylene oxide) as the stabilizer [26]. This study also showed that the formation of particle depended on the concentration of the stabilizer, the block molecular weight and the nature of continuous phase: the particles size decreased with increasing concentration of copolymer. On the other hand, copolymers with long steric stabilizing block were most effective stabilizer. In addition, the formation of monodispersion of particles depended not only on the polarity of the dispersed and continuous phase, and also on the solubility of the stabilizer in both phases. In another study, polyurethane particles were prepared by using poly(styrene)-b-poly(ethylene oxide) block copolymers and omega-hydroxypolystyrenes as steric stabilizer. The size of the particles ranged from 0,2 µm to 5 µm were obtained [27]. But the molecular weight M_n of the polymer particles was very low, only between 2000 g/mol and 3000 g/mol).

In our research group, polyurethane particles were prepare in a non-aqueous emulsion consisting of N,N'-dimethylformamide (DMF) as dispersed phase, n-hexane as continuous phase and copolymer poly(isoprene)-poly(methyl methacrylate) as the stabilizer [28]. The particles have an average size of only about 35 nm. The molecular weight of the particles reached 16 500 g/mol, which was much higher than the ones reported in other studies [26, 27, 29]. Under IR-spectroscopy, no vibration of urea from side reactions between water and diisocyanate was observed. This means that the use of non-aqueous emulsion well prevented side reactions during the polymerization.

1.3.2 Surface modification of particles in non-aqueous dispersions

Modification of the surface of particles is another way to prepare non-aqueous dispersions of particles. To understand the mechanism of this process, a theoretical model was developed in 1953. In this model, block copolymer is divided into three part: trains, loops and tails (Figure 7) [10, 30]. In the adsorption process, train block is adsorbed on the surface of particles as anchor. The tail block which has good solubility in the continuous phase stretches out as dangling tails, forming a brush-like structure on the surface. Studies show that the adsorption process depends not only on the properties of the surface of particles (functional groups, changes, polarity and surface morphology) but also on the solubility of the train block in the continuous phase [31, 32]: When the interaction of the train block with solvent molecules is weaker than with the surface of particles, the adsorption process of train block is dominant to the dissolution one in the continuous phase.

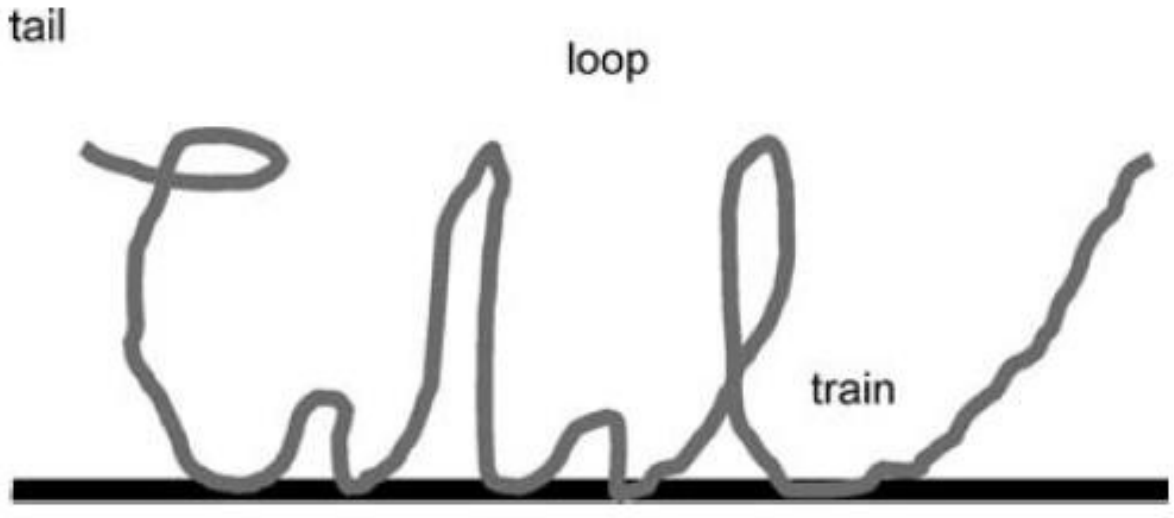

Figure 7. The structure of an adsorbed amphiphilic block copolymer on a surface [10].

In the literature, there are a lot of studies on non-aqueous dispersions of inorganic particles via surface modification are carried, for example, carbon black nanoparticles [33], Au [34] and SiO2 oxide particles [35-37], clay [38-40]. One of examples is modification of clay by use of an amphiphilic block copolymer poly(styrene)-poly(isoprene) and poly(styrene)-poly(butadiene) [37]. The copolymer consisted of 1,4-dibutanol and poly(ethylene glycol) as hydrophobic and hydrophilic blocks. With scanning electric microscopy (SEM) it was observed that clay was successfully exfoliated to nanolayers. There are also many studies on the dispersion of silica particles. One example is that silica particles was modified by an amphiphilic copolymer 2-(ethylhexyl)methacrylate (EHMA)-b-poly(ethylene oxide) methacrylate (PEOMA)-b-(2-dimethylaminoethyl) methacrylate (DMAEMA) and transported from one aqueous phase into one organic phase (n-alkane phase) [35]. The hydrophobic chain EHMA acted as steric stabilizer and the hydrophilic chain PEOMA as anchor on the surface of the particles. The similar amphiphilic block copolymers are also used to modify graphene materials, like block copolymers like polystyrene-b-polyacrylic acid (PS-b-PAA)

[22], gemini surfactant 6,6′-(butane-1,4-diylbis(oxy))bis(3-nonylbenzenesulfonic acid) [41], and single-stranded DNA (ssDNA) [42] .

Reference

1. Asus, j.M., Miniemulsion Polymerization. Prog. Polym. Sci, 2002. **27**.
2. Gerhard Lagaly, O.S., Ralf Zimehl, Disperionen und Emulsion1997.
3. Riess, G. and C. Labbe, Block copolymers in emulsion and dispersion polymerization. Macromolecular Rapid Communications, 2004. **25**(2): p. 401-435.
4. Riess, G., Micellization of block copolymers. Progress in Polymer Science, 2003. **28**(7): p. 1107-1170.
5. Harkins, W.D., A General Theory of the Mechanism of Emulsion Polymerization. J. Am. Chem. Soc, 1947. **69**(9): p. 16.
6. Schork, F.J., et al., Miniemulsion polymerization. Polymer Particles, 2005. **175**: p. 129-255.
7. Landfester, K., Synthesis of Colloidal Particles in Miniemulsions. Annual Review of Materials Research, 2006. **36**(1): p. 231-279.
8. Miller, C.M., et al., MINIEMULSION POLYMERIZATION OF STYRENE - EVOLUTION OF THE PARTICLE-SIZE DISTRIBUTION. Journal of Polymer Science Part a-Polymer Chemistry, 1995. **33**(8): p. 1391-1408.
9. Bourgeat-Lami, E., Organic-inorganic nanostructured colloids. Journal of Nanoscience and Nanotechnology, 2002. **2**(1): p. 1-24.
10. Bellmann, C., Surface Modification by Adsorption of Polymers and Surfactants. Polymer Surfaces and Interfaces 2008.
11. Müller, K., M. Klapper, and K. Müllen, Polyester nanoparticles by non-aqueous emulsion polycondensation. Journal of Polymer Science Part A: Polymer Chemistry, 2007. **45**(6): p. 1101-1108.
12. Keith, E. and J. Barrett, Dispersion Polymerisation in Organic Media. Br.Polym.J, 1973. **5**.
13. Hansen, C., m, Hansen Solubility Parameters:a User`s Handbook2000: CRC Press.
14. Distler, D., Wäßrige Polymerdispersionen1999.: Wiley-VCH, Weinheim.
15. Forster, S. and M. Antonietti, Amphiphilic block copolymers in structure-controlled nanomaterial hybrids. Advanced Materials, 1998. **10**(3): p. 195-+.
16. Hillmye, M., Block copolymer synthesis. Current Opinion in Solid State and Materials Science, 1999. **4**(6): p. 559-564.
17. Tcherkasskaya, O., et al., Energy transfer in restricted geometry: Polyisoprene-poly(methyl methacrylate) block copolymer interfaces. Journal of Physical Chemistry, 1996. **100**(17): p. 7114-7121.

18. Smulders, W.W., C.W. Jones, and F.J. Schork, Synthesis of block copolymers using RAFT miniemulsion polymerization in a train of CSTRs. Macromolecules, 2004. **37**(25): p. 9345-9354.
19. Hadjichristidis, N., S. Pispas, and G. Floudas, Block Copolymers: Synthetic Strategies, Physical Properties, and Applications2003.
20. Müller, K., Nicht-waessrige emulsionspolymerisationen, in Chemie und Pharmazie der Johannes-Gutenberg Universitaet 2008: Mainz.
21. Dawkins, J.V. and G. Taylor, Polymer Colloids II1980, New York: Plenum,.
22. Croucher.M.D, W.M., Preparation of Polymer Particles by Dispersion Polymerization. Scientific Methods of Study of Polymer Colloids and their Applications1990.
23. D, H., acta Polymerica Sinica, 1996. **47**.
24. Barrett, K.E.J., Dispersion Polymerization in Organic Media1975, New York: John Wiley.
25. Piirma, Polymeric Surfactants. Surfactant Science Series 421992.
26. Ramanathan, L.S., et al., Preparation of polyurethane microspheres via dispersion polycondensation using poly(1,4-isoprene)-block-poly (ethylene oxide) as steric stabilizer. Macromolecular Chemistry and Physics, 2002. **203**(7): p. 998-1002.
27. Radhakrishnan, B., E. Cloutet, and H. Cramail, Synthesis of uniform polyurethane particles by step growth polymerization in a dispersed medium. Colloid and Polymer Science, 2002. **280**(12): p. 1122-1130.
28. Muller, K., M. Klapper, and K. Mullen, Preparation of high molecular weight polyurethane particles by nonaqueous emulsion polyaddition. Colloid and Polymer Science, 2007. **285**(10): p. 1157-1161.
29. Tiarks, F., K. Landfester, and M. Antonietti, One-step preparation of polyurethane dispersions by miniemulsion polyaddition. Journal of Polymer Science Part a-Polymer Chemistry, 2001. **39**(14): p. 2520-2524.
30. Simha, R., H.L. Frisch, and F.R. Eirich, The Adsorption of Flexible Macromolecules. Journal of Physical Chemistry, 1953. **57**(6): p. 584-589.
31. Schwarz, S., et al., Adsorption and stability of colloidal silica. Colloids and Surfaces a-Physicochemical and Engineering Aspects, 2000. **163**(1): p. 17-27.
32. Fleer. G.J, L., Solid/Liquid Interface1983.

33. Li, Q.Y., et al., Preparation of modified carbon black with nano-scale size and enhanced stability in organic solvent by solid state method. Colloids and Surfaces a-Physicochemical and Engineering Aspects, 2008. **317**(1-3): p. 87-92.

34. Stelzig, S.H., et al., Compatibilization of laser generated antibacterial Ag- and Cu-nanoparticles for perfluorinated implant materials. European Polymer Journal, 2011. **47**(4): p. 662-667.

35. Stelzig, S.H., M. Mapper, and K. Muellen, A simple and efficient route to transparent nanocomposites. Advanced Materials, 2008. **20**(5): p. 929-+.

36. Sondi, I., et al., Encapsulation of nanosized silica by in situ polymerization of tert-butyl acrylate monomer. Langmuir, 2000. **16**(23): p. 9031-9034.

37. Korley, L.T.J., et al., Preferential association of segment blocks in polyurethane nanocomposites. Macromolecules, 2006. **39**(20): p. 7030-7036.

38. Lee, K.M. and C.D. Han, Linear dynamic viscoelastic properties of functionalized block copolymer/organoclay nanocomposites. Macromolecules, 2003. **36**(3): p. 804-815.

39. Carastan, D.J., et al., Linear viscoelasticity of styrenic block copolymers-clay nanocomposites. Rheologica Acta, 2008. **47**(5-6): p. 521-536.

40. Gaines, M.K., et al., Nanoparticle Network Formation in Nanostructured and Disordered Block Copolymer Matrices. Nanoscale Research Letters, 2010. **5**(10): p. 1712-1718.

41. Xu, R.L., et al., Characterization of Block Copolymer Micelles and Their Adsorption onto Latex-Particles. Polymer Analysis and Characterization Iv, 1992. **51**: p. 135-149.

42. Zheng, M., et al., DNA-assisted dispersion and separation of carbon nanotubes. Nature Materials, 2003. **2**(5): p. 338-342.

Chapter 2. Motivation

Amphiphilic block copolymer polyisoprene-block-poly(methyl methacrylate) (PI-b-PMMA) was intensively studied as stabilizer of non-aqueous emulsions in our work-group. With this copolymer, emulsions with hexane or cyclohexane as continuous phase and DMF as dispersed phase showed excellent stabilization for the synthesis of conjugated polymer particles, polyurethane and polyester particles [1-4]. The goal of the current work is to prepare non-aqueous dispersions of particles for special applications by using PI-b-PMMA as stabilizer. In particular, I concentrated on the following three aspects:

- In recent years, porous particles have attracted considerable attention due to their high special surface area in many research areas, for example, as catalyst carrier [5-7], filling materials of composites [8] and separation media in liquid chromatography [9-11]. A lot of studies on porous polymer particles, like polyethylene [6][8], copolymerization of styrene and divinylbenzene [9] and chlorinated polyglycol [12], have been carried out, but only few of them focused on polyurethane and polyurea porous particles. Due to the hydrogen bonds between urethane and urea groups, these particles could have excellent mechanical and chemical stability and be used as filling materials (mechanical stability) and catalyst carrier (chemical stability and polar bonds). In this work, both porous particles will be synthesized via a non-aqueous emulsion by using PI-PMMA as emulsifier; the porous structure will be generated via carbon dioxide released by the reaction between water and diisocyanate.

- The kinetic of polymerization process has been studied in detail by using different analytical techniques, like ESR spectroscopy, size-exclusion chromatography and mass spectrometry, as well as NMR and fluorescence spectroscopy [13]. However, with these techniques polymerization cannot be traced on a molecular level. Single Molecule Fluorescence Detection (SMFD) is a novel analytical method which can detect single molecule and follow their movement on nanometer scale [14, 15]. An excellent example showed that the movement of a single polymer chain was successfully traced during the radical polymerization process in bulk via SMFD [13]. Until today, SMS is not yet used to study the polymerization in non-aqueous emulsions. In this work, radical polymerization and polyaddition in non-aqueous emulsions will be studied via SMS, because radical polymerization and polyaddition have completely mechanisms. PMMA and PU particles will be synthesized via an non-aqueous emulsion (PI-b-PMMA as emulsifier, cyclohexane as continuous phase and DMF as dispersed phase). To visualize polymer chains under SMS, perylene dye molecules with double bond or OH groups will be incorporated into the polymer chains as monomers.

- Graphene sheets have unusually high thermal conductivity (~3,000Wm^{-1}K^{-1}), mechanical stiffness (1,060 GPa) [16] and extraordinary electric conductivity [17, 18]. To harness these properties, graphene sheets are normally prepared as non-aqueous dispersions for different devices, such as field-effect transistors [19], ultrasensitive sensors [20], transparent electrodes [21], and novel nanocomposites [16]. Until today, these dispersions are mostly prepared using organic solvents with high toxicity, like DMF, NMP and toluol. The goal in this work is to prepare dispersions of graphene sheets by using organic solvents with low toxicity. PI-b-PMMA will be as stabilizer, because of the conjugated double bonds which could have interaction with graphene sheets.

Reference

1. Müller, K., M. Klapper, and K. Müllen, Synthesis of Conjugated Polymer Nanoparticles in Non-Aqueous Emulsions. Macromolecular Rapid Communications, 2006. **27**(8): p. 586-593.
2. Müller, K., M. Klapper, and K. Müllen, Polyester nanoparticles by non-aqueous emulsion polycondensation. Journal of Polymer Science Part A: Polymer Chemistry, 2007. **45**(6): p. 1101-1108.
3. Muller, K., M. Klapper, and K. Mullen, Preparation of high molecular weight polyurethane particles by nonaqueous emulsion polyaddition. Colloid and Polymer Science, 2007. **285**(10): p. 1157-1161.
4. Haschick, R., et al., Nonaqueous emulsions as a tool for particles with unique core-shell topologies. Macromolecules, 2008. **41**(14): p. 5077-5081.
5. Naundorf, C., et al., Hard versus Soft Materials as Supports for Metallocene and Post-Metallocene Catalysts. Macromolecular Reaction Engineering, 2009. **3**(8): p. 456-466.
6. Lei, J.H., et al., Porous polyethylene spheres with nanofiber structure from Ziegler-Natta catalyst supported on porous polymer particles. Polymer, 2011. **52**(3): p. 602-605.
7. Aydin, B., et al., Polymer-filled composite porous catalytic particles for hydrodynamic studies in trickle-bed reactors. Industrial & Engineering Chemistry Research, 2008. **47**(8): p. 2569-2578.
8. Gokmen, M.T. and F.E. Du Prez, Porous polymer particles-A comprehensive guide to synthesis, characterization, functionalization and applications. Progress in Polymer Science, 2012. **37**(3): p. 365-405.
9. Kitahara, K.I., et al., Synthesis of monodispersed molecularly imprinted polymer particles for high-performance liquid chromatographic separation of cholesterol using templating polymerization in porous silica gel bound with cholesterol molecules on its surface. Journal of Chromatography A, 2010. **1217**(46): p. 7249-7254.
10. Unsal, E., et al., Monodisperse porous polymer particles with polyionic ligands for ion exchange separation of proteins. Analytica Chimica Acta, 2006. **570**(2): p. 240-248.
11. Sakai, K., et al., Characterization of dendritic polymer-modified porous silica particles using size exclusion chromatography. Chemistry Letters, 2001(6): p. 510-511.

12. Liu, J., et al., Fabrication of porous polymer particles with high anion exchange capacity by amination reaction in aqueous medium. Green Chemistry, 2006. **8**(4): p. 386-389.
13. Woell, D., et al., Radical polymerization tracked by single molecule spectroscopy. Angewandte Chemie-International Edition, 2008. **47**(4): p. 783-787.
14. Uji-i, H., et al., Visualizing spatial and temporal heterogeneity of single molecule rotational diffusion in a glassy polymer by defocused wide-field imaging. Polymer, 2006. **47**(7): p. 2511-2518.
15. Gavranovic, G.T., et al., Well-controlled living polymerization of perylene-labeled polyisoprenes and their use in single-molecule Imaging. Macromolecules, 2006. **39**(23): p. 8121-8127.
16. Stankovich, S., et al., Graphene-based composite materials. Nature, 2006. **442**(7100): p. 282-286.
17. Zhang, Y.B., et al., Experimental observation of the quantum Hall effect and Berry's phase in graphene. Nature, 2005. **438**(7065): p. 201-204.
18. Zhang, Y.B., et al., Electric field modulation of galvanomagnetic properties of mesoscopic graphite. Physical Review Letters, 2005. **94**(17).
19. Li, X.L., et al., Chemically derived, ultrasmooth graphene nanoribbon semiconductors. Science, 2008. **319**(5867): p. 1229-1232.
20. Schedin, F., et al., Detection of individual gas molecules adsorbed on graphene. Nature Materials, 2007. **6**(9): p. 652-655.
21. Wang, X., L.J. Zhi, and K. Mullen, Transparent, conductive graphene electrodes for dye-sensitized solar cells. Nano Letters, 2008. **8**(1): p. 323-327.

Chapter 3.

Dispersions of polyurethane and polyurea porous particles

3.1 Introduction

3.1.1 The development of porous particles

Porous polymer particles have been of great interest for different diverse applications because of their specific property: high surface area [1-7]. Catalysts supported on the porous particles showed obviously increased activity because of the high contacting surface. One example: catalyst platinum was absorbed on the porous particles TiO_2 to degrade benzene to carbon dioxide and water [1]. Porous particles were used as filling materials for composites with low density and high resistance against struck hitting [2]. As a consequence of the holes structure, porous particles were also used for column liquid chromatography with high separation rates [5].

To prepare porous polymer particles various methods have been developed [4, 8-13]. In the Most methods, an inert solvent with low bowling point was used as porogen to form porous structure. For example, n-pentane was mixed with the monomers as dispersed phase for an emulsion. After the polymerization, n-pentane was evaporated to generate pores [4]. Another method was seeded polymerization where short linear polymers (as seed) were mixed with the monomers as dispersed phase. After polymerizations the polymers were removed by washing with a solvent [9-11]. With this method different mono-disperse porous polymer particles were prepared, for example polar poly(2-hydroxyethyl methacrylate-ethylene dimethacrylate) and apolar poly(polyethylene glycol methacrylate-ethylene dimethancrylate) [11]. Controlled freezing emulsion was another method to produce porous particles [4, 12-14]. For example, Poly(ε-caprolactone) and polystyrene porous microparticles were prepared in an aqueous emulsion: these polymers were at first dissolved in *o*-xylene, then used as dispersed phase to prepare a aqueous emulsion which was later freeze-dried in liquid nitrogen [4]. In this method, the pores were formed by sublimation of ice crystal, leaving gaps or pores in their place. Since just a few organic solvents could be frozen in liquid nitrogen, such as acetone, acetonitrile, cyclohexane and dioxane, this method was strongly limited for its applications. In another method, supercritical fluids (CO_2) with physical, chemical and toxicological advantages were used to prepare porous polymer particles: liquid CO_2 as the porogen was mixed with the monomer as dispersed phase. After polymerization, liquid CO_2 was removed by decrease the pressure to form porous structure. The degree of porosity and the average pore size could be controlled by adjusting the pressure of CO_2 [12, 13]. For this method, special apparatuses with high press were needed to keep CO_2 as liquid.

All of the methods mentioned above needed a porogen which had to be added before the preparation of particles and removed later to form porous structure. Compared to them, the preparation of polyurethane foam did not use any porogens: the porous structure was formed by the released CO_2 from the reaction between monomer diisocyanate and water [15-21]. The process consisted of two steps: gelling and blowing reactions. In the first step, diisocyanate in an excess reacted with diol to prepare polyurethane chains with isocyanate end groups. In the second, the NCO end groups reacted with water, forming porous structure by the released CO_2.

By using this method, polyurethane porous particles were prepared in the previous work of the group: water and diol as monomers were dispersed in a non-aqueous emulsion. Aromatic diisocyanate 4,4′-methylenebis(phenyl isocyanate (MDI) was dropped into this emulsion (Figure 1) [22]. The chose of aromatic diisocyanates (instead of aliphatic diisocyanates) was due to their high reactivity with water (aliphatic ones reacted with water relatively slowly). Unfortunately, the non-aqueous emulsions did not keep stable during the polymerization and completely collapsed at the end of the preparation. It probably was caused by the high reactivity of aromatic diisocyanate (MDI) [23]. The dropped MDI reacted immediately with the droplets of diol and water in the emulsion before it was homogenously dispersed as small droplets [24].

Another problem in the previous work: some of particles were highly porous and some still compact. This problem was probably caused by inhomogeneous distribution of water in all of the droplets. Therefore, in the following work the development of a stable emulsion for the polymerization and the preparation of homogenously porous particles are two important tasks.

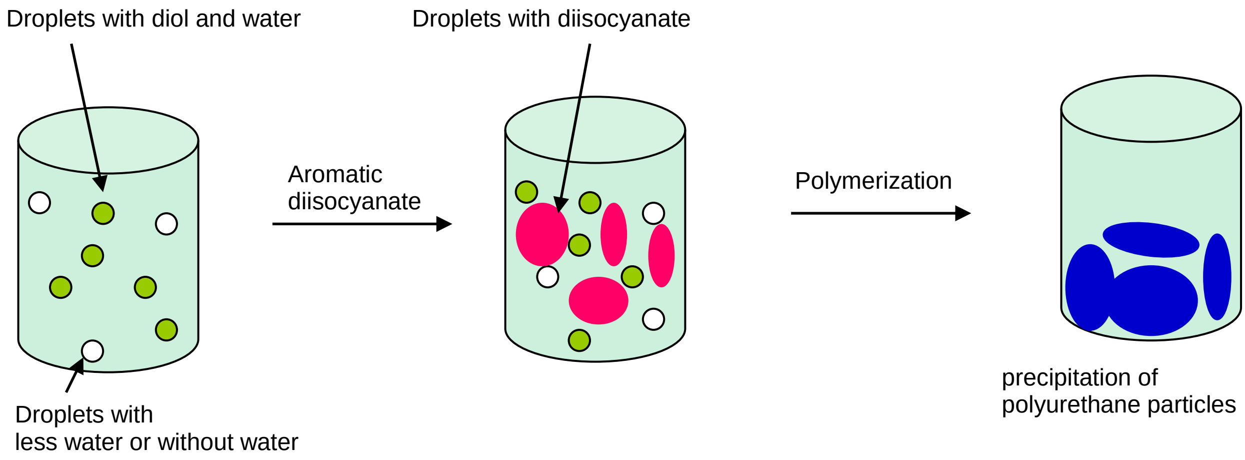

Figure 1. Schematic representation of the synthesis of porous polyurethane particles in the earlier work of our group

3.1.2 Catalysts for polyurethane

Normally two kinds of catalysts were used to regular the porous structure in polyurethane foam: One had selectivity towards water and one towards diol. The catalysts balance gellation reaction (reaction between diisocyanate and diol) and blowing reaction (reaction between diisocyanate and water) to form different porous structure (large, small, close or open pores) [25, 26]. By using a catalyst with a low selectivity for gellation and one with a high selectivity for blowing reaction, large pores and low density can be obtained. When a catalyst with strong preference for gellation and one with weak preference for blowing are chosen, polyurethane foam with small pores and high density can be produced [27].

The catalysts can be classified two categories: amine and Sn catalysts. Mostly used amine catalysts to prepare polyurethane foams are Bis(2-dimethylaminoethyl)ether (DMDEE), bis(2-dimethylaminoethyl)ether (BDMAEE), *N,N,N´,N´´,N´´*-pentamethyldipropylene triamine (PMDPTA) and triethylene diamine (TEDA) (Figure 2). DMDEE is a catalyst which has a high selectivity toward water because of the formation of chelatkomplexe [23]: with two nitrogen and three oxygen atoms, DMDEE contains five potential hydrogen-bonding sites. Compared with DMDEE, the selectivity of bis(2-dimethylaminoethyl)ether (BDMAEE) toward water is not quite high; because it dose not have so many H-bonding sites like in DMDEE. The NMe_2 nitrogen centres in BDMAEE are less steric hindered than in DMDEE, allowing access of alcohol [23]. *N,N,N´,N´´,N´´*-pentamethyldipropylene triamine (PMDPTA) has a higher preference for gellation reaction; because the active amine centres are separated by propylene bridges which places the amine centres apart, making the chelation of water entropically less favourable [23]. The catalyst TEDA is a most powerful catalyst with a high selectivity toward diols in these four catalysts. Its structure does not allow chelation of water and the nitrogen atoms have much less steric hindrance compared with the other catalysts [23]. This makes coordination of the larger diols reactants to the amine groups in diisocyanates much easier.

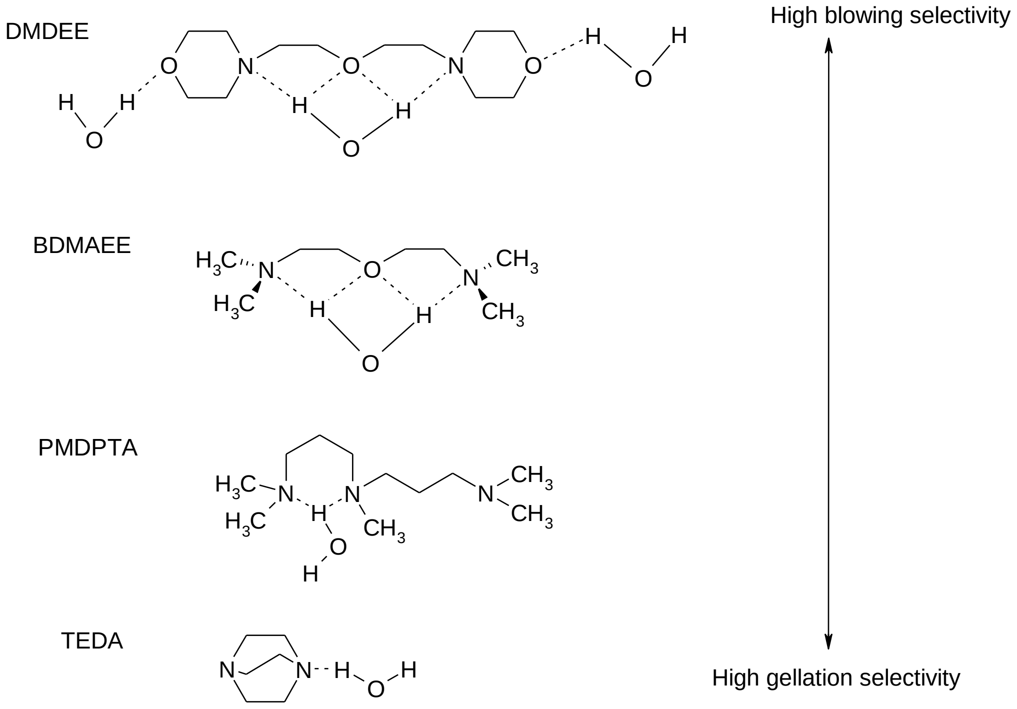

Figure 2. Amine catalysts and their selectivity [23].

3.1.3 The reactivity of diisocyanates

It is known that aliphatic diisocyanates have much lower reactivity than aromatic ones due to their chemical structure. The resonance structure of the aliphatic isocyanate shows the electron density concentrating only at the nitrogen and the oxygen atoms (Figure 3). In aromatic isocyanate, the electron density is delocalized in the whole aromatic ring causing a higher positive charge on the carbon atom of the isocyanate group NCO [23]. Hence it is more reactive towards nucleophiles such as alcohols and protic amines. One idea for a stable emulsion to prepare porous polyurethane particles is to use a mixture of aromatic diisocyanate MDI and aliphatic diisocynates hexamethylene diisocyanate (HMDI) which can suppress the reactivity of the 4,4′-methylenebis(phenyl isocyanate (MDI).

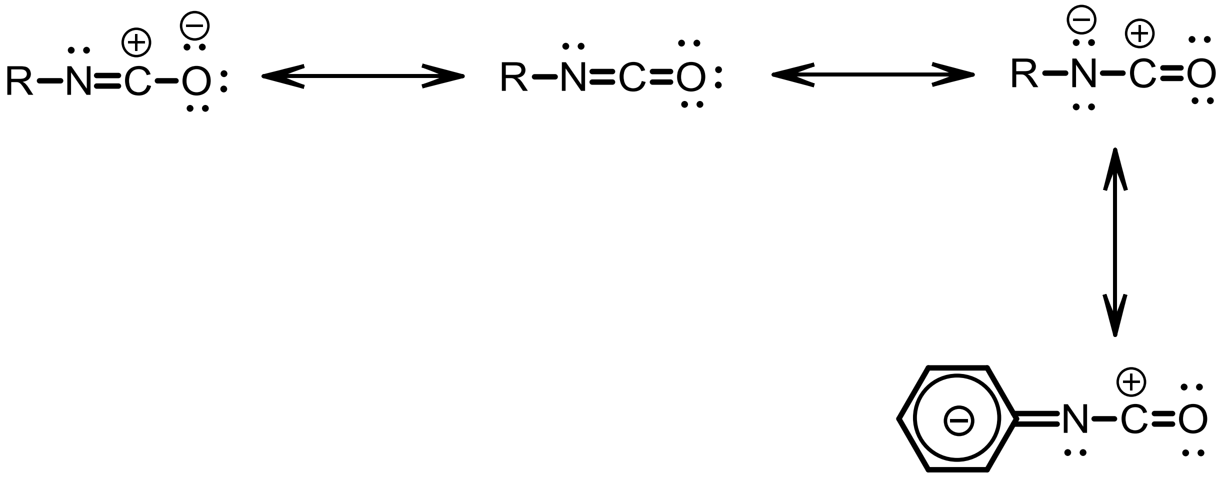

Figure 3. Resonance structure of the aromatic isocyanate group [23].

3.2 Preparation of a stable emulsion

With this idea, a set of experiments was carried out in which a mixture of aromatic and aliphatic diisocyanates with a ratio varying from 1:5 to 2:1 was used. The experiments were simplified by using only 1,4-bis(hydroxymethyl) cyclohexane (BHC) as monomer in absence of water. The preparation consisted of two steps: at first, an emulsion was formed with BHC in Dimethylformamide (DMF) as dispersed phase. BHC was catalyzed with triethylene diamine (TEDA) which had high selectivity toward diols (BHC was mixed with BHC). The mixture of aromatic and aliphatic diisocyanate in DMF was slowly dropped into this emulsion. The polymerization was carried out for eight hours and then was stopped by addition of *n*-hexane. The particles were collected by using a separating tunnel (Figure 4).

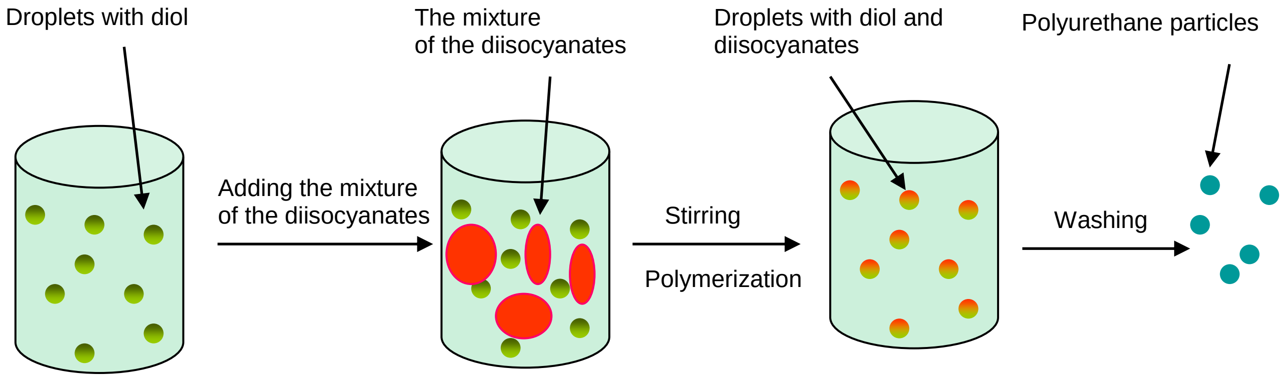

Figure 4. Schematic representation of a synthesis of polyurethane particles with a mixture of aromatic and aliphatic diisocyanates.

These emulsions showed a high stability than the one containing only aromatic diisocyanates. Only in the sample YZ140 with a ratio 2:1 a small amount of aggregates was observed. The improved stability suggested that the reactivity of diisocyanates was sufficiently suppressed by adding aliphatic ones. The reaction between diisocyanates and diols took place after that diisocyanates had been homogenously dispersed as small droplets in the emulsion. In addition, an improved solubility of aromatic diisocyanate in DMF was also observed. MDI itself could only be suspended in DMF. But the mixture of MDI and HMDI in DMF was a stable solution which could be better dispersed in the continuous phase.

Dispersion	MDI (mmol)	HMDI (mmol)	Diol (mmol)	Catalyst (mg)	Particle (nm)
YZ122	0	1	1	10	Aggregates
YZ123	0.5	2.5	2.5	10	200-500
YZ133	0.5	2.0	2.5	10	300-500
YZ135	0.5	0.5	1	10	50
YZ140	0.5	0.25	0.77	10	150-200

Table 1. Composition of the emulsions and analytical data of the polyurethane particles with different ratios of aromatic to aliphatic diisocyanates

As shown in Table 1 and SEM image (Figure 5), the ratio of aromatic diisocyanate to aliphatic showed a strong influence on the particle size. In the case of YZ123 (Figure 5-A) with a ratio 1: 5 (aromatic one to aliphatic one), the particles size had a broad distribution between 200 nm and 500 nm. Similarly by sample YZ133 (Figure 5-B) with a ratio 1:4, the particle size was in the range of between 300 nm and 500 nm. When the same amount of aromatic diisocyanate was used as the aliphatic one (sample YZ135 in Figure 5-C), the particles size showed a narrow distribution about 50 nm. When the content of aromatic diisocyanate was more than aliphatic one (sample YZ140 with ratio 2:1 in Figure 5-D), the particles size distribution became broader again between 150 nm and 200 nm with a small amount of aggregates. The dependence of the particle size on the ratio MDI/HMDI was presented in Figure 6. It showed that the ratio 1:1 gave the narrowest distribution of particle size and smallest particles.

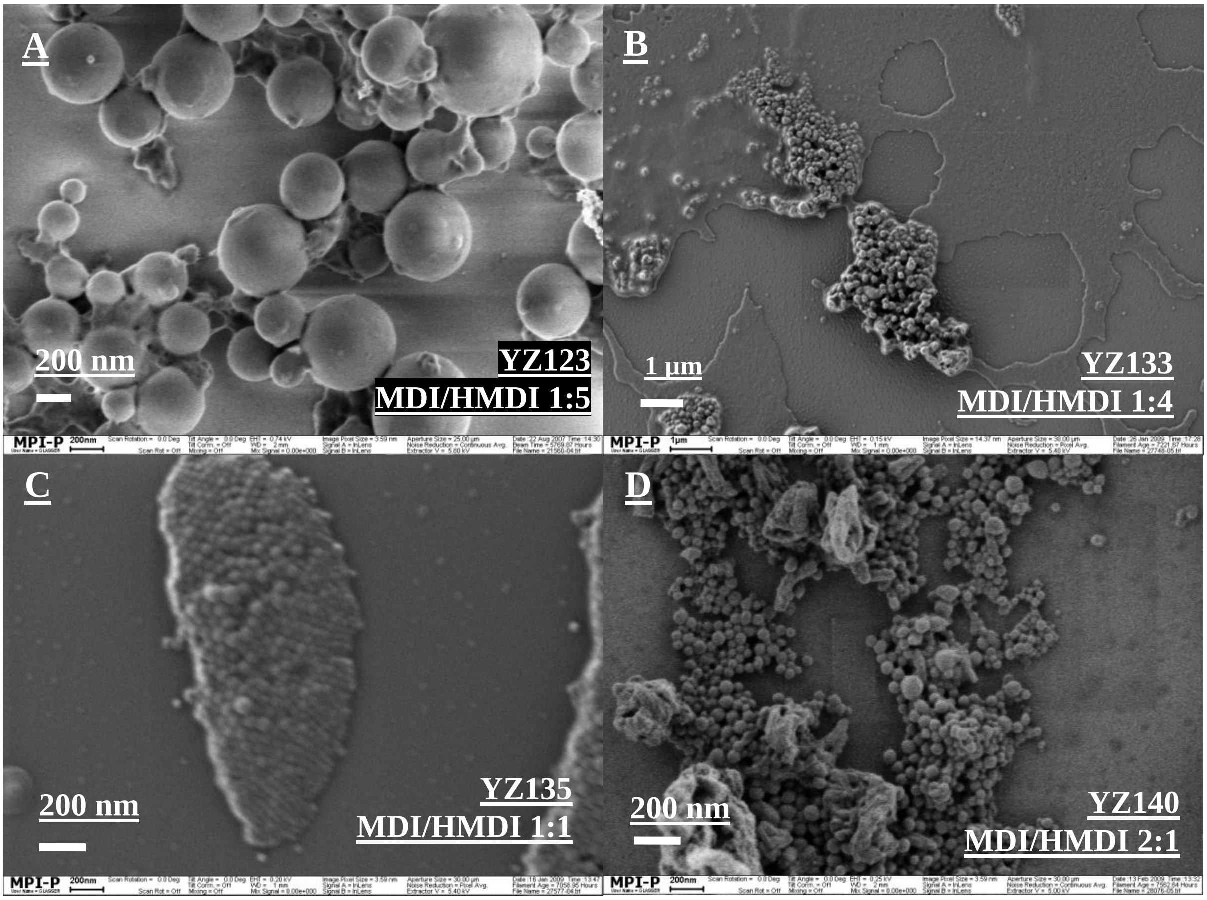

Figure 5. SEM images of polyurethane particles synthesized with different ratios of aromatic to aliphatic diisocyanates.

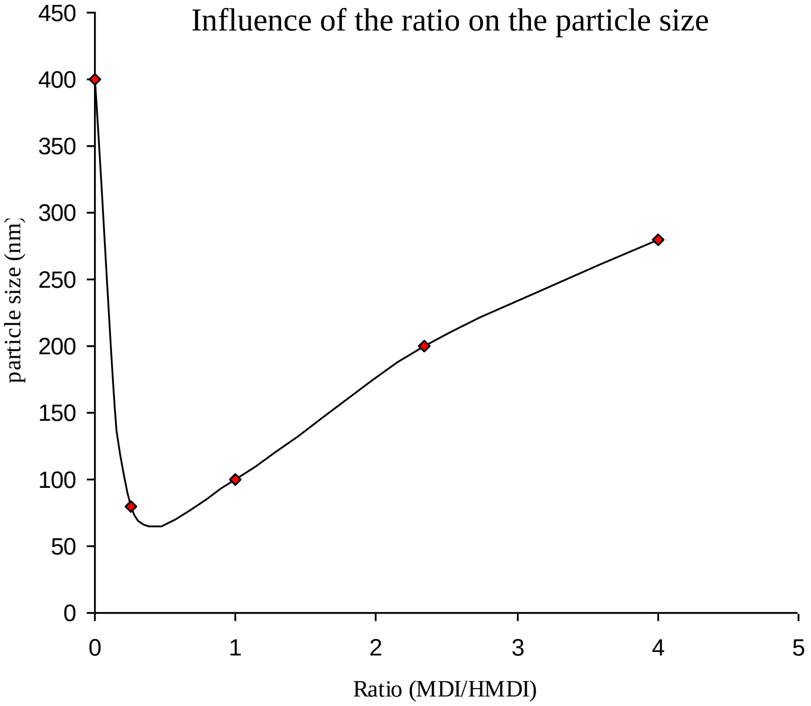

Figure 6. The diagram of the particle size versus the ratios MDI/ HMDI

The change of the particle sizes could be explained by the miscibility of the mixture of diisocyanates (MDI and HMDI) with the continuous phase *n*-hexane. Because HMDI had a good solubility in *n*-hexane, a high content of HMDI in the mixture could lead a high miscibility in the continuous phase. Therefore diisocyanate could diffuses into the continuous phase, causing Ostwald ripening effect: small droplets coalesced to large ones (as observed in sample YZ123 (HMDI : MDI 5:1,). With a suitable content of HMDI, the mixture of diisocyanate had a low miscibility in continuous phase, like in the sample YZ135 (MDI to HMDI 1:1), Ostwald ripening effect was most strongly suppressed and the particles had narrow distribution.

3.3 Preparation of polyurethane porous particles

3.3.1 Fission/fusion method

3.3.1.1 Preparation of porous particles

In preparation of porous particles, a mixture of aromatic and aliphatic diisocyanate was used to form a stable emulsion. Another problem in the previous work was that not all of particles were porous. It could be caused by inhomogenously distributed water in the emulsion. A fission/fusion method was used in this work to solve this problem. This method was reported to distribute carbon black in polymer particles: the fission/fusion process destroys all liquid droplets, and only hybrid ones being composed of all of kinds of compounds remained due to their higher stability [28]. This process could be realized by high energy ultrasound. In the present work, water and diols as monomers were dispersed in an emulsion with the fission/fusion process.

The preparation of porous polyurethane particles consisted of two steps: at first water with catalyst DMDEE (high selective toward water) and diol with catalyst TEDA (with high selective toward diol) were separately mixed with DMF. Then both mixtures were used as dispersed phase to form separated emulsions which were later mixed together by treatment of ultrasound to form a new emulsion. At the next step, a mixture of aliphatic and aromatic diisocyanates with a ratio 1:1 was dropwise added into the new formed emulsion. The polymerization was carried out for eight hours and was stopped by addition of an excess of *n*-hexane. The particles were collected from the dispersion by using a separating funnel (Figure 7).

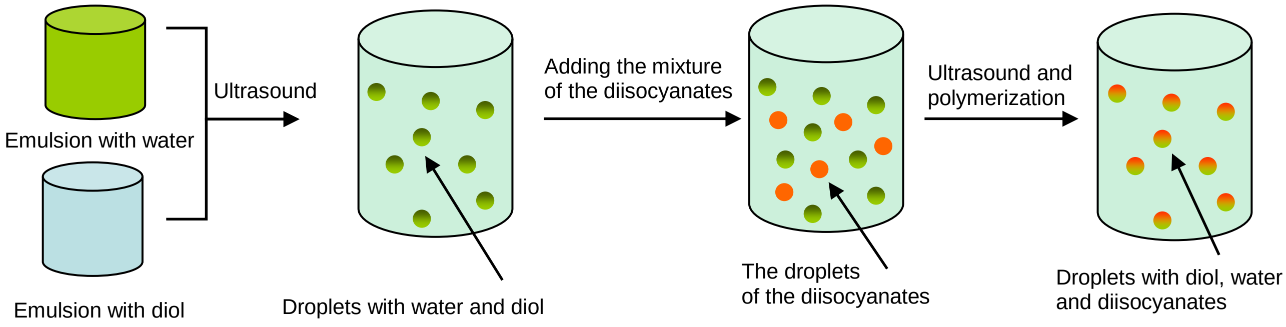

Figure 7. Schematic representation of the synthesis of polyurethane porous particles with fission/fusion method

Reaction between diisocyanate and diol

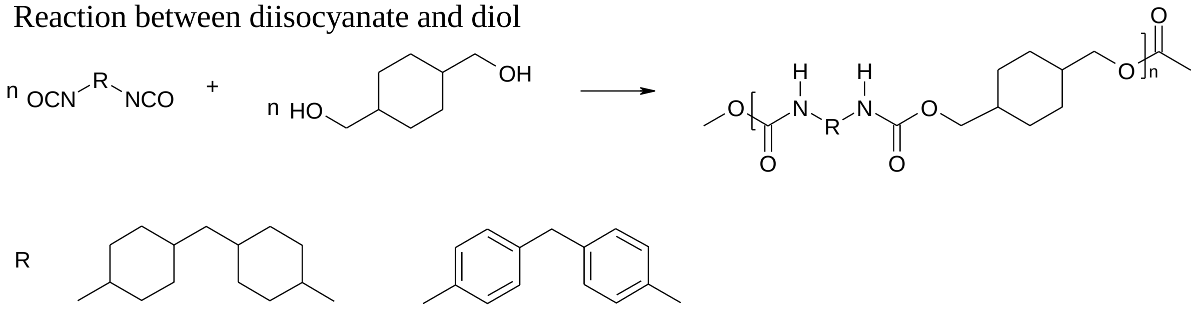

Reaction between diisocyanate and water

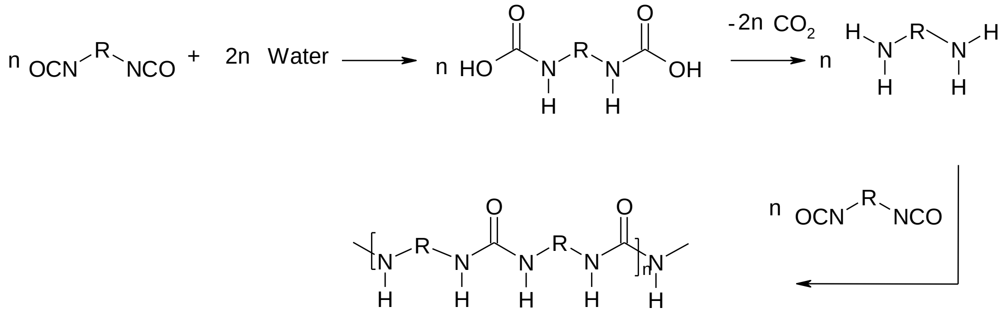

Figure 8. The reactions in preparation of porous polyurethane particles

Two reactions took place during the preparation: the reaction between diisocyanate and diol was for polyurethane pore walls (Figure 8). Diisocyanate reacts with water releasing CO_2 forming porous structure in the particles.

Dispersion	Water (mmol)	Diol (mmol)	MDI (mmol)	HMDI (mmol)	Particle (μm)	Porosity
YZ134	1	1	1	1	0.05	No
YZ136	3	1	2	2	2-2.5	Yes
YZ169	5	1	4.5	4.5	1.5-2	Yes
YZ143	10	1	5.5	5.5	1-3	Yes
YZ144	20	1	10.5	10.5	2	Yes

Table 2. The composition of the emulsions and the analytical data of the porous particles.

To investigate the influence of amount of water on the porosity, a set of experiments were carried out where the ratio water to diol varying from 1:1 to 20:1. As shown in Figure 9 (A and B), in sample YZ134 with a ratio of 1:1 (water to diol) the obtained particles had an average size 50 nm, but were not porous. When the ratio was increased to 3:1 (water to diol), the particles became porous (sample YZ136 Figure 9 C and D). Some particles with large holes were observed and some ones with polymer fibrils.

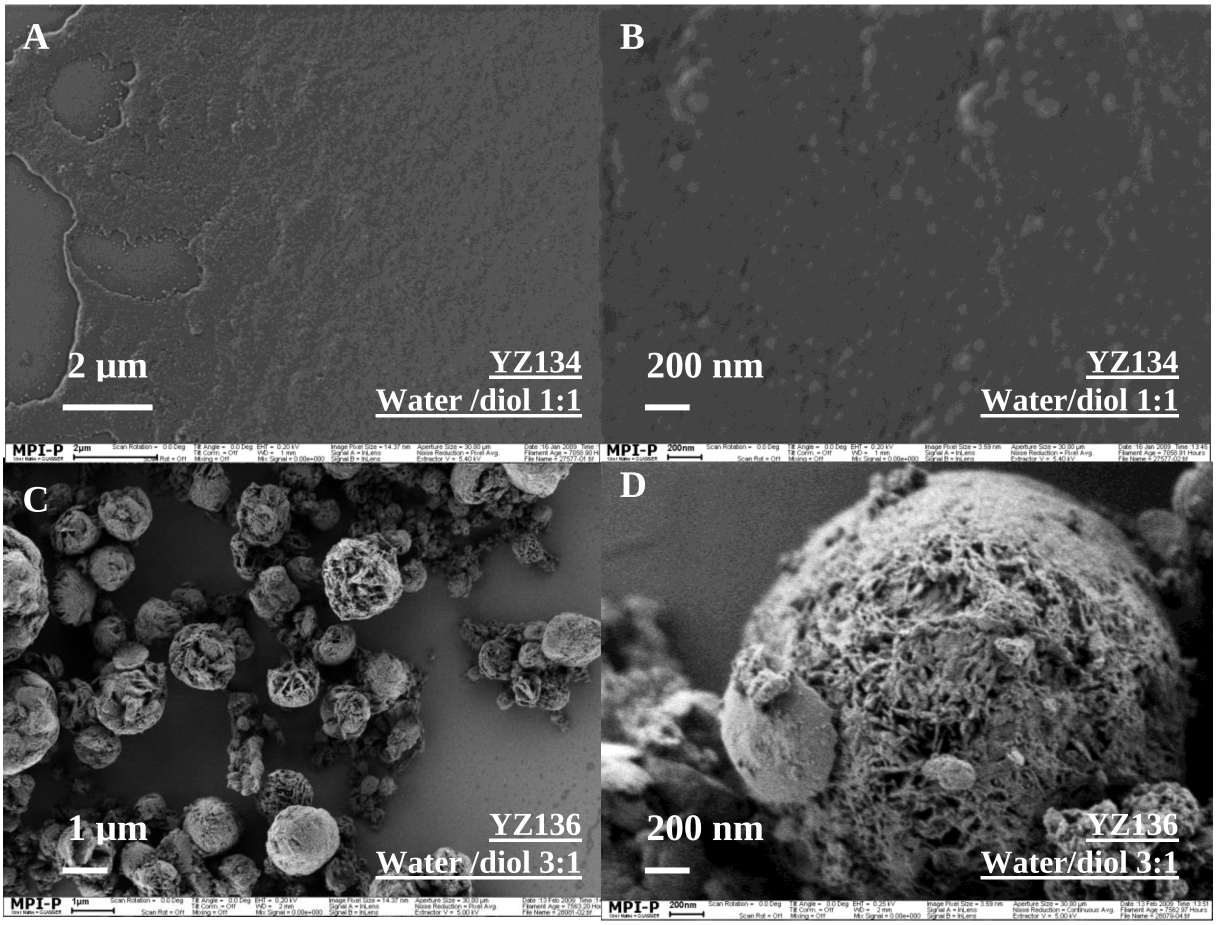

Figure 9. SEM images of sample YZ134 and YZ 136.

At the ratio of water to diol of 10:1 (sample YZ143 in Figure 10 A and B), the original spherical shape of the particles was almost completely destroyed, probably caused by a quick release of a high amount of carbon dioxide. In the sample YZ144 (Figure 10 C and D), the amount of water was twenty times higher than that of diols. Here the porous structure was very different from the other samples. It consisted of small particles with a size about 20 nm. It was reported that in polyurethane foam crystal microdomains from hard polyurea segment with a size ranging from 20 nm to 100 nm were sometimes observed [29, 30]. The small particles here could be polyurea microdomains. The results above demonstrated that the ratio of water to diol played an important role for the porous structure.

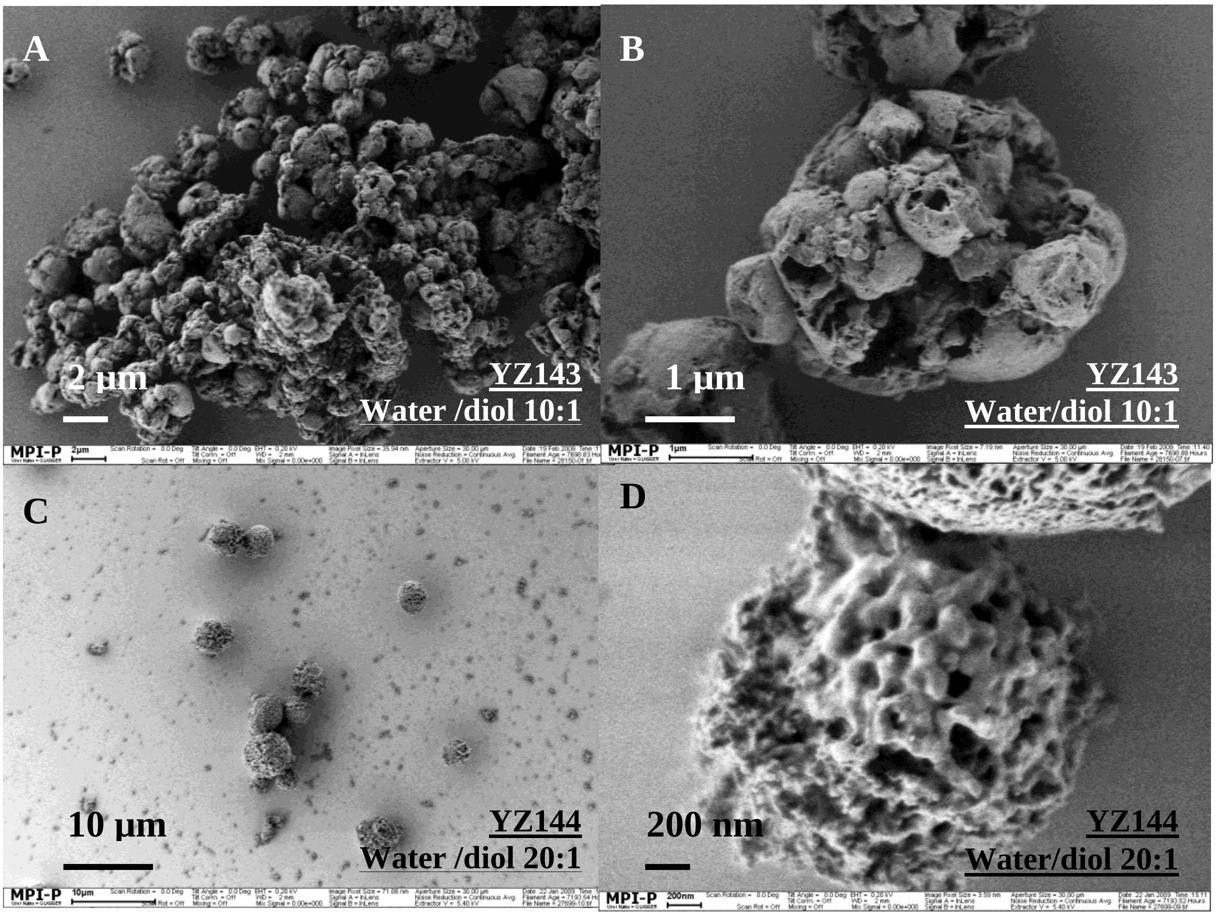

Figure 10. SEM images of sample YZ143 and YZ144

3.3.1.2 The influence of different catalysts

For preparation of polyurethane foam, the porous structure could be controlled by the chose of different catalysts. Here the influence of the catalysts on the porosity in particles was studied by using four different catalysts: DMDEE, BDMAEE, PMDPTA and TEDA. The selectivity towards to water decreases from DMDEE to TEDA, but selectivity towards diol increases (in sec 3.1.2 Figure 2). A set of experiments were carried out by using these catalysts (Table 3).

	Catalyst A	Catalyst B	Particle size (µm)
YZ51	DMDEE (100 mmol)		1
YZ52	DMDEE (50 mmol)	BDMAEE (50 mmol)	1.5
YZ53	DMDEE (50 mmol)	PMDETA (50 mmol)	2.5
YZ55	DMDEE (50 mmol)	TEDA (50 mmol)	2
YZ55	TEDA (100 mmol)		0.7

Table 3. The chosen catalysts and the amount used in the polymerization.

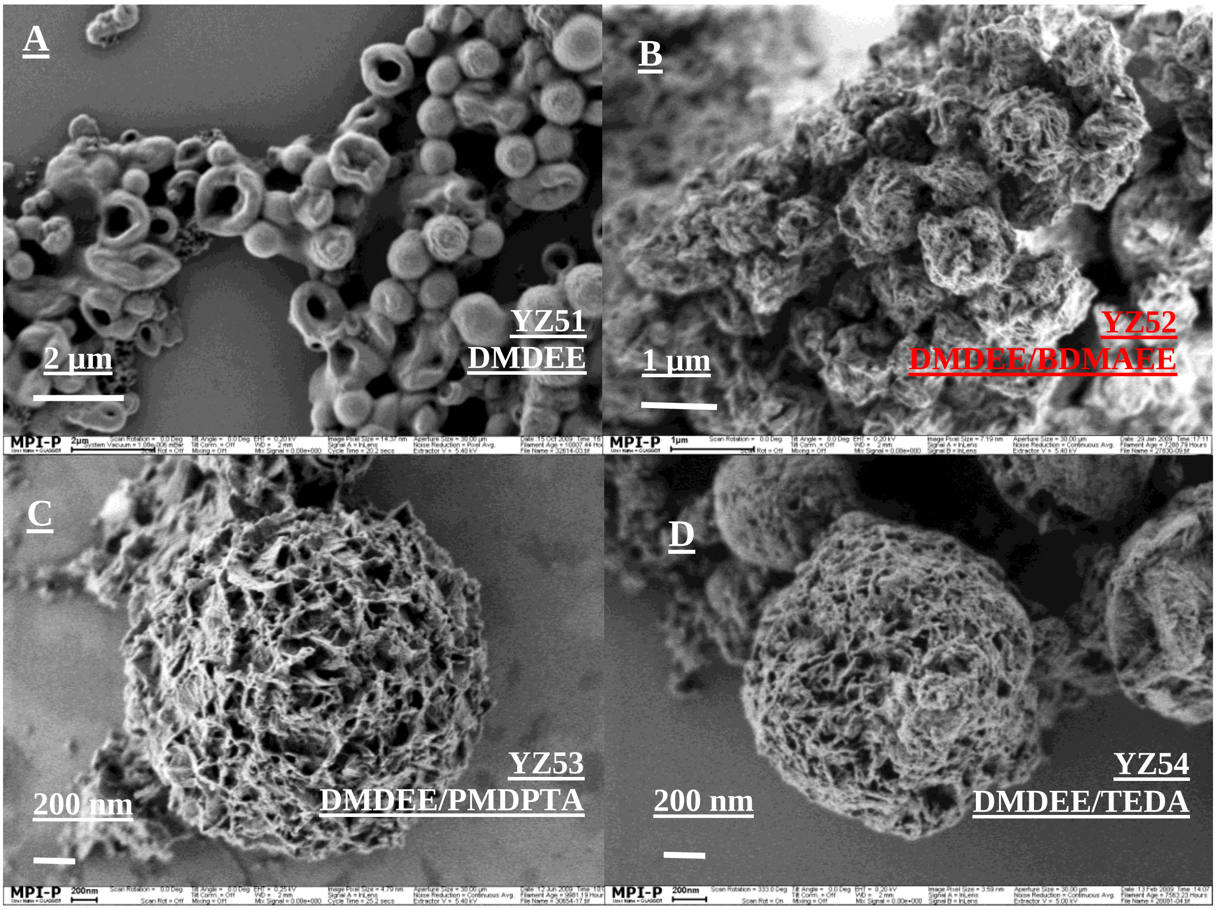

Figure 11. The SEM images of polyurethane porous particles with different catalysts.

The porosity of the obtained polyurethane particles were investigated by SEM: in the case where only DMDEE (highly selectivity toward water) was used (sample YZ51 in Figure 11 A), shrunk particles were observed. Probably CO_2 was released too early and the pore walls were still soft (low molecular weight, low mechanical strength). In the sample where reaction between diisocyanate and water was catalyzed by DMDEE (highly selectivity toward water) and the reaction between diisocyanate and diol by BDMAEE (high selectivity towards water), particles with a lot of shrunk pores were also obtained (Sample YZ52 in Figure 11 B). When both reactions were catalyzed with differently selective catalysts in sample YZ53 (DMDEE with high selectivity towards water and PMDPTA with high selectivity towards diol) and in sample YZ54 (DMDEE with high selectivity towards water and TEDA with high selectivity towards diol): particles with high homogeneous porosity were obtained (in Figure 11 C and D). When only catalyst TEDA with strong selectivity to diol was used (Sample YZ55 in Figure 12), broken particle with inhomogeneous pores were observed. Furthermore, the pore walls were much thicker than in other sample. The results demonstrated that homogenously porous structure strongly depended on the balance of two reactions: gellation reaction (reaction between diisocyanate and diol) and blowing reaction (reaction between diisocyanate and water).

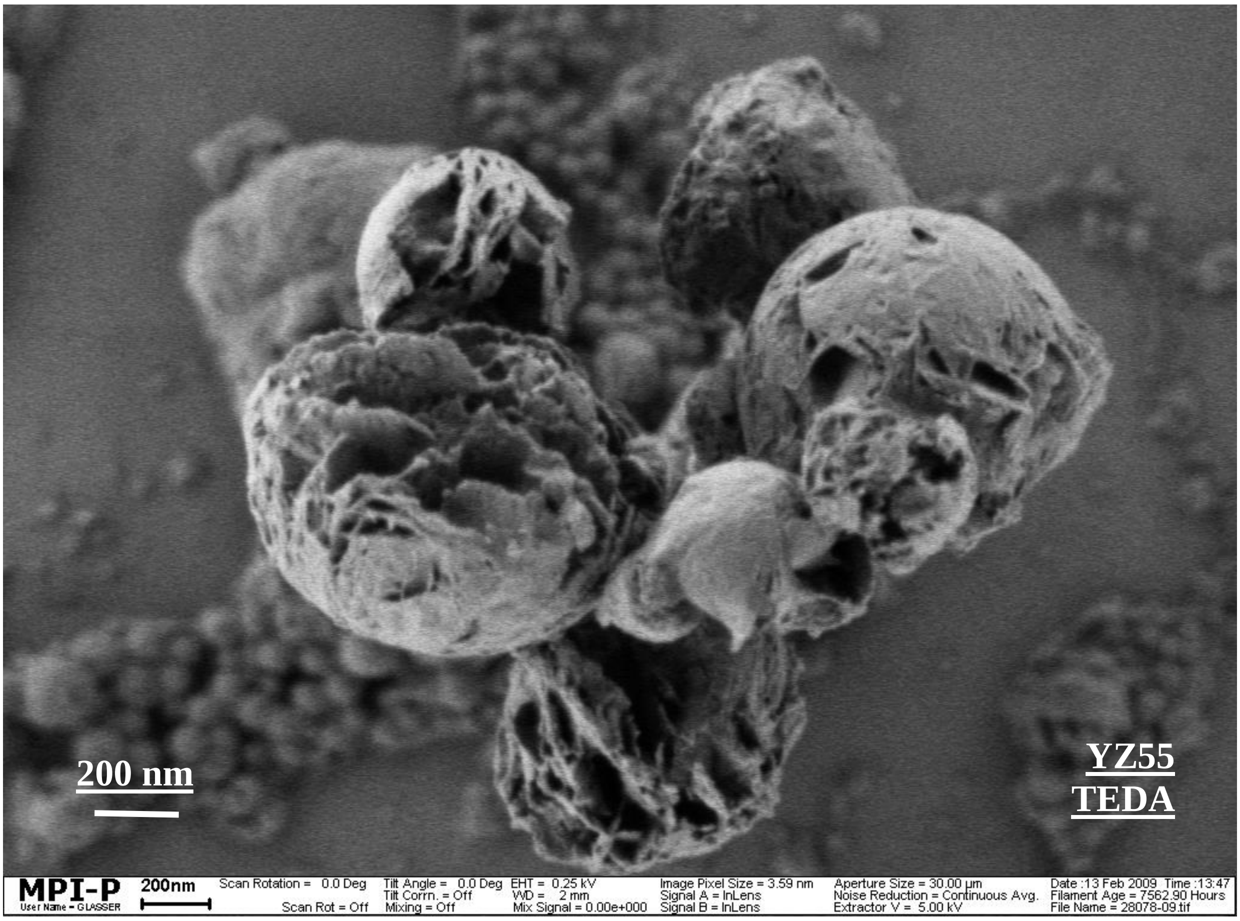

Figure 12. The SEM image of polyurethane porous particles from sample YZ55

3.3.1.3 The influence of molecular weight of diols

It was also reported that the porosity of polyurethane foams could be controlled by using diol with different molecular weights [25, 31, 32]. Hard polyurethane foams containing small pores were synthesized with low-molecular-weight polyethylenglycols (PEO) and soft foams containing large pores by using high-molecular-weight one. In the present work, PEO with different molecular weight was also studied.

Polyethylenglycols with a molecular weigh from 500 g/mol to 2000 g/mol were chosen as monomers. Two catalysts were used: DMDEE for the reaction between water and diisocyanates, TEDA for the reaction between polyethylenglycols and diisocyanates. The ratio of water to polyethylenglycols was kept constant at 3:1. It was found that polyethylenglycols were difficult dispersed in the emulsions which had to be treated by ultrasonication for one hour. The emulsions kept only stable for short time after the addition of diisocyanates. These results suggested that this emulsion could not stabilize polymers as monomers.

3.3.1.4 The drawback of fission/fusion method

In this study, “compact particles” were sometimes observed (Figure 13) in some samples, when diisocyanates were too slowly dropped into the emulsion. But when these particles were washed by THF, a layer of shin on the particles was removed and the particles became porous. The formation of shin could be caused by the side reaction of diisocyanates: Diisocyanates could react not only with water and diol, and also with the urethane and urea groups, due to their high reactivity. During the polymerisation, the viscosity of particles became higher and higher. After sometime, the viscosity was so high, that diisocyanates could not diffuse into partials, but only react on the surface of the particles where there were only urethane and urea groups. Hence a layer of skin was formed on the particles.

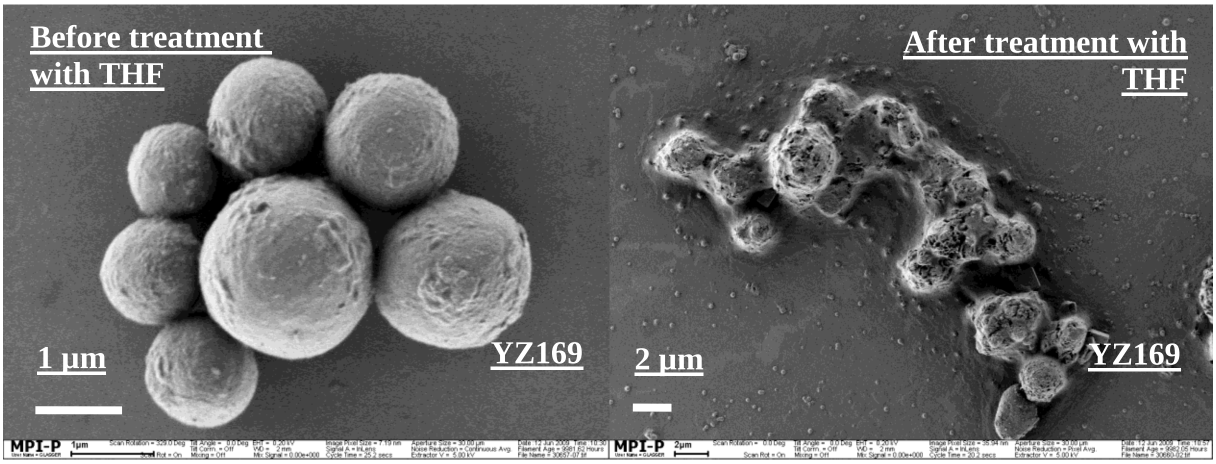

Figure 13. SEM images of sample YZ169. Left: before washing with THF; right: after washing with THF.

3.3.2 Combination method

To prevent the formation of shin, another method was investigated where diisocyanates in DMF and diol in DMF were used as dispersed phase to separately form emulsions. The particles were prepared by mixture both emulsions. An important point in this method was that diisocyanate had an excess compared with diol. The polyurethane chains in the particles were with isocyanate end groups which could react later with water, releasing CO_2 forming porous structure.

The method consisted of three steps: at the first step, two emulsions were prepared with diisocyanate (consisting of aromatic and aliphatic diisocyanate with a ratio 1:1) and diol (with a mixture of DMDEE and TEDA catalysts) as dispersed phase. At the second step, both emulsions were mixed by treatment of ultrasound. The new formed emulsion was stirred for 8 h at room temperature. At the end, the obtained particles were washed with hydrous THF. This process took one day to three days. The preparation of porous polyurethane particles was shown in the Figure 14. A series of experiments were carried out where the ratio of diisocyanates to diol varied from 6:2.5 to 3:2.5. Table 4 presented the composition of the emulsions and the analytic data of the resulting particles.

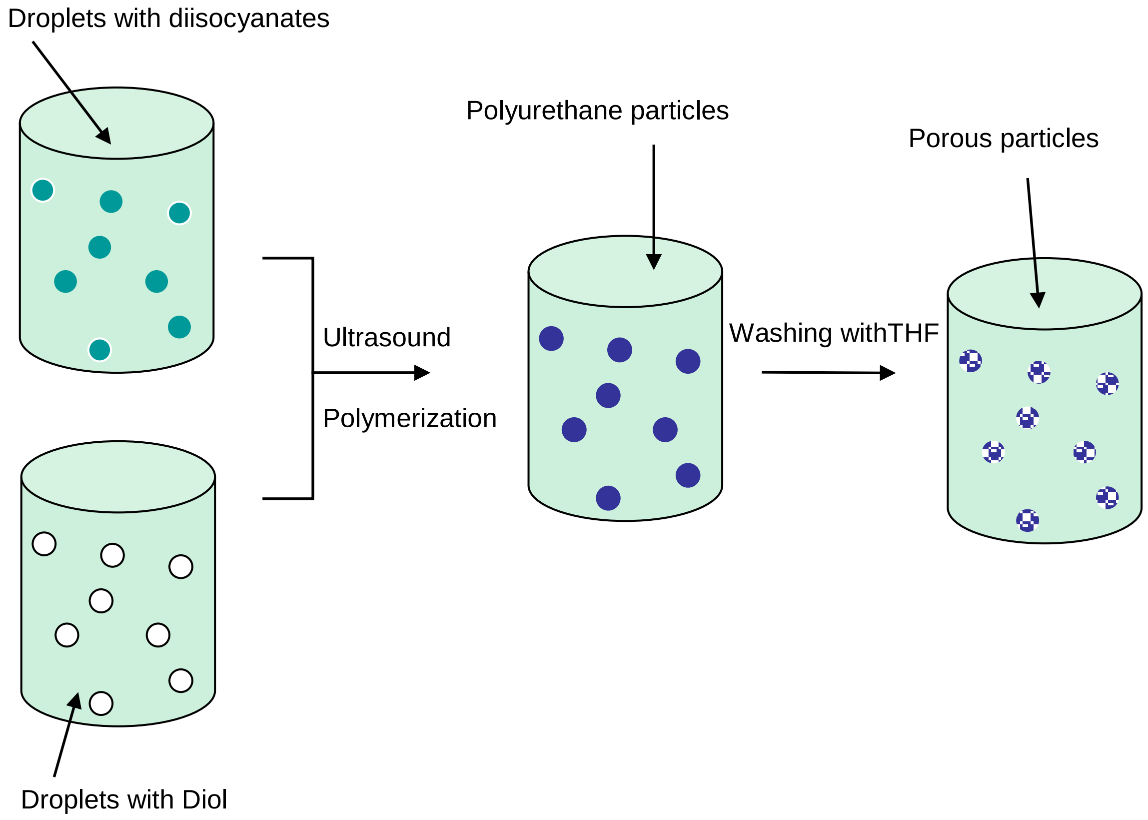

Figure 14. Schematic preparation of porous particles with combination method

Sample	MDI/HMDI (mmol)	Diol (mmol)	Particle (µm)	Yield (%)
YZ205	6	2.5	1	80
YZ235	5	2.5	1	92
YZ168	4	2.5	2.5	98
YZ197	3	2.5	2.0	91

Table 4. The composition to prepare porous particles with combination method.

Highly porous particles were obtained and it was found that the porosity was strongly influenced by the ratio of diisocyanates to diols. In the sample YZ205 with a ratio of diisocyanate to diol 6:2.5, the particles were partly dissolved in THF. When the content of diisocyanate was decreased (with a ratio of diisocyanate to diol 5:2.5 in sample YZ235), particles with small holes were observed seen in Figure 15. The surface of the particles was shrunk a little bite.

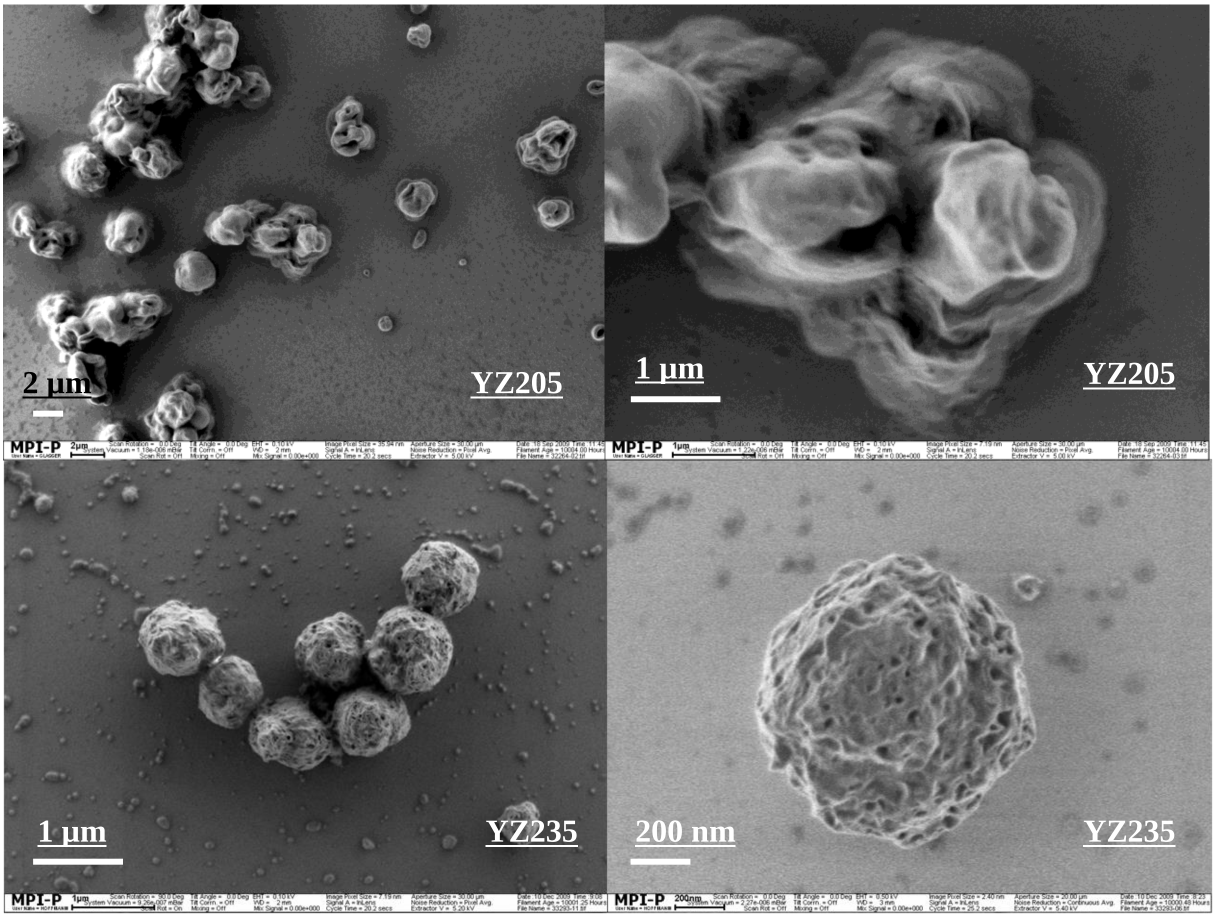

Figure 15. SEM images of sample YZ205 and YZ235

When the amount of diisocyanate monomer was two times higher than diol (sample YZ168), porous particles with highly homogenous porosity were obtained. The porous structure looked as tiny petals. On the surface of the particles, no shin was formed. Figure 16 shows the images of the particles before and after washing with THF. They became highly porous after washing and the size was increased from 0.2 µm to 1 µm. The results clearly demonstrate that water in THF was diffusing into the particles and reacted with isocyanate groups because of the diffuse gradient energy.

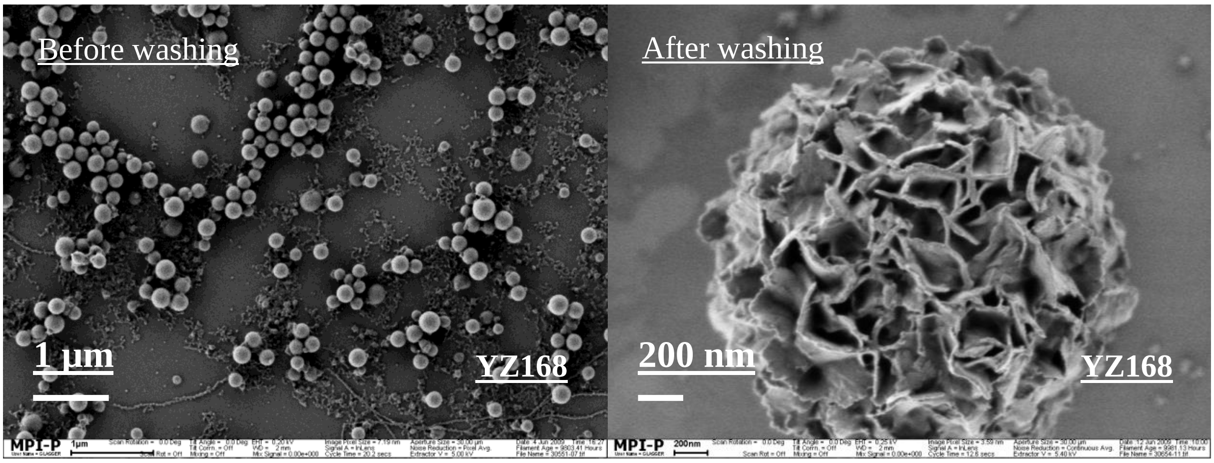

Figure 16. The SEM images of the particles from YZ168. A: the particles before washing with THF. B: after washing with THF, the particles became porous.

When the ratio was 3:2.5 (sample YZ197), the particles became only partially porous after washing in THF. They looked like blossoms that didn’t open up completely. Some of the particles were even compact (Figure 17).

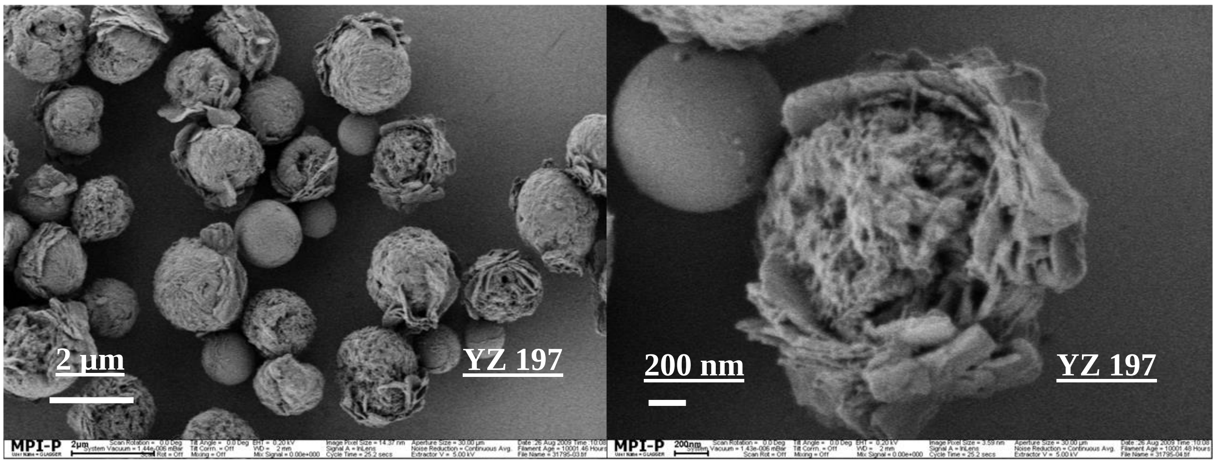

Figure 17. SEM images of porous particles synthesized with combination method

3.4 Preparation of polyurea porous particles

3.4.1 The history of polyurea particles

Polyurea, a material with excellent mechanical properties because of the rich hydrogen bonds, has been intensively studied for different applications. It was used in army vehicles for blast protection because of its high strain rates [33, 34]. Polyurea composite with the silica particles showed high flexural strength [35]. Since polyurea was completely insoluble in water, and chemically resistant to common organic solvents, polyurea capsules were used for transport and release of diverse compounds, such as ink toners, pesticides, and enzyme-loaded bioreactors [36]. Another important class of substances based on polyurea were polyurea aerogels which consisted of polyurea particles assembled together via a cluster-cluster aggregation mechanism [37, 38]. The large internal void space between particles was responsible for very low thermal conductivities and high acoustic attenuation, which was extremely attractive for practical applications. By now, porous polyurea particles were rarely reported in the literature. In the present work, porous polyurea particles will be prepared by reaction between diisocyanate and water.

3.4.2 Preparation of porous particles

The synthesis consisted of two steps: at the first step, diisocyanates (a mixture of aromatic and aliphatic diisocyanates with a ratio 1:1) and water (with DMDEE which had a high selectivity toward water) were used as dispersed phase to form separated emulsions. At the second step, both emulsions were mixed by treatment of ultrasound, and then stirred for 8 hours (Figure 18). The polymerization was carried out for eight hours and stopped by addition of *n*-hexane. The particles were collected by using a separating funnel.

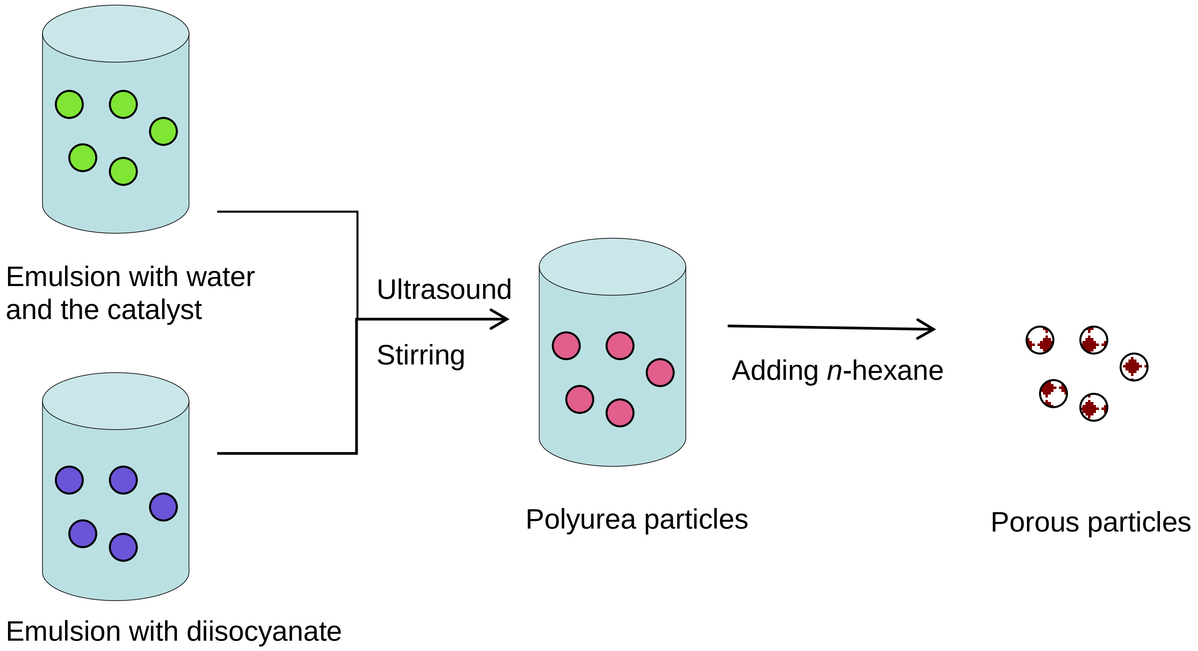

Figure 18. A schematic representation of the preparation of porous polyurea particles

Sample	MDI/HMDI (mmol)	Water (mmol)	Particle (nm)
YZ98	1	1	200-400
YZ99	1.1	1	100-400
YZ100	1.2	1	50

Table 5. Composition for preparation of porous polyurea particles.

High porous particles were obtained. To study the influence of amount of water on the porosity, the ratio of diisocyanates to water was varied from 1:1 to 1.2:1. Table 5 presented the composition of the emulsions and the analytic data of the resulting particles. It was found that the porosity of the particles was strongly influenced by the ratio (diisocyanates to water). With a ratio 1:1, porous particles with a size distribution between 200 nm to 400 nm were formed (sample YZ98 in figure 19). The particles were much smaller than porous polyurethane particles with a size about 2 µm (in section 3.3.1). The porous structure was formed by loosely contacting of small domains about 20 nm. It was similar to the one in the porous polyurethane particles with high content of water (water to diol 20:1) (section 3.3.1 sample YZ144). The domains were probably “polyurea microdomains” which were observed in polyurethane foam [25].

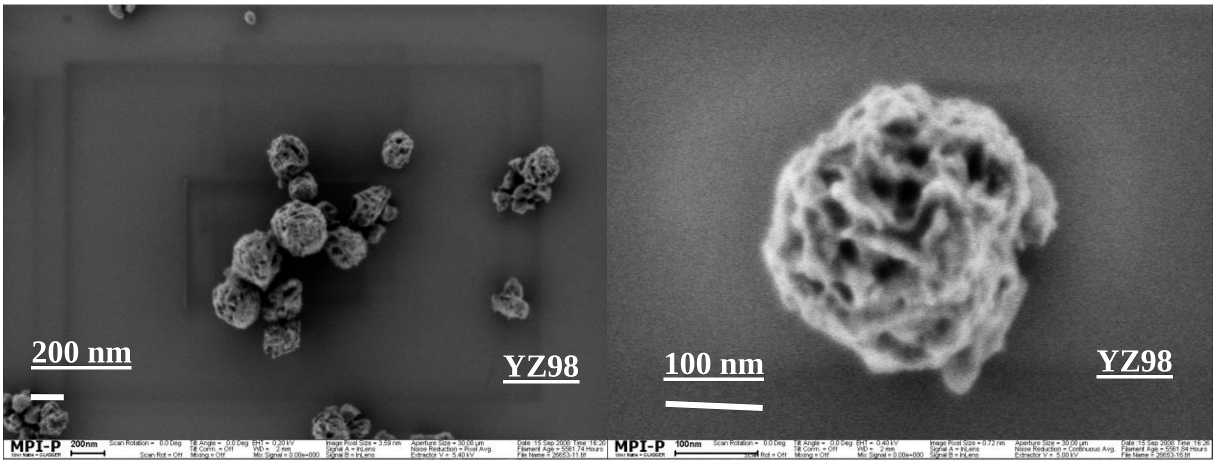

Figure 19. SEM images for porous polyurea particles (Sample YZ98).

When diisocyanate had a 10% excess compared to diols, not only spherical small porous particles with a size about 100 nm, but also porous sticks with a length of 400 nm were obtained (Figure 20). The sticks could be aggregates of small particles, because of high surface area energy of the small particles.

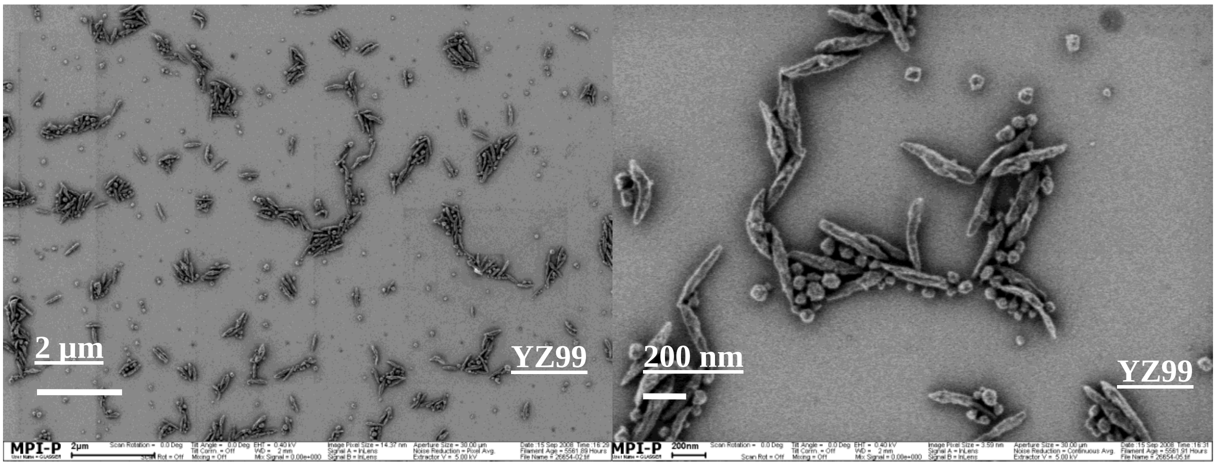

Figure 20. Porous polyurea particles from sample YZ99

As the diisocyanates had an excess of 20 % compared with diols, no spherical porous particles, but porous aggregates were formed by loosely contacting of polyurea microdomains (Figure 21).

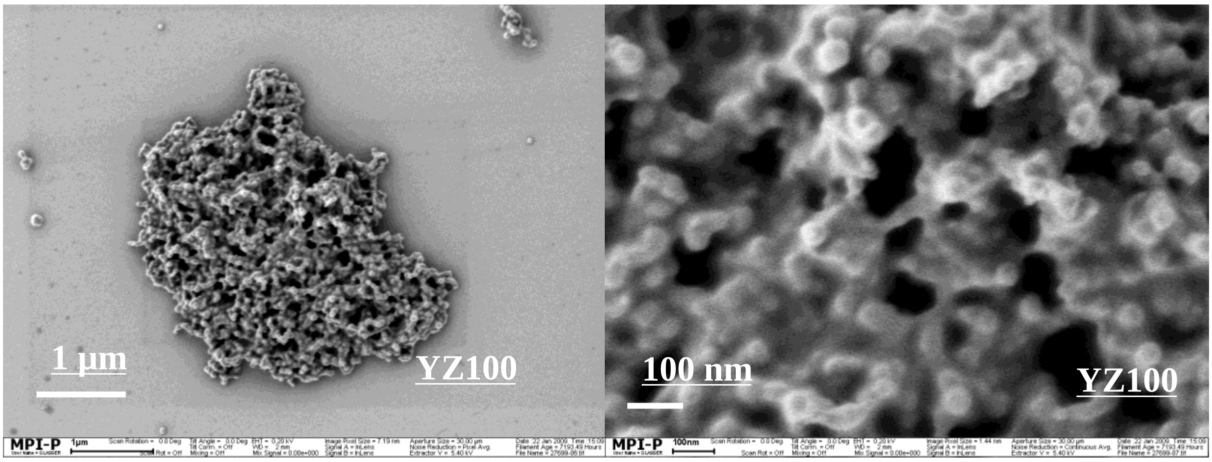

Figure 21. Porous polyurea particles from sample YZ100

3.5 Porous particles used as filling material

The obtained polyurethane porous particles were investigated as filling material for polyurethane and polystyrene composites. The addition of these particles could enhance the mechanical strength of the composites because of numerous hydrogen bonds. In addition, the large surface area could provide high amount of anchor points between matrix and porous particles, increasing the interaction.

3.5.1 Polyurethane composites

For the polyurethane composites, polyisocyanate (Desmophen) and polyol (Desmophe 680) were used as monomers to prepare polyurethane matrix. The two monomers and porous polyurethane particles were mixed together in a small amount of THF. The mixture was treated by ultrasonication for 30 minutes, and then poured into moulds which were later dried at 80 ^{o}C for 8 hours in a vacuum. A serial of sample was made that the content of porous particles was varied from 0 wt% to 7.8 wt%, to investigate the effect of the porous particles on mechanical strengths of polymer composites

At first the compatibility between polyurethane matrix and polyurethane particles were investigated by SEM (Figure 22). No aggregation of porous particles appeared in the composites. The good compatibility could be explained by the strong interaction of hydrogen bonds between them.

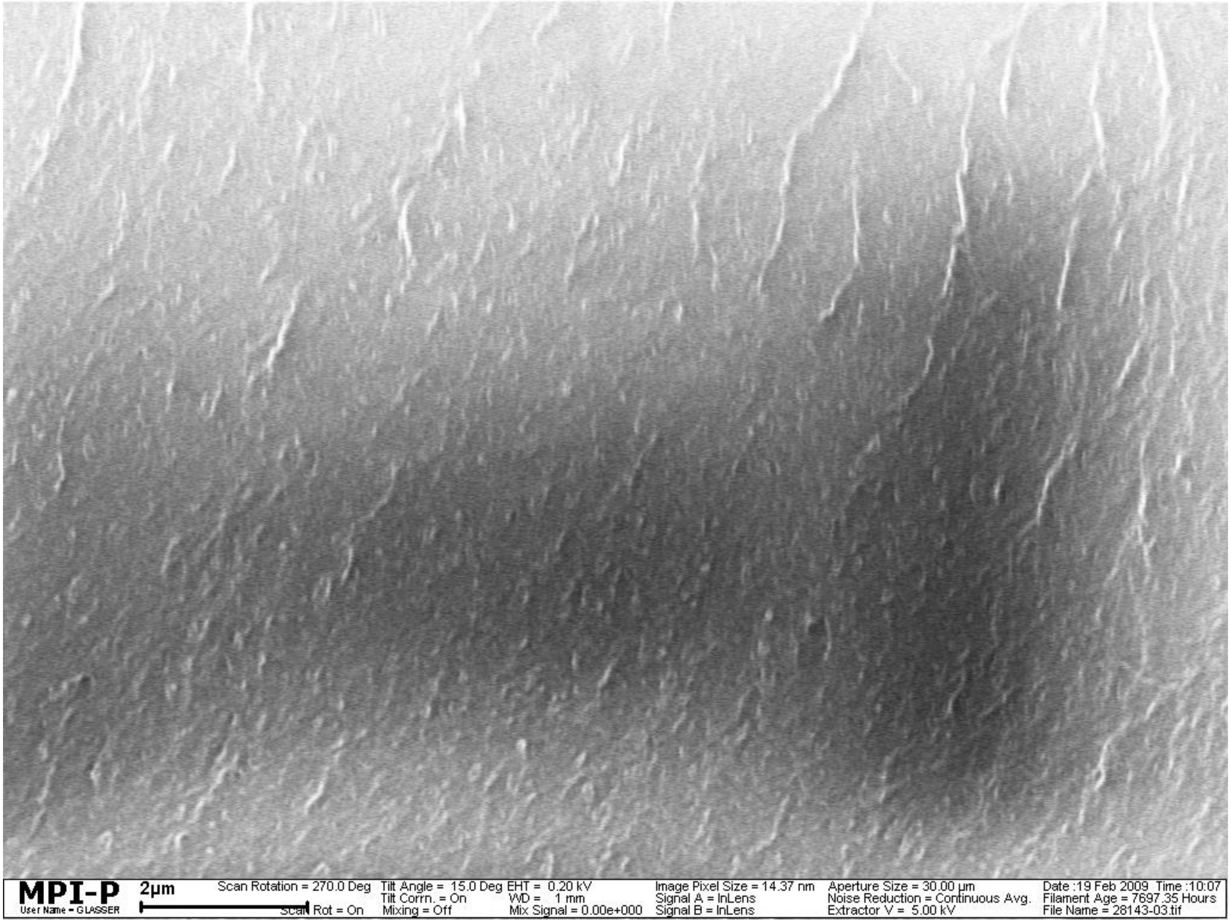

Figure 22. The SEM image of the polyurethane composites.

To investigate the influence of porous polyurethane particles on the mechanical strength, the composites were measured by dynamic mechanical thermal analysis (DMTA). The curves of the storage modulus showed high sensitivity to content of porous particles. With increasing content from 0 wt% to 7.8wt%, the storage modulus increased from $2.2x10^8$ to $6x10^8$ which were almost three times higher than the pure matrix. The enhanced storage modulus could be explained from three sides: first, porous polyurethane particle had a strong mechanical strength because of the aromatic urethane groups. Second, the particles and the matrix had good compatibility due to the strong interaction of the hydrogen bonds. At last, the porous particles had high surface area which provides large amount of anchor points with the matrix, increasing the interaction with the matrices.

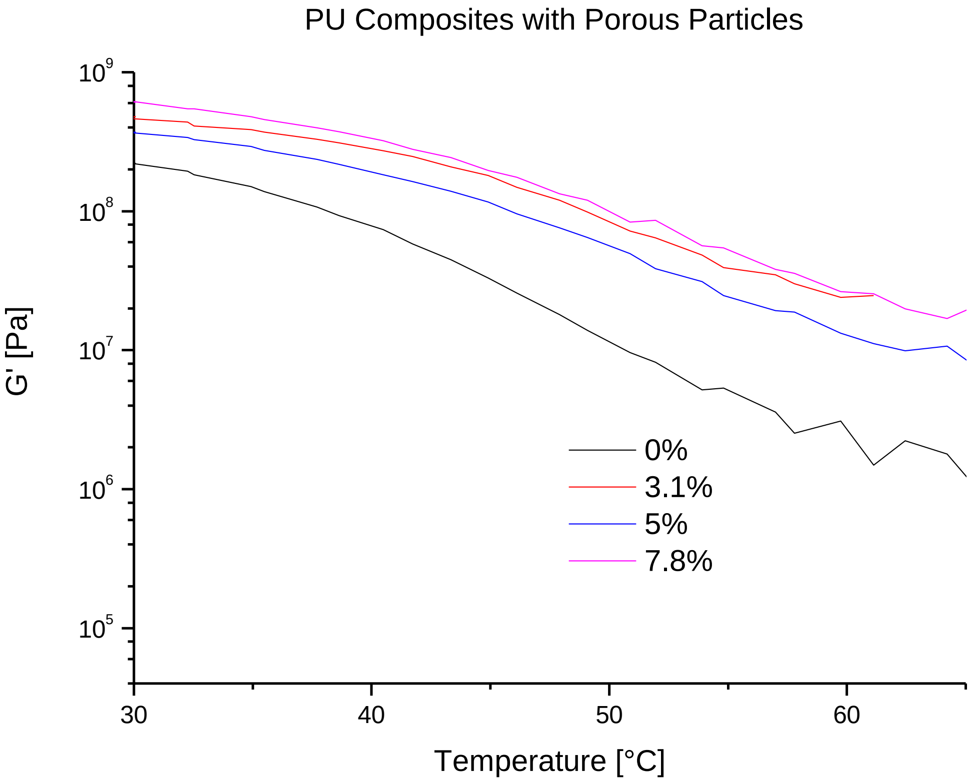

Figure 23. The diagram of the storage modulus of PU composites versus the content of porous particles

3.5.2 Polystyrene composites

Polystyrene composites were also investigated in this study: polystyrene with molecular weight 18 000g/mol was used as matrix. Porous polyurethane particles and the polystyrene were mixed in THF by treatment of ultrasonication for 30 min to obtain a homogenous dispersion. Then the mixture was poured into moulds which were dried at 80°C for 8 hours under vacuum to remove the THF. The content of the particles from 0 wt% to 10 wt% was varied to study the influence of porous particles on the mechanical strength.

The compatibility between the matrix and the porous particles was investigated by SEM. In contrast to polyurethane composites, aggregates of porous polyurethane particles were formed in the polystyrene matrix (Figure 24). In addition, phase-separation was also observed. The incompatibility between the polyurethane particles and polystyrene matrices could be explained by a weak interaction between them.

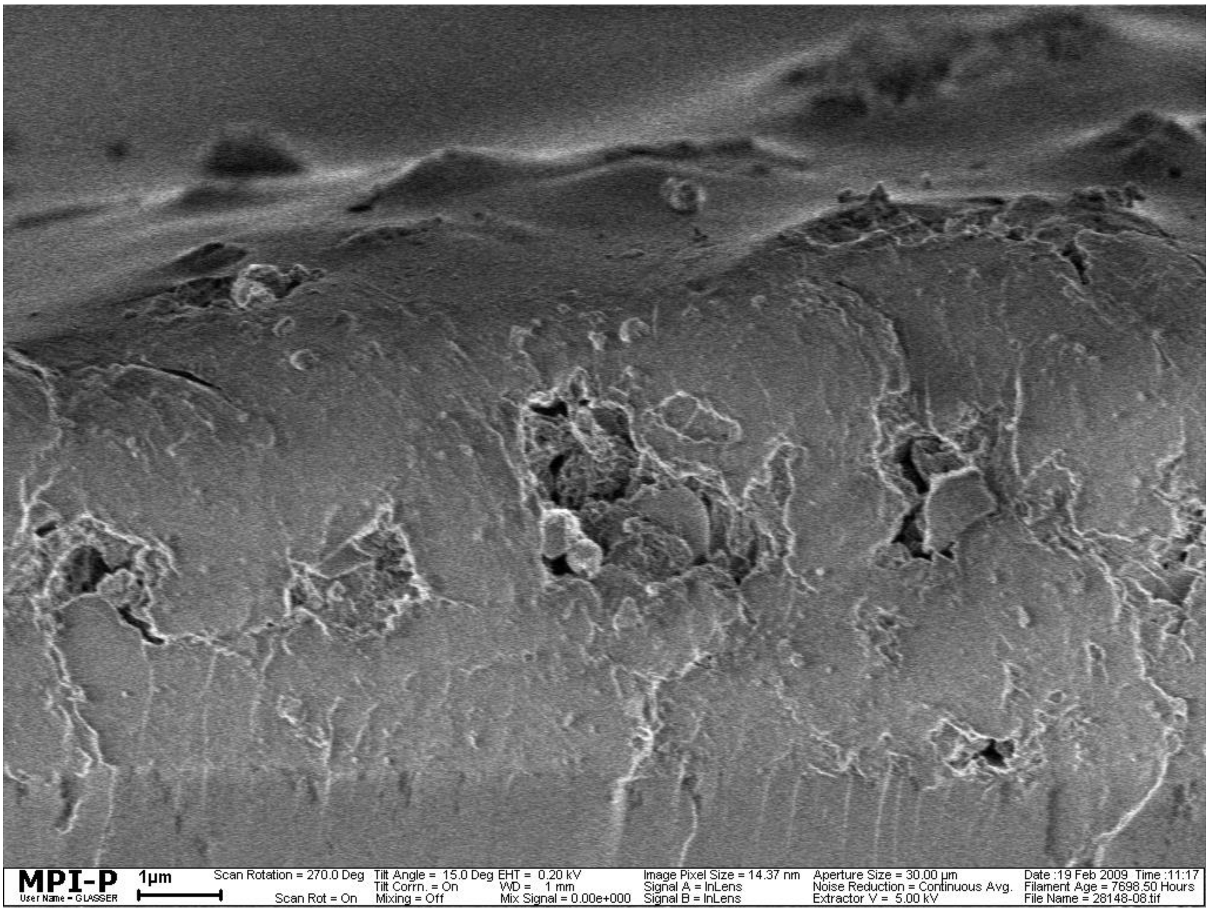

Figure 24. The SEM image of polystyrene composite with polyurethane porous particles.

The mechanical properties of the polystyrene composites were investigated by dynamic mechanical thermal analysis (DMTA) (Figure 25). The storage modulus of the composites did not show an obvious enhancement with increasing content of porous particles. For the sample with 10 wt%, the modulus had only 10 % increase compared with the pure matrix. In contrast, polyurethane composites with 7 wt% particles showed an increased about 300%. The difference could be explained by the formation of aggregates of particles in the polystyrene particles. These results clearly demonstrate that mechanical strength of composites could only be improved by addition of filler material when matrix had strong interaction with filling material (good compatibility). Weak compatibility could even weaken the mechanical properties of the matrix.

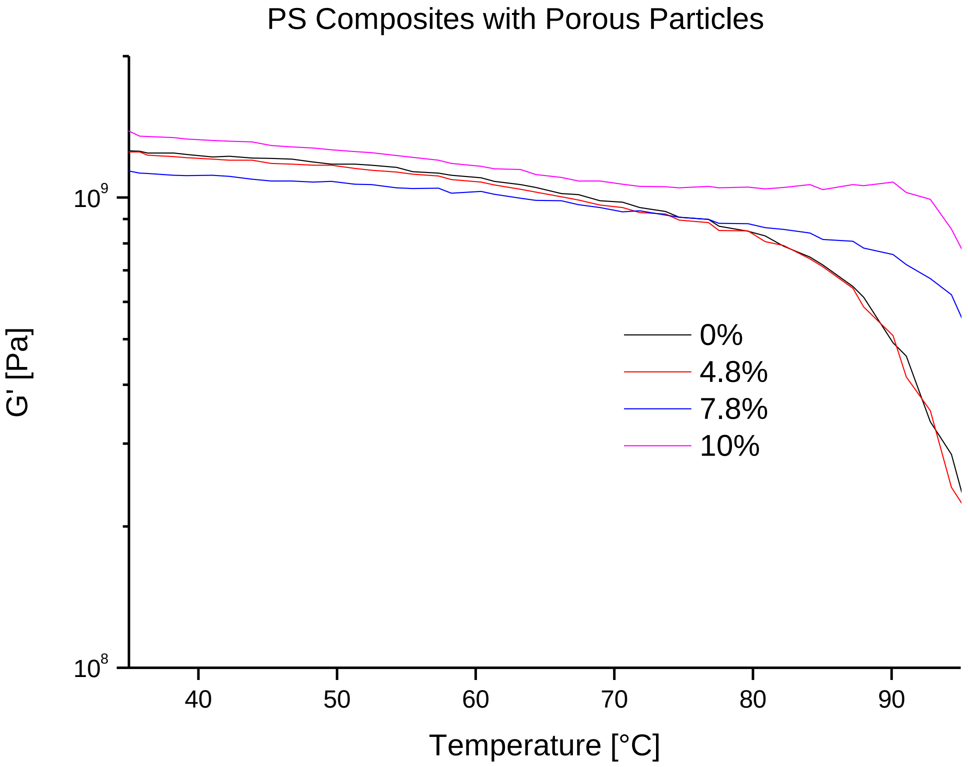

Figure 25. The diagram of the storage modulus of PS composites versus the content of porous particles

3.6 Porous particles as catalyst carriers

3.6.1 The history of catalyst carriers

Porous particles were already intensively studied as catalyst carrier in the literature. The mostly investigated ones were inorganic porous particles such as silica, Al_2O_3 and $MgCl_2$ particles [14, 39, 40]. In these studies, it was shown that the activity of the supported catalysts needed long time to reach its maximum. This phenomenon was explained with four phase [39] [40] (Figure 26): at beginning of polymerization, the catalyst was adsorbed on the pore walls of the porous particles and monomer could directly react with the active centres of the catalyst. Hence the activity of the catalyst showed a small jump. But a crystal layer of polymer was quickly built on the pore walls, which strongly hindered future diffusion of the monomer to the active centres. Therefore, at the second phase the activity decreased dramatically. During the polymerization, the growing polymer in the particles imparted hydraulic forces to the support particles and fragmented them slowly into small pieces. Little by little, more and more active centres became again accessible to the monomer. At the third phase, the activity of the catalyst slowly reached maximum, while the support particles were completely fragmented and the active centres all accessible. In the fourth phase, monomer had to again diffuse through a crystal layer of polymer to the active centres. Hence a decreasing activity of the catalysts was observed. This model of describing the polymerization in the presence of on hard inorganic supported catalysts was called “polymer-growth and particle-expansion model” .

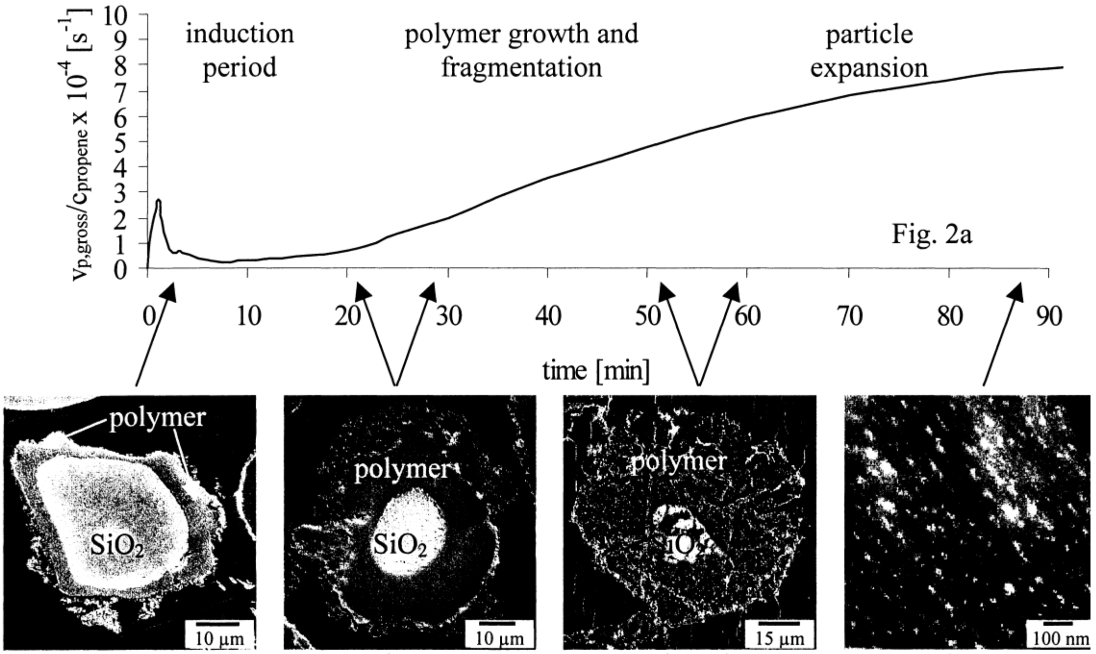

Fig. 2b Fig. 2c Fig. 2d Fig. 2e

Figure 26. The activity change of catalysts on hard inorganic support particle during the polymerization. The images are the typical profile of the polymerization with a silica supported catalyst [39].

Different to catalysts supported on hard inorganic particles, the ones supported on soft polymer particles showed a maximum activity immediately after polymerization began [40-45] (Figure 27). The explanation is that soft polymer particles could be swollen in catalyst solvents (different to inorganic particles) and monomers could be directly adsorbed in the particles, not only on surface of the pore walls. The particles were immediately fragmented by the growing polymer and all of active centres of catalysts became accessible. Hence the catalyst reached its maximum activity at the beginning of the polymerization.

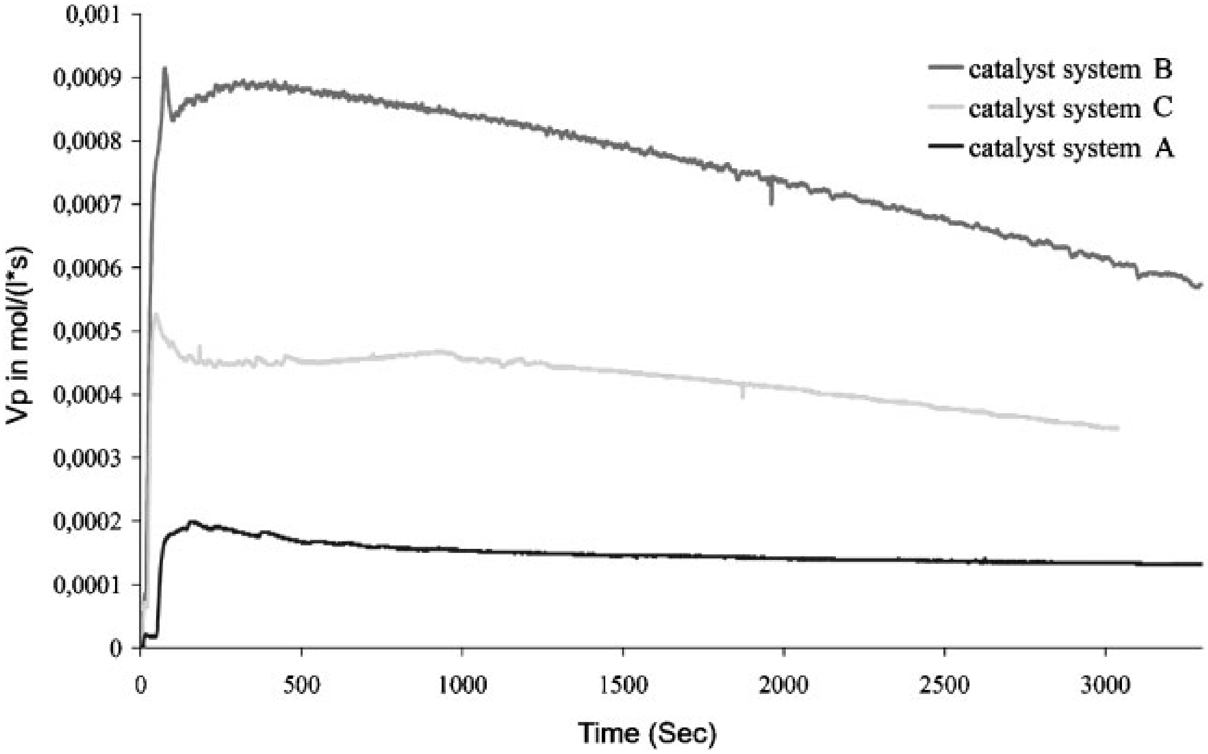

Figure 27. The activity change of catalysts on soft polymer support particles during polymerization [40].

Compared to hard inorganic particles, soft polymer support particles had another important advantage: they were easily adjustable for different catalysts due to the versatile functional of the surface [40, 45]. In present work, the obtained porous polyurethane particles were used as catalyst carrier, supporting a zirconium catalyst bearing phenoxy-imine ligand (FI-catalyst) and Methylaluminoxan (MAO) for polymerization of polyolefin. The polymerisation of polyolefin and the analyse of polyolefin is carried out by the colleague from the department of Synthetic Chemistry in Max Planck Institute for polymer research

3.6.2 The polymerization of polyolefin

The immobility of the zirconium catalyst and MAO on the porous polyurethane particles was achieved with two steps: at first, MAO was added into a dispersion of the porous particles in toluene to prepare MAO pre-activated particles. In the next step, the zirconium catalyst was dropped onto the pre-activated particles. Then these particles with zirconium catalyst and MAO were put in the stainless steel reactor with a pressure 4 bar ethylene for polymerization. The preparation of polyethylene and the polymerization is presented in Figure 28. A pressure of 4 bar was applied in order to slow down the polymerization process for accurate data. Ethylene consumption was controlled by a mass flow-meter. Video microscopy was used to observe the growth of the supporting particles during the polymerization. A snapshot of the catalyst particles was taken every 10 s over a period of 1 h. The supporting particle was measured and converted into the equivalent circle diameter (ECD) which was normalized to the diameter ECD_0 of the initial particle.

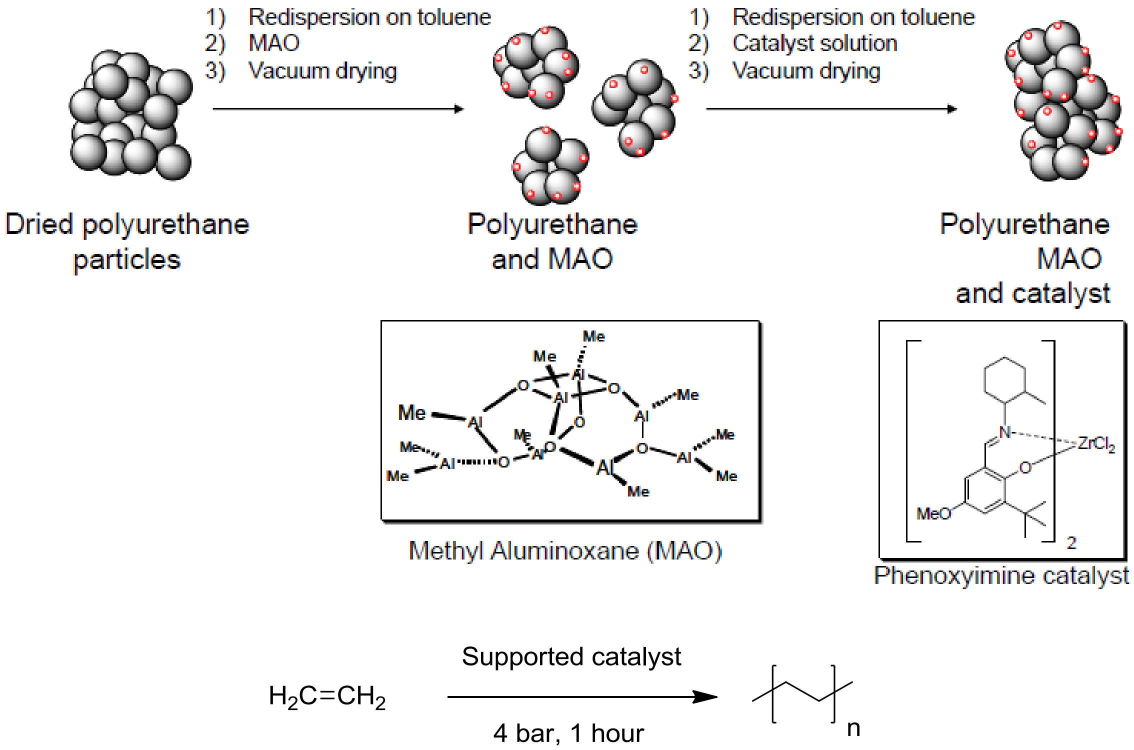

Figure 28: Polymerization of ethylene using zirconium catalyst and MAO supported on polyurethane porous particles.

In this study, the polymerization was carried out at 50 °C and 70 °C to investigate the influence of temperature on the activity of the catalyst. At 50 °C, the diameter of the particles after the polymerization showed an increase about 480% - 850% (Figure 29). From the diagram ECD/ECD_0 versus time, it was found that particles grew slowly during the polymerization and no maximum was reached after one hour (Figure 30).

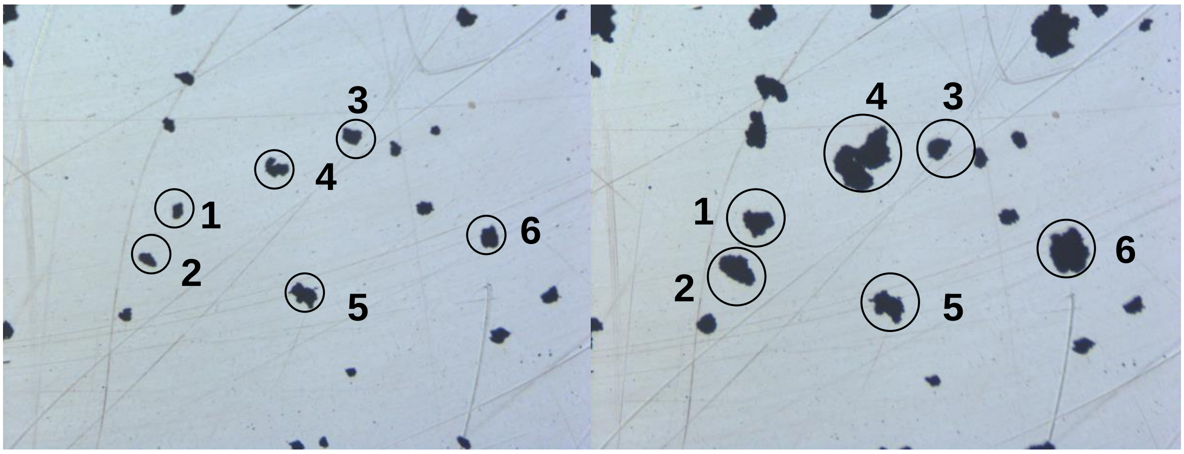

Figure 29. Porous particles before polymerization (left) and after polymerization at 50 ^{o}C (right).

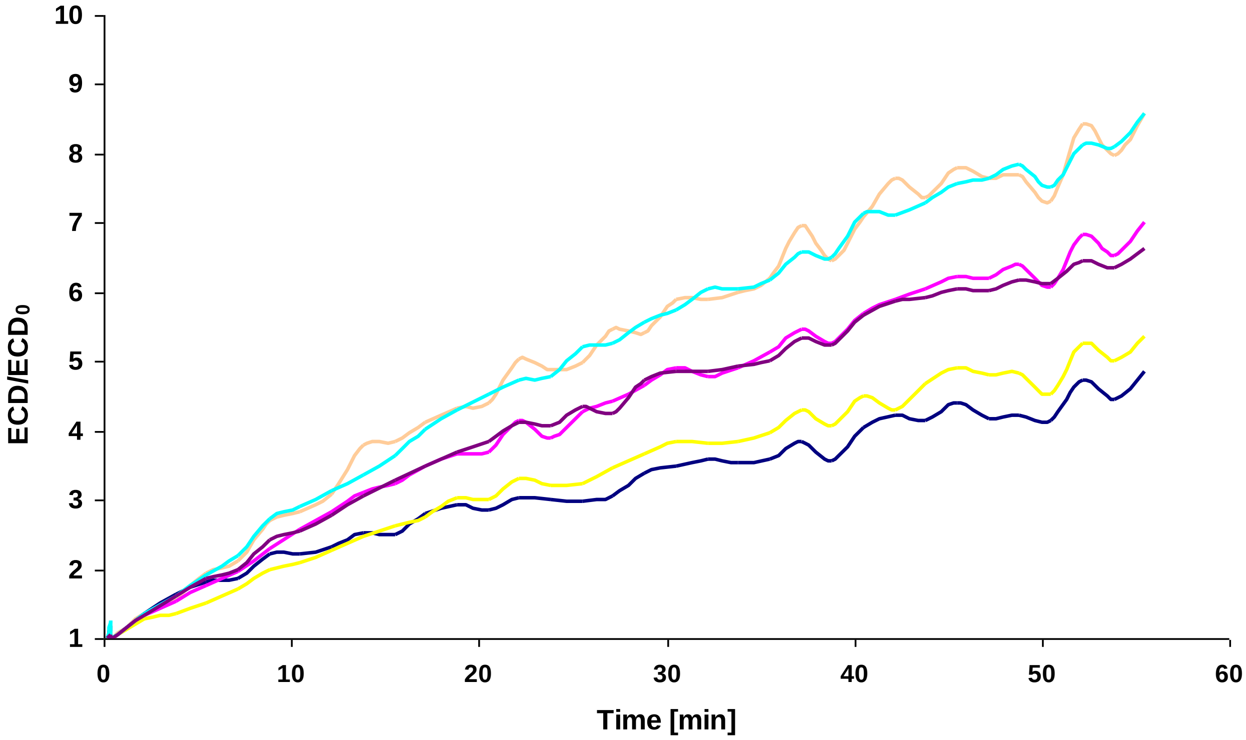

Figure 30. The diagram of ECD/ECD$_0$ versus time for the polymerization at 50 ^{o}C.

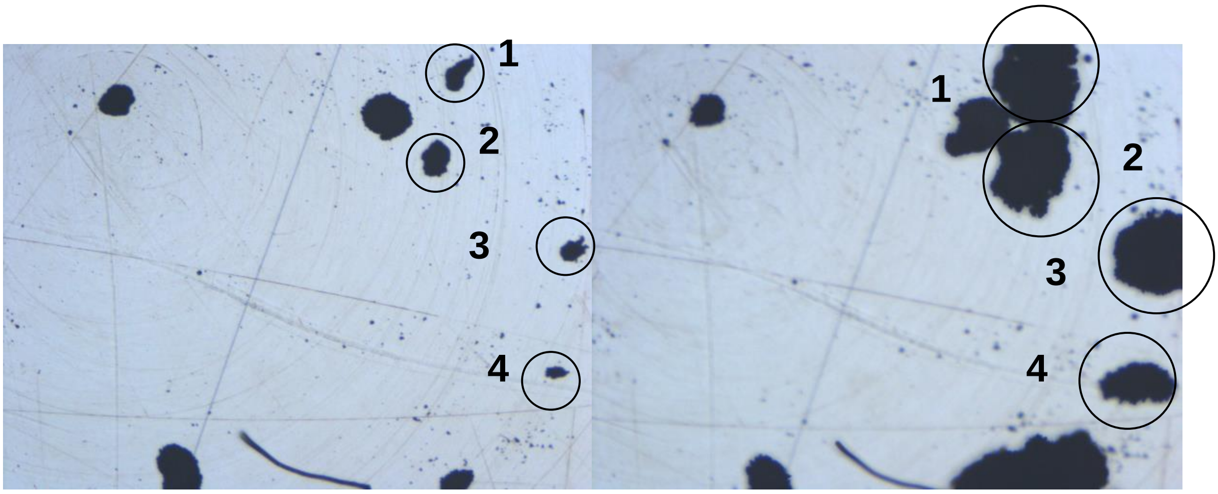

Figure 31. Porous particles after polymerization and after polymerization at 70 °C.

At 70 °C, the particle sizes showed a growth about 750% to 1970% which was much higher than at 50 °C (Figure 31). The diagram ECD/ECD$_0$ versus time showed that the size of the particles reached a maximum in the first 40 min (Figure 32). This growth tendency was similar to soft polymer particles, suggesting that the porous polyurethane particles were fragmented at begin of the polymerization.

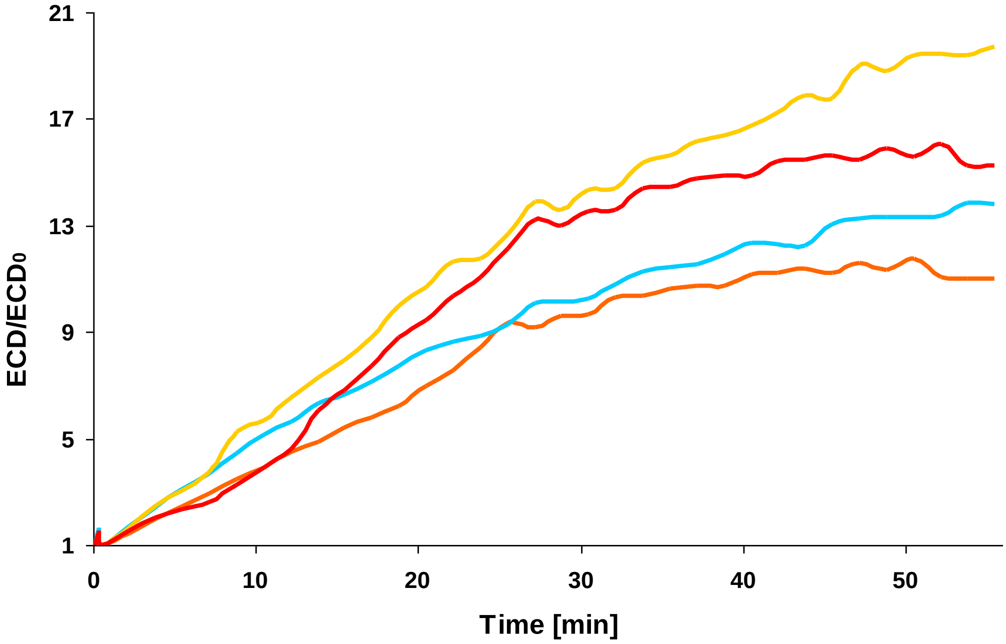

Figure 32. The diagram of ECD/ECD$_0$ versus time for polymerization at 70 °C.

The morphology of the particles was observed by SEM (Figure 33). While image (a) showed a porous polyurethane particle with zirconium catalyst and MAO, images (b) and (c) show the particles after 1 hour of polymerization at 50 °C and 70 °C (Figure 33). The pores in the polyurethane particles were filled with the polymer after polymerization at both temperatures. But the particles from 70 °C showed polymer fibrils on the surface (Figure 34). The formation of filaments was caused by the fragmentation of the supporting and high amount of accessible active centres of the catalyst. Such filaments were not observed on the surface of the polymer particles from 50 °C. The observation from SEM images agreed to the supposition from diagram ECD/ECD_0 versus time.

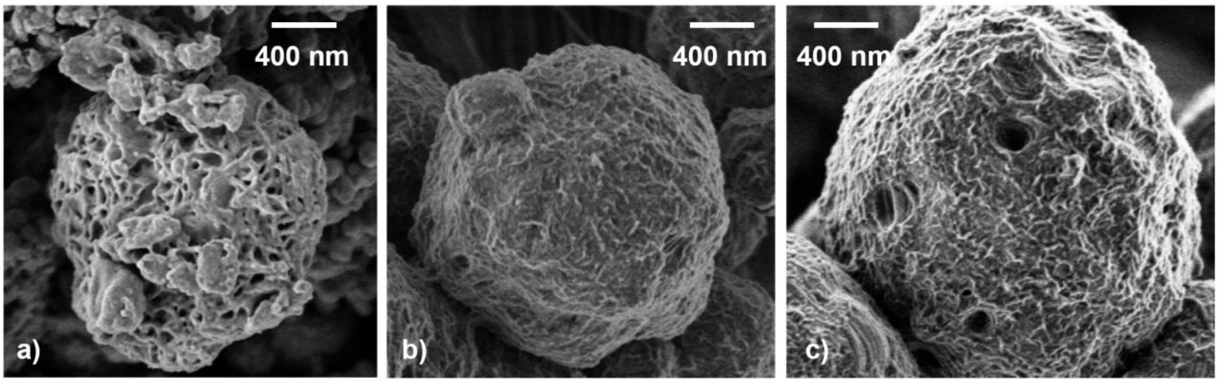

Figure 33. SEM images of polyurethane porous particle, (a) before the polymerization, after the polymerization at (b) 50 °C, and (c) 70 °C

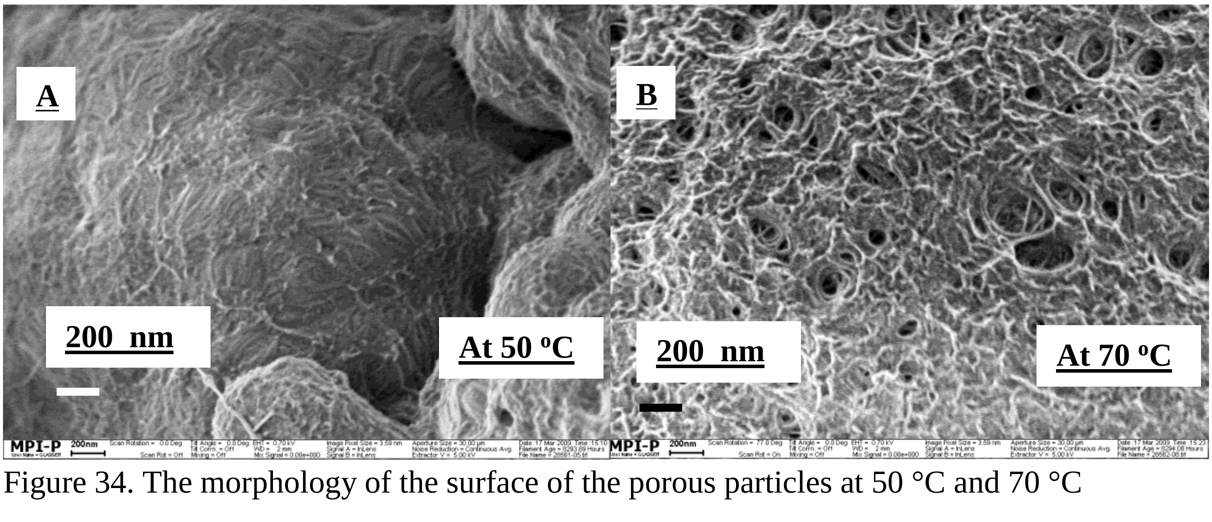

Figure 34. The morphology of the surface of the porous particles at 50 °C and 70 °C

3.7 Conclusion

In this study, highly porous polyurethane and polyurea particles were prepared in a non-aqueous emulsion. The porous structure was formed by the released CO_2 from the reaction between diisocyanates and water. The preparation of porous particles consisted of two parts: at first, a system was developed where the emulsion had high stability for the polymerization among diisocyanate, diol and water. In the second part, porous particles were prepared by using two methods fission/fusion and combination by which highly porous particles were obtained. In this study, the applications of porous particles were also investigated where polyurethane particles were tested as filling material for polymer composites and as catalyst carrier for polyethylene polymerization. As filling material, the porous polyurethane particles obviously increased the mechanical properties of polyurethane composites because of the strong interaction between the particles and the matrix (strong hydrogen bonds). As catalyst carried, the catalyst zirconium and MAO were successfully mobilized on the porous polyurethane particles. The catalyst showed high activity by that the supporting porous particles were fragmented during the polymerization.

Reference

1. Fu, X. and W. Teltner, *The gas-phase photocatalytic mineralization of benzene on porous titania-based catalysts.* Applied Catalysis B-Environmental, 1995. **6**: p. 209-224.
2. Hiromichi, H., T. Naomitsu, and M. Yoshikazu, in *Jpn. Kokai Tokkyo Koho*2002.
3. Edwards, D.A., et al., *Large porous particles for pulmonary drug delivery.* Science, 1997. **276**(5320): p. 1868-1871.
4. Zhang, H., et al., *Synthesis of porous microparticles with aligned porosity.* Advanced Functional Materials, 2008. **18**(2): p. 222-228.
5. Dawkins, J.V., *Chromtographic Characteristics Of Polymer-Based High-Performance Liquid Chromatography Packings.* Journal of chromatography 1986. **352**: p. 157-167.
6. Recknor, J.C. and J.B. Recknor, *Oriented astroglial cell growth on micropatterned polystyrene substrates.* Biomaterials, 2004. **25**(14): p. 2753-2767.
7. Sahoo. S. K, P.A. K, and Labhasetwar. V. , Biomacromolecules, 2005. **6**.
8. Fang, D.Y., Q.M. Pan, and G.L. Rempel, *Preparation and characterization of 2-hydroxyethyl methacrylate-based porous copolymeric particles.* Journal of Applied Polymer Science, 2007. **105**(5): p. 3138-3145.
9. Cheng, C.M., et al., *Synthesis and Characterization of Monodisperse Porous Polymer Particles.* Journal of Polymer Science Part a-Polymer Chemistry, 1992. **30**(2): p. 235-244.
10. Cheng, C.M., J.W. Vanderhoff, and M.S. Elaasser, *Monodisperse Porous Polymer Particles - Formation of the Porous Structure.* Journal of Polymer Science Part a-Polymer Chemistry, 1992. **30**(2): p. 245-256.
11. Unsal, E., et al., *Monodisperse–porous particles with different polarities by “modified seeded polymerization” and their use as chromatographic packing in HPLC.* Reactive and Functional Polymers, 2004. **61**(3): p. 353-368.
12. Cooper, A.I., *Porous materials and supercritical fluids.* Advanced Materials, 2003. **15**(13): p. 1049-1059.
13. Wood, C.D. and A.I. Cooper, *Synthesis of macroporous polymer beads by suspension polymerization using supercritical carbon dioxide as a pressure-adjustable porogen.* Abstracts of Papers of the American Chemical Society, 2001. **221**: p. U368-U368.
14. Maria Kaliva, G.S.A., and Maria Vamvakaki *Microporous Polystyrene Particles for Selective Carbon Dioxide Capture.* Langmuir, 2012. **28** (5).

15. Sivak, W., et al., *Catalyst-dependent drug loading of LDI–glycerol polyurethane foams leads to differing controlled release profiles.* Acta Biomaterialia, 2008. **4**(5): p. 1263-1274.

16. Guelcher, S., et al., *Synthesis of biocompatible segmented polyurethanes from aliphatic diisocyanates and diurea diol chain extenders.* Acta Biomaterialia, 2005. **1**(4): p. 471-484.

17. Guelcher, S., et al., *Synthesis, In Vitro Degradation, and Mechanical Properties of Two-Component Poly(Ester Urethane)Urea Scaffolds: Effects of Water and Polyol Composition.* Tissue Engineering, 2007. **13**(9): p. 2321-2333.

18. Maher, S.A., et al., *Evaluation of a Porous Polyurethane Scaffold in a Partial Meniscal Defect Ovine Model.* Arthroscopy-the Journal of Arthroscopic and Related Surgery, 2010. **26**(11): p. 1510-1519.

19. Liu, S.Q. and M. Kodama, *Porous Polyurethane Vascular Prostheses with Variable Compliances.* Journal of Biomedical Materials Research, 1992. **26**(11): p. 1489-1502.

20. Grenier, S., M. Sandig, and K. Mequanint, *Polyurethane biomaterials for fabricating 3D porous scaffolds and supporting vascular cells.* Journal of Biomedical Materials Research Part A, 2007. **82A**(4): p. 802-809.

21. Fassina, L., et al., *Effects of electromagnetic stimulation on calcified matrix production by SAOS-2 cells over a polyurethane porous scaffold.* Tissue Engineering, 2006. **12**(7): p. 1985-1999.

22. Müller, K., *Nicht-waessrige emulsionspolymerisationen*, in *Chemie und Pharmazie der Johannes-Gutenberg Universitaet* 2008: Mainz.

23. Rogers, M., E and T. long, E, *Sythetic Methods In Step-Growth Polymers*2003, New Jersey: John Wiley & Sons.

24. Tiarks, F., K. Landfester, and M. Antonietti, *One-step preparation of polyurethane dispersions by miniemulsion polyaddition.* Journal of Polymer Science Part a-Polymer Chemistry, 2001. **39**(14): p. 2520-2524.

25. Armistead, J.P., G.L. Wilkes, and R.B. Turner, *Morphology of Water-Blown Flexible Polyurethane Foams.* Journal of Applied Polymer Science, 1988. **35**(3): p. 601-629.

26. HERRINGTON, *FLEXIBLE POLYURETHAN*1997.

27. Yan, Y., et al., *Preparation and characterization of water blown polyurethane foams from liquefied cornstalk polyol.* Journal of Applied Polymer Science, 2008. **110**: p. 1099-1111.

28. Tiarks, F., K. Landfester, and M. Anonietti, *Encapsulation of carbon black by miniemulsion polymerization.* Macromolecular Chemistry and Physics, 2001. **202**(1): p. 51-60.

29. Neff, R., et al., *Urea hard segment morphology in flexible polyurethane foam.* Journal of Polymer Science Part B-Polymer Physics, 1998. **36**(4): p. 573-581.

30. Kaushiva, B.D., et al., *Surfactant level influences on structure and properties of flexible slabstock polyurethane foams.* Polymer, 2000. **41**(1): p. 285-310.

31. Dounis, D.V., et al., *The Mechanosorptive Behavior of Flexible Water-Blown Polyurethane Foams.* Journal of Applied Polymer Science, 1993. **50**(2): p. 293-301.

32. Dounis, D.V. and G.L. Wilkes, *Structure-property relationships of flexible polyurethane foams.* Polymer, 1997. **38**(11): p. 2819-2828.

33. Hong, K. and S. Park, *Polyurea microcapsules with different structures: Preparation and properties.* Journal of Applied Polymer Science, 2000. **78**(4): p. 894-898.

34. Duong, H.T.T., T.L.U. Nguyen, and M.H. Stenzel, *Micelles with surface conjugated RGD peptide and crosslinked polyurea core via RAFT polymerization.* Polymer Chemistry, 2010. **1**(2): p. 171-182.

35. Erdelyi, S., J. Karger-Kocsis, and G. Nagy, *Polyurea resins with in situ produced silicate filler from water glass: Static and dynamic mechanical properties.* Journal of Macromolecular Science Part B-Physics, 2007. **46**(1): p. 21-31.

36. Yin, W., et al., *Biocompatibility of surfactant-templated polyurea-nanoencapsulated macroporous silica aerogels with plasma platelets and endothelial cells.* Journal of Biomedical Materials Research Part A, 2010. **92A**(4): p. 1431-1439.

37. Zhu, L., et al., *Synthesis of porous polyurea with room-temperature ionic liquids via interfacial polymerization.* Macromolecular Rapid Communications, 2006. **27**(16): p. 1306-1311.

38. Leventis, N., et al., *Multifunctional Polyurea Aerogels from Isocyanates and Water. A Structure-Property Case Study.* Chemistry of Materials, 2010. **22**(24): p. 6692-6710.

39. Fink, G., et al., *The particle-forming process of SiO2-supported metallocene catalysts.* Macromolecular Symposia, 2001. **173**: p. 77-87.

40. Naundorf, C., et al., *Hard versus Soft Materials as Supports for Metallocene and Post-Metallocene Catalysts.* Macromolecular Reaction Engineering, 2009. **3**(8): p. 456-466.

41. Nishida, H., et al., *POLYSTYRENE-SUPPORTED METALLOCENE CATALYSTS FOR OLEFIN POLYMERIZATIONS.* Macromolecular Rapid Communications, 1995. **16**(11): p. 821-830.

42. Hong, S.C., et al., *Ethene polymerization with a poly(styrene-co-divinylbenzene) beads supported rac-Ph2Si(Ind)(2)ZrCl2 catalyst.* Macromolecular Chemistry and Physics, 1998. **199**(7): p. 1393-1397.
43. Kitagawa, T., et al., *Syndiospecific propene polymerization with polymer-supported metallocene catalyst.* Polymer, 1997. **38**(3): p. 615-620.
44. Roscoe, S.B., et al., *Polyolefin spheres from metallocenes supported on noninteracting polystyrene.* Science, 1998. **280**(5361): p. 270-273.
45. Diesing, T., et al., *Spatially Resolved Catalysis for Controlling the Morphology of Polymer Particles.* Angewandte Chemie-International Edition, 2009. **48**(35): p. 6472-6475.

Chapter 4.

Dispersions of polymer particles loaded with perylene dye

4.1 Introduction

4.1.1 Study of polymerization process

Understanding the polymerization is a crucial issue for polymer science. Whereas many details of the macroscopic structure of polymer chains are obtained with traditional analytical techniques (such as ESR spectroscopy [1], size-exclusion chromatography [2], mass spectroscopy [3], NMR [4] and fluorescence spectroscopy [5]), but some properties can be only understood in terms of the molecular structure. Single Molecule Fluorescence Detection (SMFD) is a technique which can resolve details of individual polymer chains at manometer scale. With this technique, the conformation [6, 7] and mobility of the polymer chains [8, 9] are investigated by detection of the inbuilt dye molecules in the chains. For example, conjugated polyfluorene chains were investigated by detecting the distance between two end-capping perylene-imide dyes [6]. It was found that the polyfluorene polymer chains predominantly had a linear conformation, but with some kinks due to rotations of C-C bonds [6] (Figure 1).

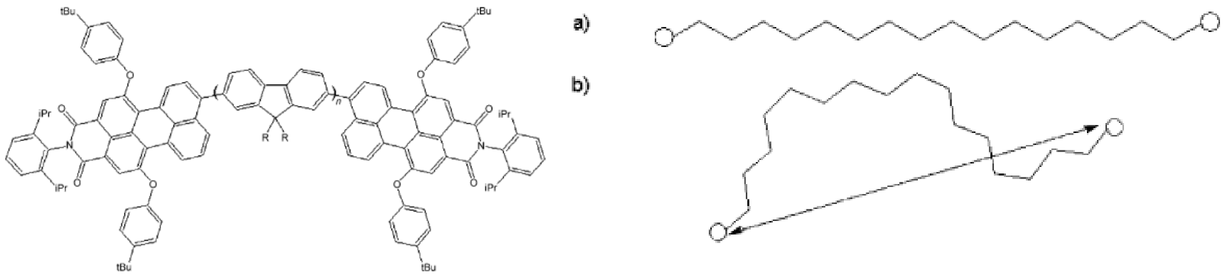

Figure 1. Left: perylene-imide end-capped polyfluorene. Right: schematic representation of the effect of the rotation of polymer chains on their conformation [6].

Polyfluorene conjugated polymers was also studied in another research group by labeling up to seven perylene-imide dyes in the chains [8] (Figure 2). It was found that the chains had a relatively rigid conformation which agreed with the results in the first study [6].

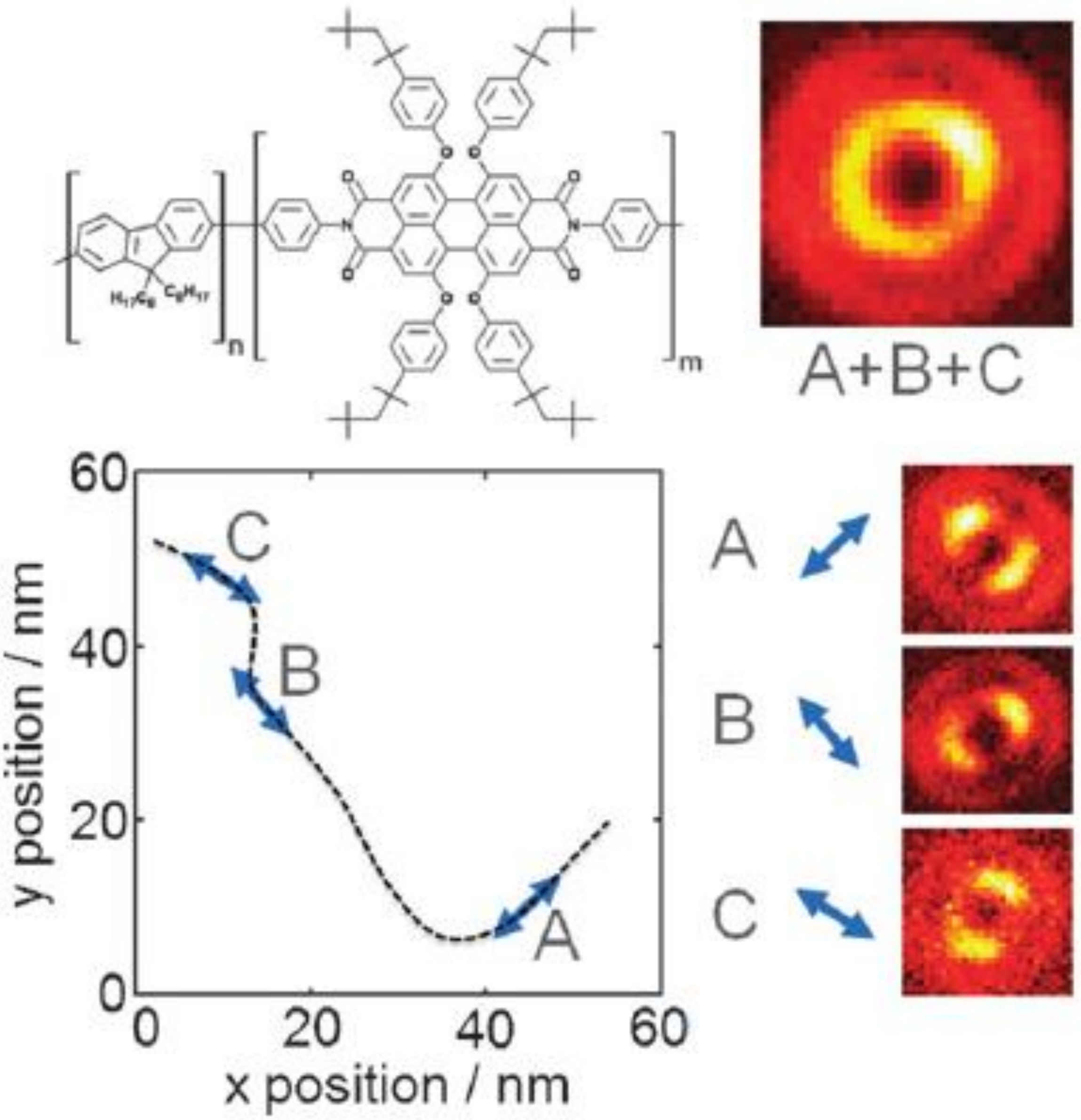

Figure 2. Determination of the conformation of a polyfluorene conjugated chain with incorporated PDI labels [8].

Until today, SMFD is not yet used to investigate the details of polymer particles prepared via emulsion. In the present work, PMMA and polyurethane (PU) particles will be investigated with this method. Both polymers are typical for radical polymerization and polyaddition which have different polymerization mechanisms. In addition, in this work perylene-imide dyes (PDI) with good photo-stability, high molar extinction coefficient and fluorescence quantum yield will be used as labels incorporated into the polymer chains. The incorporation will be achieved by using PDI containing double bonds or hydroxyl groups, acting as monomers. Both kinds of particles will be prepared via a non-aqueous emulsion in which the dispersed phase DMF is an excellent solvent for the perylene-imide dyes. It is very important for a stable emulsion and a homogenous distribution of the dye molecules in the particles. Otherwise non-aqueous emulsion hinders the side reaction between monomer diisocyanates and water.

4.1.2 Chain-growth and step-growth Polymerization

Based on the significant difference in the mechanism, polymerization is classified into chain-growth and step-growth polymerization. There are several features in which both polymerizations are different. But the most important difference is the characters of monomers which they use.

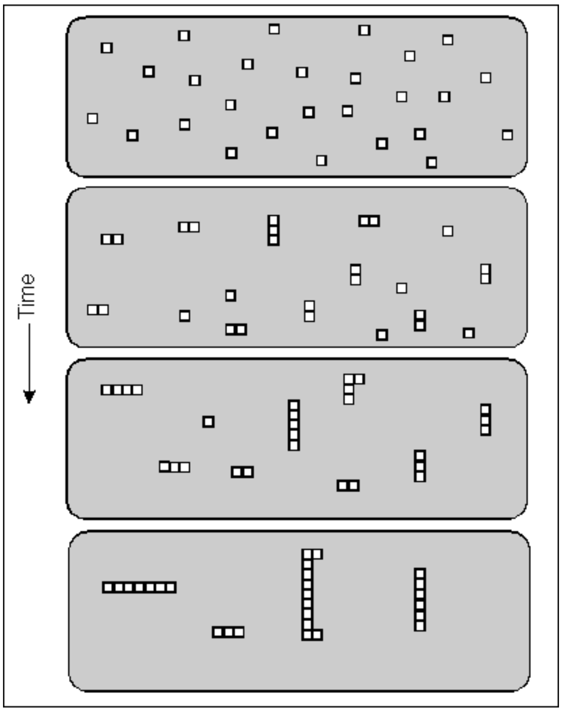

Figure 3. A generic representation of a chain-growth polymerization (Single dots represent monomers and chains of dots represent polymers) [10].

The monomers for chain-growth polymerization do not react with each other, but only with a reactive center. An initiator is used to produce the reactive center which can be a free radical, cation or anion. Polymer chains propagate at the reactive center by successive additions of monomers one by one (Figure 3). The growth can be stopped by destroying the reactive centre, called termination reaction. The process of chain-growth polymerization can be depicted as:

Star Initiator $I \rightarrow 2R^*$

Propagation $R^* + M \rightarrow R\text{-}M^*$

$R\text{-}M^* + nM \rightarrow R\text{-}M_{n+1}^*$

Termination $R\text{-}M_{n+1}^* + R\text{-}M_{m+1}^* \rightarrow R\text{-}M_n\text{-}M\text{-}M\text{-}M_m\text{-}R$

In step growth polymerization, each monomer molecule must contain at least two functional groups. Depending on the assignation of the functional groups to the monomers, step growth polymerization is divided into AABB-type and AB-type. When each monomer has only one kind of functional group, two different types of monomers with complementary functional groups are required [11]. This process is called AABB-type reaction (1.1). If each monomer molecule has two complementary functional groups, step growth polymerization can occur with only one type of monomer. This is called AB-type reaction (1.2). Normally in step-growth polymerization, monomers are tied by conventional organic reactions, such as esterification, amidation and the formation of urethanes, [11].

$$n\ A{-}A \quad + \quad n\ B{-}B \longrightarrow \left[{-}A{-}A{-}B{-}B{-} \right]_n \qquad (1.1)$$

$$n\ A{-}B \longrightarrow \left[{-}A{-}B{-}A{-}B{-} \right]_n \qquad (1.2)$$

The growth of polymer chains is a rather slow process: the first step is the formation of dimers from monomers, which proceed to react with monomers or themselves to form trimers and tetramers [11, 12] (Figure 4). This reaction continues until large polymer chains have been formed.

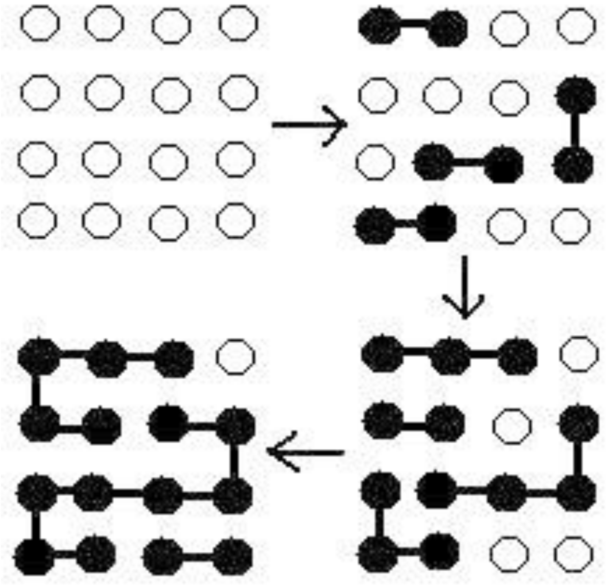

Figure 4. A generic representation of a step-growth polymerization. (Single white dots represent monomers and black chains represent oligomers and polymers) [13]

4.1.3 Fluorescence Detection

When a dye molecule absorbs photons, the electrons staying in the Highest Occupied Molecular Orbital (HOMO) S_0 of the molecule can be promoted onto the Lowest Unoccupied Molecular Orbital (LUMO) S_1. These promoted electrons are not stable, so that they have strong trendy to go back to HOMO, emitting luminescence (fluorescence or phosphorescence). The Perin-Jablonski diagram explains the possible emission processes (fluorescence or phosphorescence) in a simple way (Figure 5). The emission of fluorescence happens during the transition of an electron from $S_1 \rightarrow S_0$. The fluorescence band is located at higher wavelength than the absorption one, because a part of energy is lost by vibration relaxation as heat. The electron can also be transited into another energy level $S_1 \rightarrow T_1$ called intersystem crossing (ISC) with a vibrational relaxation. But the electron is still instable in this level and goes continuously into lower energy level $T_1 \rightarrow S_0$ with an emission of phosphorescence (Figure 5). The phosphorescence is located at wavelength higher than the fluorescence due to ISC vibrational relaxation.

When an electron is promoted onto orbital with high energy level (S_n n>1), a directly transition from $S_n \rightarrow S_0$ ($n > 1$) is hardly probable because of too large energy gap between S_n and S_0. An internal conversion of the electron from $S_n \rightarrow S_1$ (IC) oft occurs in this case (Figure 5). The excited electron undergoes vibrational relaxation and release energy to the environment as heat. At the next step, the electron is converted from $S_1 \rightarrow S_0$ with emission of photons (fluorescence). The fluorescence band is also located at higher wavelength than the absorption one, because a part of energy is lost by IC vibration relaxation.

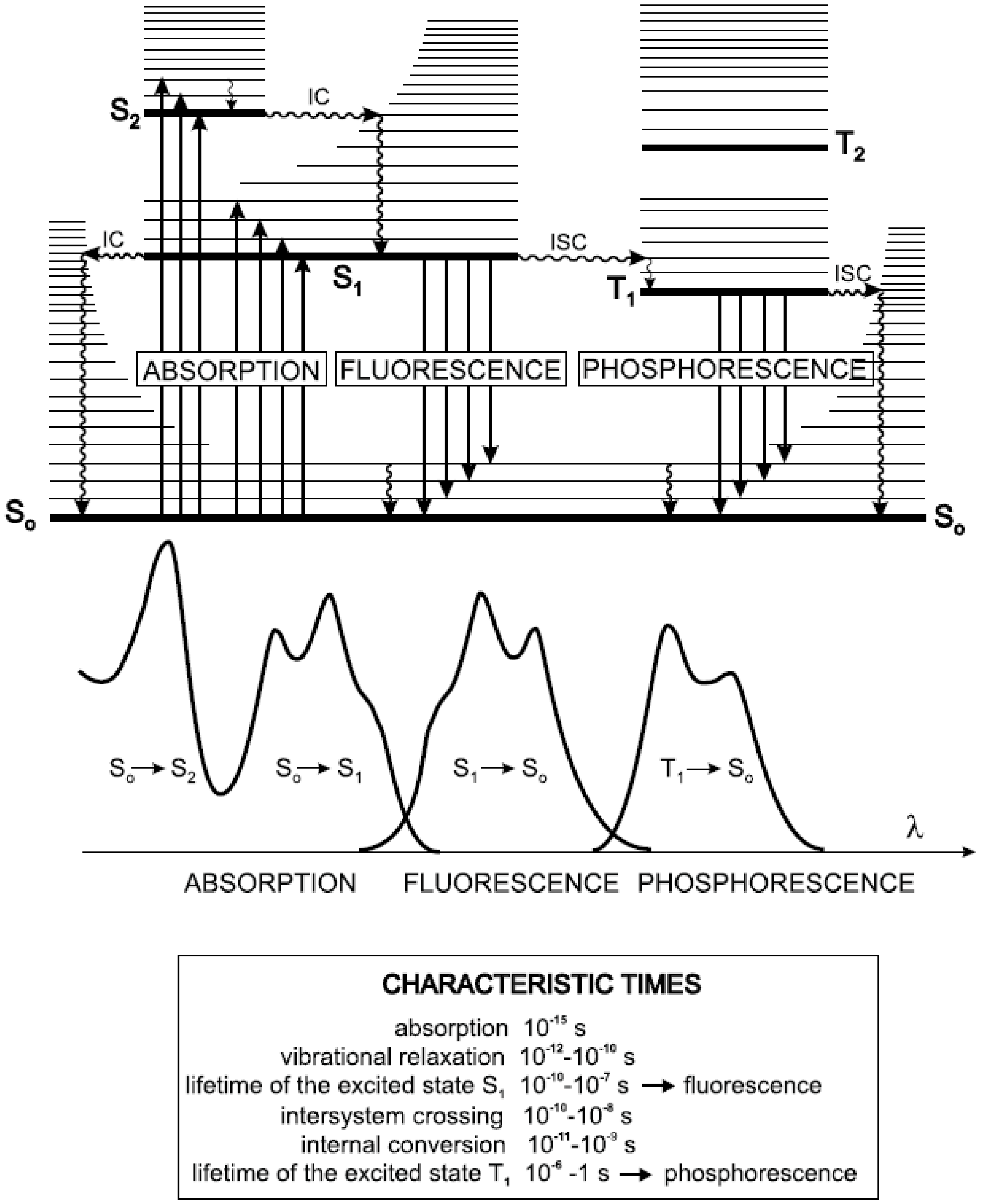

CHARACTERISTIC TIMES	
absorption	10^{-15} s
vibrational relaxation	10^{-12}-10^{-10} s
lifetime of the excited state S_1	10^{-10}-10^{-7} s → fluorescence
intersystem crossing	10^{-10}-10^{-8} s
internal conversion	10^{-11}-10^{-9} s
lifetime of the excited state T_1	10^{-6} -1 s → phosphorescence

Figure 5. Perrin-Jablonski diagram and illustration of absorption of fluorescence and phosphorescence.

4.1.4 Single Molecule Fluorescence Detection

A fluorescent dye molecule is essentially considered as a dipole antenna with an anisotropic emission in space, meaning that individual molecules do not emit photos equally in every direction. The transition dipole moment of the emission from a dye molecule can be detected by defocused wide-field imaging method, one of single molecule fluorescence detections [8]. A charge-coupled device (CCD) camera gathers the anisotropic emission and takes photos as patterns. To obtain a clearer pattern, a sample should be moved slightly toward the objective (or the objective toward the sample) over a short distance (defocusing depths d) (Figure 6a) [8]. The resulting image patterns are then matched to the closest patterns in a theoretical library (figure 6b-6c) to turn out the in-plane (ϕ) and out-of-plane (θ) orientation of the dye molecule (Figure 6d-6e) [14-16]. The two-lobe of the patterns of a dye changes their orientations and structure, when in-plane (ϕ) and out-of-plane (θ) angles vary [17]. One example of two typical patterns are shown in Figure 6d and 6e (experimental patterns (left) and the calculated theoretical fits (right)).

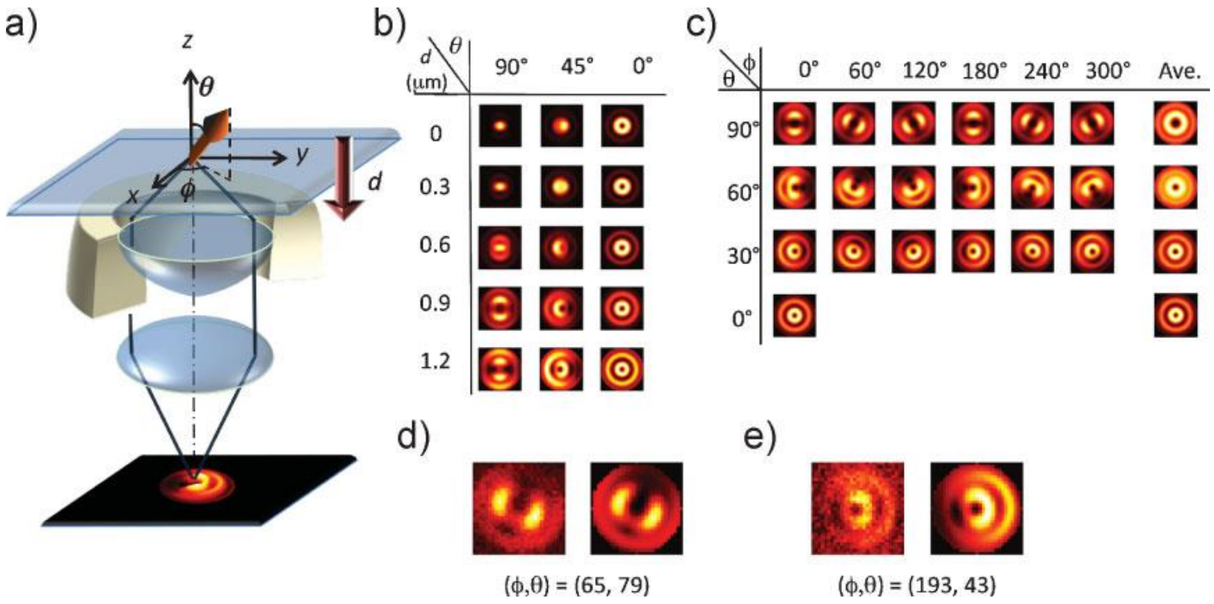

Figure 6. Defocused wide-field imaging [8].

a) When a dye molecule emits, the resulting image becomes anistropic and provides information on its orientation.

b) Example for emission patterns for different defocusing depths (*d*) and different out-of-plane angles (*θ*).

c) Example for emission patterns for different out-of-plane (*θ*) and in-plane (*ϕ*) angles.

d–e) Example for experimental patterns (left) and the calculated theoretical fits (right).

The spatial resolution of fluorescence microscopy in defocused wide-field imaging method is limited to hundreds nanometer. But when dye molecules stay together in a distance of a few of nanometers, the obtained patterns are not from a single dye, but all of them. This problem can be solved by isolating the emission of a single dye molecule from others by use of stochastic fluorescence photobleaching, so that the position and orientation of each dye molecule can be accurately determined. In figure 7, an example is given in which a spot consists of two dye molecules. In the step I, a pattern of the sum emission of both dyes is taken. In step II, a dye molecule undergoes photobleaching and only another surviving dye emits fluorescence. The obtained pattern in step II belongs to this surviving dye. By subtracting the pattern of the surviving dye from the sum emission, the pattern of the second dye can be obtained (Figure 7) [8].

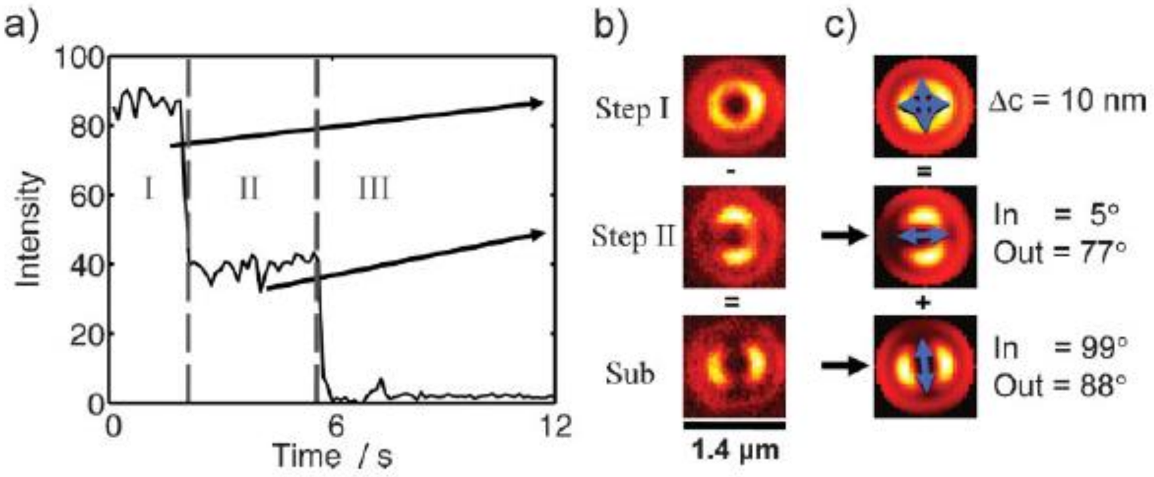

Figure 7. Determination of the positions and orientations of a two-chromophore system [8].

a) Fluorescence intensity traces of an emission spot containing the contributions of two PDI dyes.

b) The normalized emission patterns corresponding to the different steps in the intensity trace.

c) The fitted theoretical patterns together with their orientations and the relative distance between the two emitters. .

4.1.5 Synthesis of perylene dye

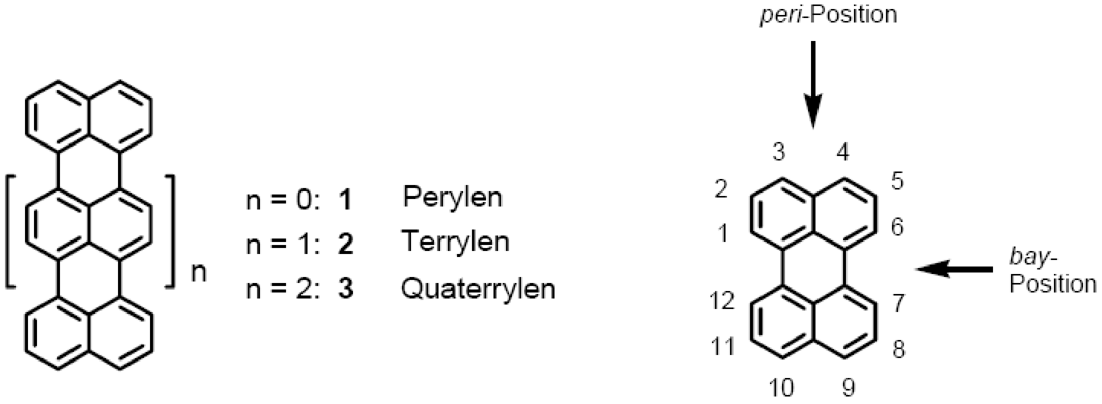

Figure 8. The structure of polycyclic aromatic compound (left) and numeration of perylene (right)

Well-known pigment perylene is a polycyclic aromatic compound with five phenyl rings. Its physical and chemical properties can be designed by introduction of suitable functional groups at the *bay*- and *peri*- position of the five rings (Figure 8 right). For example, at the *bay* position sterically hindering function groups like phenolyl functional groups can be introduced to improve the solubility of perylene dye; because the four phenol groups do not lie on one plane, but form a 3-dimensional structure, preventing aggregation of perylene molecules (Aggregation of dye molecules is caused by the large conjugating π-network in the five phenyl rings). The transition of phenol groups is achieved by substantiation of chloride derivate (Figure 9-6). The chloride derivative is commonly synthesized by chlorinating 3,4,9,10-perylenetetracarboxylic acid dianhydride with chlorine (Figure 9-3 or 9-2). At the *peri* position, functional groups are usually introduced to “design” chemical characters of perylene dyes. For example, OH or double bonds can be introduced by that perylene 3,4,9,10-tetracarboxylic acid dianhydrides reacts with primary amine containing the functional groups (Figure 9-1 or 9-4).

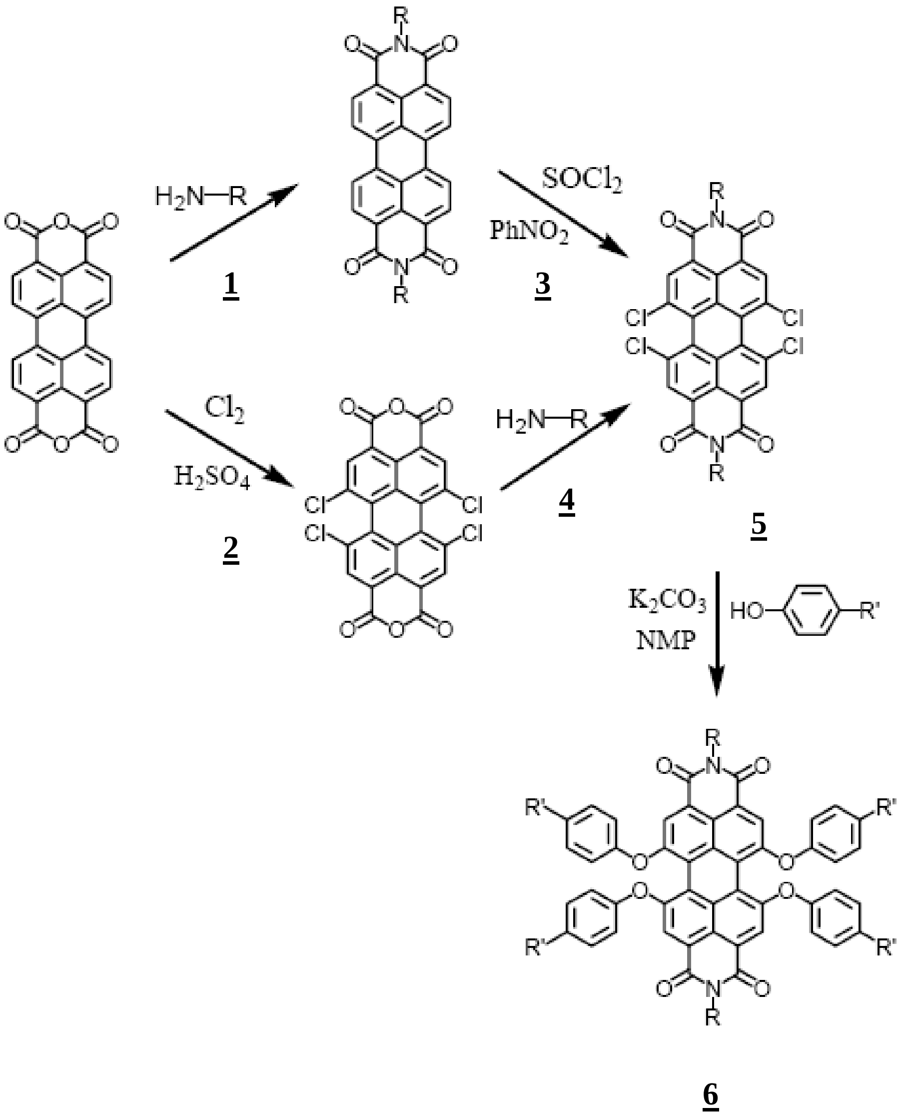

Figure 9. The preparation of a perylenediimide derivative (PDI) by substitution at *bay* or *peri* positions.

In the present work, perylenediimide derivative (PDI) with double bonds and hydroxyl groups are chosen as monomers for the polymerization. PDI with double bonds was already synthesized for a study of heterogeneities of radical polymerization in bulk (Figure 10) [9]. The reaction between perylenetetracarboxy dianhydride (1) and aminalkylstyrene (2) affords carbodiimid (3) with two double bonds at *peri* position. The four chlorides in the *bay* regions are substituted by tert-octylphenol as steric hindrance (4). The reaction is carried out for 16 hours by using *N*-methylpyrrolidone as a solvent at 90°C. K_2CO_3 as a catalyst is used. After acidic workup, the desired product (5) is purified with column chromatography on silica with 26% yield [9]. The PDI for this work is synthesized by the colleague form the department of Synthetic Chemistry in Max Planck Institute for polymer research.

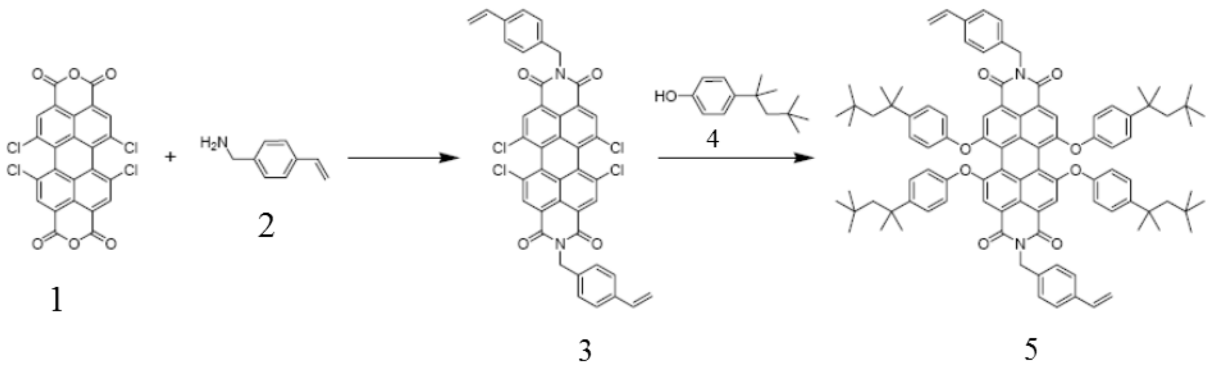

Figure 10. The synthesis of PDI with double bond [9].

4.2 PMMA particles loaded with PDI dyes

4.2.1 Preparation of PMMA particles with PDI dyes

Before preparation of PMMA particles, the amount of PDI had to be determined which played very important role for the single molecule fluorescence detection. When only one or two dye molecules were in a particle, the information was not enough to describe their distribution. When there were too many dyes which could stay very close to each other, energy hopping could happen (when the center-to-center distance between two dye molecules is lower than 3 nm, the absorbed photon is then only transferred between these two molecules without emission of fluorescence [18]). PMMA and PU blank particles without PDI had a diameter about 500 nm. Therefore at the beginning of this study the amount of dye molecules would be calculated with this particle size für 10 dye molecules in every particle.

The amount of PDI for 1 mmol PMMA particles was calculated as follows: it was assumed that the PMMA particles with dye have the same density and diameter as pure PMMA particles (density = 1g/cm^3, Diameter = 500 nm). The mass of one particle can be calculated with the formula $m = V^* d$ (V is volume and d is density). The amount of particles in 1 mmol PMMA could be calculated with the formula $n = M/m_p$ (M is the mass of 1 mmol PMMA, m_p is the mass of a PMMA particle). The required amount of PDI for 1 mmol PMMA particles was 10*n.

In the next step, PMMA particles with PDI were prepared via a non-aqueous emulsion in which DMF was used as dispersed phase, *n*-hexane as continuous one and PI-*b*-PMMA as emulsifier. With a fusion/fission method, monomer MMA and the PDI with double bonds were dispersed in two separated emulsions and then mixed together by treatment of ultrasonication to form hybrid droplets (Figure 11). This method was used to distribute carbon black in polymer particles: the fission/fusion process destroys all liquid droplets, and only hybrid ones being composed of all of kinds of monomers remain due to their higher stability [19]. This process can be realized by high energy ultrasound. The mixed emulsion was degasified with nitrogen in order to remove the oxygen which can deactivate the initiator. An initiator 2,2′-azobis(4-methoxy-2,4-dimethylvaleronitrile) (V-70) was used due to its low decomposition temperature (at 25 °C), because the polymerization had to take place under 45 °C. Above the temperature, the emulsion became instable due to the increased miscibility between dispersed and continuous phase (DMF and hexane). The polymerization began by adding the initiator V-70 under strong stirring. The reaction took 8 h and was stopped by adding hexane. The obtained PMMA particles had a broad size distribution between 20 nm and 200 nm (Figure 12).

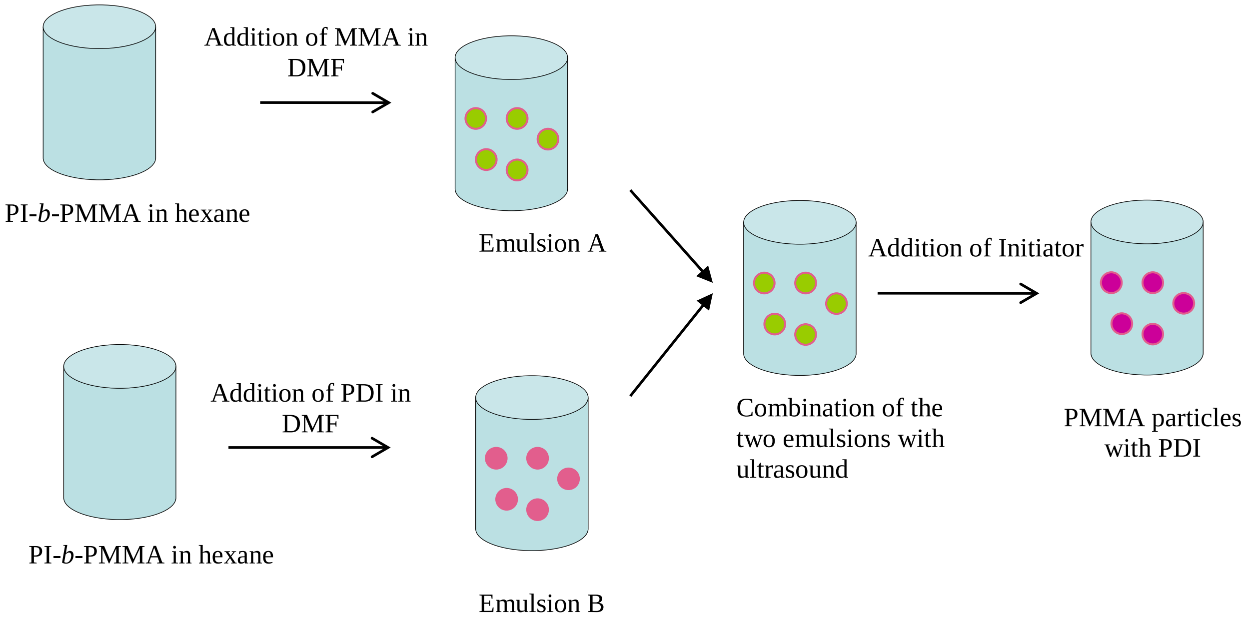

Figure 11. Preparation of PMMA particles loaded with PDI via a non-aqueous emulsion.

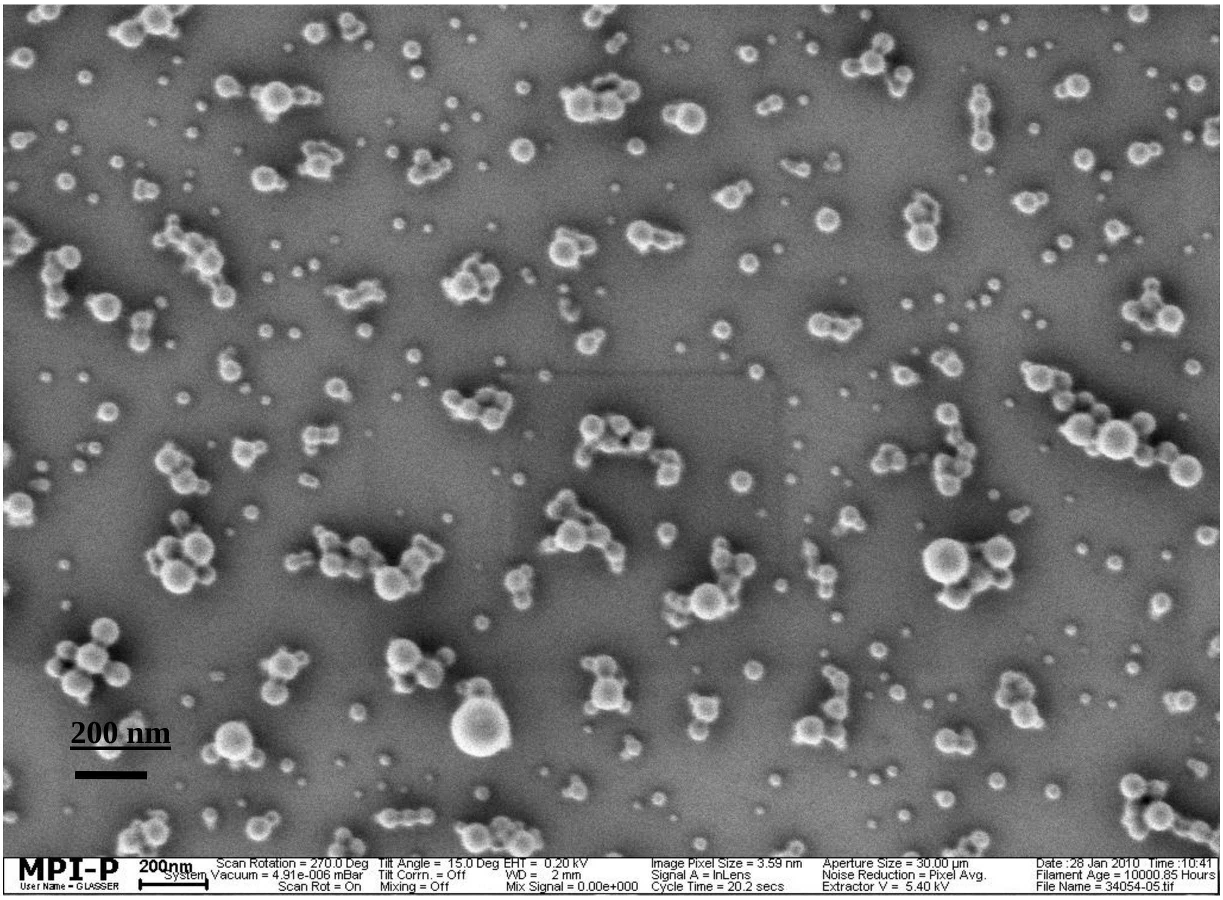

Figure 12. The SEM image of PMMA particles with PDI

4.2.2 Distribution of PDI molecules in particles

In this part, all of the measurements of the particles with PDI war carried out by the colleague from Department of Chemistry in Katholieke Universiteit Leuven. Before the particles were detected by single molecule fluorescence detection, they were analysed at first by other three analyse methods: dark-field microscopy, atomic force microscopy (AFM) and fluorescence microscopy to answer the first question: whether all of PMMA particles contained PDI molecules. The dark-field microscope and atomic force microscopy detect scattering light from the polymer particles, no matter they contain PDI or not. AFM is much more accurate than dark-field microscopy. Fluorescence microscope detects where the PDI dyes are located. Dark-field microscope and fluorescence microscope can detect a sample at the same time. A same place on a coverslip could be observed with both methods to compare whether same spots were detected.

The dispersion of the PMMA particles was spin-casted on a coverslip with a sufficiently low concentration in order to prevent the formation of aggregates of the particles. Figure 13 shows the dark-field and fluorescence microscopy images of a same area on the coverslip.

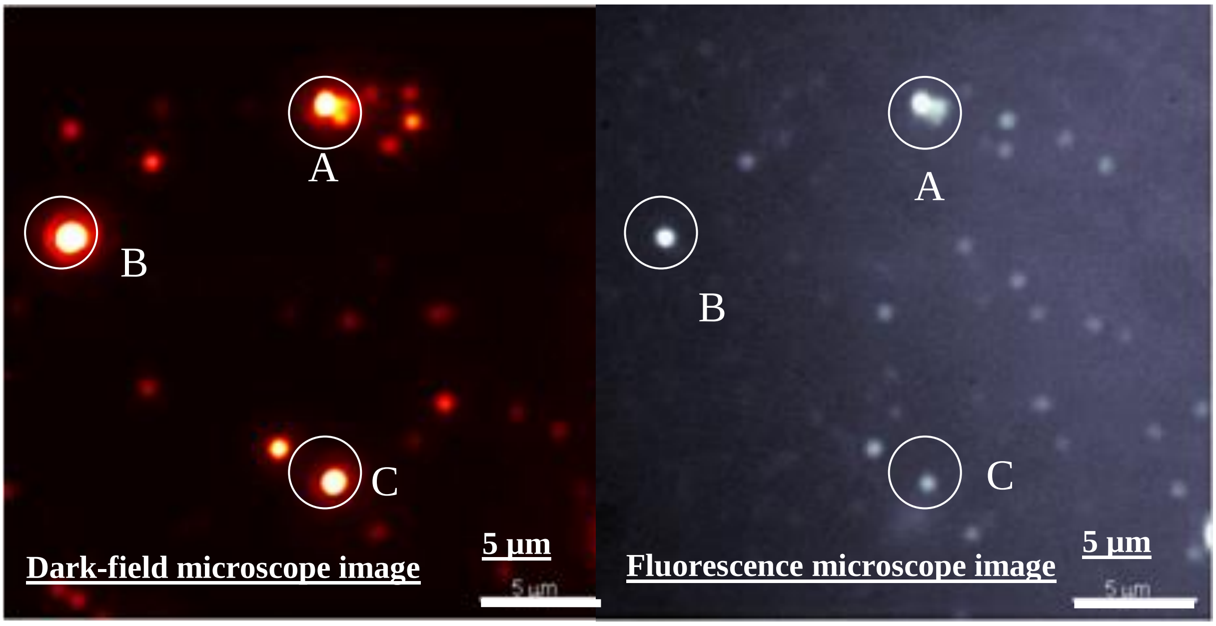

Figure 13. Dark-field (left) and fluorescence microscope (right) images of a same area on a coverslip.

Most of the spots in the dark-field image had their corresponding spots in the fluorescence microscope image, suggesting that PDI dyes had been successfully incorporated into the PMMA particles. But there were some relatively dim spots in the fluorescence microscope image that could not be observed in the dark-field image. These spots could be free PDI molecules which were not incorporated in polymer particles, or PDI molecules in very small particles (smaller than 20 nm) which hardly scattered light and were invisible in the dark-field image. In SEM image there were acutely particles with a size about 20 nm (Figure 12). In addition, the dark-field image and the fluorescence microscope image showed a few strongly lighting spots which could be aggregates of small particles (A and B in Figure 13).

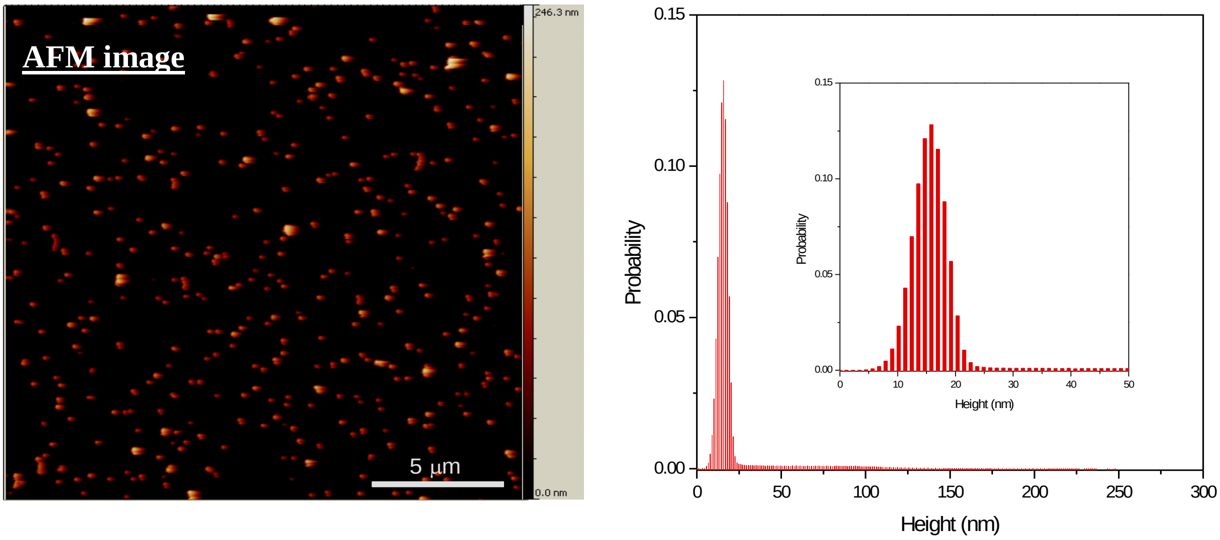

Figure 14. Left: an AFM image of the same sample. Right: the size distribution of PMMA particles from AFM measurement.

The sample was further measured by Atomic force microscopy which has a very high-resolution of scanning microscopy in the order of nanometer. All particles, even ones smaller than 20 nm could be observed with this method (Figure 14). AFM measurement showed that most particles had a size ranging from 5 to 25 nm (Figure 14 left).The same measured area in fluorescence microscopy could not be found again. But particle density (number of particles per unit area) could be compared in both methods (fluorescence microscope and AFM). A higher density was obtained in AFM images, meaning some particles did not contain PDI (Figure 15).

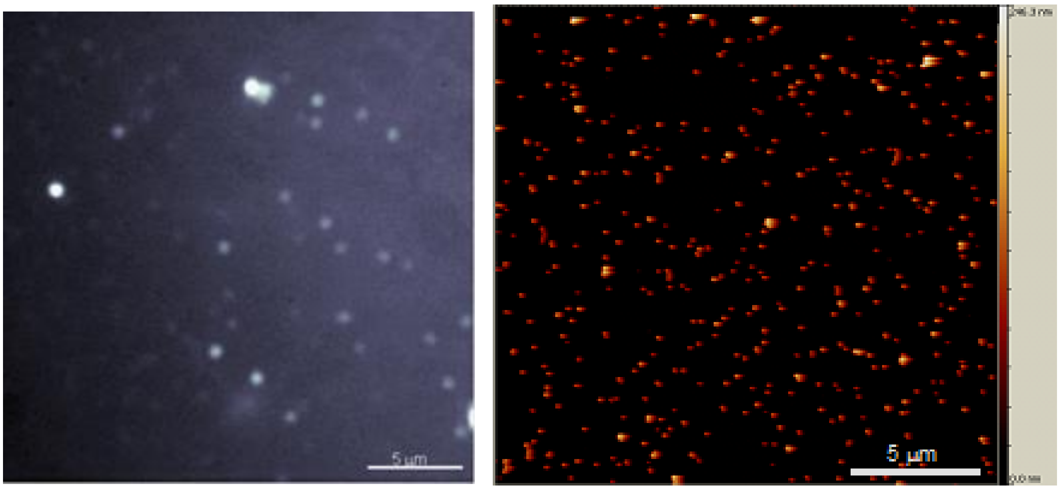

Figure 15. The comparison of the particle density in fluorescence microscopy (left) and Atomic force microscopy (right)

From these results it could be concluded that PDI molecules were not homogeneously distributed in all particles. Some of particles did not contain PDI dye. There could be also some of PDI molecules which were not incorporated into the particles and freely swung in the continuous phase.

For the second question: the amount distribution of dye molecules in the particles, 64 particles were chosen from dark-field microscope and inflorescence microscope image, insuring no free PDI molecules and only particles with PDI dyes.

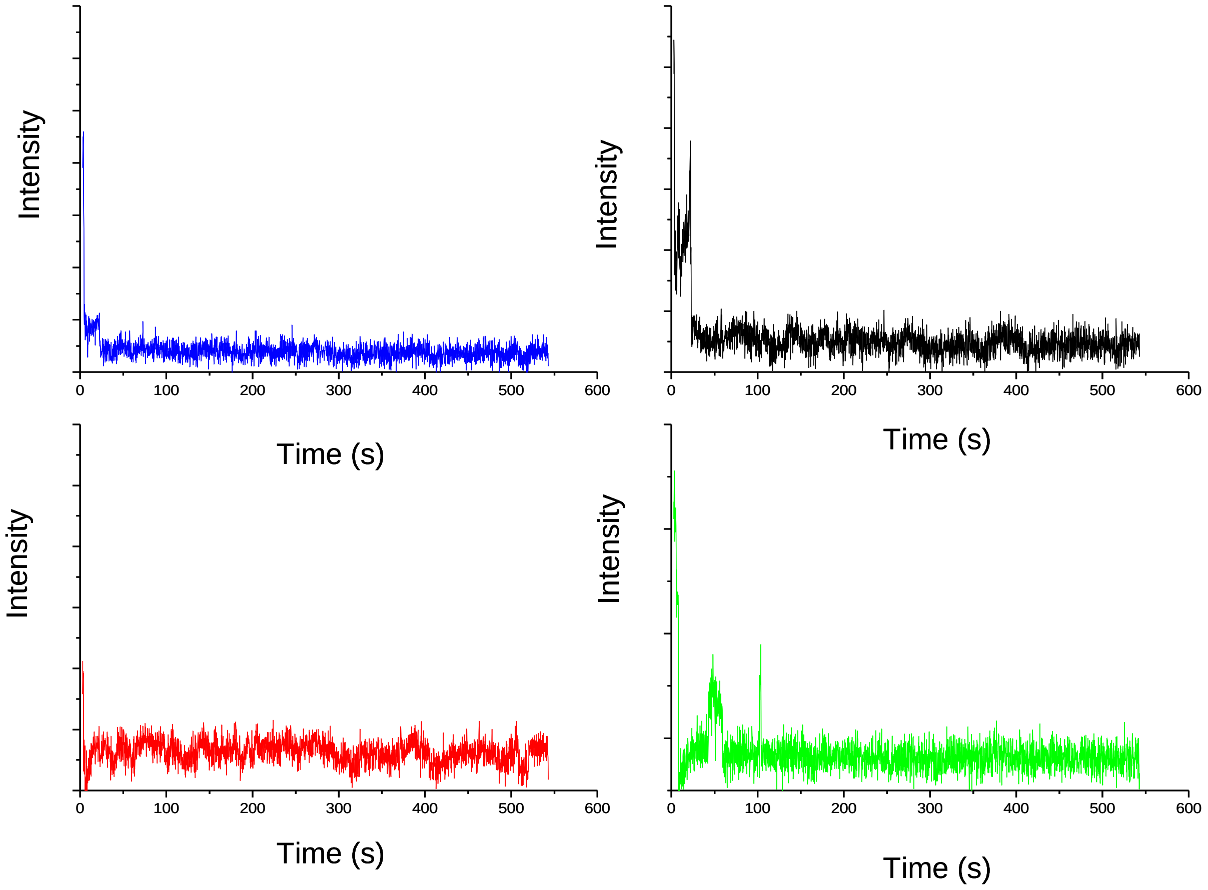

Figure 16. Single-step bleaching of the particles containing one PDI molecule.

The number of PDI dyes in each particle was determined by counting the bleaching steps. Single-step bleaching was observed for more than 30% of 64 particles, meaning that these particles contained only one PDI molecule (four examples showed in Figure 16).

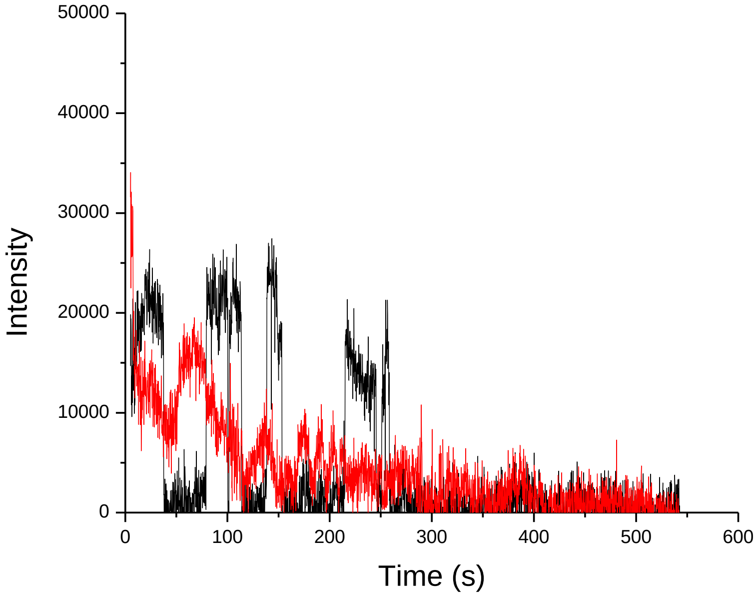

Figure 17. Multi-step bleaching for the particles containing over ten PDI molecules. Red and black curves are for two particles

Another about 15 % of the particles showed so many bleaching steps, that the bleaching depth in each step was very small, comparing to the total intensity. For accurate count of bleaching steps it was extremely difficult (Figure 17). These particles probably possessed more than 10 PDI molecules.

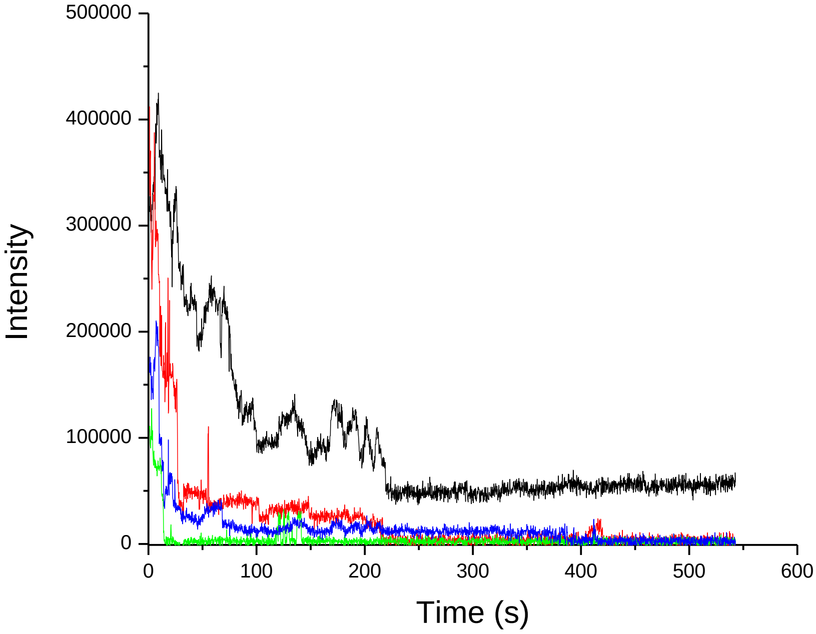

Figure 18. Multi-step bleaching of the particles contained up to ten PDI molecules.

The other 55 % of the particles showed bleaching steps with a bleaching depth which was comparable to the total intensity. Accurate counting of bleaching steps of these particles was possible (Figure 18). These particles were continuously analysed for the next study: the positions and orientations of PDI molecules inside of the particles.

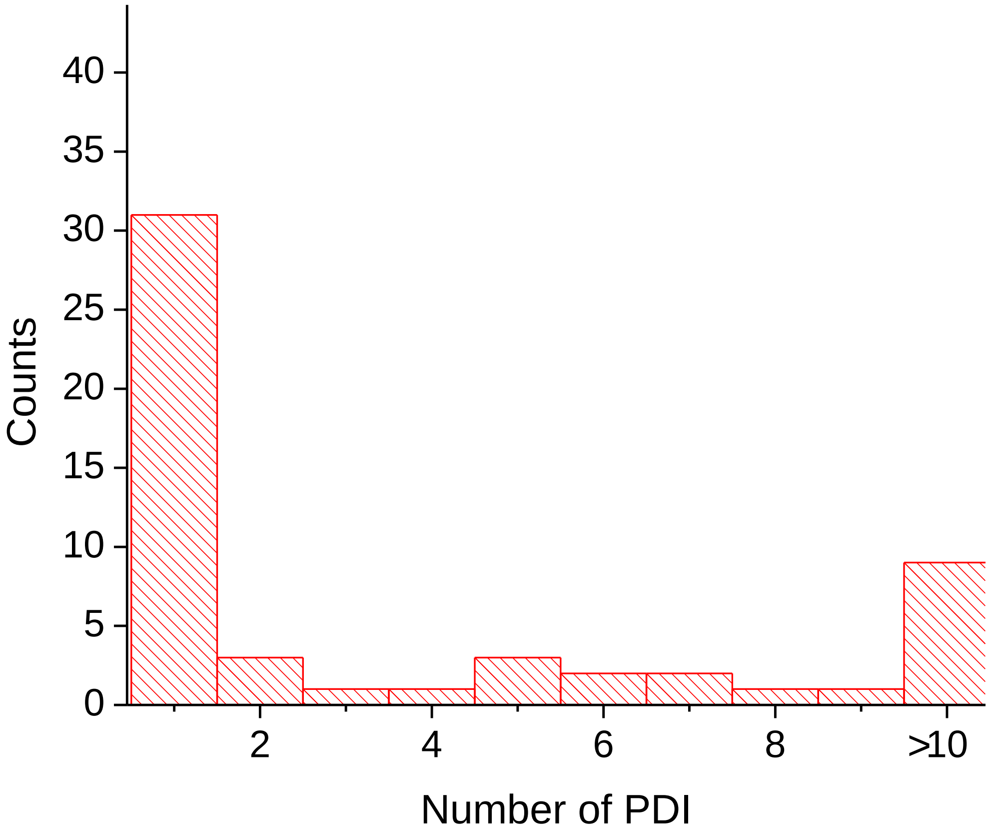

Figure 19. The distribution of the number of PDI molecules in 64 particles.

The distribution of PDI amount in the 64 particles were summarised in a diagram (Figure 19). It showed that over 30% particles contained only one or two dye molecules, about 10% over tens, the other about 60% particles with between 3 and 9 dyes.

4.2.4 Positions and orientations of PDI molecules inside of particles

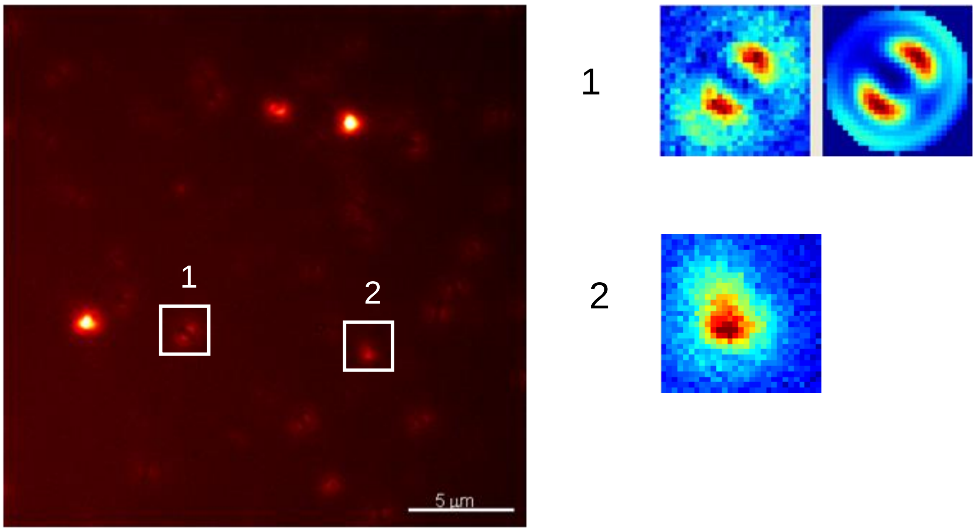

Figure 20. A defocused wide-field image of PMMA particles with PDI molecules.

Two particles were chosen for the investigation of the positions and orientations of PDI molecules (Figure 20). Particle 1 had four intensity levels in the intensity trace diagram, meaning that the particle contained four PDI molecules (Figure 21). By stochastic fluorescence photobleaching, temporary "bleaching" oft occurred (The same emission pattern were always detected). It could be explained that the PDI molecules stayed too close with each in the particle, causing energy hopping (where the adsorbed energy was only transferred between the close staying dyes without emission of fluorescence). The patterns (T_1, T_2, T_3, T_4, T_5 and T_7) were for one PDI molecule and the patterns T_6 and T_8 for another PDI molecule (Figure 22). The detection of the positions of the four PDI molecules conformed that they real stayed in a distance of smaller than 5 nm and could not be separated from each other. Hence making distribution diagram of these four molecules in particle 1 was not possible.

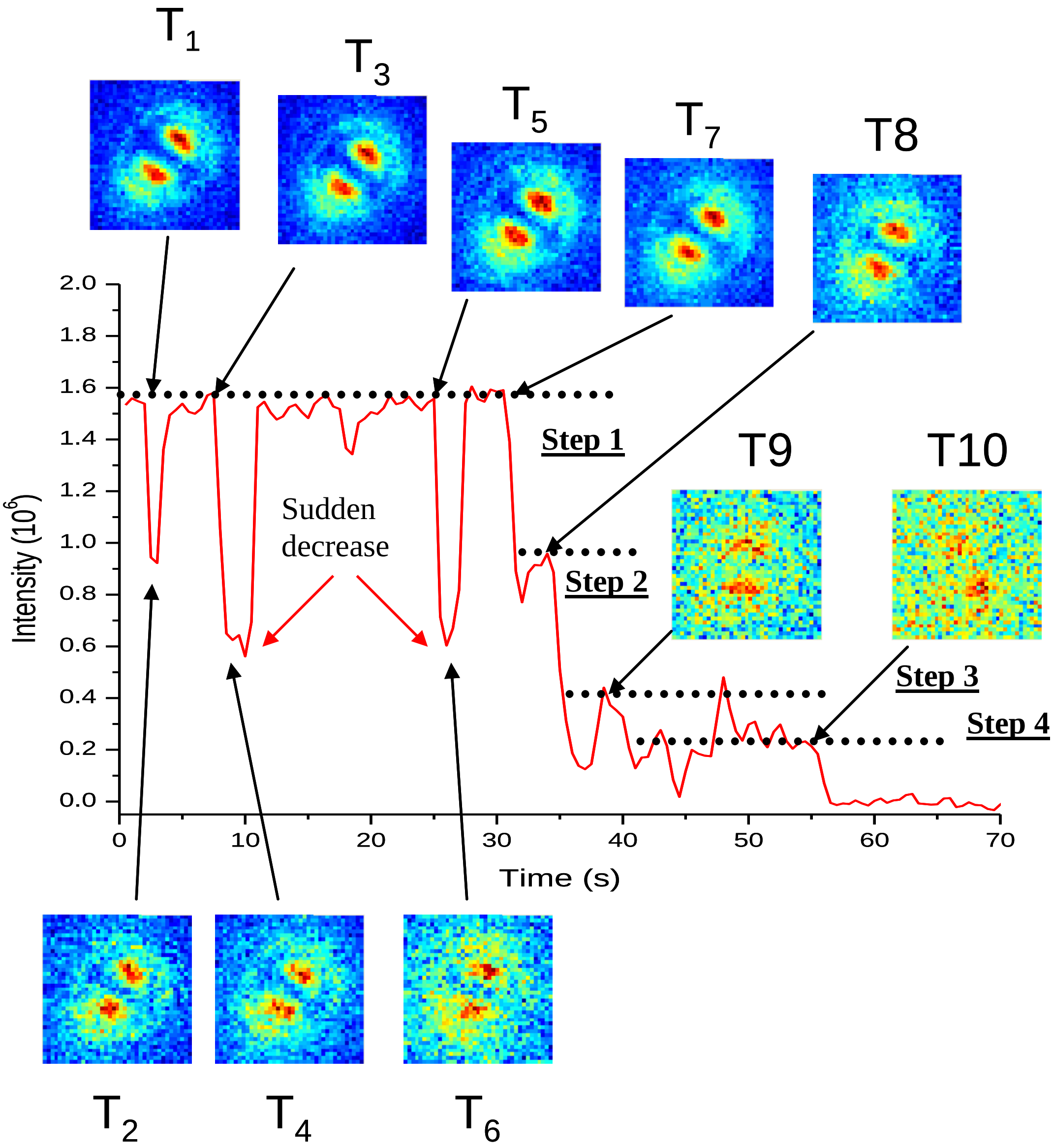

Figure 21. The fluorescence intensity trace and the obtained emission patterns of the particle 1

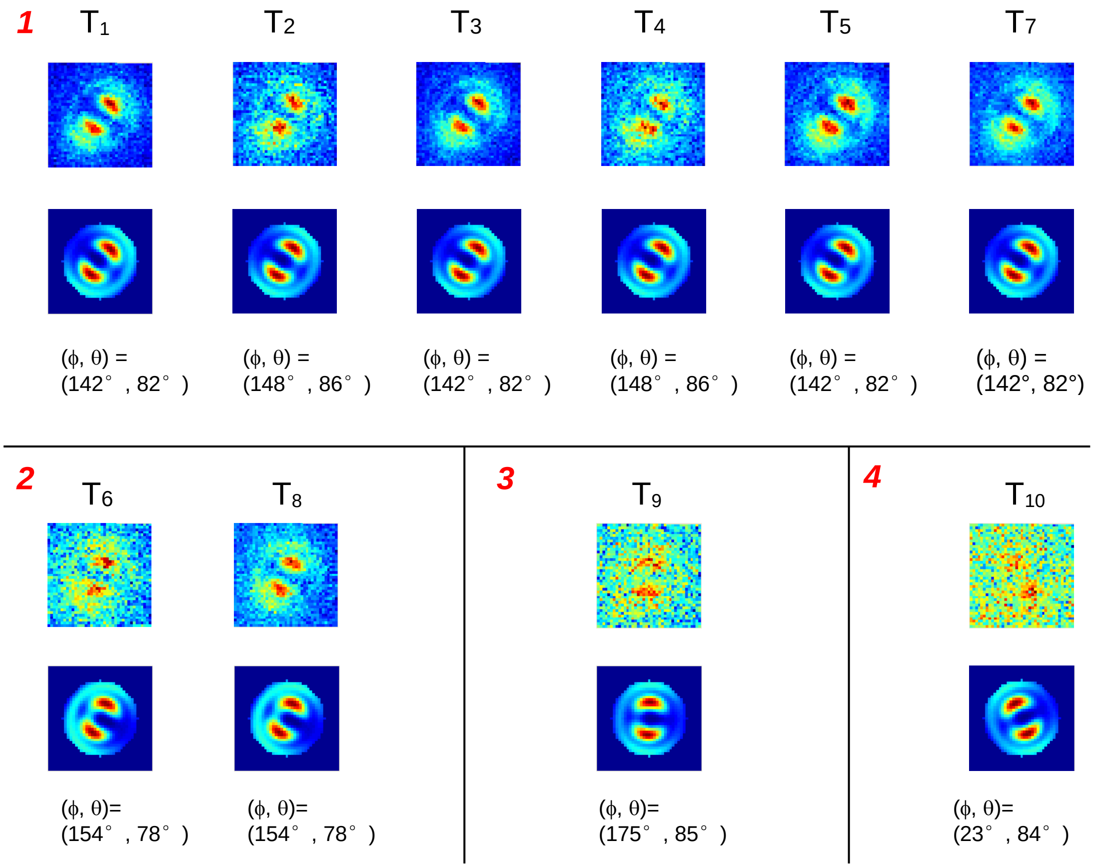

Figure 22. The orientations of the four PDI molecules in particle 1

Particle 2 did not show any temporary “bleaching”, meaning the PDI molecules had a relative large distance to each other (Figure 23). Eight-step-bleaching were observed in the fluorescence intensity trace diagram, responding eight PDI molecules. The PDI molecules had randomly orientated in the particle, with an in-plane angle varying from 34^{o} to 178^{o} and an out-of-plane angle from 86^{o} to 40^{o} (Figure 24).

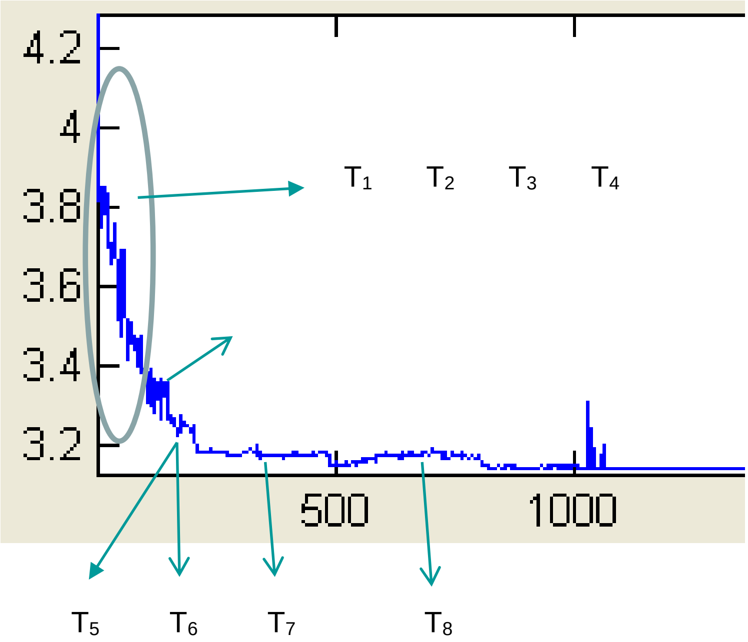

Figure 23. Fluorescence intensity trace of particle 2

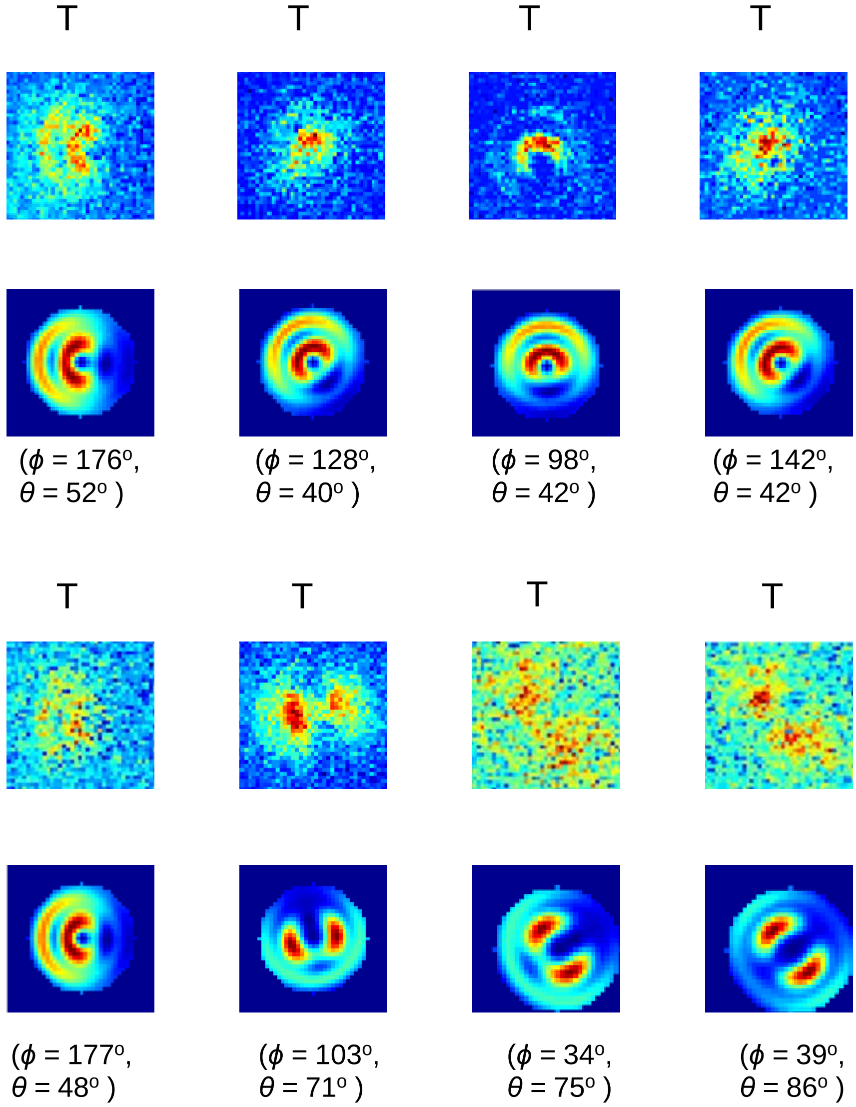

(ϕ = 176°, θ = 52°)

(ϕ = 128°, θ = 40°)

(ϕ = 98°, θ = 42°)

(ϕ = 142°, θ = 42°)

(ϕ = 177°, θ = 48°)

(ϕ = 103°, θ = 71°)

(ϕ = 34°, θ = 75°)

(ϕ = 39°, θ = 86°)

Figure 24. The measured emission patterns of the eight PDI molecules in particle 2

To determine the position of the PDI molecules in particle 2, a spot was arbitrarily set as the centre of the particle (the red spot figure 25). The positions of the eight PDI molecules were then plotted relative to this red spot. As shown in Figure 25, PDI molecules were distributed within a circle with a diameter of 400 nm as a particle. It could be also assumed that the dye molecules belonged to two small particles with diameters of 150 nm and 160 nm, agreeing with the measurement of SEM (see section 4.4) where the particles have sizes from 20 nm to 200 nm.

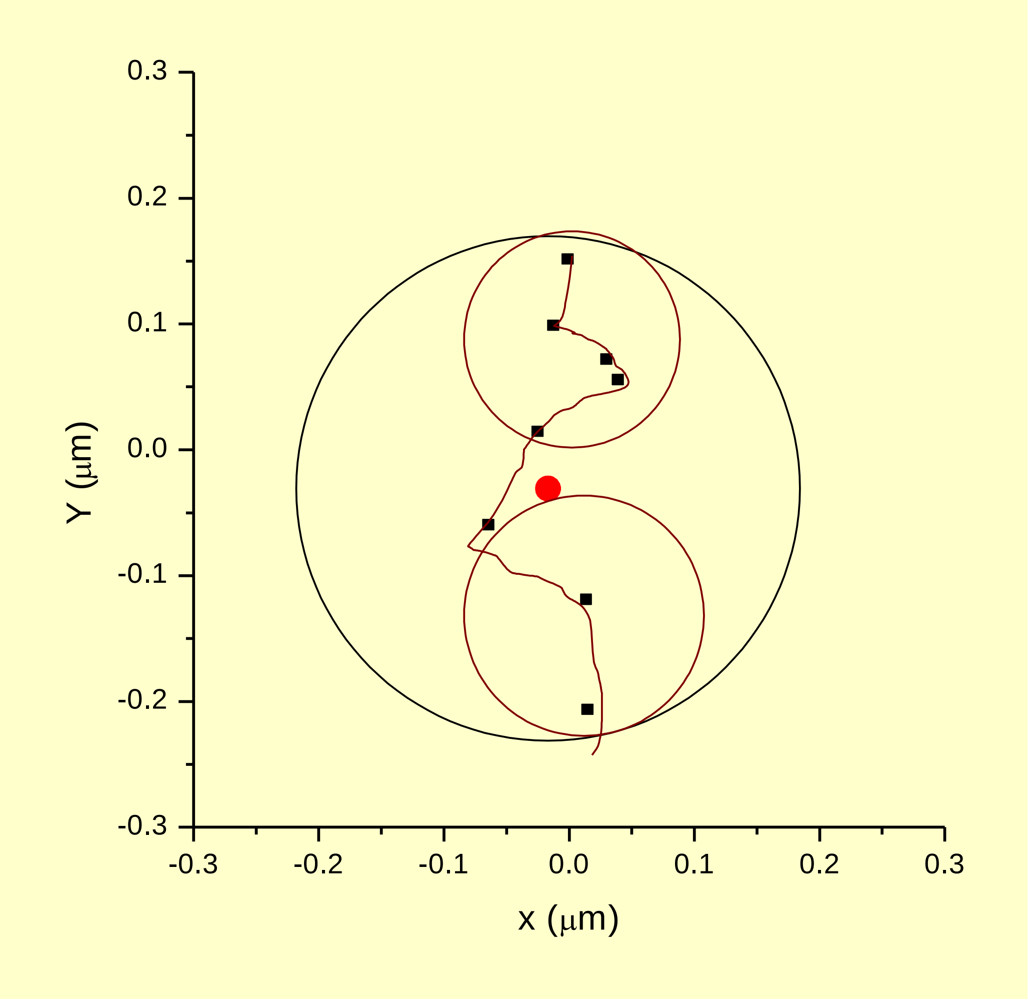

Figure 25. The distribution of PDI molecules in particle 2.

In both possibility (in a large particle or in two small particles), the PDI molecules were relatively homogeneously distributed with a distance of about 100 nm. It is known that monomers in chain-growth polymerization react only with the reactive centre at the end of the polymer chains. By synthesis of copolymer, monomers with high reactivity could preferentially react and built a block in the chains. Here, no block of PDI molecules was observed, suggesting the reactivity of MMA and PDI was not much different.

From the results it could be concluded that PDI molecules were relatively homogenously distributed in side of the particle 2. The random orientation of PDI molecules suggested that no aggregation of dye molecules was built in the particle. It could suppose that the polymer chain freely twisted. When the particles were bound together, a curve was obtained like random coil (Figure 26-I). It meant that the polymer chain had high flexibility. It is suitable to the chemical nature of PMMA in which methylmethacrylate groups have only weak interaction and the chains have high mobility. It was also possible that the PDI molecules could belong to more than one chain.

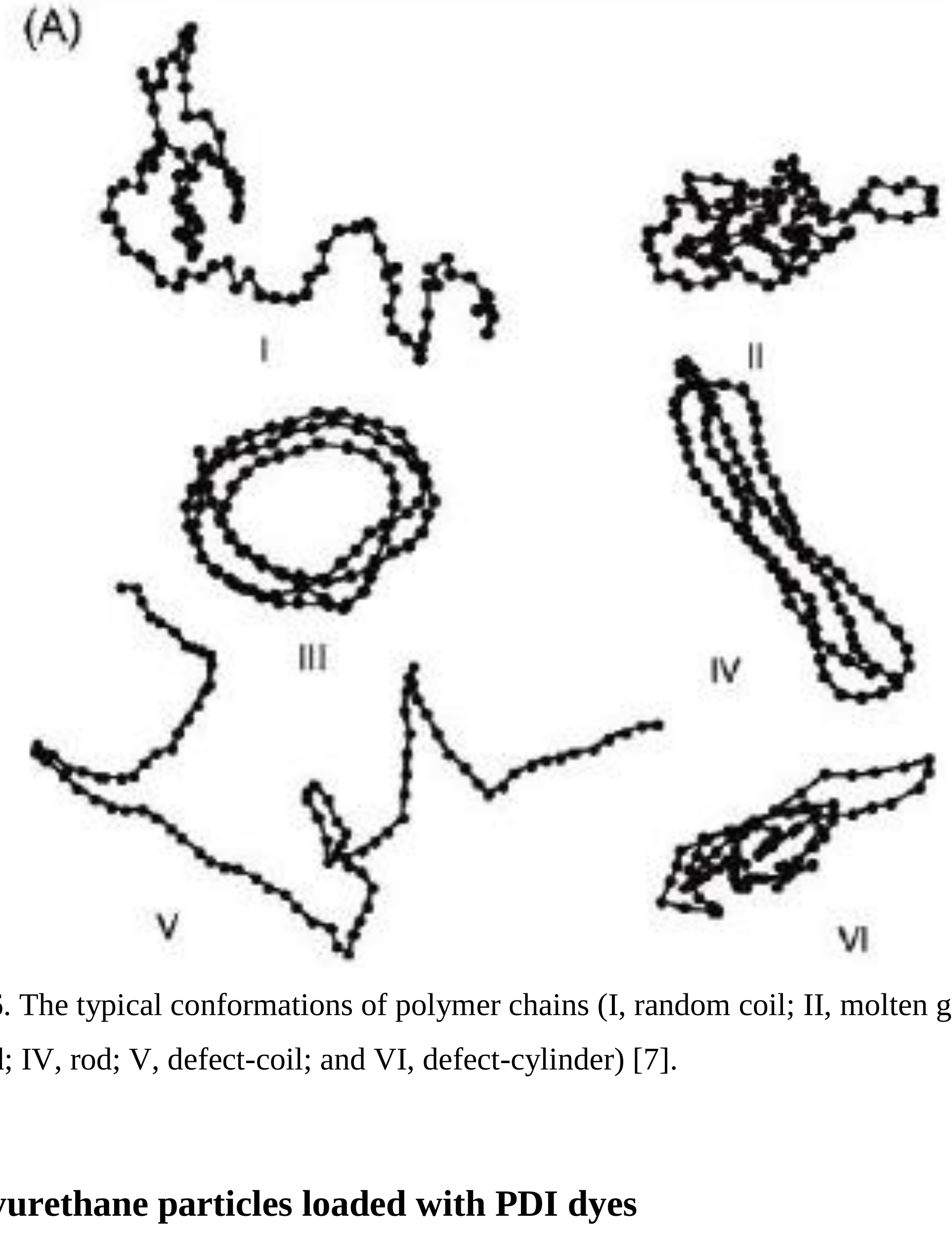

Figure 26. The typical conformations of polymer chains (I, random coil; II, molten globule; III, toroid; IV, rod; V, defect-coil; and VI, defect-cylinder) [7].

4.3 Polyurethane particles loaded with PDI dyes

The synthesis of the PDI with OH-group was already reported in the literature (Figure 27) [20]: it began with tetrakis chlorid-3,4,9,10-perylenetetracarboxylic dianhydride. Imidization of perylenetetracarboxylic dianhydride with 4-amino phenol carried two OH-groups into the *peri* regions. In this reaction, propanoic acid was used as solvent because of its high boiling temperature. In the next step, it was substituted in the 1,12,6,7- positions with tetramethylbutylphenol. The end product was precipitated with aqueous hydrochloric acid and then purified by column chromatography. The PDI for this work was synthesized by the colleague from Synthetic Chemistry in Max Planck Institute for Polymer Research.

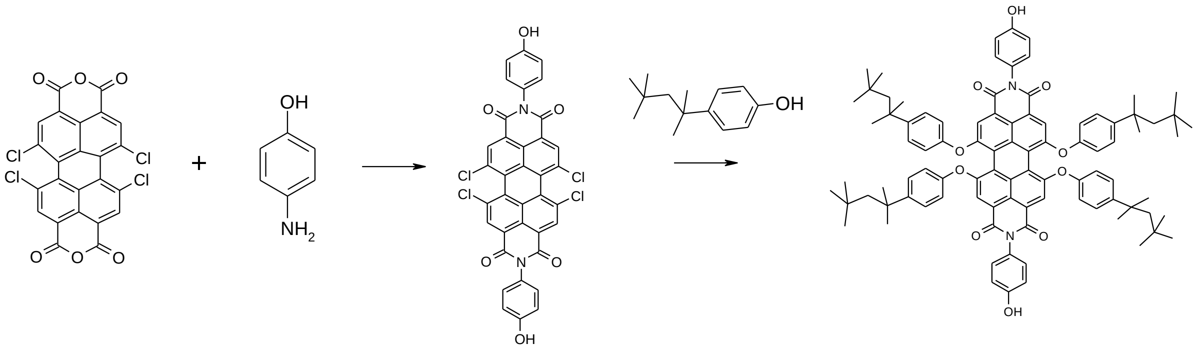

Figure 27. The synthesis of PDI with two OH groups [20].

The amount of PDI was so calculated, that each particle should contain 10 PDI molecules. In the preparation of the particles, PDI and diol were dispersed in two separated emulsions and then mixed by treatment with ultrasound to obtain hybrid droplets with diol and PDI (Figure 28). The polymerization was carried out by adding the monomer diisocyanate HMD into the obtained emulsion. The polymerization took eight hours and then was stopped by adding *n*-hexane. The particles were washed with *n*-hexane three times in order to remove the remaining surfactant on the surface. The obtained particles had a size ranging from 200 nm to 500 nm (Figure 29).

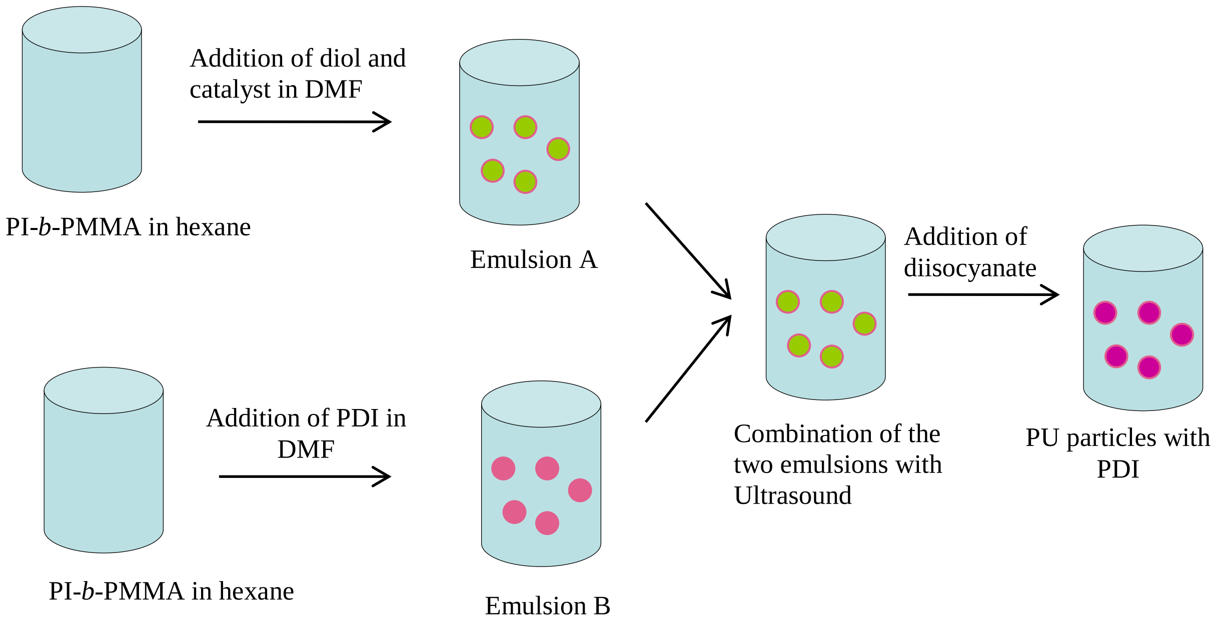

Figure 28. The synthesis of polyurethane particles with PDI.

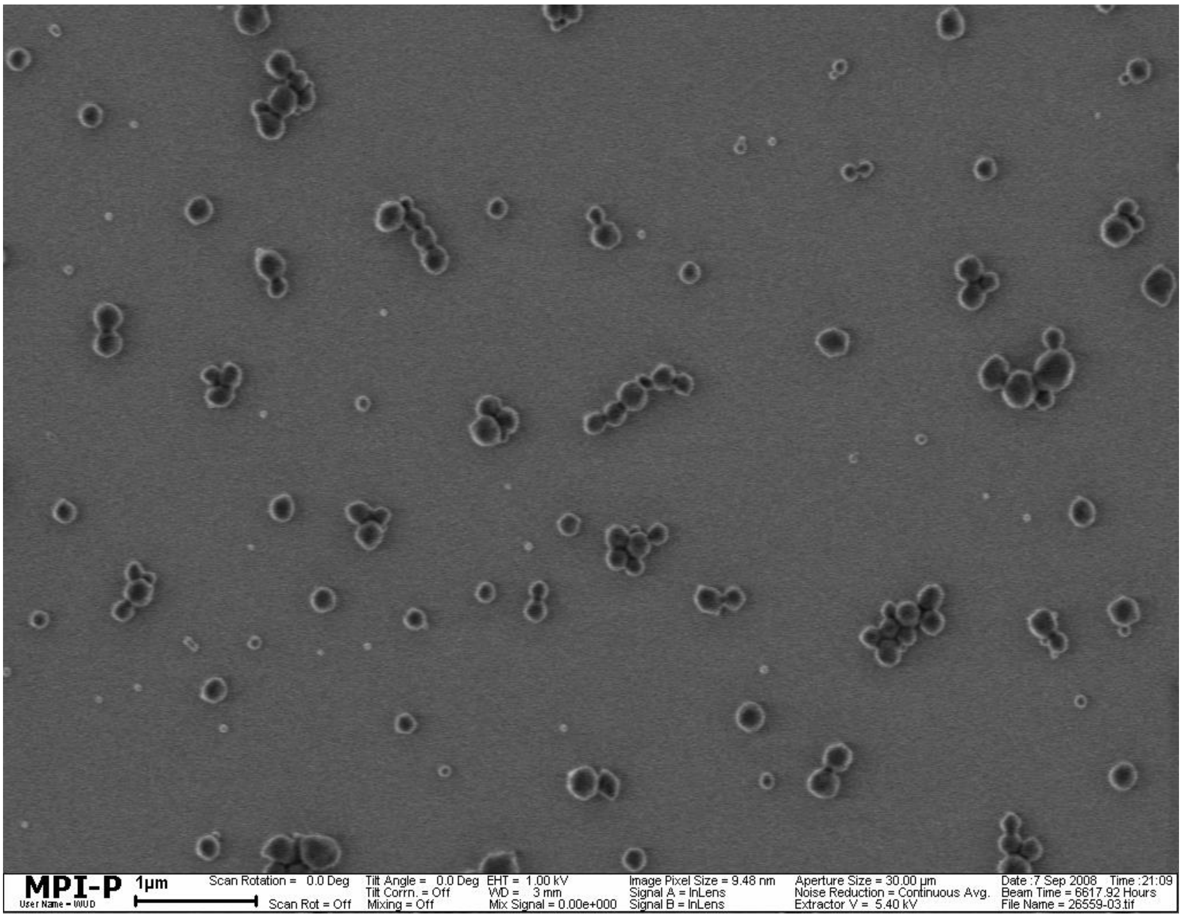

Figure 29. SEM image of polyurethane particles with PDI

In the following part, all of the measurements of the particles with PDI war carried out by the colleague from Department of Chemistry in Katholieke Universiteit Leuven. For the single molecule fluorescence detection, the obtained polyurethane particles were dispersed in hexane and spin-casted on a coverslip with a low concentration, preventing formation of aggregates. A defocused wide-field fluorescence image showed that some of the particles emitted very strong light, probably containing too many PDI molecules. Some emitted very dim light, maybe containing only one or two PDI molecules (Figure 30). There were also some particles with two-lobe patterns which could be detected by stochastic fluorescence photobleaching.

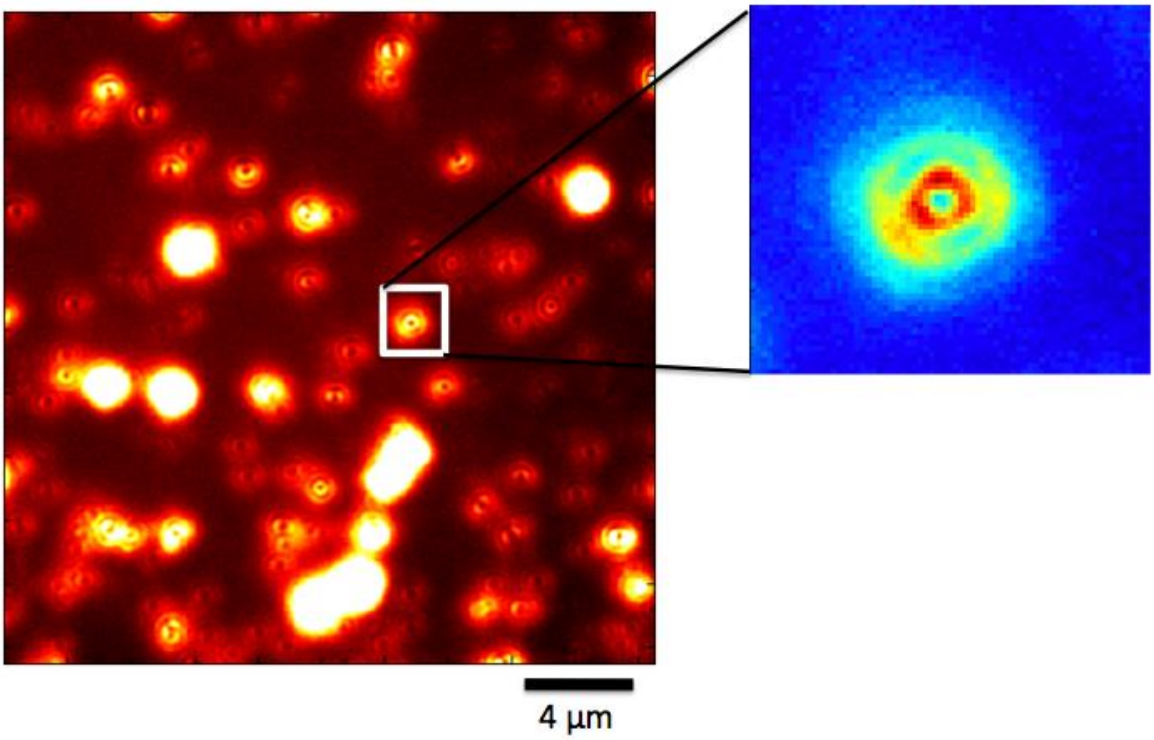

Figure 30. Left: defocused wide-field fluorescence imaging of the polyurethane particles with PDI. Right: a typical emission pattern of a particle.

One particle in Figure 30 was chosen to detect the positions and orientations of PDI molecules. Its intensity traces diagram displayed eight bleaching steps, meaning eight PDI molecules in this particle. These PDI molecules had random orientations: the out-of plane angle varied from 4 ° to 84 ° and the in-plane angle from 7 ° to 300 ° (Figure 31).

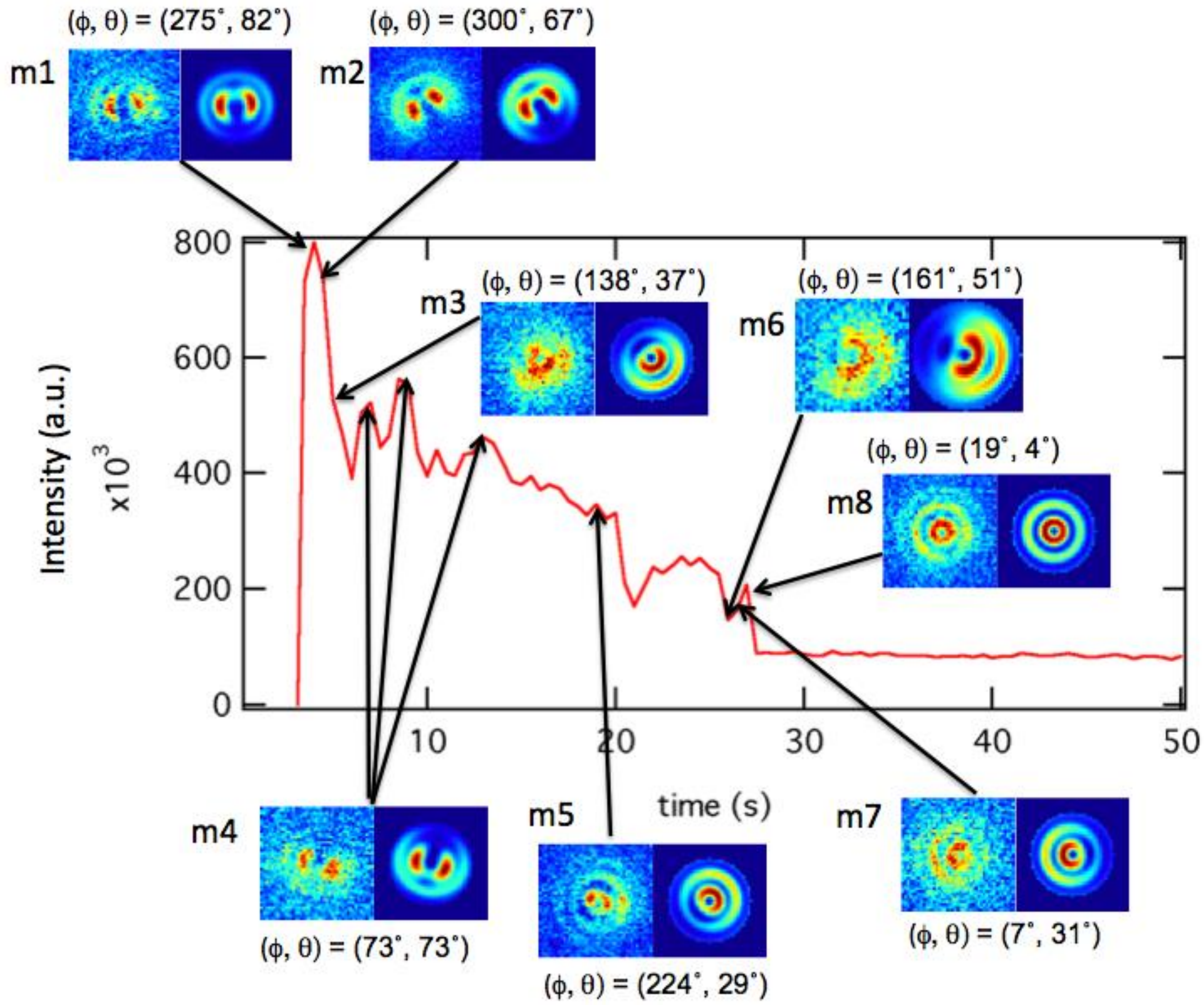

Figure 31. Emission patters of one polyurethane particle with eight PDI molecules.

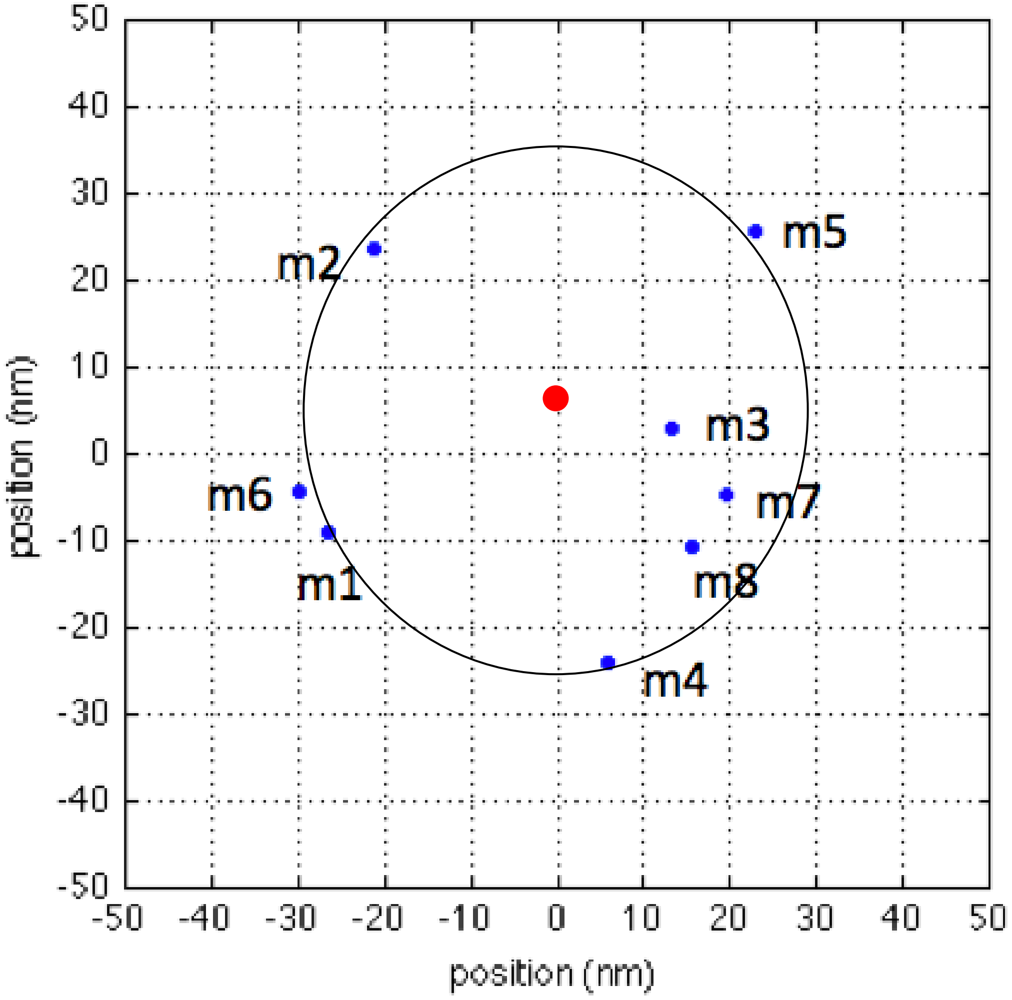

Figure 32. The distribution of PDI molecules in the particle

The positions of the PDI molecules inside of this particle were represented graphically in Figure 32. The distances between neighbourhood PDI molecules varied from 10 nm to 40 nm, smaller than the one in PMMA particles (about 100 nm). The orientation of the neighbourhood PDI molecules was different, meaning that no aggregates of PDI molecules were built. This result agreed to the expectation for step-growth polyaddition: monomers were built in polymer chains by reaction from short chains to long ones. Therefore the formation of aggregates of PDI molecules in PU chains was almost impossible. The PDI molecules were distributed almost on the edge of a circle with a size of about 60 nm. It could suggest that the conformation of the polymer chain looked like a toroid (Figure 33-III). It agreed to the chemical nature of polyurethane in which urethane groups had strong interaction with each other. Hence the chains had less reflexivity, compared to PMMA ones.

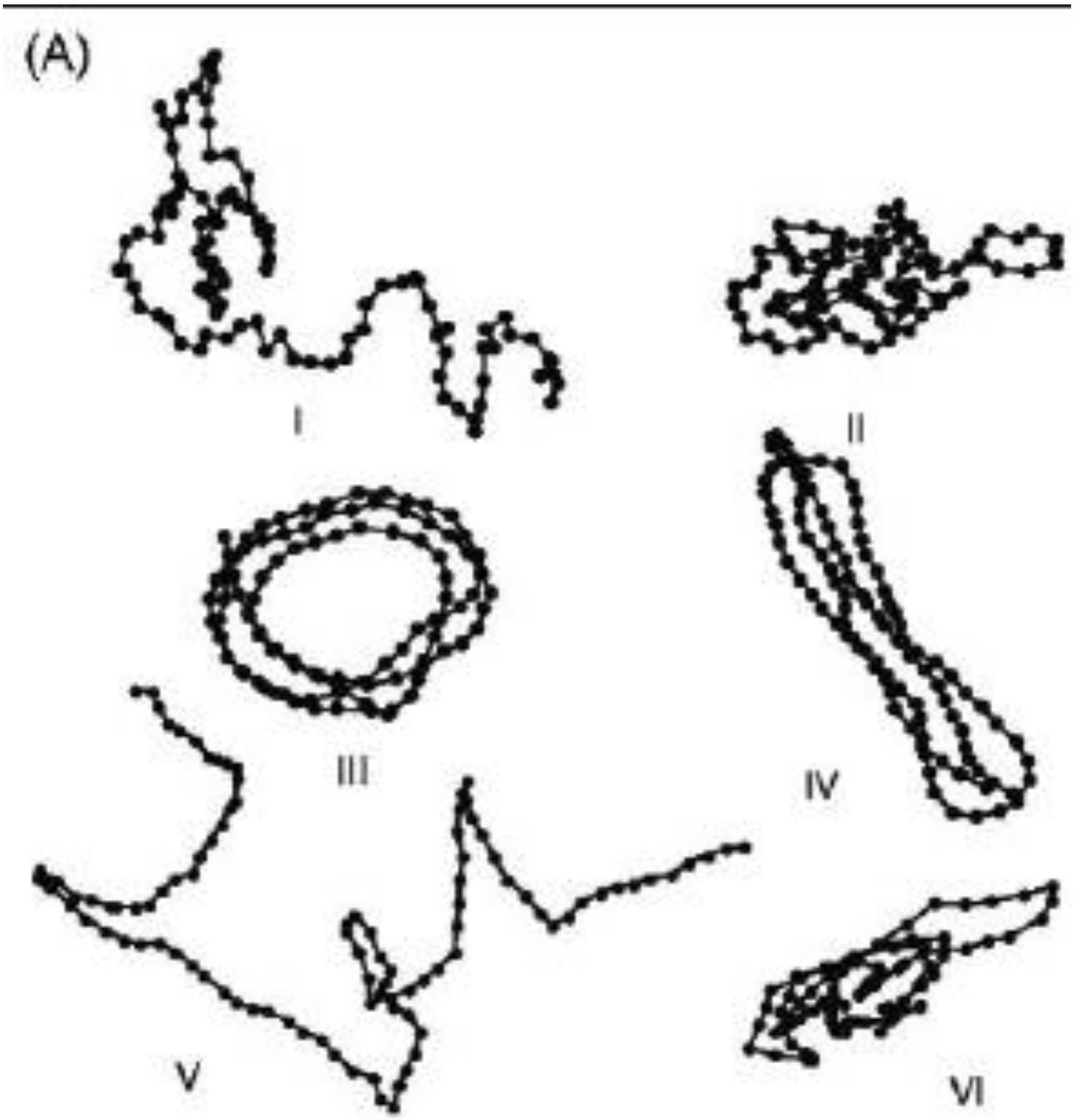

Figure 33. The typical conformations of polymer chains (I, random coil; II, molten globule; III, toroid; IV, rod; V, defect-coil; and VI, defect-cylinder) [7].

4.4 Conclusion

In this study, PMMA and PU particles from one non-aqueous emulsion were investigated via single molecule fluorescence detection. At first the particles were loaded with PDI dye which were detected by fluorescence microscopy. The distribution and orientation of the PDI molecules in the particles were successfully observed by Single Molecule Fluorescence Detection. The molecules were relatively distributed inside of the particles. In addition they had random orientation, meaning that no aggregation of dye molecules were formed. With the results, it could be supposed that the polymer chains were also relatively homogenously distributed in the particles and the conformation was relatively flexible. From the comparison of the results for PMMA and PU particles, it was found that the conformation of the chains in the particles strongly depended on the chemical nature of the polymers: low interaction between the chains and more flexibility of the conformation.

References

1. Yamada, B., et al., *ESR spectroscopic studies of radical polymerization.* Progress in Polymer Science, 1999. **24**(4): p. 565-630.
2. Beuermann, S. and M. Buback, *Rate coefficients of free-radical polymerization deduced from pulsed laser experiments.* Progress in Polymer Science, 2002. **27**(2): p. 191-254.
3. Schweer, J., et al., *Pulsed-laser polymerization/matrix-assisted laser desorption/ionization mass spectrometry: An approach toward free-radical propagation rate coefficients of ultimate accuracy?* Macromolecules, 1996. **29**(13): p. 4536-4543.
4. Heatley, F., P.A. Lovell, and J. Mcdonald, *Nmr-Studies of Free-Radical Polymerization and Copolymerization of Monomers and Polymers Containing Allyl Groups.* European Polymer Journal, 1993. **29**(2-3): p. 255-268.
5. Frahn, M.S., L.H. Luthjens, and J.M. Warman, *N-(2-anthracene)methacrylamide: a new fluorogenic probe molecule for monitoring in situ the radiation-induced polymerization of methyl methacrylate in bulk and in solution.* Polymer, 2003. **44**(26): p. 7933-7938.
6. Muls, B., et al., *Direct measurement of the end-to-end distance of individual polyfluorene polymer chains.* Chemphyschem, 2005. **6**(11): p. 2286-2294.
7. Barbara, P.F., et al., *Single-molecule spectroscopy of conjugated polymers.* Accounts of Chemical Research, 2005. **38**(7): p. 602-610.
8. Dedecker, P., et al., *Defocused Wide-field Imaging Unravels Structural and Temporal Heterogeneity in Complex Systems.* Advanced Materials, 2009. **21**(10-11): p. 1079-1090.
9. Woell, D., et al., *Radical polymerization tracked by single molecule spectroscopy.* Angewandte Chemie-International Edition, 2008. **47**(4): p. 783-787.
10. *Introduction to Polymer Chemistry*, 2003: Department of Chemistry University of Rochester.
11. Braun, D., et al., *Polymer Synthesis: Theory and Practice*2005, Berlin: Springer.
12. Odian, G., *Principles of Polymerization*2004, Island: Wiley-Interscience.
13. Cowie, J.M.G.A., V.,, *Chemistry and Physics of Modern Materials*, in *Polymer*2008.
14. Patra., D., I. Gregor., and J. Enderlein, *Image Analysis of Defocused Single-Molecule Images for Three-Dimensional Molecule Orientation Studies.* J. Phys. Chem. A, 2004. **108** (33).

15. Bohmer, M. and J. Enderlein, *Orientation imaging of single molecules by wide-field epifluorescence microscopy*. Journal of the Optical Society of America B-Optical Physics, 2003. **20**(3): p. 554-559.
16. Bohmer, M. and J. Enderlein, *Fluorescence spectroscopy of single molecules under ambient conditions: Methodology and technology*. Chemphyschem, 2003. **4**(8): p. 793-808.
17. Uji-i, H., et al., *Visualizing spatial and temporal heterogeneity of single molecule rotational diffusion in a glassy polymer by defocused wide-field imaging.* Polymer, 2006. **47**(7): p. 2511-2518.
18. Hofkens, J., *Revealing competitive Forster-type resonance energy-transfer pathways in single bichromophoric molecules.* Proceedings of the National Academy of Sciences, 2003. **100**(23): p. 13146-13151.
19. Tiarks, F., K. Landfester, and M. Anonietti, *Encapsulation of carbon black by miniemulsion polymerization.* Macromolecular Chemistry and Physics, 2001. **202**(1): p. 51-60.
20. H. Quante, 1995, Universität Mainz (Germany).

Chapter 5.

Dispersions of graphene nanosheets

5.1 Introduction

5.1.1 The history of graphene nanosheets

Graphene sheets have recently attracted a lot of attentions because of their fascinating properties: high values of Young's modulus (~1,100 GPa), thermal conductivity (~5,000 W $m^{-1}K^{-1}$), mobility of charge carriers (200,000 $cm^2\ V^{-1}\ s^{-1}$), fracture strength (125 GPa), and specific surface area (calculated value 2,630 $m^2\ g^{-1}$) [1-6]. It is promising candidates as components in applications such as energy-storage materials, 'paper-like' electric conductive materials, liquid crystal devices and mechanical resonators, polymer composites, [2, 7-14].

Graphene nanosheets were generally prepared with four methods reported in the literature. The first one was chemical vapor deposition where carbon hydrogen compounds were decomposited at high temperature, and then condensed on the surface of a special metal, for example C-doped nickel single crystals, to form monolayer of graphene [15]. The second method was the micromechanical exfoliation of graphite, also known as the 'Scotch tape' or peel-off method where monolayer of graphene nanosheets (the sheets contained only one layer of graphene) were peeled off from the surface of graphite by use a tape [16]. The third one was thermal reduction of expanded graphite prepared by intercalating nature graphite with a mixture of nitric and sulphuric acids [17]. From this method, graphene sheets with a surface area from 30 to 60 m^2/g were obtained [18-22]. Surface area is an indication of exfoliation degree of graphene sheets (how many monolayers graphene sheets contain). The theoretical surface area of monolayer is 2,630 $m^2\ g^{-1}$ for monolayer with a thickness about 0,34 nm [23]. Compared with theoretical surface, it was supposed that the graphene sheets from expanded graphite (30 to 60 m^2/g) had a thickness between 5 µm and 20 µm, contain 50 to 80 monolayers [21]. In the fourth method, graphene oxide sheets, prepared by oxidization of natural graphite with concentrated acids, were reduced by chemical or thermal routs to graphene sheets [24-26]. By chemical reduction, hydrazine was usual as reduction agents [27]. The obtained graphene sheets had a surface area between 200 nm and 400 m^2/g, containing from 10 to 20 monolayers (thickness from 5nm to 10 nm) [27]. By thermal exfoliation (thermal reduction), graphene oxide were pyrolyzed at 1000 °C. The obtained graphene nanosheets had a surface area between 500 m^2/g and 900 m^2/g, containing from 5 to 10 monolayers (thickness from 3nm to 5nm) [28].

Incorporation of graphene sheets into polymer matrices is one possible route to harnessing their excellent properties (high mechanical, electrical and thermal stability) for practical applications. The ways to introduce graphene sheets in polymer matrices could be classified into melt and solution mixing. Melt mixing was often considered to be an economical method for many current industrial processes [29, 30]. However, the low bulk density of graphene material made handling of this material very difficult [26]. In method based on solution, dispersions of graphene sheets in organic solvents were mixed with desired polymers. To improve compatibility between the matrices and the graphene, the sheets were normally modified by surfactants or other block copolymer [29]. An excellent example for the modification of graphene sheets by using isocyanate: on graphene oxide sheets, the carboxylic acid and hydroxyl groups could react with aliphatic and aromatic isocyanate to build amide and carbamate ester groups. Such modified sheets were then chemically reduced with dimethylhydrazine to graphene nanosheets which could be stably dispersed in DMF. Polystyrene composites with a low concentration of these graphene sheets showed high electric conductivity [12, 31]. In this method, a solvent with high boiling point and toxicity DMF was used to prepare the dispersion of graphene nanosheets. Such solvent caused problems for environments, safety of production process and high cost.

The focus of the present work is to develop an economical, healthy and safe process to prepare dispersions of graphene sheets in organic solvents for polymer composites. In the first part of the work, graphene sheets will be prepared by thermal reduction of graphene oxide sheets. To obtain a stable dispersion, the sheets will be modified by different modifiers, for example block copolymer PMMA-b-PI. Different solvents with low boiling points and low toxicity will be tested as dispersion solvents. In the second part of the work, the dispersions of graphene sheets will be used to prepare polymer composites. The influence of graphene sheets on the electric, mechanic and thermal stability of the composite will be also studied in the study.

5.1.2 Graphite, graphene oxide and graphene nanosheets

5.1.2.1 Graphite

Figure 1. Nature graphite

In graphite (Figure 1), the carbon atoms are trigonally hybridized (sp^2) and arranged in layer structure in which atoms form hexagonal patterns with metallic bond (length 0.142 nm). This structure results in a good electrical and thermal conductivity within the layers (Figure 2). The distance between the layers (0.335 nm) is considerably larger than the in-plane bond (0.142 nm). The layers are organized in an AB-sequence with weak van der Waals forces (Figure 3). Hence they can be easily slipped against each other. Due to this property, graphite is used for lubrication in industry. But when air or water molecules are intercalated between the layers, the van der Waals forces are destroyed, and lubrication does not work anymore. This discovery helped researchers to prepare expanded graphite by intercalation of acid molecules between the layers of graphite.

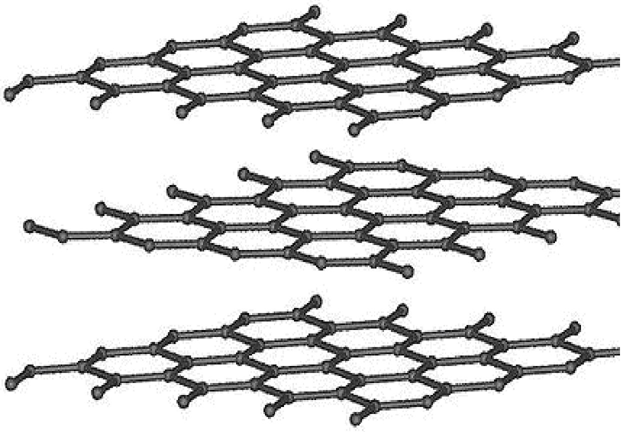

Figure 2. The layer structure of graphite

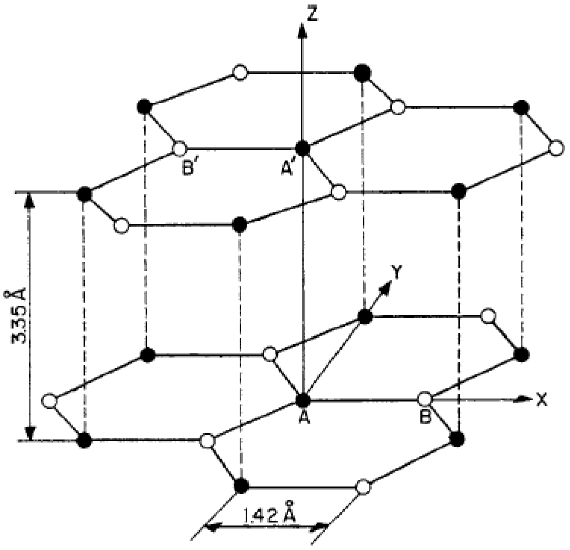

Figure 3. The atom structure of graphite.

5.1.2.2 Graphene oxide

Graphene oxide is a very import precursor to prepare graphene nanosheets. In 1859 Brodie first oxidized graphite by using a mixture of potassium chlorate and fuming nitric acid [32]. Later Studenmaier slightly changed the recipe by working with concentrated sulphuric, nitric acids and potassium chlorate instead [33]. To improve this method which was time consuming and hazardous, Hofmann and Hamdi had the idea to oxidize graphite with concentrated sulphuric acid and nitric acid. But this method had high explosion risk. In the last fifty years, the most commonly used method was Hummer's method, in which graphite was oxidized in a water-free mixture of concentrated sulphuric acid, sodium nitrate and potassium permanganate [34]. The reaction was carried out below 45 °C and took less than two hours. Oxidation reaction in Hummer's method was more effective than in Studenmaier's one (27.93 % oxygen content in Hummer`s method, in Studenmaier's method 23.99 %) (Table 1).

Method	Carbon %*	Oxygen %	Water %	Ash%	Carbon to Oxygen atomic ration
Hummer	47.06	27.97	22.99	1.98	2.25
Staudenmaier	52.11	23.99	22.22	1.90	2.89

*% by weight

Table 1. Elementary analysis of graphene oxide from Hummer's and Staudenmaier's methods

The presence of functional groups in graphene oxide, such as hydroxyl, epoxy and carboxyl groups, led to a very stable dispersion of graphene oxide (GO) in water [35, 36]. AFM images revealed monolayer of graphene oxide with uniform thickness around 1 nm [19, 23]. Compared to monolayer of graphene (0.34 nm), it was much thicker due to the presence of oxygenated functional groups above and below the layers [19].

The conformation of graphene oxide were studied in a few of research groups and different structure models have been built: Hoffmann and Holst proposed that hydroxyl and carboxyl groups lay on the edge of graphene oxide sheets, and the epoxyl groups were distributed on the both sides of the surface [37]. In the Ruess model, the graphene oxide sheets were assumed to have a trans-cyclohexane chair structure, not plane, because of the destroyed aromatic hexagon structure [38]. In the Lerf model, oxidized rings and aromatic entities were statistically distributed in graphene oxide sheets where epoxyl and hydroxyl groups were very close to each other [39]. Based on the Lerf model, Gao et al. described graphene oxide with five- and six-membered-ring lactols which were detected by ^{13}C-NMR [40].

5.1.2.3 Graphene nanosheets

Because of the disrupted conjugated π-system, graphene oxide does not have electrical conductivity and strong mechanical stiffness. With reduction methods the π-system can be restored and graphene oxide is converted again to graphene-like layers. There are now two principal methods which are widely used: chemical and thermal reduction.

By thermal reduction (thermal exfoliation), graphite oxide was pyrolyzed under hydrogen, nitrogen or argon atmosphere at about 1000 ºC in order to remove the oxygenated functional groups (Figure 4). A proposed mechanism explained the thermal reduction with formation of carbon dioxide, free radical intermediates and double bonds [41].

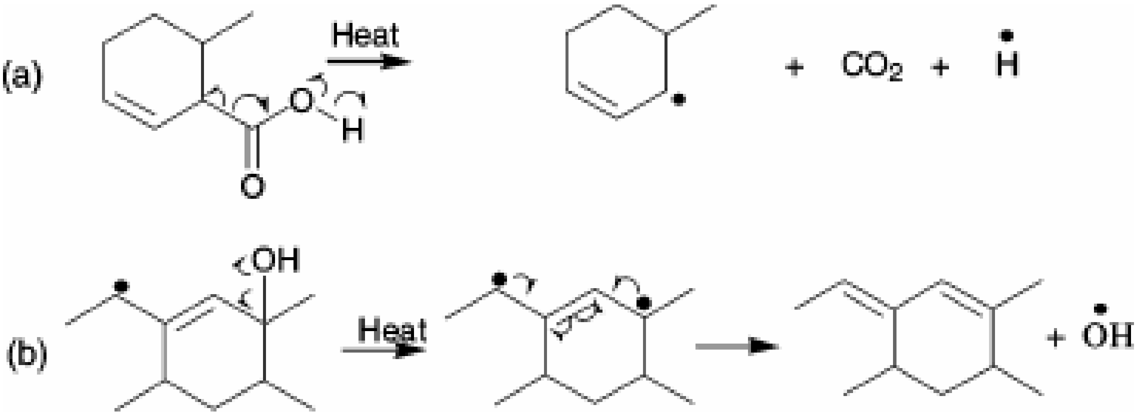

Figure 4. The mechanism of thermal reduction of graphene oxide [41].

The obtained graphene nanosheets surface area is between 500 m^2/g to 900 m^2/g [28]. Such high value is caused by two effects: On the one hand, a large amount of carbon atoms is taken away by the thermal expansion. The loss of carbon forms numerous holes in the sheets, resulting in a porous structure (Figure 5). On the other hand, carbon atoms react with the oxygenated functional groups, generating carbon dioxide and carbon monoxide. The resulting pressure compensates the van der Waals forces which hold the graphene sheets together, splitting graphene sheets into nanosheets [24].

Figure 5. Left: thermally reduced graphene nanosheets [28]

5.2 Preparation of graphene nanosheets

5.2.1 Preparation of graphene oxide foam

In the presently work, graphene sheets were prepared by thermal reduction of graphene oxide, which was prepared with the recipe from Hummers: natural graphite flakes was oxidized by a mixture of concentrated sulphuric acid, sodium nitrate and potassium permanganate. After oxidation, the mixture got brown paste which then was dialyzed with distilled water until PH about 7. Further, the brown dispersion was treated with ultrasound for 8 h in order to loose the contact between the sheets. By atomic force microscopy (AFM), the thickness of the sheets was about 1 nm. It meant they were monolayer of graphene oxide in the dispersion (Figure 6) [42].

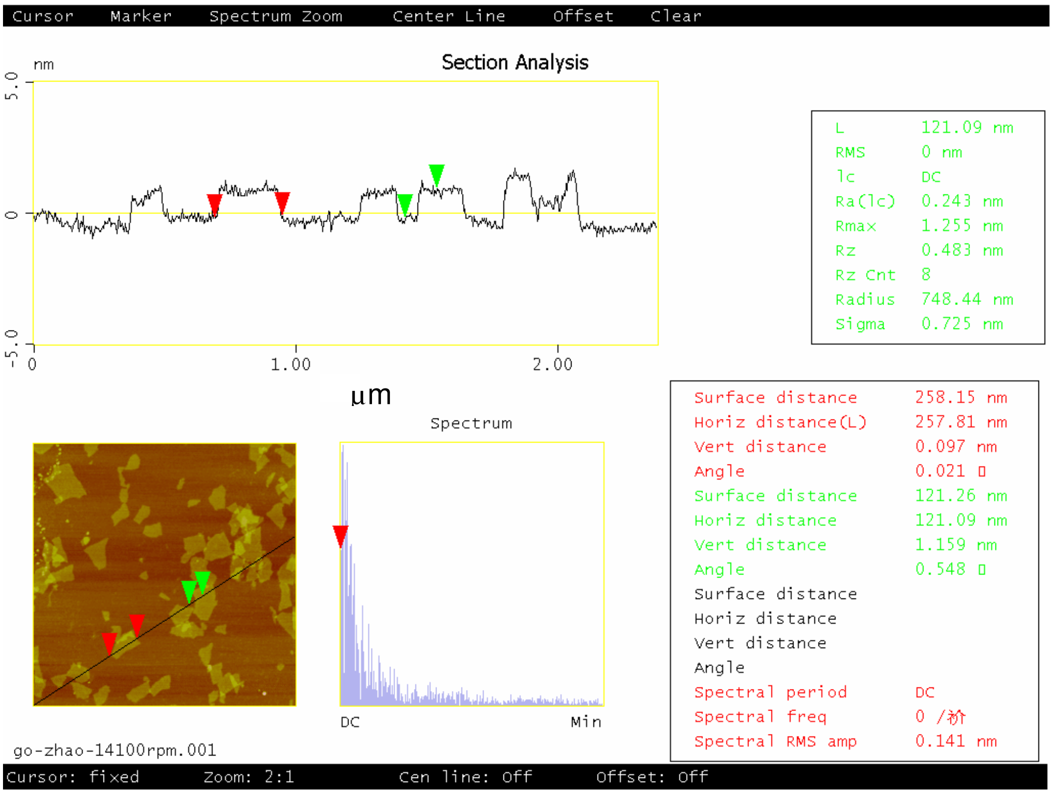

```
L          121.09 nm
RMS        0 nm
lc         DC
Ra(lc)     0.243 nm
Rmax       1.255 nm
Rz         0.483 nm
Rz Cnt     8
Radius     748.44 nm
Sigma      0.725 nm
```

```
Surface distance       258.15 nm
Horiz distance(L)      257.81 nm
Vert distance          0.097 nm
Angle                  0.021 □
Surface distance       121.26 nm
Horiz distance         121.09 nm
Vert distance          1.159 nm
Angle                  0.548 □
Surface distance
Horiz distance
Vert distance
Angle
Spectral period        DC
Spectral freq          0 /祄
Spectral RMS amp       0.141 nm
```

```
Cursor: fixed      Zoom: 2:1        Cen line: Off       Offset: Off
```

Figure 6. AFM image of graphene oxide nanosheets

Before thermal reduction of graphene oxide, water had to be removed from the dispersion. In the first experiment, the dispersion of graphene oxide was dried by a rotary evaporator under vacuum at 50 °C. It was found that the dispersion got slowly dark and aggregates were slowly formed (Figure 7 link). The change of the color was caused by the loss of oxygenated functional groups which were very sensitive to temperature. Such sheets with less functional group had strong tendency to form aggregates.

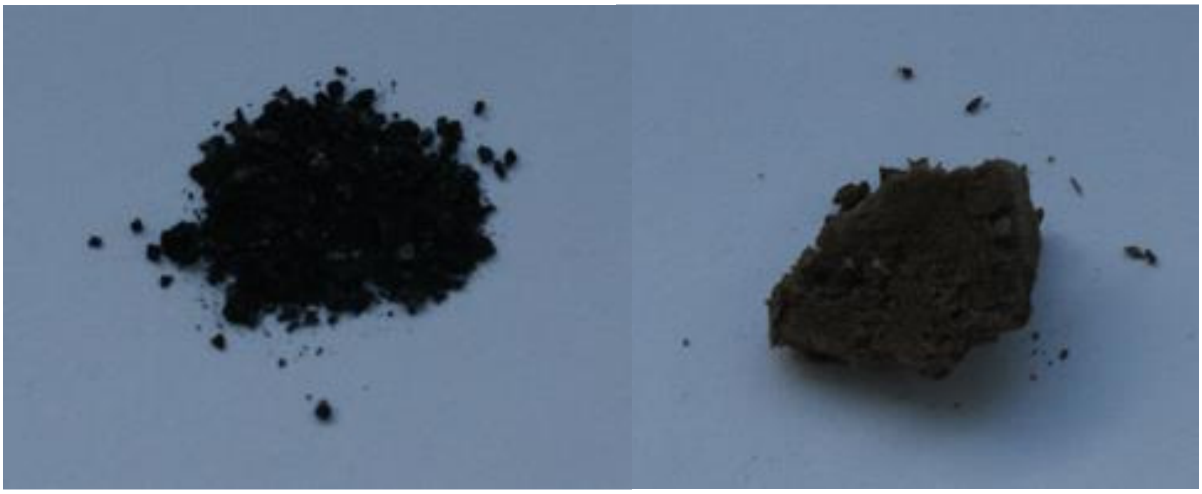

Figure 7. Graphene oxide Dried by rotary evaporator under vacuum at 50 ºC (left); graphene oxide foam prepared by freeze drying (right).

In the next experiment, the dispersion of graphene oxide was freeze-dried which was oft used in biology to produce porous materials. A flask with the dispersion of graphene oxide was at first frozen in liquid nitrogen and then hanged on a lyophilizer at a temperature of -50 ºC. After two days, brown, light and fragile graphene oxide foam without any aggregates was obtained (Figure 7 right). Liquid nitrogen had temperature about -176 ºC. Such low temperature could prevent the loss of oxygenated functional groups. Scanning electron microscopy (SEM) image showed that the foam consisted of loosely stacked sheets with a thickness of about 100 nm (Figure 8). The loose structure was created by sublimation of ice crystals which isolated the graphene oxide sheets. After sublimation of the ice, gaps or pores were left between the sheets.

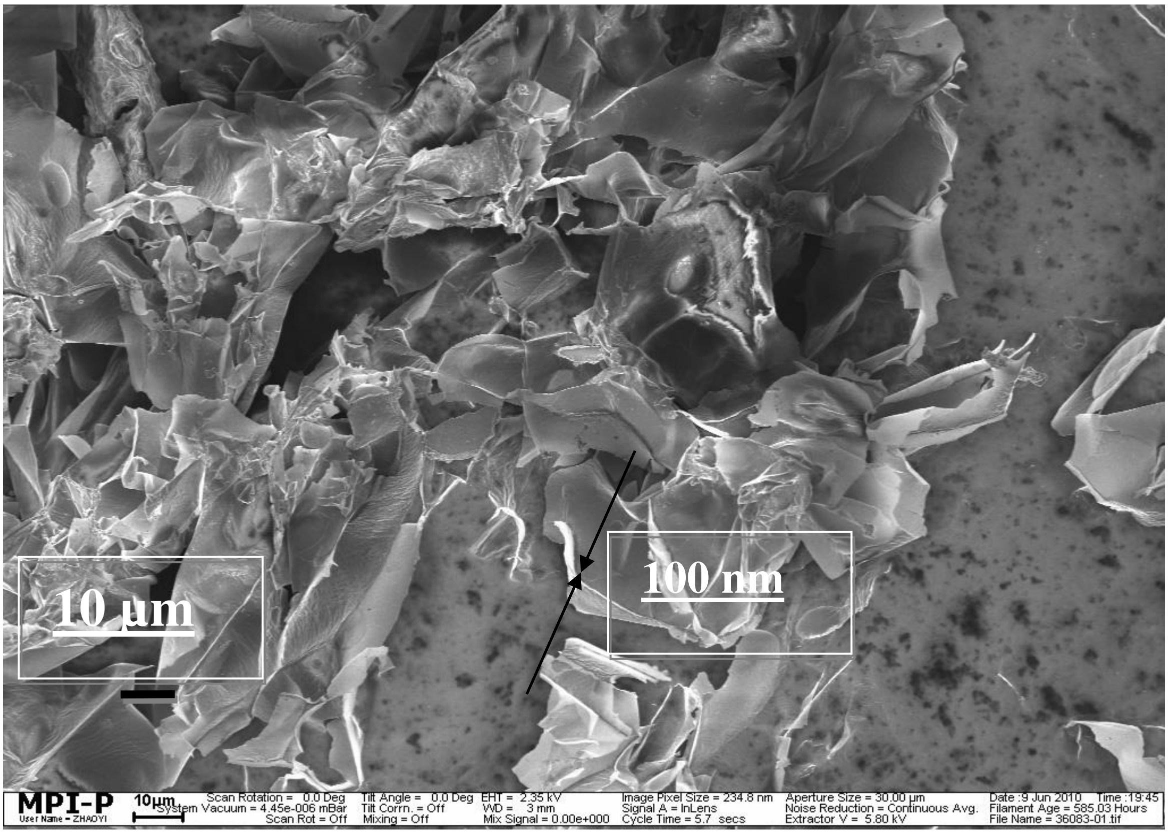

Figure 8. The SEM image of the graphene oxide foam.

5.2.2 Thermal reduction of graphene oxide foam

For thermal reduction, at first one experiment was carried out in which graphene oxide foam was directly put in an open oven with a temperature 1000 ºC. A strong explosion occurred after only a few of seconds. It was probably caused by a quick release of carbon monoxide and dioxide which came from the reaction between carbon atoms and the oxygenated functional groups [24]. Graphene sheets then began to burn, probably due to the presence of oxygen diffusing from outside.

To avoid burning, graphene oxide foam was put in a closed oven in the next experiment. Before raising the temperature, the oven was blown with dried nitrogen for 1 hour to remove O_2. Then the oven was heated from room temperature to 1000 ºC with a heating rate of 30ºC/min. Graphene sheets like black feather were obtained. The thickness of the sheets decreased to a few of nanometer by SEM (Figure 9). The exact value was measured by the high-resolution TEM. It was found that the sheets had an average thickness of about 4 nm with 5 layers (Figure 10). A surface area 710 m^2/g was measured by nitrogen adsorption.

The theoretical surface area of monolayers of graphene sheets was calculated as 2.620 m^2/g in a hypothetical case where the layers did not overlap with each other [12]. In a real case, there are significant amount of close room in graphene nanosheets which are not available for nitrogen. Hence the measured value of surface area was always lower than theoretical one. It was reported that graphene nanosheets with a surface area about 500 m^2/g were supposed with about seven single layers [28]. In this work, the sheets with 700 m^2/g probably have about five layers. This supposition agreed with the investigation of TEM (Figure 10) where graphene nanosheets contained 5 single layers. The surface area of graphene nanosheets in this work was comparable with the best ones reported in the literature (700 m^2/g to 900 m^2/g) [24, 26, 28, 43].

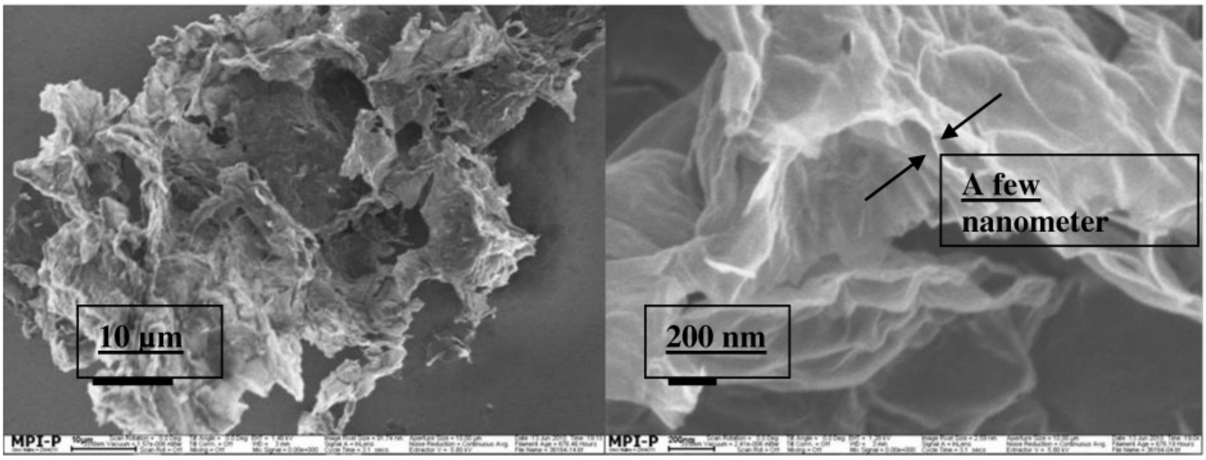

Figure 9. Left: a low magnification of SEM images of graphene nanosheets; Right: a high magnification of SEM images of the same sample.

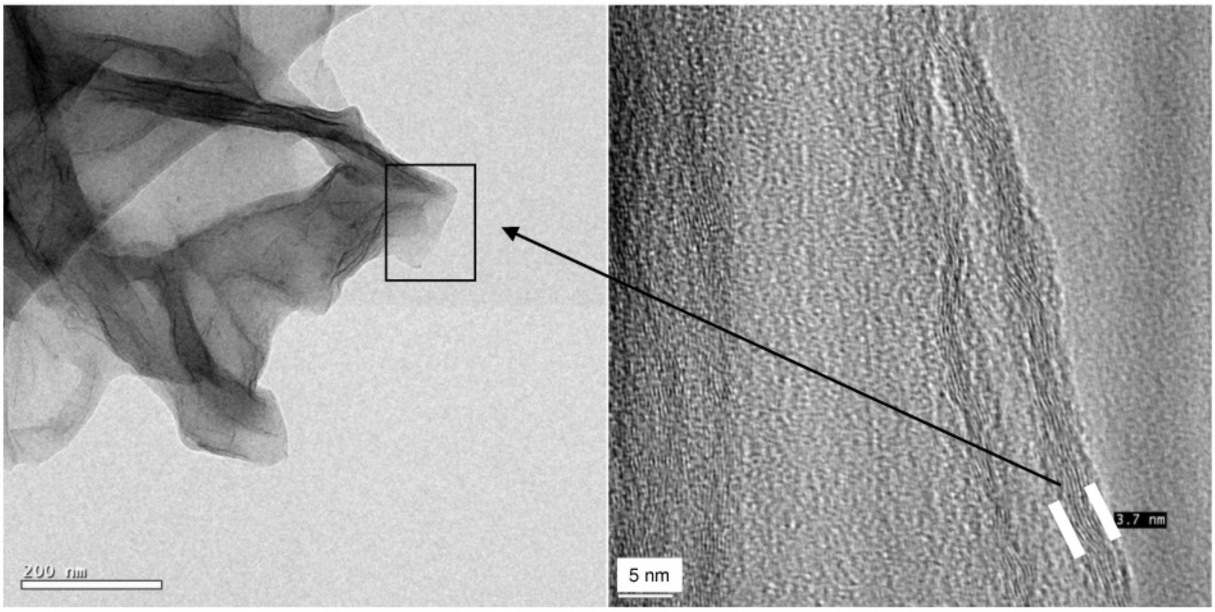

Figure 10. A TEM image of graphene nanosheets exfoliated at 1000 °C with a heating rate 30 °C /min.

The reduction degree of oxygenated functional groups was determined by elemental analysis. An atomic ratio of C to O in the graphene nanosheets with 10.3 was obtained. Compared to the initial graphene oxide foam (0.79), most of oxygenated functional groups were removed after the thermal reduction. The measurement of thermogravimetric analysis with a heating rate 10 °C/min (TGA) showed at which temperature the functional groups were removed (Figure 11). At 100 °C 20 % of the initial mass was lost, mainly due to the vaporization of adsorbed water, but not the functional groups [19, 23]. At about 200 °C, a mass loss of 80 % observed. The light debris of sheets flew away from the pan of TGA, probably caused by a explosion. It was maybe caused by quick release of carbon dioxide and carbon monoxide. In the next measurement, a low heating rate of 1 °C/min was chosen to prevent the explosion. At this time, a mass lost began at about 200 °C (Figure 11). A decrease from 35% to 55% was observed between 250 °C and 900 °C. These results suggested that the thermal reduction must be carried out at about 900 °C to completely remove the functional groups.

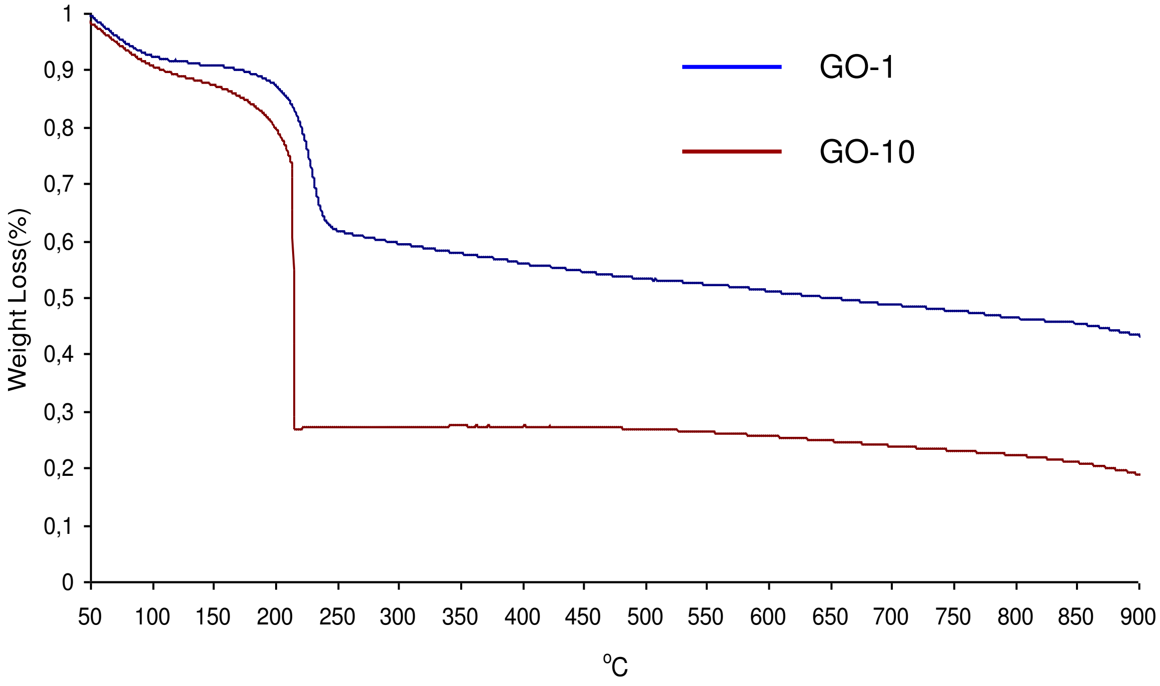

Figure 11. TGA diagram for graphene oxide foam measured with different heating rate.

5.2.3 Influence of heating rates on the exfoliation degree

The TGA measurement above showed that different heating rates influenced on the thermal reduction process: with a high heating rate (10 °C/min), an explosion happened, but with a low heating rate (1 °C/min), not. To deeply study the influence of heating rate on the thermal reduction process, graphene oxide foam was pyrolyzed with heating rates ranging from 1 to 30 °C/min.

It was found that the graphene sheets from heating rate 1 °C/min and 5 °C/min only got silver gray and the foam structure was not destroyed, meaning that no explosion has happened. The samples from heating rate 10 °C/min, 20 °C/min and 30°C/min got black and the foam structure was completely destroyed into small debris.

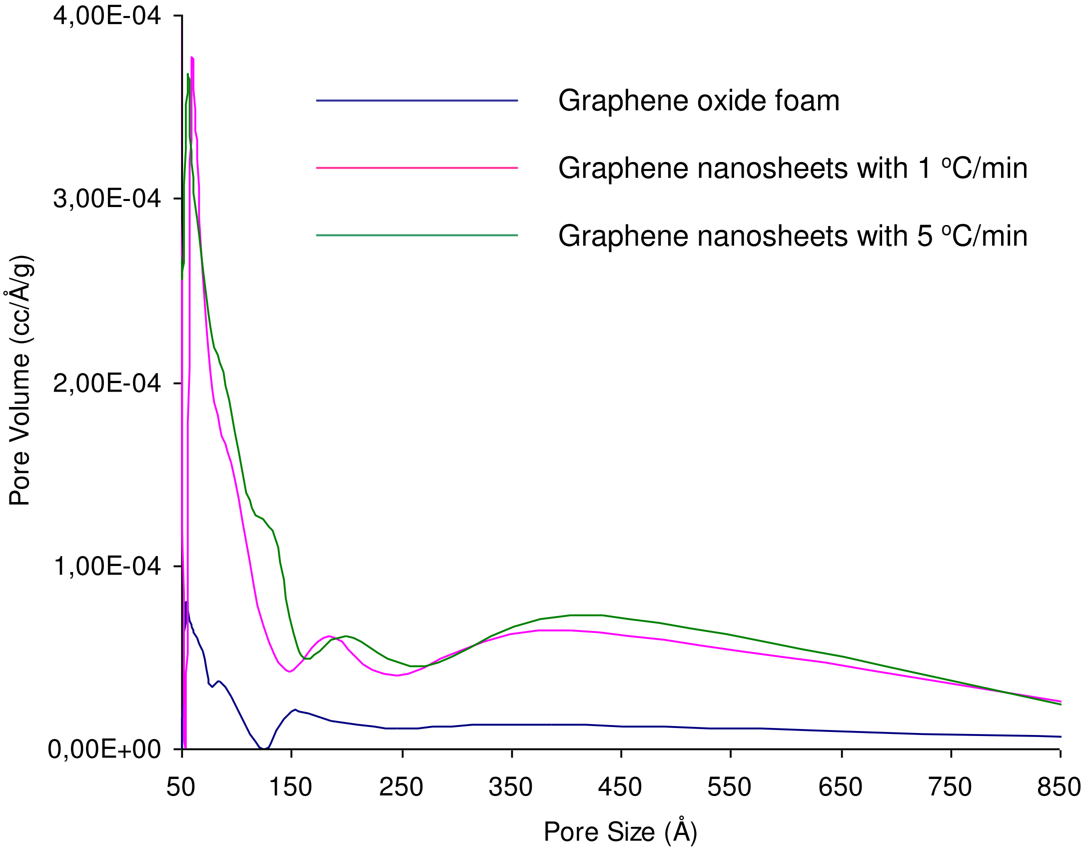

Figure 12. Distribution of pore size of graphene oxide foam and graphene sheets with 1 °C/min and 5 °C/min.

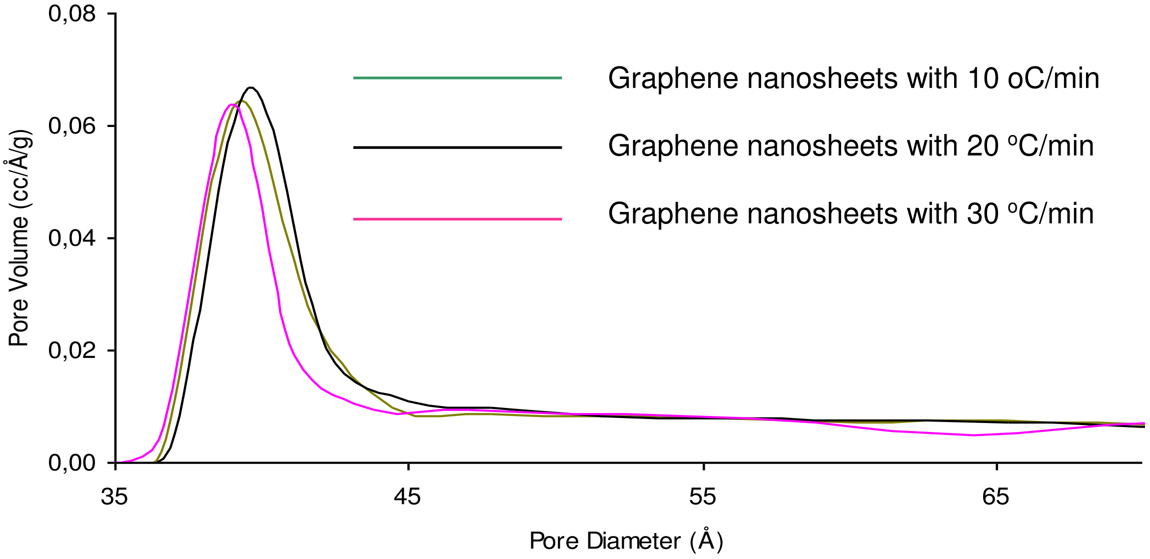

Figure 13. Distribution of pore size of graphene nanosheets with 10 °C/min, 20 °C/min and 30 °C/min

The surface area of the obtained graphene sheets were measured by nitrogen adsorption determination. The samples from heating rate of 1 °C/min and 5 °C/min had a surface area only about 60 m^2/g (Figure 12), but for samples with a heating rate 10, 20 and 30 °C/min about 700 m^2/g (Figure 13). These results suggested that a higher heating rate caused a quicker release of carbon dioxide and carbon monoxide which could form higher pressure in the foam, splitting the graphene into nanosheets. It was also found that the surface area was not strongly changed, when the heating rate was above 10 °C/min (Figure 14).

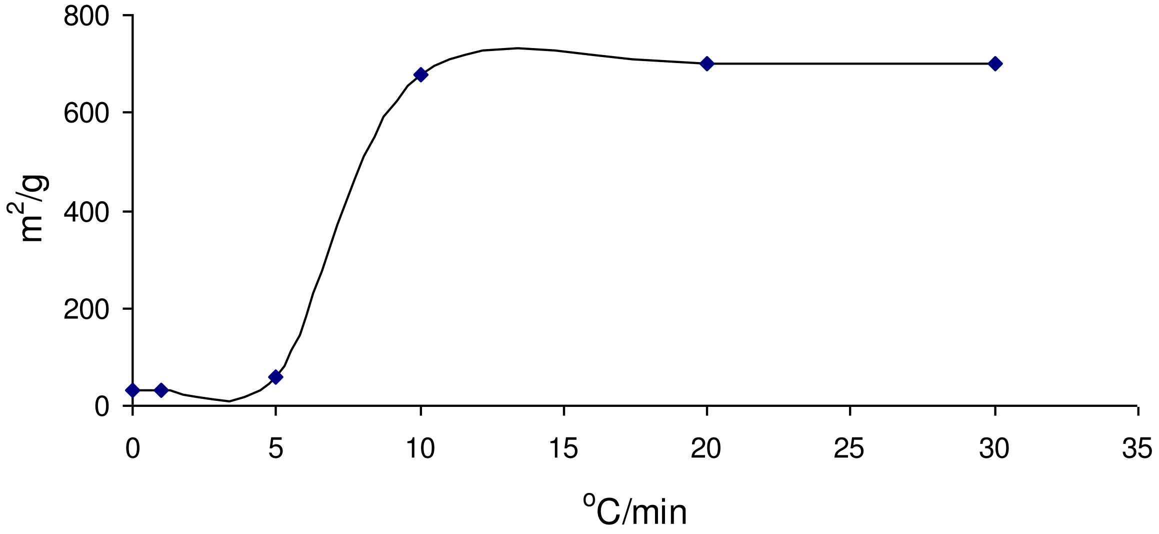

Figure 14. The effect of heat rates on the surface area of graphene nanosheets

5.2.4 Influence of temperature on the exfoliation degree

Besides heating rate, temperature could be also an important factor to influence the thermal reduction process of graphene oxide foam. Here, graphene oxide foam was pyrolyzed with a heating rate of 30 °C/min to temperature of 250, 550, 750 and 1000 ºC.

It was found that at 250 ºC graphene oxide foam was not destroyed into small debris. Only the color was changed from brown to dark silver grey. The sheets in SEM image looked like smooth foils with a thickness about 100 nm (Figure 15-A). At 550 ºC and above, graphene oxide foam was completely destroyed into black small debris. Nanosheets looked like thin wrinkled paper in SEM images (Figure 15-B). The thickness was only a few of nanometer.

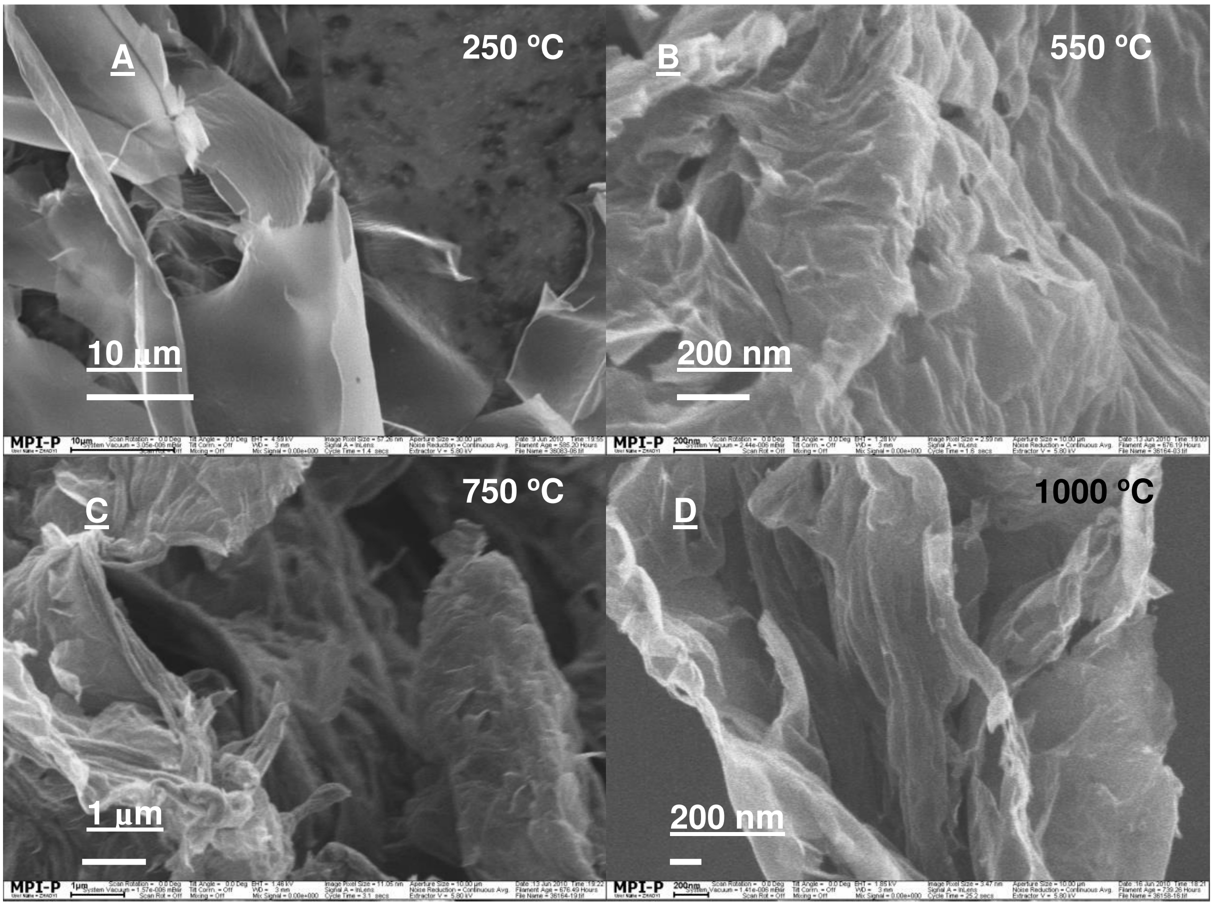

Figure 15. SEM images of graphene nanosheets reduced at 250, 550, 750 and 1000 ºC .

The surface area of the obtained sheets was investigated with nitrogen adsorption determination. The graphene sheets from 250 ºC had only a surface area of 33 m^2/g (Figure 16). This result agreed to TGA measurement (5.2.2 Figure 11): the thermal reduction process just began at 200 ºC where only small amount of oxygenated function groups were converted to CO_2 and CO. Hence the graphene sheet from 250 ºC had low surface area. From 550, 750 or 1000 °C, the graphene sheets had a surface area 660 m^2/g, 660 m^2/g and 680 m^2/g, respectively (Figure 17).

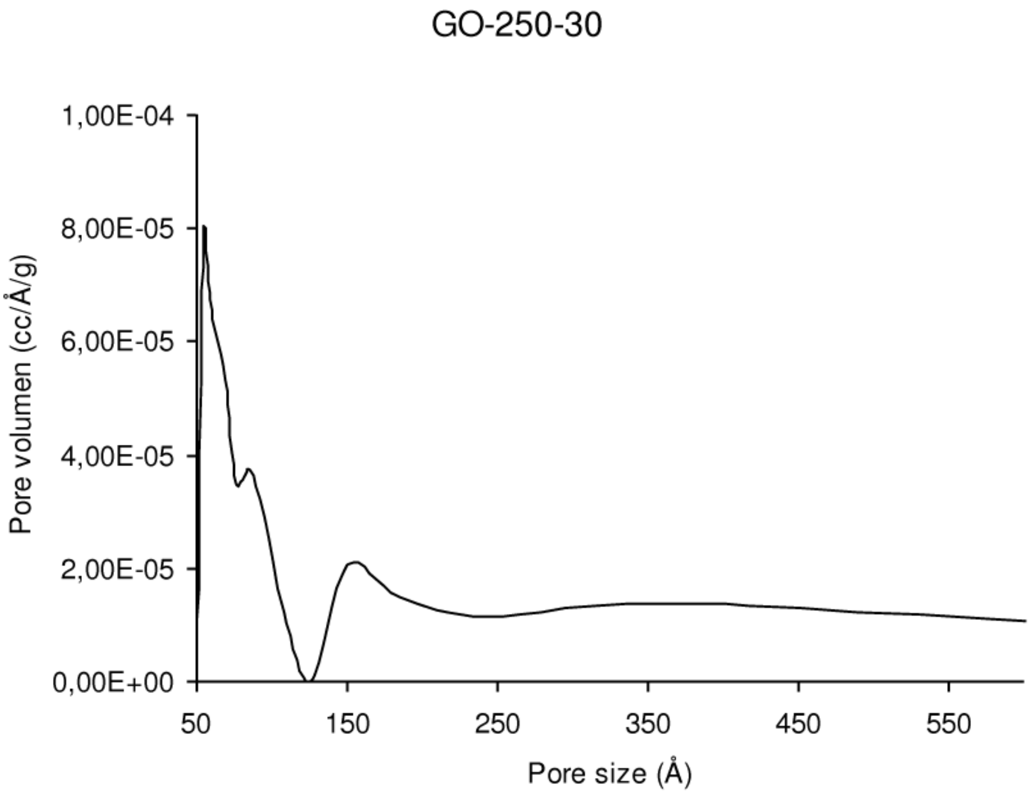

Figure 16. The distribution of pore size of graphene nanosheets from 250 °C

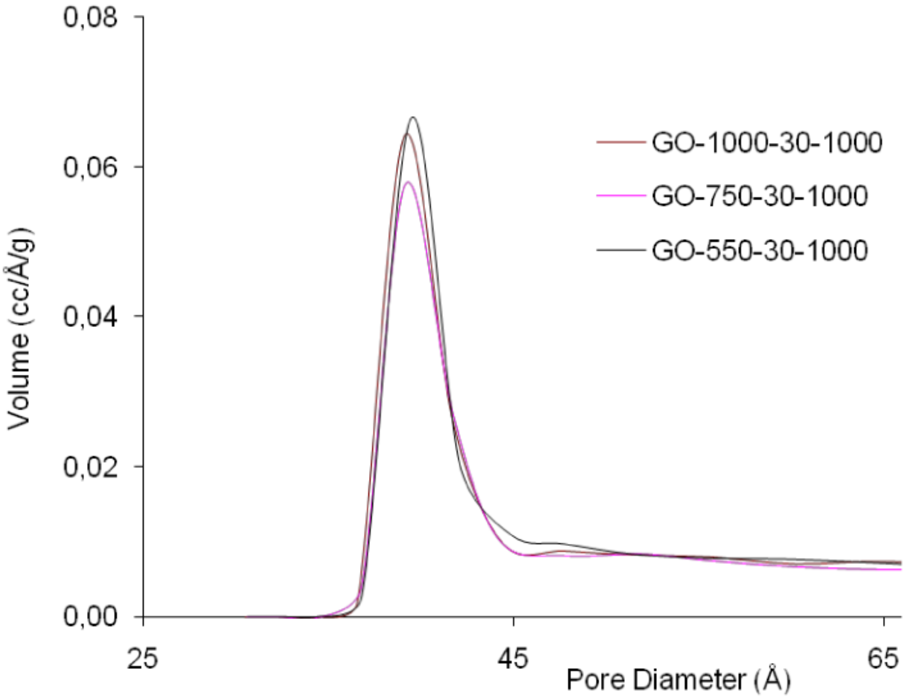

Figure 17. The distribution of Pore size of graphene sheets exfoliated from 550 °C, 750 °C and 1000 °C.

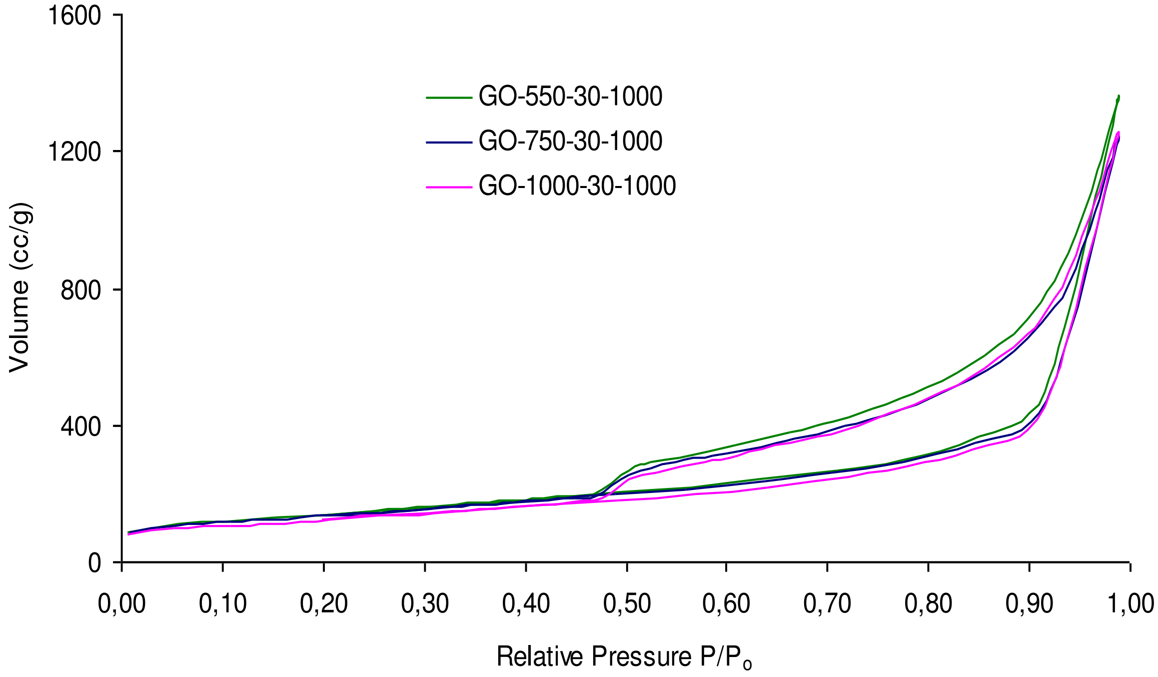

Figure 18. N_2-adsorption-desorption isotherms of graphene nanosheets from 550 ºC, 750ºC and 1000 ºC

The oxygenic function groups remaining after thermal reduction were investigated with elemental analysis. As shown in Table 2, the content of oxygen decreased with increasing temperature. Only 11.32% oxygen was in graphene nanosheets from 1000 ºC, which was almost 5 times lower than in graphene oxide foam (54.88%) and three times lower than the one from 250 ºC (29.38%).

Nr	C%	H%	O%	C/O
GO	43.68	1.44	54.88	0.79
GO-30-250	68.04	2.03	29.38	2.3
GO-30-550	77.11	2.86	18	7.3
GO-30-750	80.73	2.89	14.09	8.7
GO-30-1000	82.45	2.76	11.32	10.3

Table 2. The elemental analysis of graphene oxide foam and graphene nanosheets from different temperature.

5.2.5 Summary

In this part, graphene nanosheets were prepared by thermal reduction of graphene oxide foam which was prepared with freeze-drying method (Figure 19). No aggregates were formed in the foam, different to the traditional drying method: rotary evaporator. At 1000 ºC and with heating rate 30 ºC/min graphene nanosheets were obtained with a surface area about 700 m^2/g. These sheets were about 3 nm thick with 5 monolayers. In this study, the influence of heating rates and temperature on the thermal reduction process of graphene oxide foam were systematic and detailed investigated. The table 3 showed that when the heating rate was higher as 10 ºC/min and the temperature higher as 550 ºC, graphene nanosheets with a surface area about 700 m^2/g (the thickness was about 4 nm) could be obtained. These results were comparable with the best ones reported in the literature [24, 26, 28, 43].

Figure 19. Left: graphene sheets from graphene oxide dried by rotary evaporator; Right: graphene sheets from graphene oxide foam by freeze drying.

	250 ºC	550 ºC	750 ºC	1000 ºC
1 ºC/min				60 m^2/g
5 ºC/min				60 m^2/g
10 ºC/min				700 m^2/g
20 ºC/min				700 m^2/g
30 ºC/min	33 m^2/g	660 m^2/g	680 m^2/g	730 m^2/g

Table 3. The list of the experiments for the study of thermal reduction.

5.3 Dispersions of graphene nanosheets

In the following work, the obtained graphene sheets will be used as filling material for polymer composites. At first, dispersions of graphene nanosheets in organic solvents were prepared by using different surfactants and block polymers.

It was reported that sodium dodecylbenzene sulfonate (SDBS), sodium dodecyl sulfate (SDS), Lutensol and AT50 (PE-b-PEO unites 50:20) were used to prepare dispersions of graphene nanosheets [44]. These surfactants have the same block: alkyl chains. PI-b-PMMA is an emulsifier for a non-aqueous emulsion (DMF in n-hexane). Polyisoprene chains with conjugated double bonds are more hydrophobic than alkyl chains and could have strong interaction with graphene sheets. The above mentioned surfactants and emulsifier will be tested to disperse graphene nanosheets. Hexane and THF are solvents with low boiling point and toxicity. PI-b-PMMA builds in hexane micelles in which PI stretched outside and PMMA inside. THF with is a good solvent for PI-b-PMMA, in which chains high flexibility. In the following work, graphene nanosheets will be dispersed in both solvents.

5.3.1 Testing different surfactants and PI-b-PMMA

The dispersions were prepared with 1 mg/ml graphene nanosheets and 5 mg/ml one of the surfactants and PI-b-PMMA (Figure 20). The mixture was treated with ultrasound for eight hours to insure that the compounds and graphene sheets have enough contact with each other. The obtained dispersions showed very different stability (Figure 21). In the dispersions with SDBS, SDS, Lutensol and AT50, almost all of the graphene nanosheets were precipitated after one day. The low stability of these dispersion suggested that alkyl chains did not have strong interaction with graphene sheets.

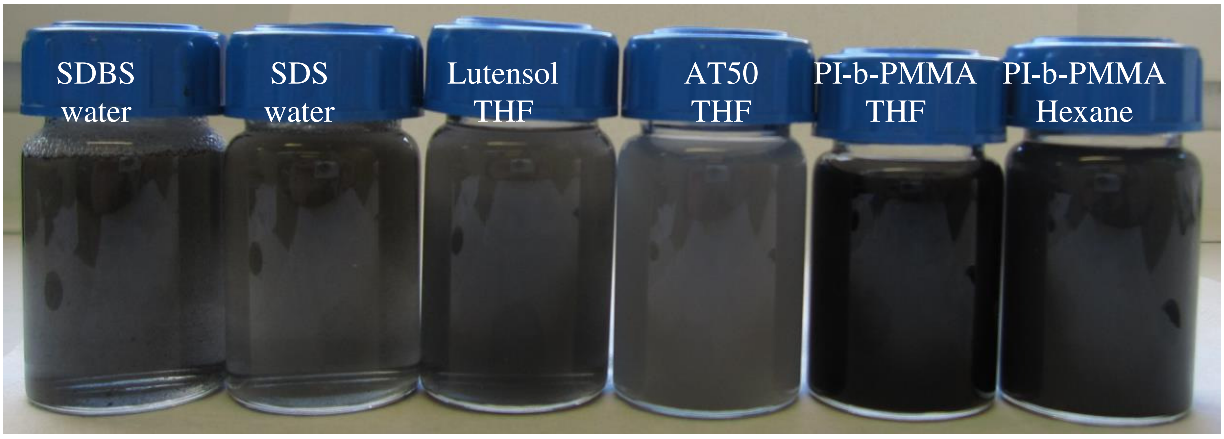

Figure 20. The dispersions of graphene nanosheets with different surfactants and solvents.

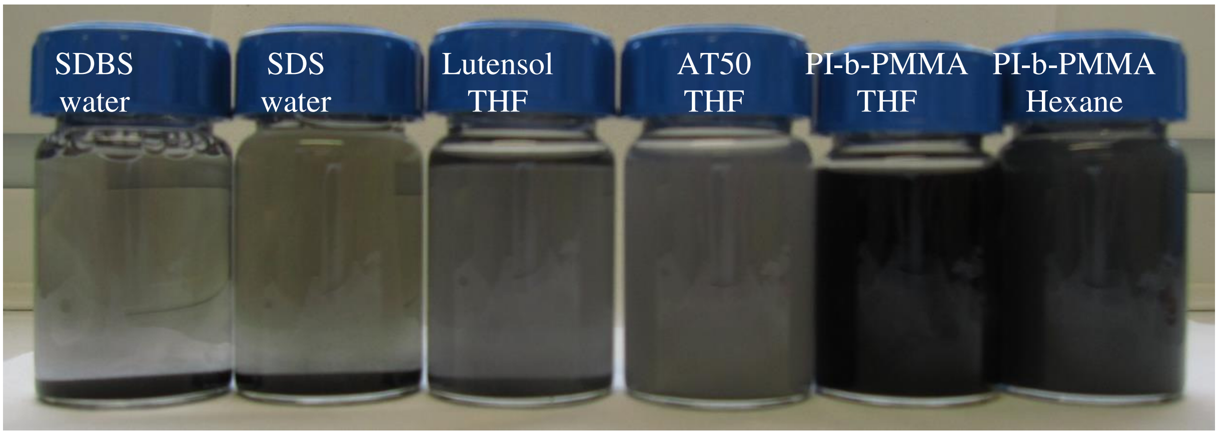

Figure 21. The dispersions one month after the treatment of ultrasound.

The dispersions PI-b-PMMA showed better stability: In hexane only small amount of sediment appeared after one month (Figure 21). In the dispersion with THF, hardly graphene sheets were observed on the bottom. The less stability of the dispersion in hexane could be explained by the formation of micelles of PI-b-PMMA. Polyisoprene stretched outside in n-hexane and PMMA crouched inside of the micelles [45, 46]. Such structure limited the mobility of the polymer chains to diffuse into the interspaces of the graphene sheets. In contrast, THF was a good solvent for polyisoprene and PMMA chains which had high flexibility in the medium. They could easily diffuse into the interspaces of the sheets and be adsorbed on them.

The sediment from sample with SDBS, SDS, Lutensol and AT50, and the dispersed graphene sheets in THF with PI-b-PMMA was investigated by SEM (Figure 22). As shown in the images, the sediment was small aggregates in which graphene sheets had still contact with each other, no individual sheets. But the dispersed sheets in THF looked like wrinkled papers, meaning that PI-b-PMMA was absorbed on the sheets and isolated them from each other.

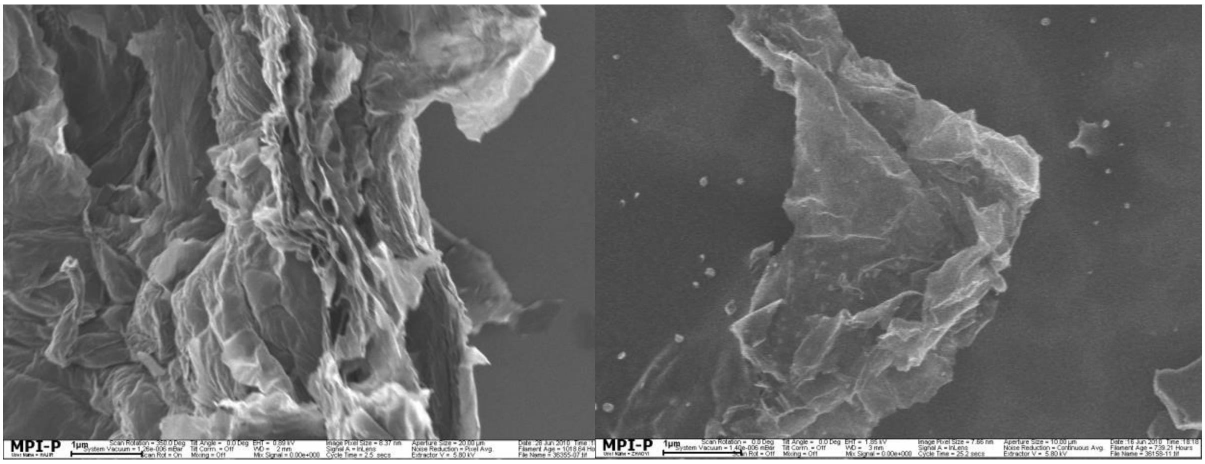

Figure 22. SEM images of sediment from sample with SDBS, SDS, Lutensol and AT50 (left), dispersed graphene sheets in THF with PI-b-PMMA (right).

For the question: which one actually stabilizes graphene nanosheets: the solvent THF or PI-b-PMMA, an experiment was carried out: graphene sheets were only dispersed in THF solvent without PI-b-PMMA. All of sheets fell on the bottom after the treatment of ultrasound. It meant that THF could not stabilize the sheets, but PI-b-PMMA (Figure 23).

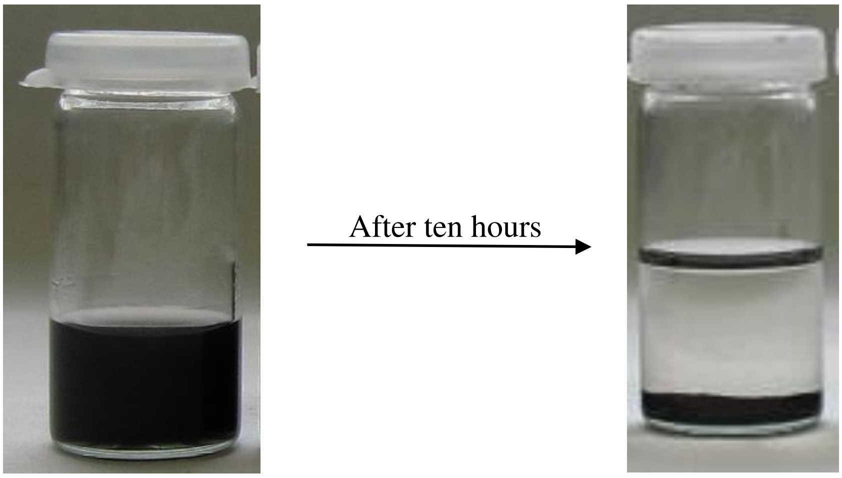

Figure 23. Dispersion of graphene nanosheets in THF without PI-b-PMMA.

For another question: which chains were absorbed on the graphene nanosheets as anchor and which ones worked as steric stabilizer, an experiment was carried out: PMMA (molecular weight 20000 g/mol) was used to disperse graphene nanosheets in THF. After the treatment of ultrasound, graphene nanosheets completely precipitated from the dispersions (Figure 24). These results suggested that PMMA chains did not have interaction with graphene nanosheets. Polyisoprene ones had strong interaction with grapgene sheets, which anchored on the sheets (Figure 25).

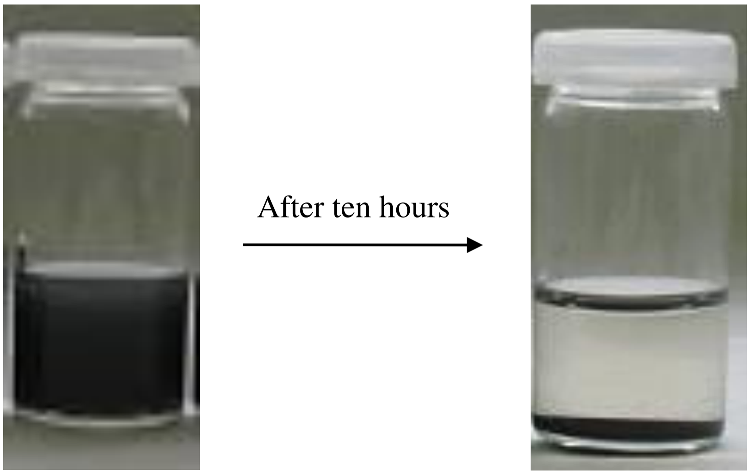

Figure 24. The dispersion of graphene nanosheets with PMMA in THF.

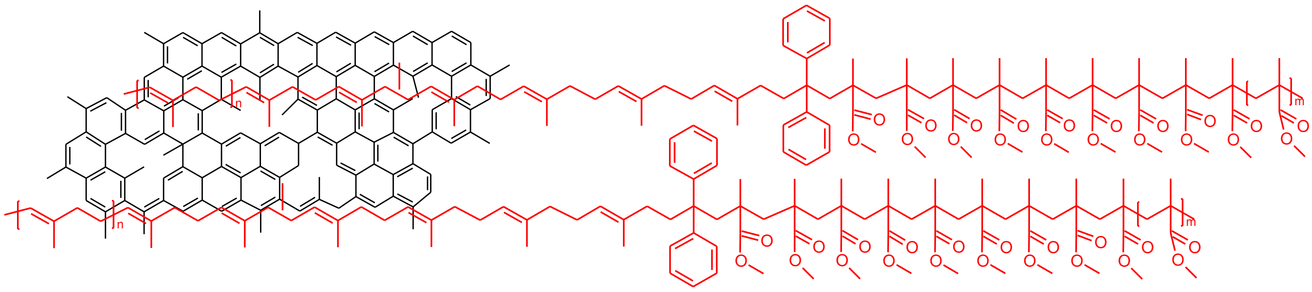

Figure 25. Scheme of interaction between graphene sheets and PI-b-PMMA.

5.3.2 Stability of the dispersions with PI-b-PMMA

To investigate the stability of the dispersions of graphene nanosheets in THF with PI-b-PMMA, the dispersions will be centrifuged and the concentration will be measured by UV-spectroscopy. With the Beer–Lambert law, the total intensity of the dispersion can be descript as eq (1)

$$A(\lambda) = c_1\varepsilon_1(\lambda) + c_2\varepsilon_2(\lambda). \qquad (1)$$

Here ε_1 and ε_2 are the absorption coefficients of both components (graphene sheets and PI-b-PMMA). When the concentration c_1 of one component remains constant, then the total intensity $A(\lambda)$ only depends on the varying concentration of the other component:

$$A(\lambda) = A_1 + c_2\varepsilon_2(\lambda) \qquad (2)$$

The concentration c_2 of the second substance can be obtained once its absorption coefficient ε_2 is known. In this study, the concentration of PI-b-PMMA will keep constant. To obtain the concentration of graphene nanosheets, the absorption coefficient of graphene nanosheets have to be determined at first. The dispersion with a known concentration 0.2 mg/ml of graphene nanosheets and 5 mg/ml PI-b-PMMA was at first measured to determine the absorption coefficient.

For the UV-spectroscopy measurement, a baseline was at first measured by using a solution with 5 mg/ml PI-b-PMMA in THF as blank sample (all of dispersions had this concentration). In the next step, the dispersions with concentration of graphene nanosheets 1 mg/ml and PI-b-PMMA 5 mg/ml were separately centrifuged for 30 min with different speeds (1000, 2000, 3000, 4000 and 5000 rpm) and then measured by UV-spectroscopy. They gave absorbance 1.702, 0.858, 0.398, 0.170, 0.092 at 550 nm which responded the concentrations of graphene 0.105, 0.053, 0.025, 0.0105, 0.006 mg/ml, respectively (Figure 26 and 27). This concentration (0.105 mg/ml) was higher than the one in N,N-dimethylacetamide (DMA), *γ*-butyrolactone (GBL) and 1,3-dimethyl-2 imidazolidinone (DMEU), N-methylpyrrolidone (NMP) [44].

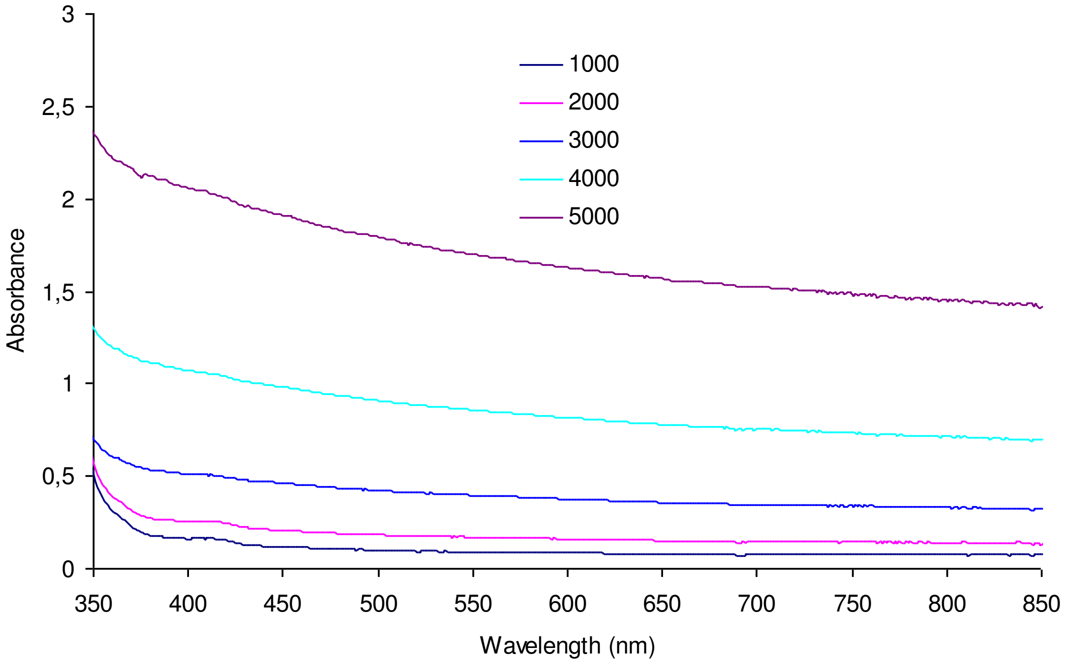

Figure 26. UV measurement of the dispersions of graphene nanosheets after different centrifugation.

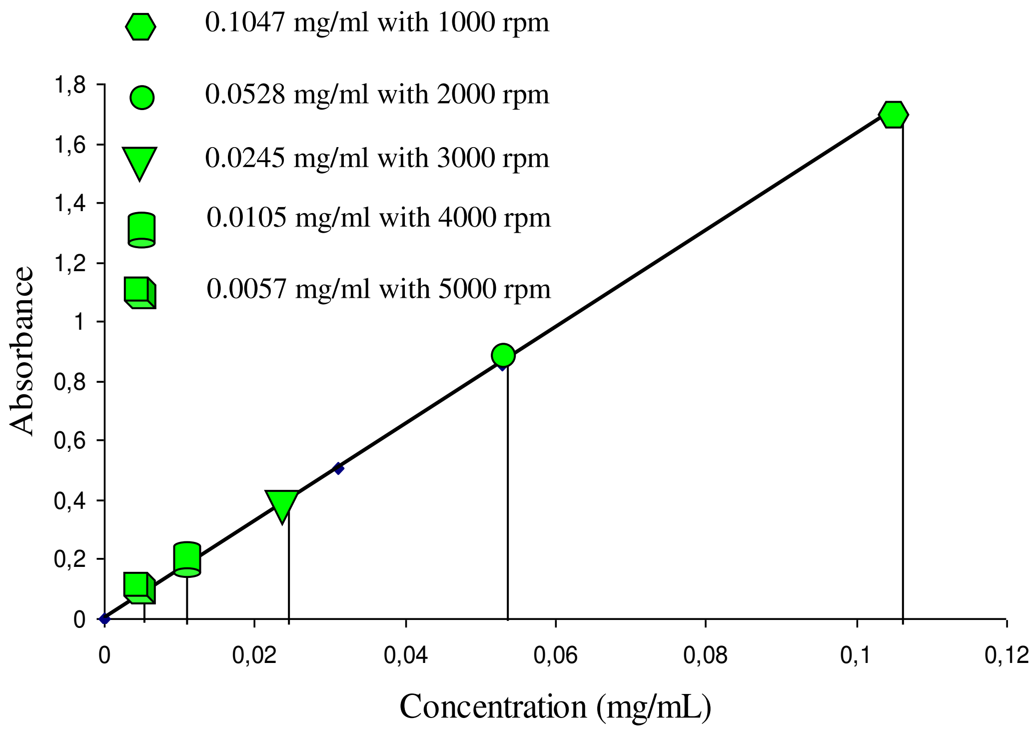

Figure 27. The concentration of the dispersions of graphene nanosheets after centrifugation.

5.3.3 Study of the dispersion mechanism with PI-b-PMMA

To deeply understand the mechanism of the dispersion process with PI-b-PMMA, an experiment was carried out: Expanded graphite sheets (with a surface area 30 m^2/g) were dispersed in THF with PI-b-PMMA. One day after treatment of ultrasound, almost all of sheets were precipitated on the bottom. This result could be explained by the stacking structure of graphene sheets. As shown in the Diagram of X-ray, expanded graphite had a sharp pick, meaning that the sheets were arranged with relatively perfect stacking structure (figure 28). In contrast, the graphene nanosheets from thermal reduction of graphene oxide foam had broad curves, meaning that the sheets were amorphous with a strong disorder. This random stacking benefited the diffusion of polymer chains into the interspaces of the sheets (Figure 29).

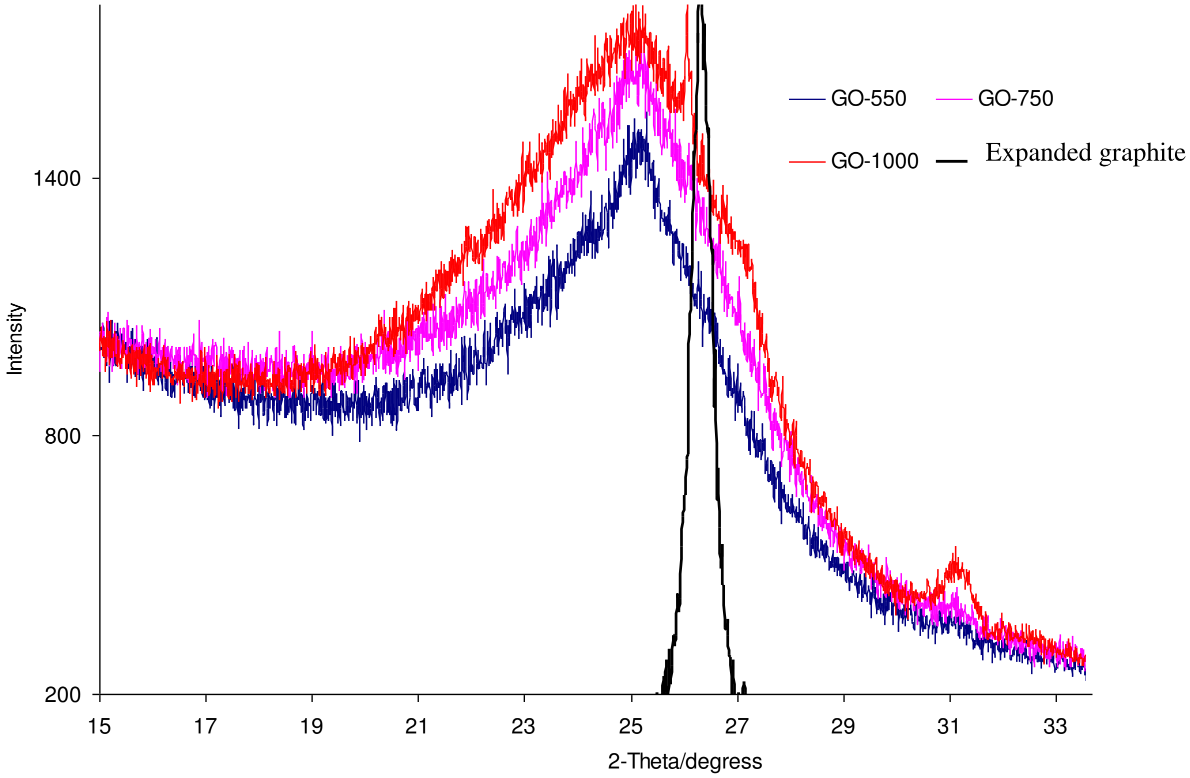

Figure 28. X-ray diagram of expanded graphite and graphene nanosheets from this study.

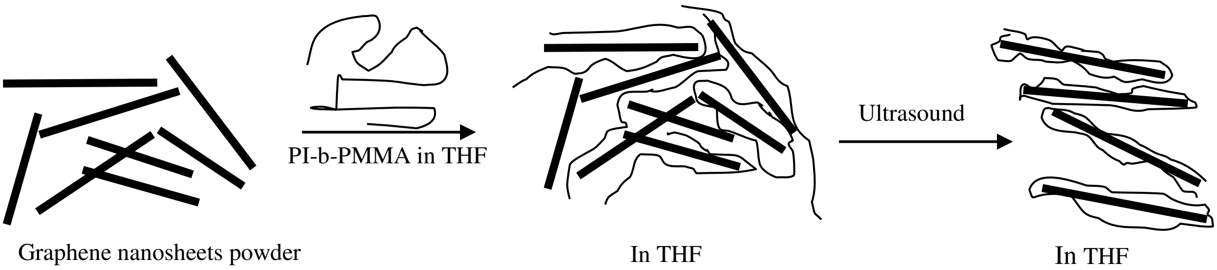

Figure 29. Schematic dispersion process of graphene nanosheets stabilized by PI-b-PMMA in THF.

5.4 Polymer composites with graphene nanosheets

5.4.1 Preparation of polymer composites

The stable dispersion of graphene nanosheets in THF was used to prepared polymer composites here. The ratio of graphene nanosheets to PI-b-PMMA was kept at 1:1. Two commercial polymers were chosen as polymer matrices: polystyrene (PS) and poly(methyl methacrylate) (PMMA).

At first, graphene nanosheets were dispersed in THF with PI-b-PMMA by treatment of ultrasound for 8 h. The polymer matrix was added into the dispersion and then treated by ultrasound for 30 min and stirring for 8 hours. The mixture was precipitated in methanol. The obtained precipitate was dried by vacuum at room temperature overnight to remove remaining THF. To conveniently investigate the properties of the composites, the powder was pressed at about 180 ºC to a film with thickness between 200 µm to 250 µm (Figure 30).

Figure 30. Left: the powder of graphene polystyrene composite. Right: the film of graphene polystyrene composite

The compatibility between sheets and polymer matrices were investigated by SEM. The lateral sides of PS and PMMA film with 6 wt% graphene nanosheets were shown in Figure 31. It was found that the graphene nanosheets were homogenously dispersed in both polymer matrices without any aggregates. The thickness of nanosheets is similar to the one in the dispersion (a few nanometers), indicating that the nanosheets were not aggregated together during the preparation of the composites. Moreover, graphene nanosheets did not show any preferential orientation in the matrices. The disordered distribution could benefit to form a conducting network with a low concentration in the matrices.

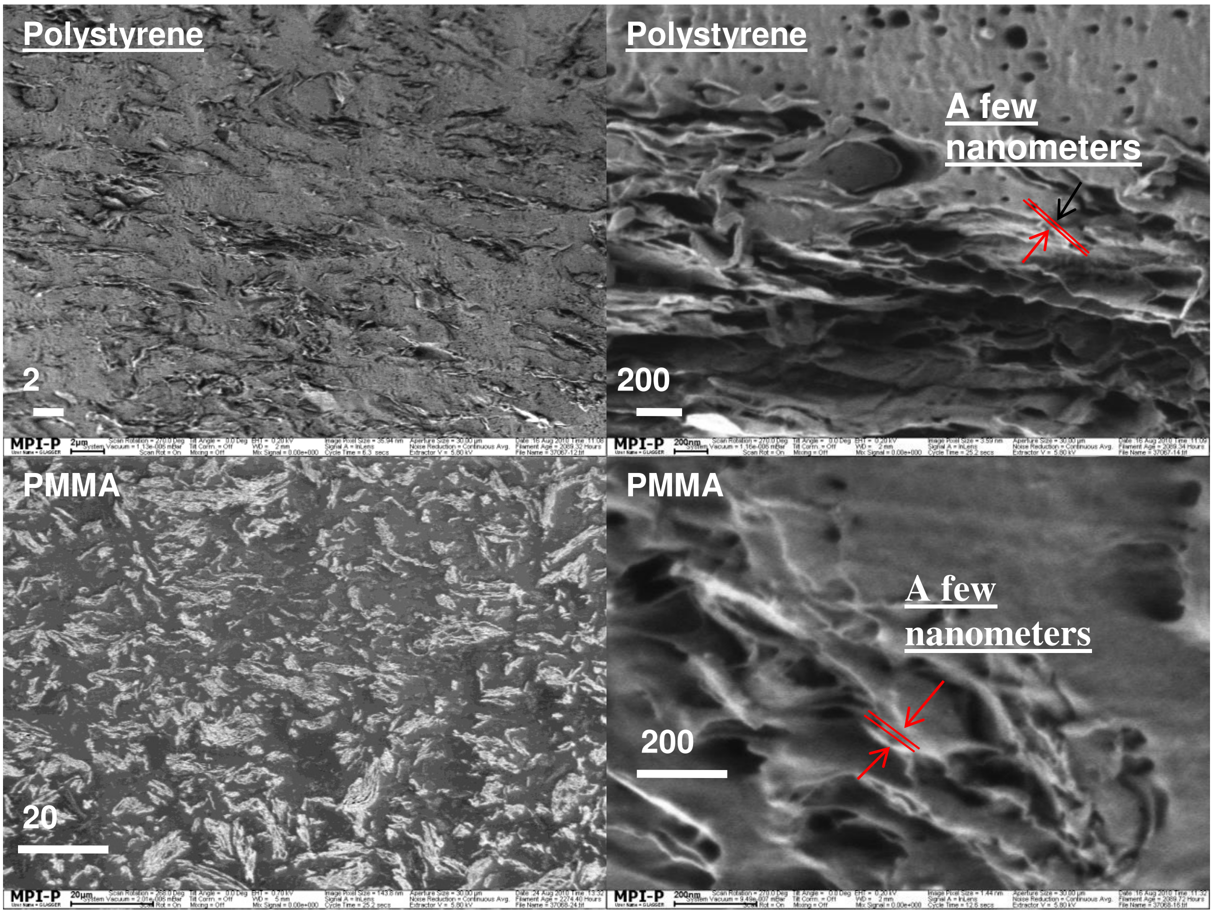

Figure 31. SEM images of nanocomposites with 6 wt% graphene nanosheets.

5.4.2 Electrical properties of polymer composites

The concentration of graphene sheets, at which composites are converted from an insulator to a conductor, is the percolation threshold P_c. According to percolation theory, a continuous conducting network is formed in the matrices and the direct current conductivity increased instantly by a factor of 10 or more at this concentration [47]. In the present work, the percolation threshold of both composites will be determined. In addition, the influence of frequency of the current and temperature on the electrical properties of the both composites will be also investigated.

5.4.2.1 The percolation threshold

The dependence of the direct current conductivity σ_{DC} on the concentration of graphene sheets can be described by a power law (percolation theory). When the concentration (P) is higher than the percolation threshold (P_c):

$$\boldsymbol{\sigma_{DC} \approx (P - P_c)^t} \tag{1}$$

where the value t is the critical exponent.

When the concentration (P) is lower than the percolation threshold (P_c):

$$\sigma_{DC} \approx (P_c - P)^{-s} \qquad (2)$$

where the value s is another critical exponent. The critical exponents depend primarily on the dimensionality of the percolating systems (network formed by connecting filling materials is 2D or 3D.), and not on the details of the geometric structures of filler material [48]

To determine percolation threshold P_c, the direct current conductivity σ_{DC} of the composites were measured by a two-contact method with a Dielectric Analyzer. The films were fixed between two copper plates with a diameter of 10 mm which were then placed in the central part of the measurement cell.

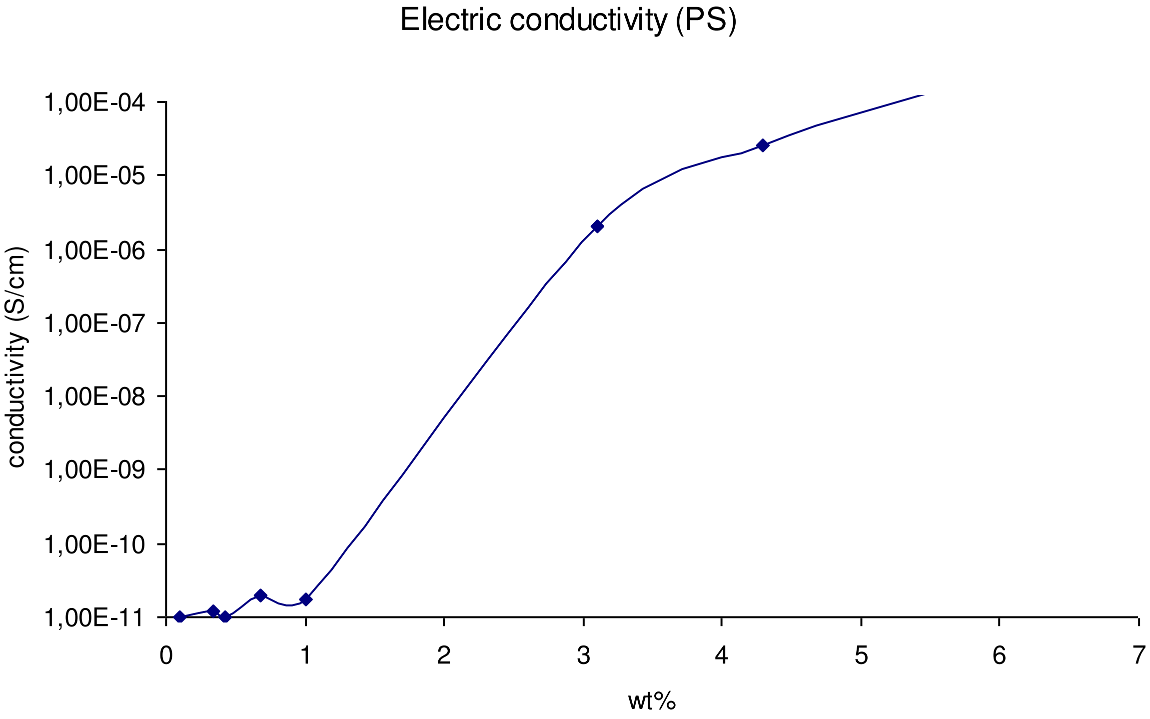

Figure. 32. The direct current conductivity of the PS composites versus different weight content of graphene nanosheets

Figure 32 showed the dependence of the direct current conductivity (σ_{DC}) on the weight content of graphene nanosheets for PS nanocomposites. An abrupt conductivity transition with an increase of a factor of 10^5 occurred at a concentration between 2 and 3 wt%, meaning percolation threshold P_c was between 2 wt% and 3 et%. To estimate P_c and the critical exponent s, a set of P_c varying between 2 wt% and 3 w% with distance 0.1 (2.1, 2.2, 2.3 …)

was chosen. With each chosen P_c, the current conductivity data σ_{DC} for P (P < P_c) were substituted into equation (2). Then the value of s was determined from the slope of the linear relation of σ_{DC} and (P_c –P). The lowest value of the root mean square error was found for P_c = 3.0 wt% with s = 1.7 (Figure 33). With the same method, P_c and t were also determined: the σ_{DC} data for P (P >P_c) were substituted into equation (1) for each chosen P_c., varying between 2 wt% and 3 w% with distance 0.1 (2.1, 2.2, 2.3 …). The lowest value of the root mean square error was found for P_c = 3.0 wt% with t = 1.3 (Figure 34). The obtained critical exponent t = 1.3 and s = 1.7 was in good agreement with the theory value between 1.5 to 2.0 for carbon black composites [49]. It suggested that graphene nanosheets were homogenously distributed in polystyrene matrix, with a 3D network.

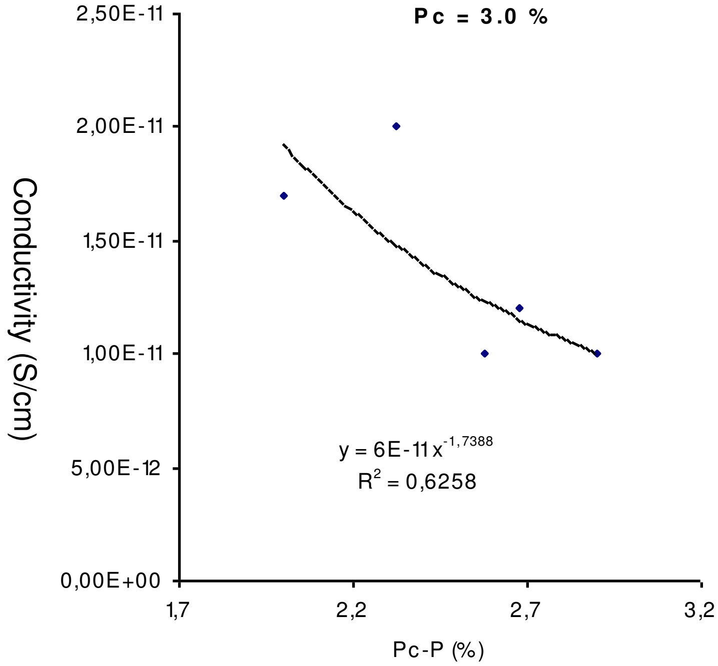

Figure 33. The values of direct current conductivity versus (P_c -P) to determine the critical exponent s of PS composites.

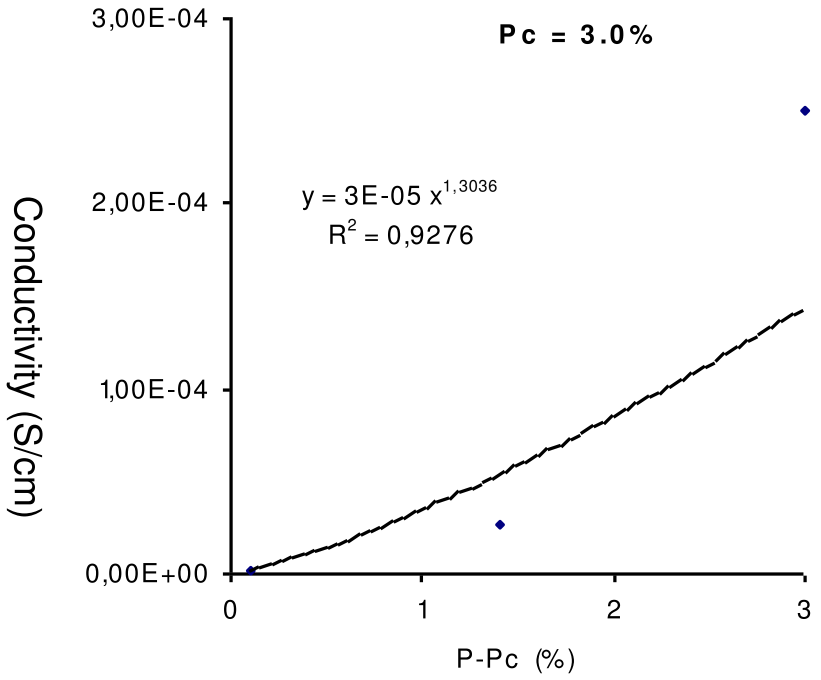

Figure 34. The values of direct current conductivity versus (P - P_c) to determine the critical exponent t of PS composites.

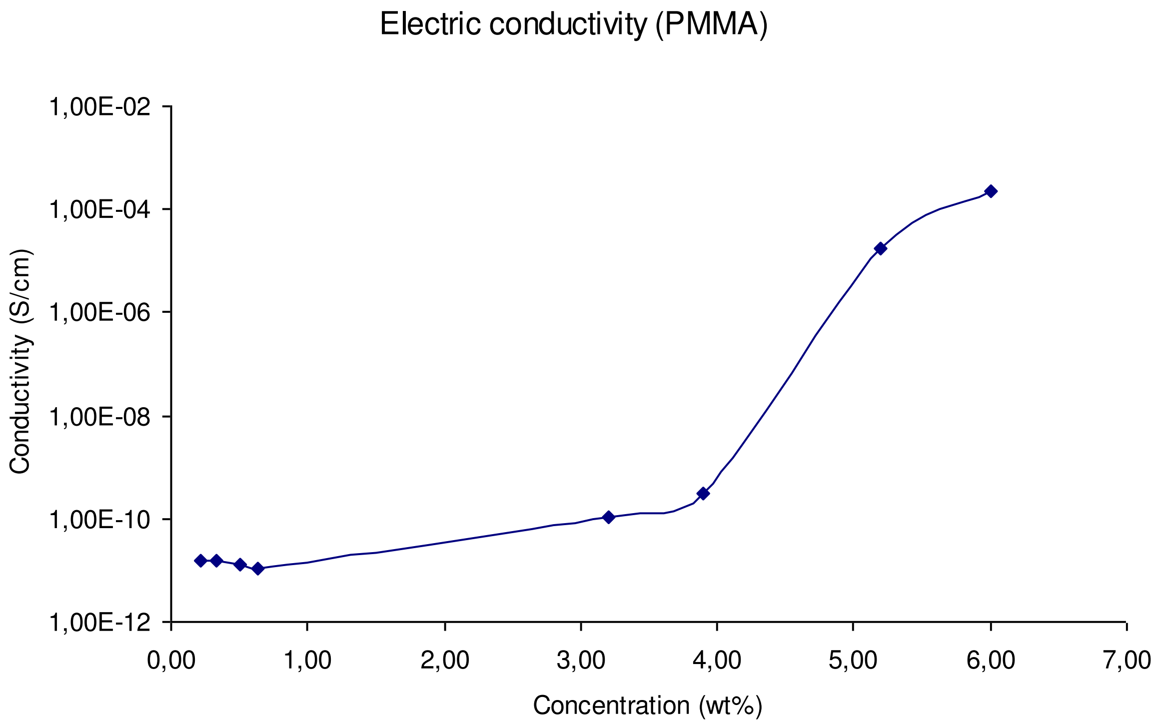

Figure 35. The direct current conductivity of the PMMA composites versus the weight content of graphene nanosheets.

The dependence of the direct current conductivity σ_{DC} of PMMA composites on the weight content of graphene nanosheets is shown in Figure 35. It is found the insulator-conductor transition was between 3 wt% and 4 wt% where the conductivity strongly increases from 3.0×10^{-10} to 1.8×10^{-5} S/cm. With the same method for PS composites, the percolation threshold was determined: a set of values P_c between 3 wt% to 4 wt% with a distance 0.1 was chosen. In order to estimate P_c and the critical exponent s, the direct current conductivity data σ_{DC} were substituted for P ($P < P_c$) into equation (2). The lowest value of the root mean square error was found for P_c = 3.3 wt% with the exponent s = 0.623 (Figure 36). Critical exponent s was close to the one of polyethylene graphite composites (s = 0.93) where graphene sheets were homogenously distributed in a 3D network [50]. The obtained critical exponent t = 9.14 is much higher than the theory values, probably due to measurement error (Figure 37).

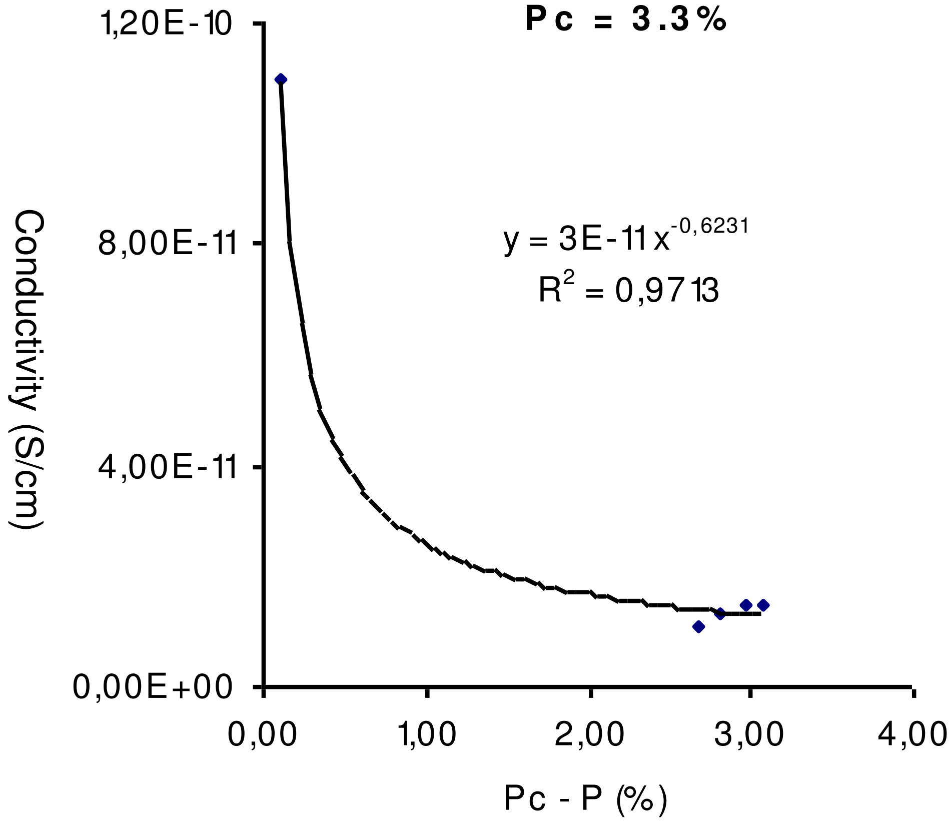

Figure 36. The values of direct current conductivity versus (P_c -P) to determine the critical exponent s of PMMA composites.

Compared with PS composites, the percolation threshold of PMMA composites with a value 3.3 wt% was relatively higher. Similar results were also reported for single-wall carbon nanotube (SWNT): The SWNT/polystyrene composites had a percolation threshold 0.3 wt%, whereas for PMMA it is about 1 wt% [51]. This could be explained by the fact that polystyrene had phenyl rings which could have better interaction with sheets [12].

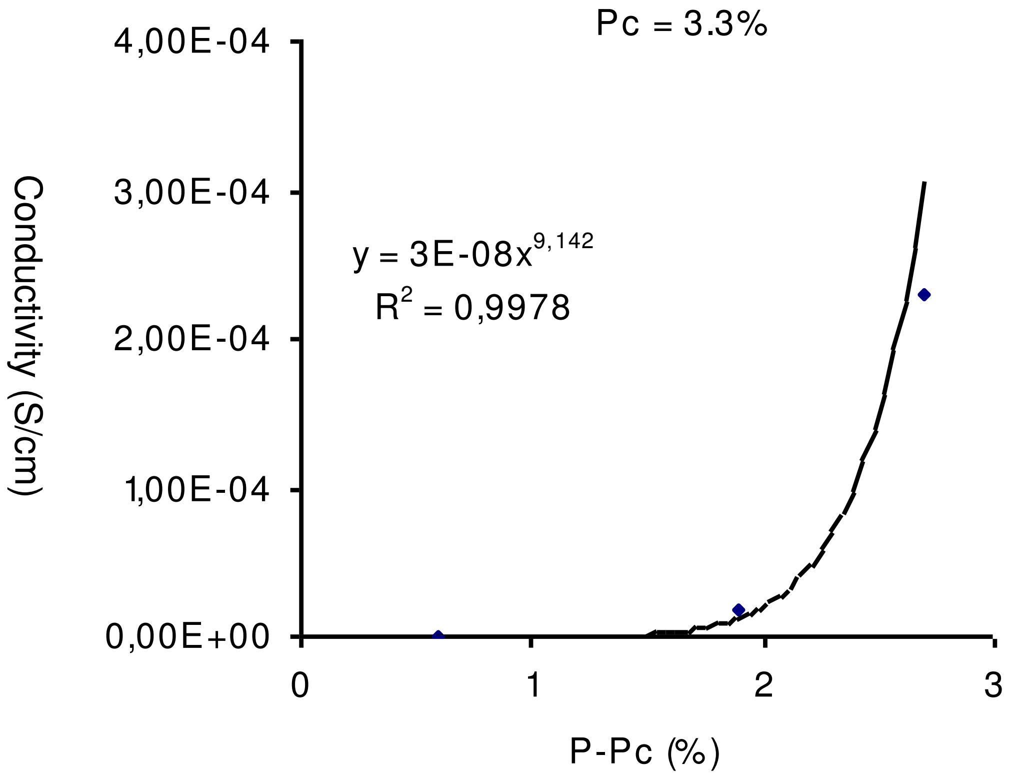

Figure 37. The values of direct current conductivity versus (P - P_c) to determine the critical exponent t of PMMA composites.

The percolation threshold P_c = 3.0 wt% (about 0.1 vol%) for the PS graphene nanosheets compared well with the best values reported in the literature. Polymer composites made of natural graphite flakes posed a percolation threshold of 20 wt% (about 3 vol%) [21]. Polymer composites with expanded graphite exhibited a lower percolation threshold of 10 wt% (about 0.3 vol%) [52-54]. The lowest percolation threshold of 3 wt% (about 0.1 wt%) reported in the literature was for a composite prepared by using modified graphene nanosheets [12]. A mainly disadvantage in these studies was that organic solvents with high boiling point and toxicity DMF were used, causing high production costs and pollution of the environment. In this work, THF, a solvent with low boiling point and low toxicity, was used for the preparation of graphene composites.

5.4.2.2 The influence of the frequency

The dependent of electrical conductivity and dielectric constant of the polymer nanocomposites on the frequency of the alternating current will be investigated, which are important factors for electric conductor. In this study the frequency will be varied from 1 to 10^7 Hz using a two-contact method.

For the measurement, the films of nanocomposites were fixed between two copper plates with a diameter of 10 mm and then placed in the central part of the measurement cell. Before the measurement, the films were polished with grater paper to obtain a smooth surface for a good conducting surface with copper plates. The electric conductivity σ of the PS composites with different content of graphene nanosheets showed a diverse tendency by varying frequency of the alternating current (Figure 38). For the composites with contents P ($P > P_c$), the electrical conductivity remained constant at the frequency between 1 to 10^5 Hz. A transition region began at 10^5 Hz and the response slowly increased. In contrast, for $P < P_c$, the conductivity increased linearly with increasing frequency from 1 to 10^7 Hz, demonstrating the power law behavior eq(2).

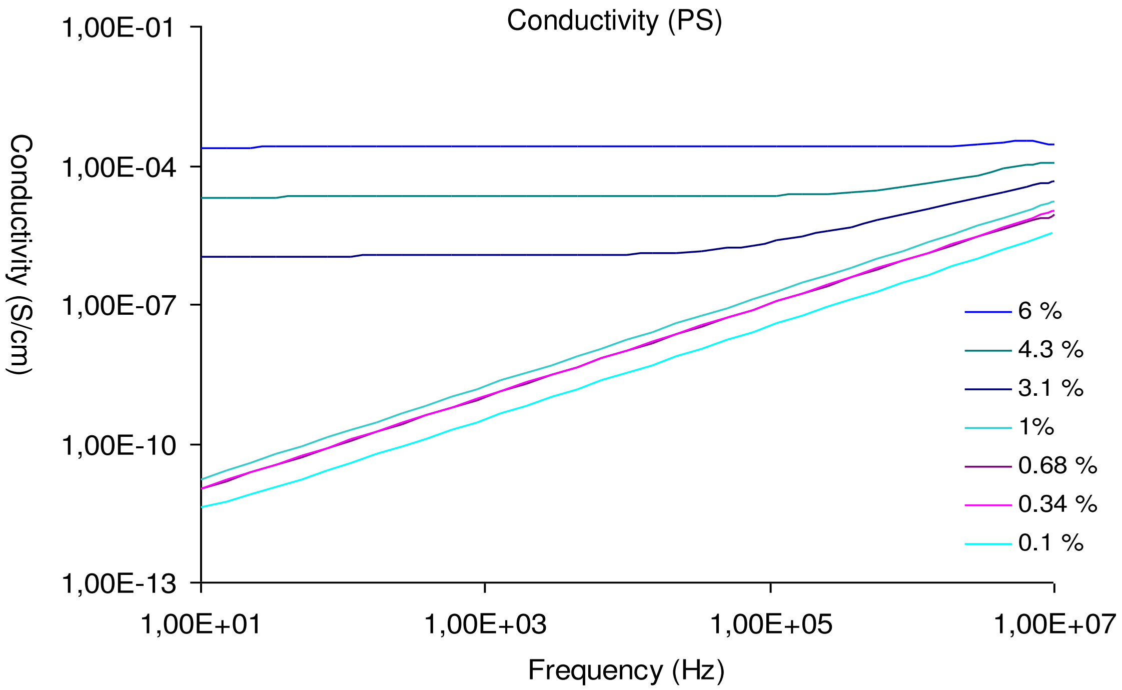

Figure 38. Electric conductivity of polystyrene composites as a function of the frequency.

Figure 39 showed the dependency of electric conductivity of the PMMA composites on the frequency between 1 and 10^7 Hz. At contents lower than P_c, a linear dependence of the electric conductivity on the frequency was observed. At contents above P_c, the electrical conductivity was constant at frequency (below 10^5 Hz). Above 10^5 Hz, the conductivity showed a small increase, demonstrating the power law behavior eq(2).

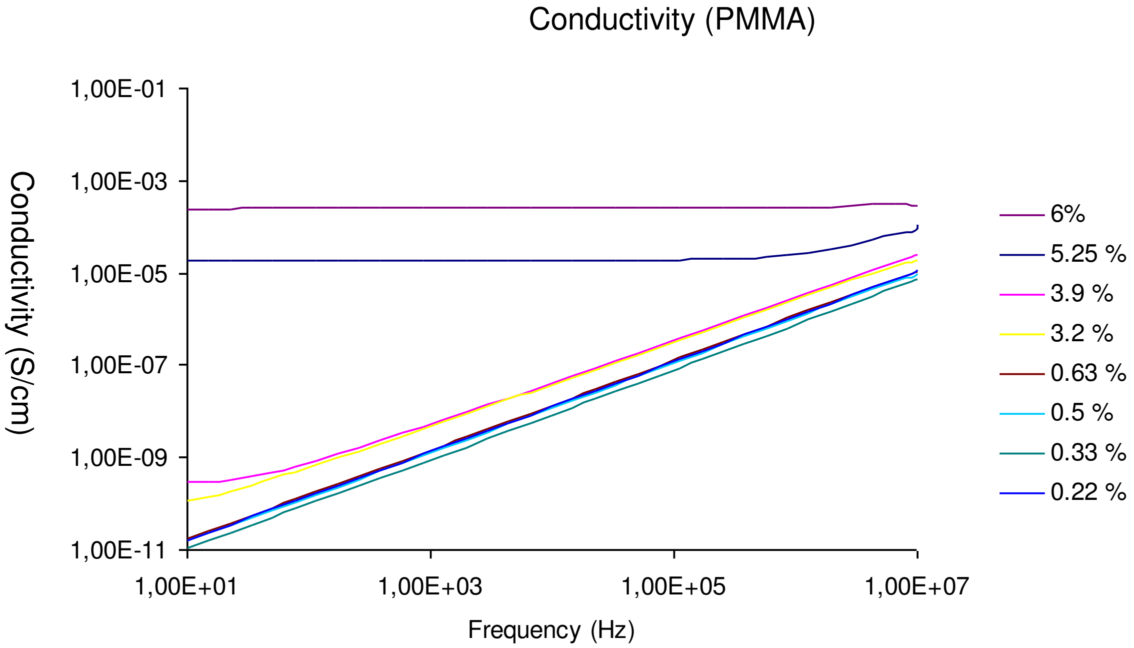

Figure 39. Electric conductivity of the PMMA composites as a function of the frequency

Next, the influence of frequency on the dielectric constants ε′ (the so-called real permittivity) of the PS composites with contents from 0.1 wt% to 3.1 wt% of graphene nanosheets was investigated. For the samples with contents higher than 3.1 wt%, the constants could not be measured because of the high electric conductivity. The ε′ for the contents from 0.1 wt% to 3.1 wt% was plotted on a logarithmic scale as a function of the applied frequency (Figure 40). The behavior of the dielectric constant depending on the frequency was obviously different from the one of electric conductivity. The dielectric constants ε′ remained constant with increasing frequency. Especially, the samples with contents close to P_c (about 3 wt%) showed a constant value at frequency lower than 10^5 Hz and strongly decreases at frequencies above 10^5 Hz.

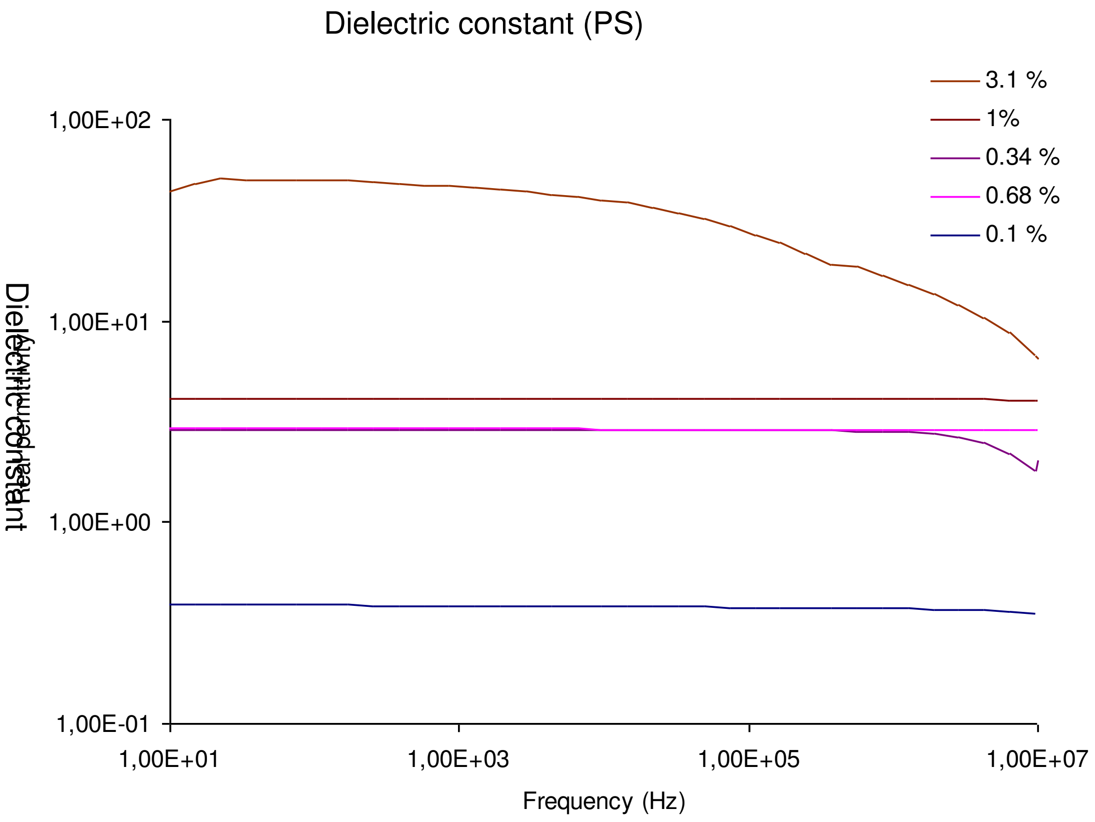

Figure 40. Dependency of the dielectric constant of polystyrene composites on the frequency.

The dependence of the dielectric constant ε′ on the frequency for PMMA composites with contents from 0.22 wt% to 3.9 wt% was shown in figure 41. The tendency of dielectric constants to varying frequency for PMMA composites was similar to PS composites. For composites with contents lower than 3 wt%, the dielectric constants ε′ remained constant at varying frequency. For contents over 3 wt%, the dielectric constants strongly decreased with increasing frequency.

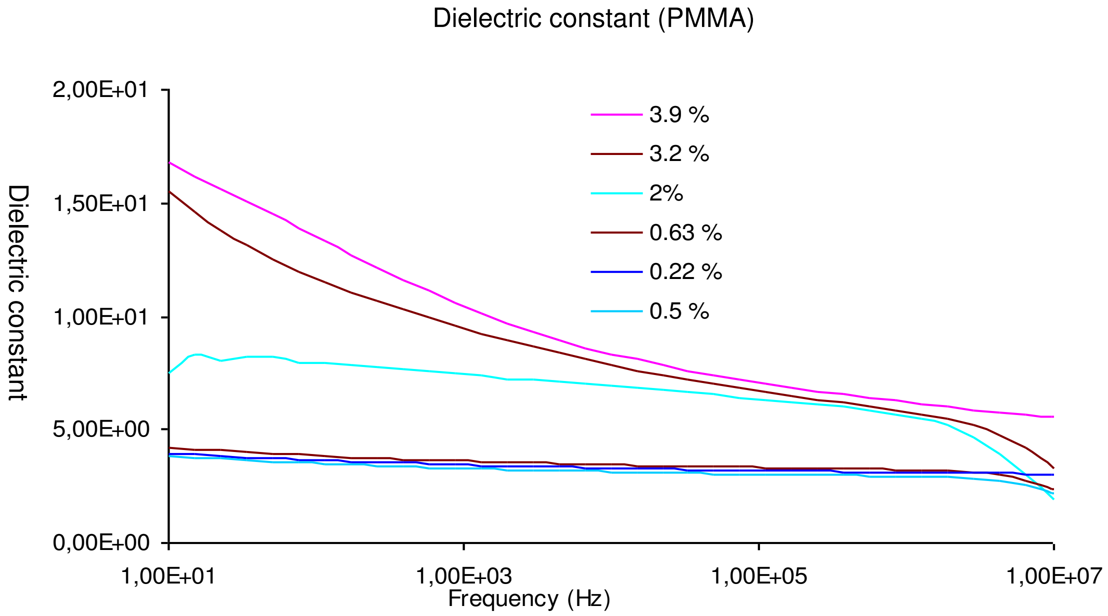

Figure 41 . Dependency of the dielectric constant of PMMA composites on the frequency.

5.4.2.3 The influence of the temperature

In this study, the influence of temperature on electric conductivity and dielectric constants of the PS and PMMA nanocomposites was also investigated from 25 °C to 100 °C with a constant frequency 100Hz. It was found that the electrical conductivity remained constant with increasing temperature, regardless of the varying contents (Figure 42 and 43). Similar to the electric conductivity, with increasing temperature dielectric constants ε' remained almost unchanged for PS and PMMA composites (Figure 44 and 45).

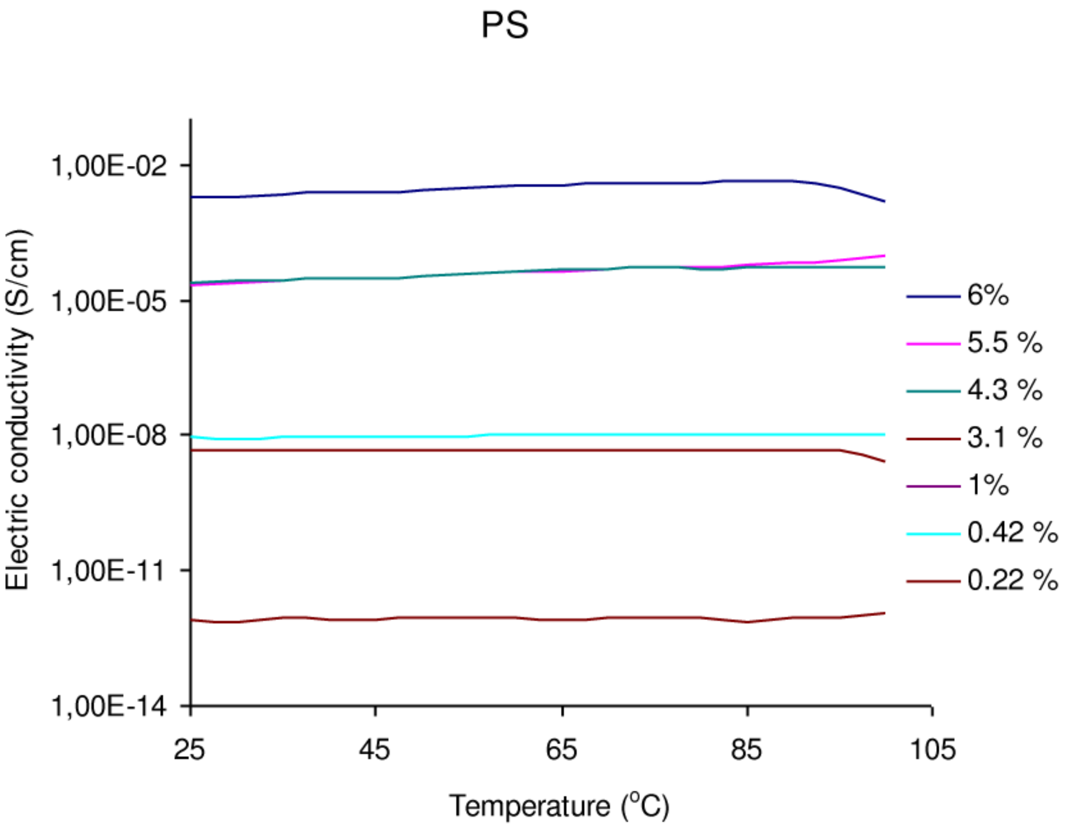

Figure 42. Dependence of electric conductivity of PS composites on the temperature.

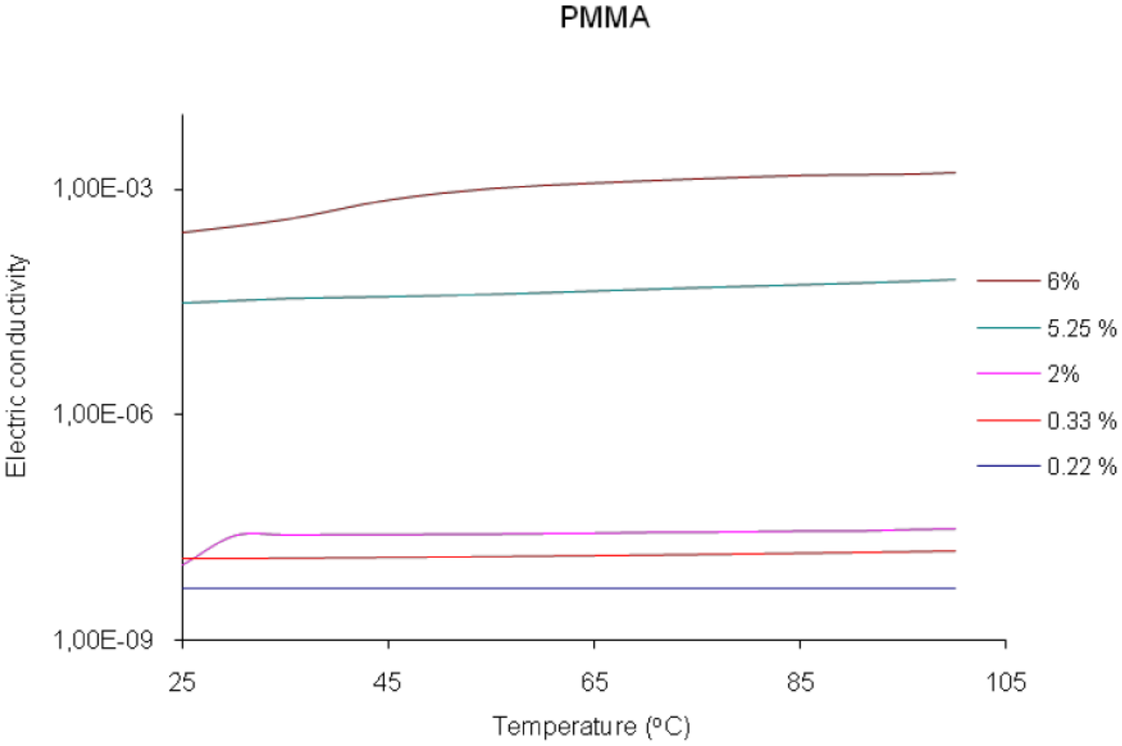

Figure 43. Dependence of electric conductivity of PMMA composites on the temperature.

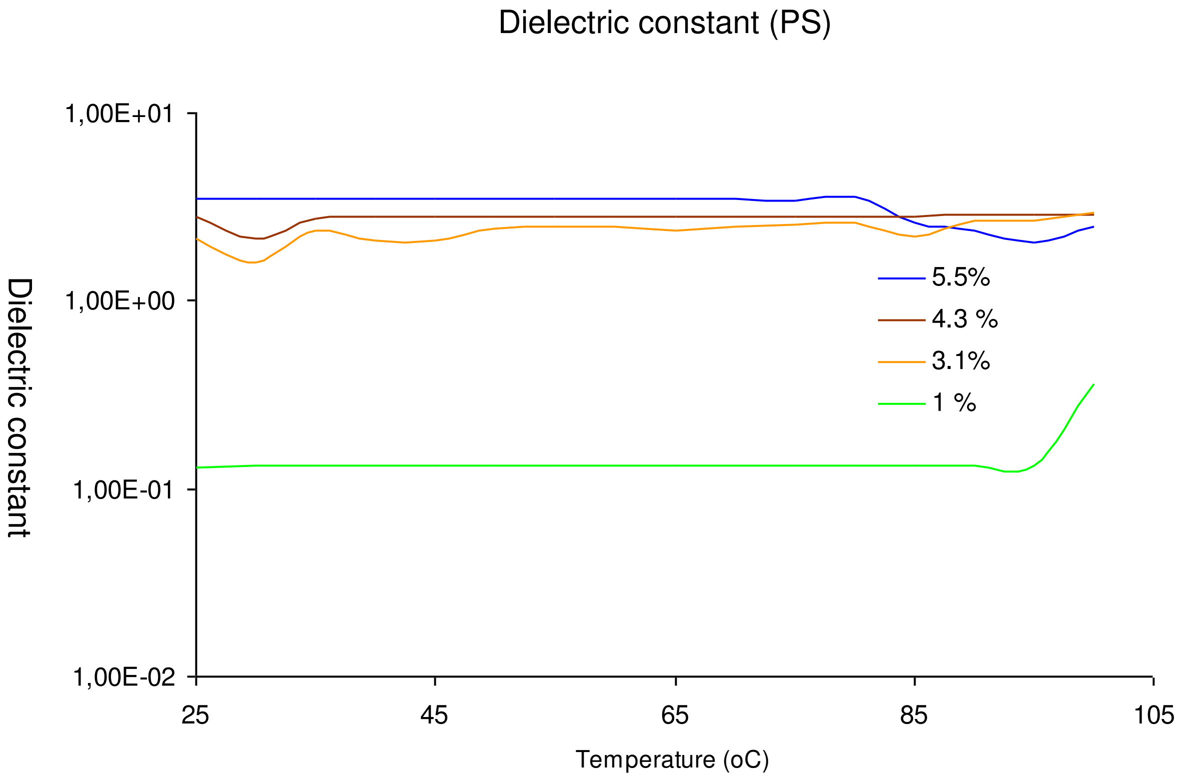

Figure 44. The dielectric constant ε’ of PS composites as a function of the temperature.

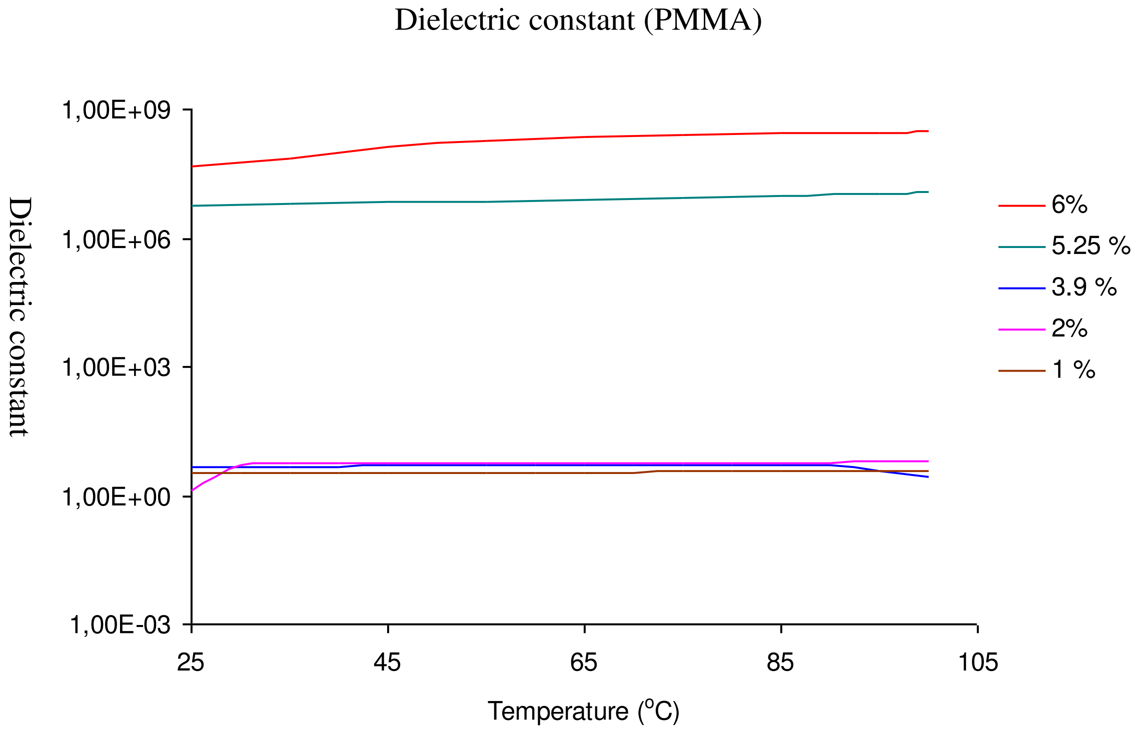

Figure 45. The dielectric constant ε’ of PMMA composites as a function of the temperature.

5.4.2.4 Mechanism of electric conducting in graphene nanocomposites

The mechanism to explain how charges were transported in composites was intensively studied in the last thirty years [50, 55-58]. Hopping effect and fluctuation-induced tunneling effect were the mostly accepted models for the mechanism.

The idea for the hopping effect was that electrons were transported between valence band and conducting band in crystalline array (Figure 46) [56, 58]. Because the energy gap between them was large, electrons were localized in the valence band [59]. With provision of energy, part of electrons could jump over the energy gap into conducting band. The upper boundary of the valence band was shifted towards the conducting one, and both bands overlap with each other. The electrons which were in overlapping area could freely move in the crystal, leading to an electric conductivity.

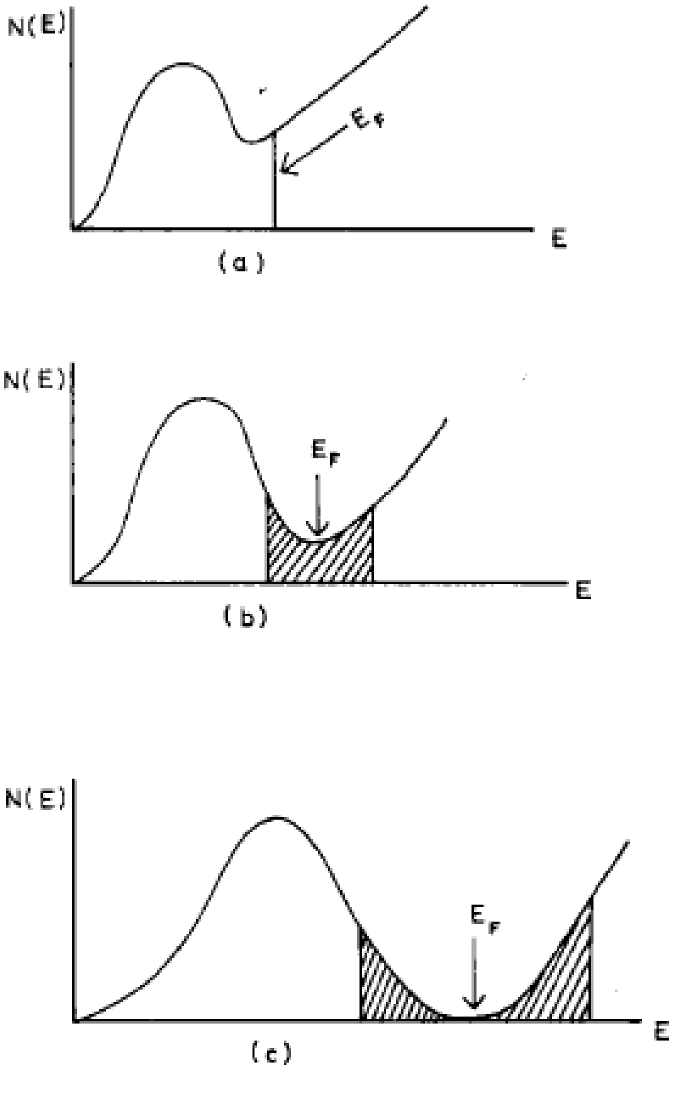

Figure 46. Hopping effect: **(a)** Conduction is metallic. **(b)** Conduction is by hopping. **(c)** Conduction involves excitation of electrons from the valence to the conduction band [59].

In the fluctuation induced tunneling effect, electrons tended to tunnel isolating region where two conducting particles were very close (Figure 47) [55]. These particles were approximated like parallel plate capacitors. Owing to the random thermal motion of electrons, transient excess or deficit of charges appeared at such region [55]. Hence high or low voltage could be produced there. With the high voltage, electrons could tunnel the region from one particles to another, resulting in electric conductivity.

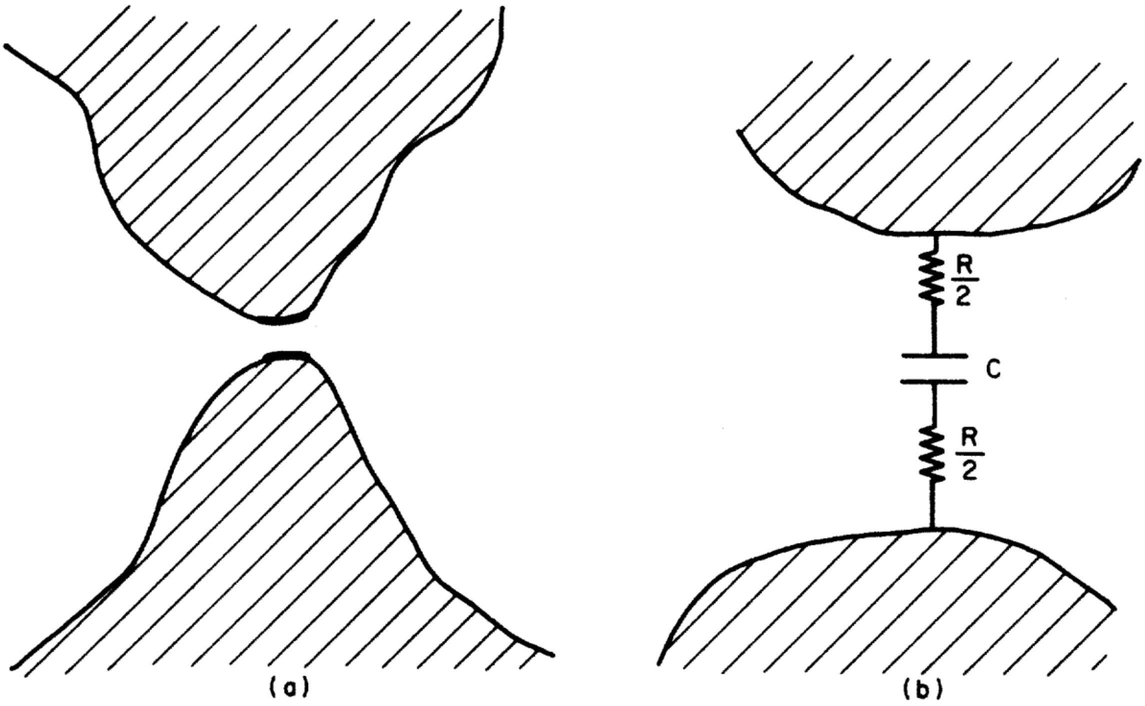

Figure 47. Fluctuation induced tunneling effect in a region of close approach point between two conducting particles. Shaded area denotes conductors. a) The heavy lines delineate the surface areas where most of the tunneling occurs. This tunnel junction is schematically depicted as a parallel plate capacitor in (b) [55].

The effect that electric conductivity of the nanocomposites increased with increasing frequency could be explained by the friction heat between electrons and matrices. At higher frequency the electrons had more friction with matrices due to quickly changing orientation of current. Hence more friction heat was produced. When electrons adsorb the energy, they could jump over the energy gap from the covalent band into the conducting one, resulting electric conductivity. The effect could be also explained that the produced heat causes highly random thermal motion of electrons at the close approach point of two conducting particles, leading high voltage there. Hence, the electrons could tunnel from one particle to another.

The phenomenon that the temperature did not show any influence on the electrical properties could be explained by the fluctuation induced tunneling effect. In theoretical physics the tunneling effects were classified into thermally activated tunneling at high temperature and temperature independent tunneling effects at low temperature [55]. With increasing temperature, the electrons had increasing random thermal moving, leading not only to increase tunneling probability, but also to a decreased occupation probability on the boundary surface. Only above a certain temperature the increase of the tunneling probability dominated the decrease of the occupation probability, and the electrical conductivity increased with increasing temperature [55]. In this study, the temperature was varying from 25 ºC to 100 ºC where the decrease of the occupation probability maybe offset the increase of the tunneling probability. Therefore no change of electrical properties was observed with the varying temperature.

5.4.3 Thermal stability of polymer nanocomposites

The thermal stability of the nanocomposites was measured by using a thermo-gravimetric analyzer (TGA). The TGA curves of the pure polymer matrices and the nanocomposites with different contents of graphene sheets were shown in Figure 48 and Figure 49. It was observed that the onset of the thermal degradation of the pure PS was a little bite higher than the ones of PS composites. The result could be explained by the addition of PI-b-PMMA which had a lower degradation temperature (200 ºC). The composites showed a more remaining content of graphene nanosheets at 410 °C than pure PS. It indicated that introduced graphene nanosheets enhanced the thermal stability of the PS matrix.

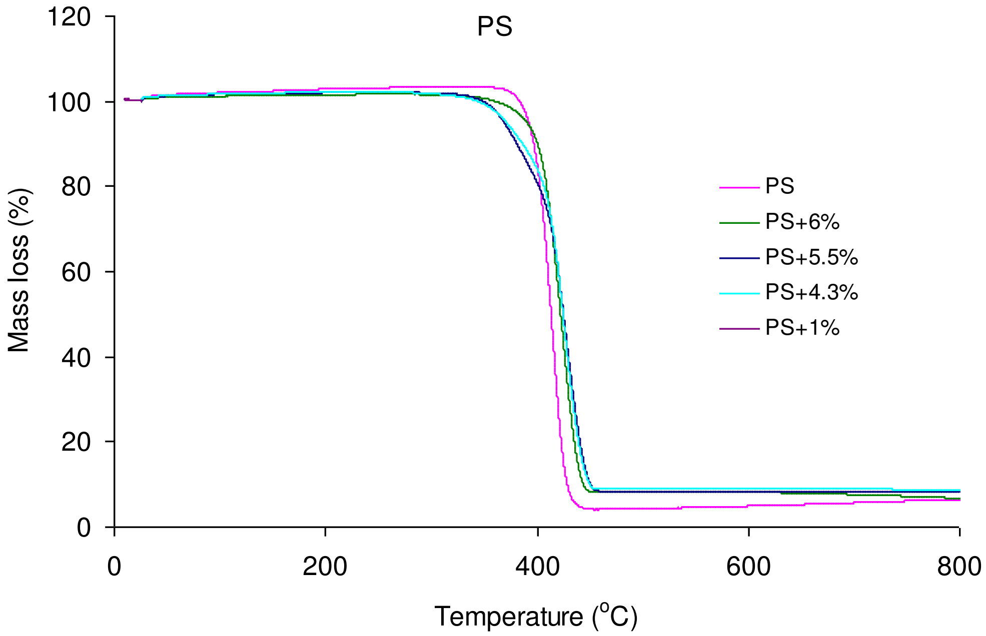

Figure 48. TGA spectra of PS graphene nanocomposites with a heating rate of 10 °C/min from room temperature to 800 °C under N_2.

Figure 49 shows the TGA for the pure PMMA and PMMA nanocomposites with 3 to 6 wt.% graphene nanosheets. Pure PMMA and the nanocomposites started to decompose at about 260 °C. At about 410 °C, the content of the remaining weight of PMMA composites was a little bite higher than pure PMMA, meaning the thermal stability of the composites was increased by addition of graphene nanosheets.

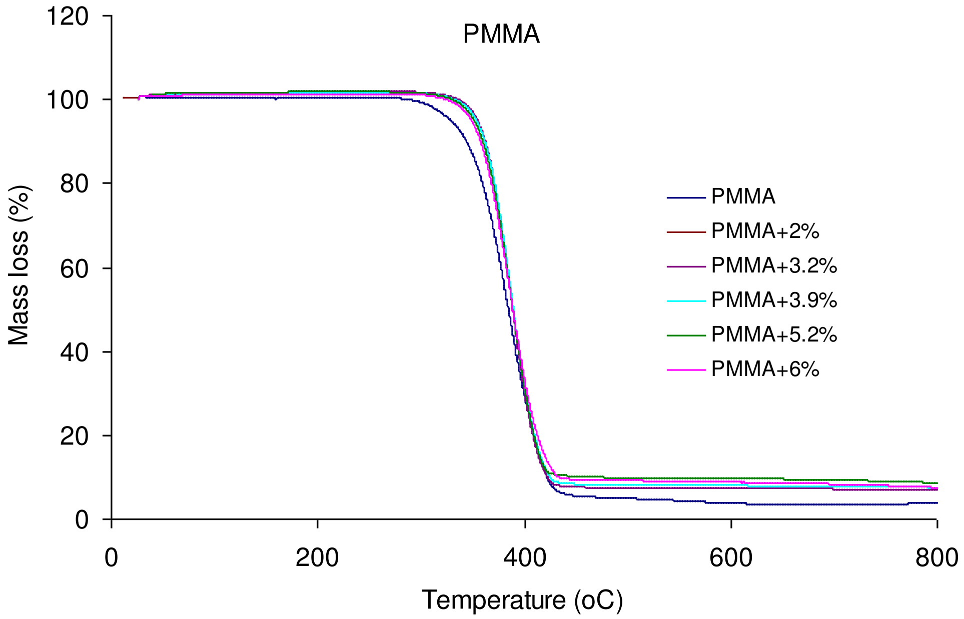

Figure 49. TGA of PMMA graphene nanocomposites with a heating rate of 10 °C/min from room temperature to 800 °C under N_2.

The influence of the addition of graphene nanosheets on the glass transition temperature of the composites was investigated by using Differential Scanning Calorimetry (DSC). For PS and PMMA nanocomposites, the glass transition temperature was hardly changed with a content of graphene nanosheets varying from 1 wt% to 6 wt% (Figure 50).

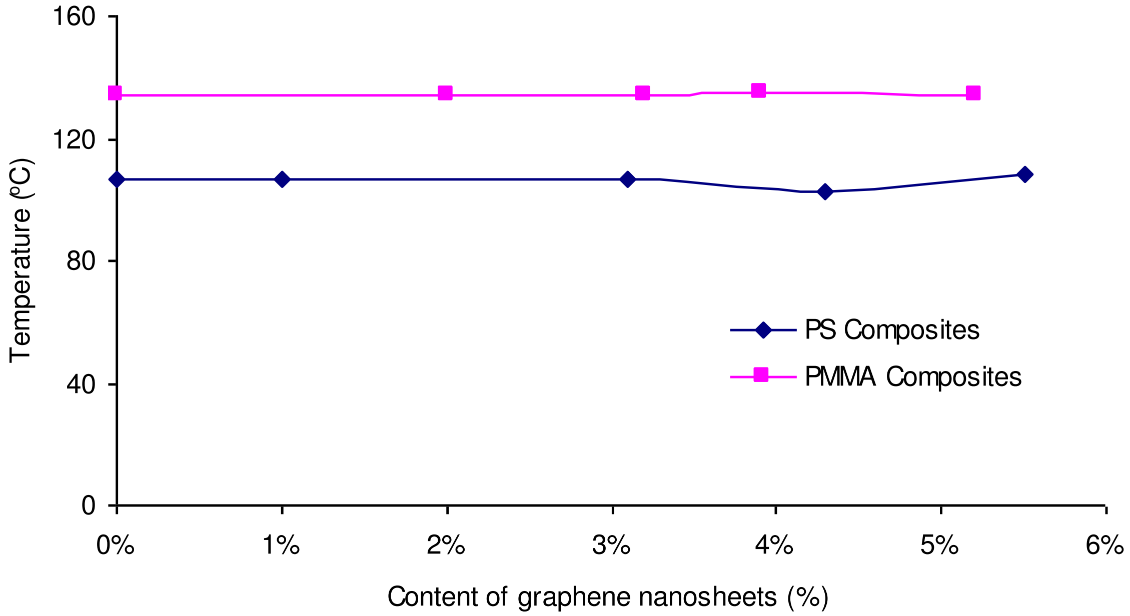

Figure 50. The glass transition temperature of the composites with different contents of graphene nanosheets.

Another method to determine the glass transition temperature is by use of a tan δ curve.

$$\tan\delta = \frac{E''}{E'}$$

where E´´ is storage modulus which measures the stored energy, representing the elastic portion, and E´ is the loss modulus which measures the energy dissipated as heat, representing the viscous portion [60]. The temperature where tan δ is maximal indicates the glass transition temperature.

In Figure 51 and 52, the maximum of the tan δ curves of PS and PMMA nanocomposites were not strongly influenced by adding graphene nanosheets. The results agreed with the DSC measurement. But it was found that the curves became broader at the side of high temperature with increasing content of graphene nanosheets. It could be explained that at higher content of graphene sheets the mobility of polymer chains were more strongly hindered by the sheets. Hence the chains needed more energy to get mobile. This result suggested that graphene sheets had strong interaction with the polymer chains.

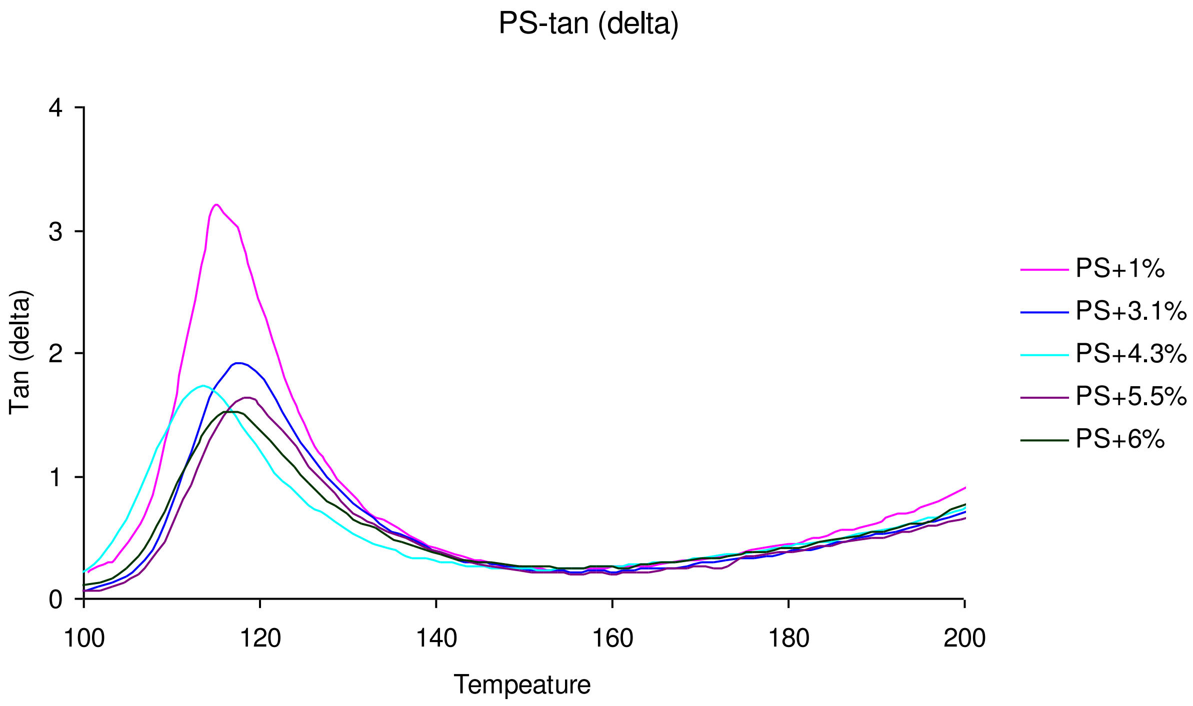

Figure 51. The dependency of Tan (δ) of PS composites on the temperature.

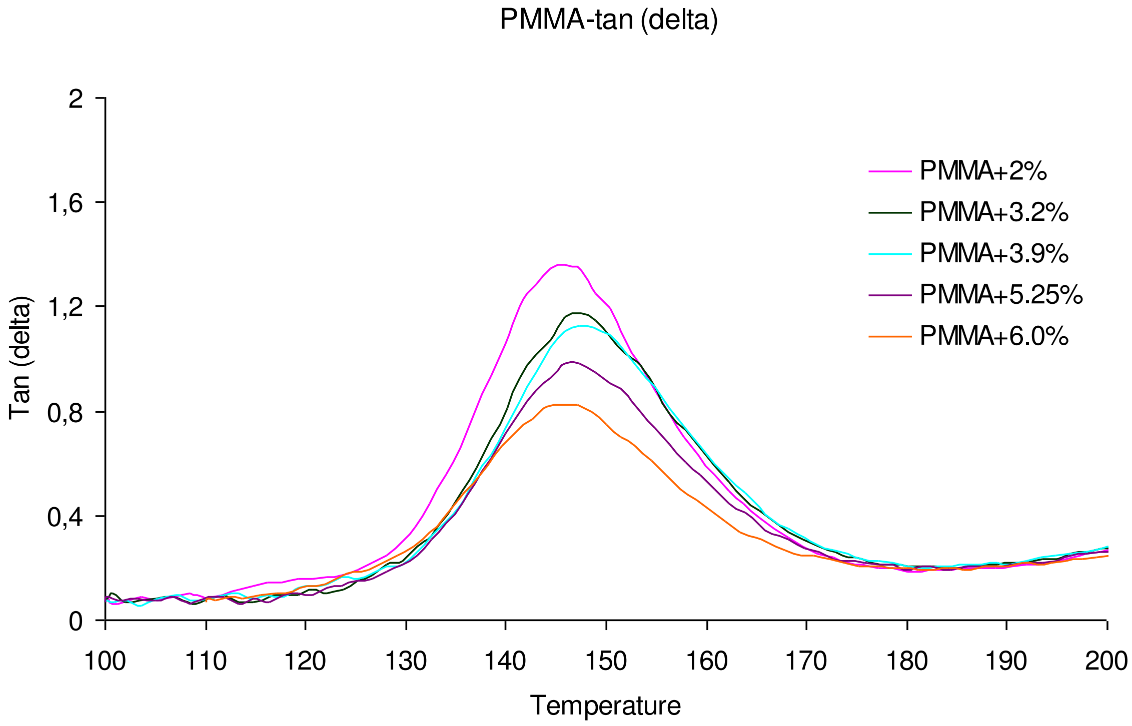

Figure 52. The dependency of Tan δ of PMMA composites on the temperature.

5.4.4 Mechanical stability of polymer nanocomposites

The mechanical stability of the graphene nanosheets composites were characterized by dynamic mechanical thermal analysis (DMTA). Figure 53 and 54 show the storage modulus which was measured from room temperature to 200 °C. Below 120 °C the storage modules of remained unchanged for composites with different contents of graphene nanosheets. At120 °C, a transition from the glassy state to the rubbery state appeared. Above 120 °C (in the rubbery state), the contents of graphene nanosheets had a significant influence on the storage modulus: with increasing contents of graphene nanosheets, the storage modulus increased obviously. Similar results were also obtained for PMMA composites (Figure 54).

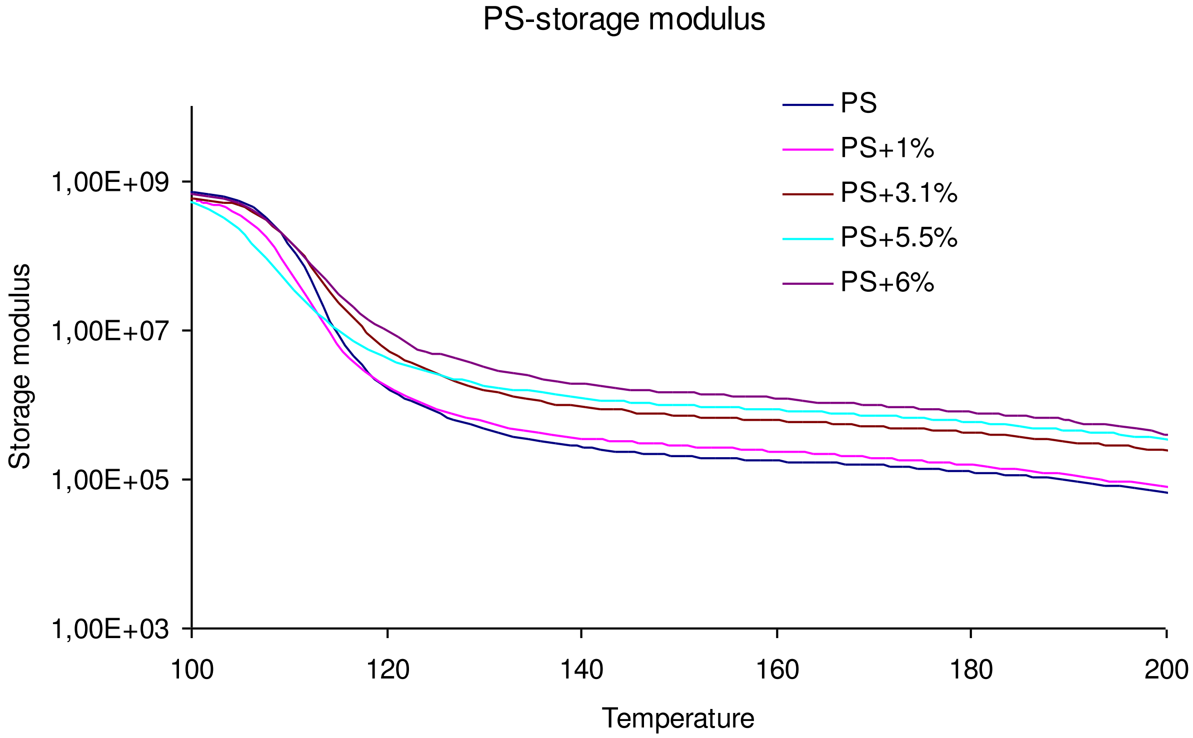

Figure 53. The dependency of storage modulus of PS on the concentrations of graphene nanosheets.

The small influence of graphene nanosheets on the mechanical properties of the composites at room temperature could be explained by that graphene nanosheets from graphene oxide foam had many defect holes [28, 61]. Such sheets did not have strong mechanical stability like perfect sheets prepared by peeling off graphite with "Scotch" tape [16]. Therefore nanocomposites did not show an improved mechanical stability.

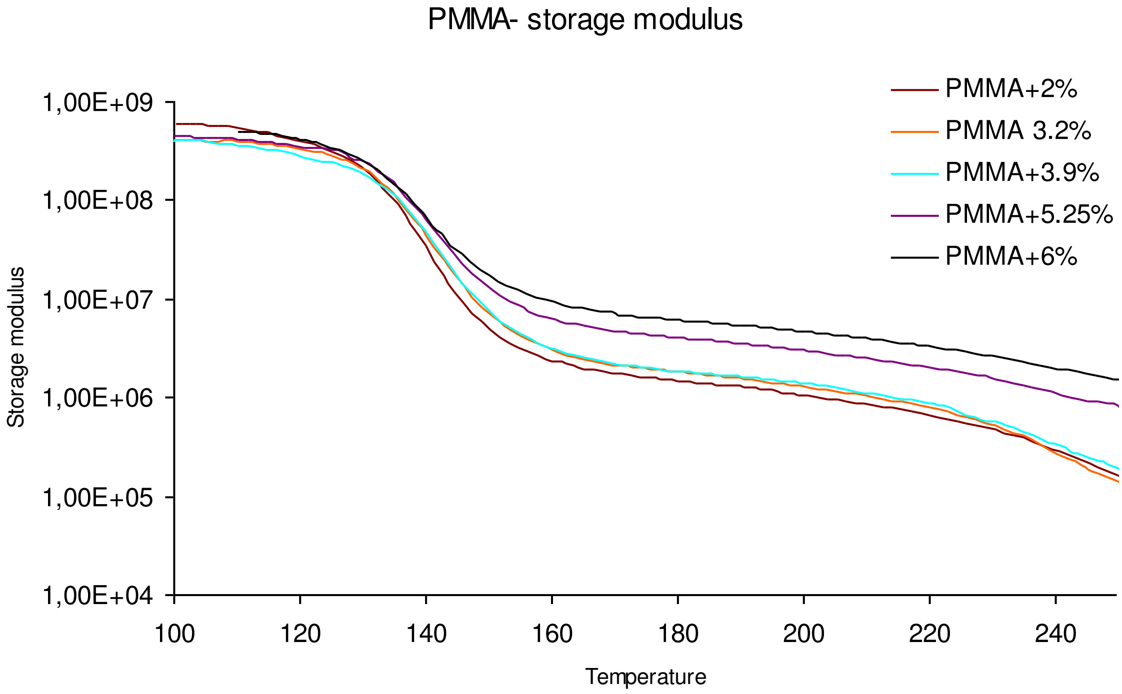

Figure 54. The dependency of storage modulus of PMMA on the concentrations of graphene nanosheets.

5.4.5 Summary

In this part of the study, graphene nanosheets with high surface area were dispersed in an organic solvent with low boiling point and low toxicity, THF, stabilized with a block copolymer PI-b-PMMA. The dispersion showed high stability after centrifugation for 30 min with 1000 rpm. It meant that PI-b-PMMA had strong interaction with graphene nanosheets. The dispersion was used to prepared polymer composites. It was shown that the modified graphene nanosheets had good compatibility with the PS and PMMA matrices. Especially, the electric properties of the composites were obviously improved: with about 3 wt% of graphene sheets the composites were converted to electric conducing materials. These results were comparable with the best ones reported in the literature. The thermal and mechanical stability was not strongly changed by addition of the graphene nanosheets. It could be explained by the defect holes in the sheets from the oxidation process for the preparation of graphene oxide.

Reference

1. Geim, A.K. and K.S. Novoselov, The rise of graphene. Nature Materials, 2007. **6**: p. 183-191.
2. Park, S. and R.S. Ruoff, Chemical methods for the production of graphenes. Nature Nanotechnology, 2009. **4**(4): p. 217-224.
3. Lee, C., et al., Measurement of the elastic properties and intrinsic strength of monolayer graphene. Science China-Chemistry, 2008. **321**: p. 385-388.
4. Balandin, A.A., Superior thermal conductivity of single-layer graphene. Nano Letters, 2008. **8**: p. 902-907
5. Bolotin, K.I., Ultrahigh electron mobility in suspended graphene. Solid State Communications, 2008. **146**: p. 351-355.
6. Stoller, M.D., et al., Graphene-based ultracapacitors. Nano Letters, 2008. **8**: p. 3498-3502.
7. Stoller, M.D., et al., Graphene-based ultracapacitors. Nano Letters, 2008. **8**.
8. Zhang, Y.B., et al., Experimental observation of the quantum Hall effect and Berry's phase in graphene. Nature, 2005. **438**(7065): p. 201-204.
9. Dikin, D.A.e.a., Preparation and characterization of graphene oxide paper. Nature Biotechnology, 2007(448).
10. Park, S.e.a., Graphene oxide papers modified by divalent ions-Enhancing mechanical properties via chemical cross-linking. ACS Nano, 2008. **2**.
11. Ramanathan, T., et al., Functionalized graphene sheets for polymer nanocomposites. Nature Nanotechnology, 2008. **3**(6): p. 327-331.
12. Stankovich, S., et al., Graphene-based composite materials. Nature, 2006. **442**(7100): p. 282-286.
13. Blake, P.e.a., Graphene-based liquid crystal device. Nano Lett., 2008. **8**.
14. Bunch, J.S.e.a., Electromechanical resonators from graphene sheets. Science China-Chemistry, 2007(315).
15. Eizenberg, M. and J.M. Blakely, Carbon monolayer phase condensation on Ni(111). Surf. Sci., 1970. **82,**.
16. Novoselov, K.S., Electric Field Effect in Atomically Thin Carbon Films. Science, 2004. **306**(5696): p. 666-669.
17. Bunnell, 1991.
18. Lee, S., D. Cho, and L.T. Drzal, Real-time observation of the expansion behavior of intercalated graphite flake. Journal of Materials Science, 2005. **40**(1): p. 231-234.

19. Stankovich, S., et al., Synthesis of graphene-based nanosheets via chemical reduction of exfoliated graphite oxide. Carbon, 2007. **45**(7): p. 1558-1565.
20. Chen, G.H., et al., PMMA/graphite nanosheets composite and its conducting properties. European Polymer Journal, 2003. **39**(12): p. 2329-2335.
21. Chen, G.H., et al., Preparation and characterization of graphite nanosheets from ultrasonic powdering technique. Carbon, 2004. **42**(4): p. 753-759.
22. Celzard, A., J.F. Mareche, and G. Furdin, Modelling of exfoliated graphite. Progress in Materials Science, 2005. **50**(1): p. 93-179.
23. Stankovich, S., et al., Stable aqueous dispersions of graphitic nanoplatelets via the reduction of exfoliated graphite oxide in the presence of poly(sodium 4-styrenesulfonate). Journal of Materials Chemistry, 2006. **16**(2): p. 155-158.
24. McAllister, M.J., et al., Single sheet functionalized graphene by oxidation and thermal expansion of graphite. Chemistry of Materials, 2007. **19**(18): p. 4396-4404.
25. Jang, B.Z. and A. Zhamu, Processing of nanographene platelets (NGPs) and NGP nanocomposites: a review. Journal of Materials Science, 2008. **43**(15): p. 5092-5101.
26. Schniepp, H.C., et al., Functionalized single graphene sheets derived from splitting graphite oxide. Journal of Physical Chemistry B, 2006. **110**(17): p. 8535-8539.
27. Stankovich, S., et al., Synthesis of graphene-based nanosheets via chemical reduction of exfoliated graphite oxide. Carbon, 2007. **45**(7): p. 1558-1565.
28. Boehm, H.P., et al., Das Adsorptionsverhalten Sehr Dunner Kohlenstoff-Folien. Zeitschrift Fur Anorganische Und Allgemeine Chemie, 1962. **316**(3-4): p. 119-127.
29. Potts, J.R., et al., Graphene-based polymer nanocomposites. Polymer, 2011. **52**(1): p. 5-25.
30. Paul, D.R. and L.M. Robeson, Polymer nanotechnology: Nanocomposites. Polymer, 2008. **49**(15): p. 3187-3204.
31. Stankovich, S., et al., Synthesis and exfoliation of isocyanate-treated graphene oxide nanoplatelets. Carbon, 2006. **44**(15): p. 3342-3347.
32. Brodie, B., Phil. Trans., 1859. **149**: p. 249.
33. Staudenmaier, L., ibid, 1898. **31**: p. 1481.
34. Hummers, W., S, and R. Offeman, E,, Prepartion of Graphitic oxide. Contribution from the baroid division, National lead Company, 1957

35. Hirata, M., T. Gotou, and M. Ohba, Thin-film particles of graphite oxide. 2: Preliminary studies for internal micro fabrication of single particle and carbonaceous electronic circuits. Carbon, 2005. **43**(3): p. 503-510.

36. Szabo, T., A. Szeri, and I. Dekany, Composite graphitic nanolayers prepared by self-assembly between finely dispersed graphite oxide and a cationic polymer. Carbon, 2005. **43**(1): p. 87-94.

37. Hofmann, U. and R. Holst, The acidic nature and the methylation of graphitoxide. Berichte Der Deutschen Chemischen Gesellschaft, 1939. **72**: p. 754-771.

38. Ruess, G., Uber das Graphitoxyhydroxyd (Graphitoxyd). Monatsch Chem, 1956. **76**: p. 381.

39. Lerf, A., et al., Structure of graphite oxide revisited. Journal of Physical Chemistry B, 1998. **102**(23): p. 4477-4482.

40. Gao, W., et al., New insights into the structure and reduction of graphite oxide. Nature Chemistry, 2009. **1**(5): p. 403-408.

41. Ali, F., et al., Chemical route to the formation of graphene. Current Science, 2009. **97**(5): p. 682-684.

42. Stankovich, S., et al., Synthesis and exfoliation of isocyanate-treated graphene oxide nanoplatelets. Carbon, 2006. **44**(15): p. 3342-3347.

43. Lee, J.H., et al., The Superior Dispersion of Easily Soluble Graphite. Small, 2010. **6**(1): p. 58-62.

44. Hernandez, Y., et al., High-yield production of graphene by liquid-phase exfoliation of graphite. Nature Nanotechnology, 2008. **3**(9): p. 563-568.

45. Müller, K., et al., Synthesis and Layer-by-Layer Deposition of Spherical Poly(3,4-ethylenedioxythiophene) Nanoparticles - Toward Fast Switching Times between Reduced and Oxidized States. Macromolecular Chemistry and Physics, 2007. **208**(13): p. 1394-1401.

46. Müller, K., M. Klapper, and K. Müllen, Synthesis of Conjugated Polymer Nanoparticles in Non-Aqueous Emulsions. Macromolecular Rapid Communications, 2006. **27**(8): p. 586-593.

47. Flandin, L., et al., Anomalous percolation transition in carbon-black-epoxy composite materials. Physical Review B, 1999. **59**(22): p. 14349-14355.

48. Song, Y., et al., Experimental-Study of the 3-Dimensional Ac Conductivity and Dielectric-Constant of a Conductor-Insulator Composite near the Percolation-Threshold. Physical Review B, 1986. **33**(2): p. 904-908.

49. Karasek, L., et al., Percolation concept: Polymer-filler gel formation, electrical conductivity and dynamic electrical properties of carbon-black-filled rubbers. Polymer Journal, 1996. **28**(2): p. 121-126.

50. Ezquerra, T.A., et al., Charge Transport in Polyethylene Graphite Composite-Materials. Advanced Materials, 1990. **2**(12): p. 597-600.

51. Regev, O., et al., Preparation of conductive nanotube-polymer composites using latex technology. Advanced Materials, 2004. **16**(3): p. 248-+.

52. Wei, T., et al., Preparation of graphene nanosheet/polymer composites using in situ reduction–extractive dispersion. Carbon, 2009. **47**(9): p. 2296-2299.

53. Ramanathan, T., et al., Graphitic nanofillers in PMMA nanocomposites - An investigation of particle size influence on nanocomposite and dispersion and their properties. Journal of Polymer Science Part B-Polymer Physics, 2007. **45**(15): p. 2097-2112.

54. Zheng, W., X.H. Lu, and S.C. Wong, Electrical and mechanical properties of expanded graphite-reinforced high-density polyethylene. Journal of Applied Polymer Science, 2004. **91**(5): p. 2781-2788.

55. Sheng, P., Fluctuation-Induced Tunneling Conduction in Disordered Materials. Physical Review B, 1980. **21**(6): p. 2180-2195.

56. Mott, N.F., Conduction and Switching in Non-Crystalline Materials. Contemporary Physics, 1969. **10**(2): p. 125-&.

57. Adriaanse, L.J., et al., High-dilution carbon-black/polymer composites: Hierarchical percolating network derived from Hz to THz ac conductivity. Physical Review Letters, 1997. **78**(9): p. 1755-1758.

58. Ambegaokar, V., B.I. Halperin, and J.S. Langer, Hopping Conductivity in Disordered Systems. Physical Review B-Solid State, 1971. **4**(8): p. 2612-+.

59. Mott, N.F., Conduction in Non-Crystalline Materials .3. Localized States in a Pseudogap and near Extremities of Conduction and Valence Bands. Philosophical Magazine, 1969. **19**(160): p. 835-&.

60. Meyers, M.A. and C. K.K., Mechanical Behavior of Materials1999: Prentice-Hall.

61. Dreyer, D.R., et al., The chemistry of graphene oxide. Chemical Society Reviews, 2010. **39**(1): p. 228.

Chapter 6. Conclusion

In the current work, three studies about non-aqueous dispersions of particles were carried out by using an amphiphilic block copolymer poly(isoprene)-block-poly(methyl methacrylate) (PI-b-PMMA) as stabilizer:

1. Dispersions of polyurethane and polyurea porous particles for polymer composites
2. Dispersions of PMMA and PU particles with PDI dye for study of Single Molecule Spectroscopy Detection
3. Dispersions of graphene nanosheets for polymer composites

6.1 Dispersions of polyurethane and polyurea porous particles for polymer composites

The study of dispersion of polyurethane porous particles extended the work of a previous PhD thesis, where porous polyurethane particles were prepared via a non-aqueous emulsion (PI-b-PMMA as emulsifier) [1]. In this early work, the emulsion showed weak stability, appearing precipitation during the polymerization. The goal of this work was to develop a stable system and particles with homogenous porous structure. By using a mixture of aliphatic and aromatic diisocyanate, different to the previous work where only aromatic diisocyanate was used, the emulsion showed high stability, without appearing any precipitation. After a series of experiments, varying the ratio of aliphatic to aromatic diisocyanate, it was found that the emulsion with a ratio near to 1:1 (aliphatic to aromatic diisocyanate) had highest stability. The improved stability could be explained by the much lower reactivity of aliphatic diisocyanate compared to aromatic one. The reaction between diisocyanate and diol (and water) was strongly suppressed at the beginning of polymerization, so that diisocyanates had enough time to be homogenously dispersed in the emulsion. Based on this system, polyurethane particles with high porosity were prepared by dropwise addition of diisocyanates into an emulsion containing droplets of diol and water. The porous structure was formed by releasing carbon dioxide from the reaction between water and diisocyanate.

In the study, these questions seat in the background: how the conditions (the amount of water and the kinds of catalysts) influenced the formation of porosity. After a serial of experiments, it was found when the amount of water was about three times higher as diol, particles was strongly porous. By the study on the influence of catalysts on the porosity, a series of catalysts with different selectivity to water and diol were investigated. The results showed that balancing the reaction of diisocyanate with diol and with water played an important role for forming homogenous pores. When only a catalyst with a high selectivity to water was used, the particles collapsed. Probably the carbon dioxide was released too early, while the pore wall was still soft. With only a catalyst with a high selectivity to diol, many particles were broken into two parts. The pore wall would have already too high modulus, while carbon dioxide was released, so that the wall could not be reformed. A mixture ratio 1:1 of these two kinds of catalysts showed the particles with high homogenous porosity.

During the study, an interesting phenomenon was observed: when diisocyanates was too slowly dropped into the emulsion, thin skin was formed on the surface of the particles. It could be caused by the side reaction between diisocyanate and urethane groups, because urethane is a relatively reactive functional group. To prevent this side reaction, another method was developed: at first two emulsions were separated prepared, one with diisocyanate as dispersed phase and one with diol. Both emulsions were mixed together in such a way that the diisocyanate had an excess compared to diol, in order to obtain polymer chains with NCO groups in the particles. The obtained particles were washed with hydrous THF in which water could diffuse into the particles and reacted with the NCO groups, releasing carbon dioxide. With this method, highly porous particles without formation of any skin were obtained. It meant that water did diffuse into the particles and react with the NCO end groups. In addition, the porous structure was much more homogenous than by the first method. The influence of the ratio between diisocyanate and diol on the porosity was also studied. An optimal ratio was found at 8 : 5.

With a similar method, polyurea particles were prepared: water and diisocyanate as monomers were used to form separated emulsions which were later mixed together. Highly porous particles with an average size of only 500 nm were obtained, which were much smaller than the polyurethane ones (with a size ranging from 1 µm to 3 µm).

Furthermore the porous polyurethane particles were investigated as a filler material for polyurethane (PU) and polystyrene (PS) composites. Homogenous distribution of particles in PU matrices was observed, due to the strong interaction of hydrogen bonds between urethane groups. The mechanical properties of polyurethane composites were also studied by varying the concentration of the particles. The tensile strength considerably increased with an increasing concentration of particles. In contrast, a lot of aggregates of particles in PS matrices were observed, probably due to the weak interaction between the particles and PS. Here the tensile strength was not altered in a noticeable way by varying the concentration of the particles.

Another application of porous polyurethane particles was performance as catalyst carrier for polyethylene (PE) polymerization. A zirconium phenoxyimine catalyst and methylaluminoxane (MAO) were successfully immobilized on the porous particles. The activity of the catalyst was studied at 50°C and 70°C. It was found that the activity at 70°C was two times higher ($6x10^3$ Kg.mol $^{-1}$.h $^{-1}$.bar $^{-1}$) than at 50°C ($6x10^3$ Kg.mol $^{-1}$.h $^{-1}$.bar $^{-1}$). The particles sizes increased to about 1970% at 70°C, but at 50°C only 450%. In addition, the diagram of particle size growth versus time showed that at 70°C the particles quickly reached maximum size at beginning of the polymerization. The similar phenomena were also reported in the study where soft swollen polystyrene particles (PS) were used as catalyst carrier [2]. The explanation was that: the catalyst and MAO were adsorbed inside of the soft swollen particles, not only on the surface. Hence the amount of active centres of the catalyst in the particles was dramatically increased. The polymerization ratio reached immediately maximum at the beginning. Porous particles have more surface area which could adsorb more catalyst and MAO and have more active centres of catalyst accessible to monomers. In other hand, the porous structure could make easier for catalyst and MAO to diffuse into the particles. The different activity of the catalyst at 70°C and 50°C could be explained by kinetic movement.

In this study, polyurethane and polyurea particles with homogenous porosity were prepared in a non-aqueous emulsion with PI-b-PMMA as emulsifier. The obtained porous polyurethane particles showed good compatibility with polyurethane matrix. The mechanical strength of the polyurethane composite was strongly increased. In addition, the porous particles also showed strong interaction with a zirconium phenoxyimine catalyst for polyethylene (PE) polymerization. The catalyst was successfully immobilized in them and had high activity. In this work, many other applications of the porous particles were not studied yet, for example separating process, drug delivery and scaffold for medicine. Especially, when the porous particles are for medicinal application, a lot of work should be done, because some of chemicals used in this study have high toxicity, like MDI, HMDI and DMF.

6.2 Dispersions of polymer particles with perylene dye for SMFD study

At the beginning of this study, a few of terms should be decided at first: which dispersions of polymer particles were investigated in this study? Two dispersions of polymer particles from radical polymerization and polyaddition were chosen, because both polymerizations have very different mechanisms. PMMA and PU are typical polymers from them. The next question was how to make polymer chains visible under SMFD. Polymer chains in the particles must have dye molecules which should be detected via SMFD. Perylene dye, with double bonds (for PMMA particles) and OH (for PU particles) groups, was chosen and could act as monomers. Perylene dye has very high fluorescence activity and stability. The third question was which emulsion was suitable to prepare the dispersions. Perylene dye has high solubility in DMF. It was very important for the stability of a emulsion and the homogenous distribution of dye molecules in the particles. Hence one emulsion with DMF as dispersed phase was chosen, in which PI-b-PMMA was emulsifier.

In this study, the prepared particles were studied with several steps, in order to answer following questions:

1. Whether all of particles obtained dye molecules.
2. The amount distribution of dye molecules in the particles.
3. How dye molecules are distributed inside of one particle.
4. How the supposed conformation and distribution of polymer chains in particles.

The prepared PMMA particles had a relatively homogenous size distribution, ranging from 50nm to 200nm. The particles were at first detected by dark-field microscopy and fluorescence microscopy to know whether all of particles obtained dye molecules. It was found that some of particles did not obtain any ones and some over tens. About 55% particles were with dye molecules from 2 to 10. One particle with 8 dye molecules was chosen for detection of SMFD. The dye molecules were homogenously distributed in a circle with a diameter of 400 nm (Figure 1 left). The distance between the neighbourhood dyes was about 100 nm. From the results it could conclude that the polymer chains were homogenously distributed inside of particles. The orientation of the eight dye molecules varied from 40 degree to 86 degree to Z axis and 177 degree to 34 degree to X axis, suggesting that no aggregates of dye molecules were built and the polymer chains freely twisted in the particles. When all of dye molecules were bound together with one curve, it looked like a random coil (Figure 1 left), meaning the polymer chain had a flexible conformation (Figure 2-I). This supposition is suitable to the chemical nature of PMMA chains which are relatively flexible because of weak interaction between methylmethacrylate groups.

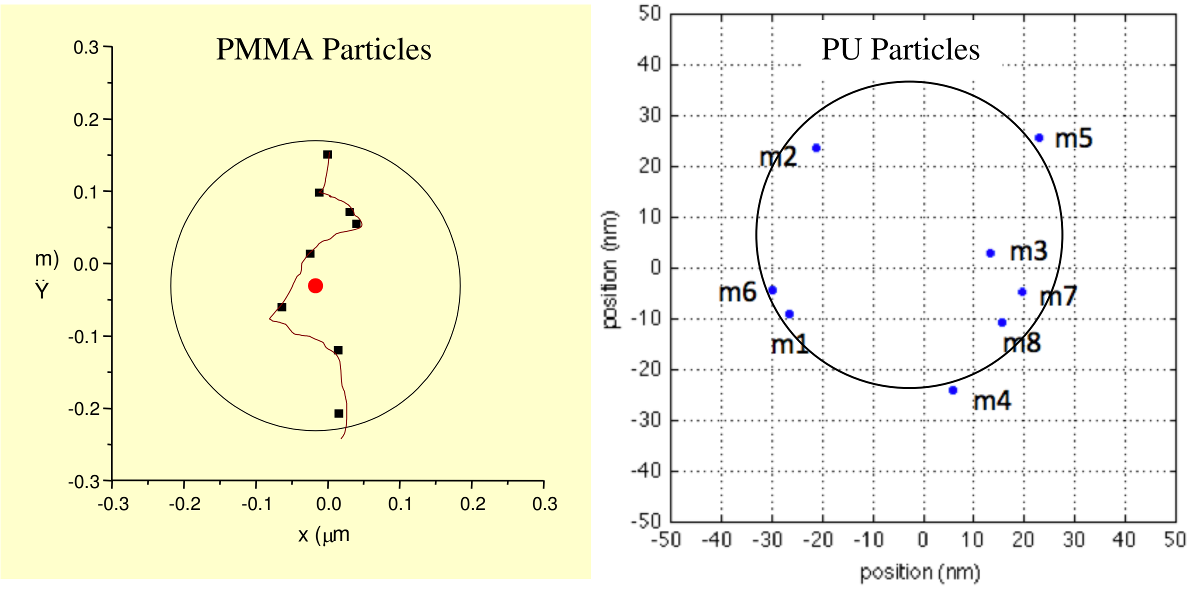

Figure 1. The distribution of dye molecules in one PMMA particle left.
The distribution of dye molecules in one PU particle right.

The prepared PU particles with dye molecules had homogenous size distribution, ranging from 150nm to 200nm. The overlook of amount distribution of dye molecules in all of PU particles was not investigated because of personal organisation. One particle with 8 dye molecules was detected via SMFD, The dyes were mostly distributed on the range of a circle with a size of 60 nm (Figure 1 right), different to PMMA particles in which dyes were homogenously distributed inside of a circle. It could propose that the polymer chains were mostly distributed on the surface of the particle. The dyes molecules were freely orientated from 4 degree to 82 degree to Z axis and from 7 degree to 161 degree to X axis. It meant that dye molecules did not build aggregates in the particles and the polymer chains freely twisted in the particles. When all dye molecules were bound with a curve, it looked like a toroid (Figure 1 right), suggesting a rigid polymer chains. This result was suitable to the chemical nature of polyurethane chains: the polymer chains are relatively stiff because of strong interaction between urethane groups (Figure 2-III).

The mechanism of radical polymerization and polyaddition are very different: in radical polymerization each polymer chain has only one reactive end and the chance that monomers react with this end is controlled by their reactivity. In polyaddition, monomers are polymerized to oligomers at first step in which all of monomers are statistically distributed in the oligomers. Hence it was expected that the distribution of dye molecules in PU particles should be more homogenous than in PMMA. From the observation via SMFD, it was not found obvious difference between both kinds of particles. Dye molecules were all relatively homogenously distributed in them.

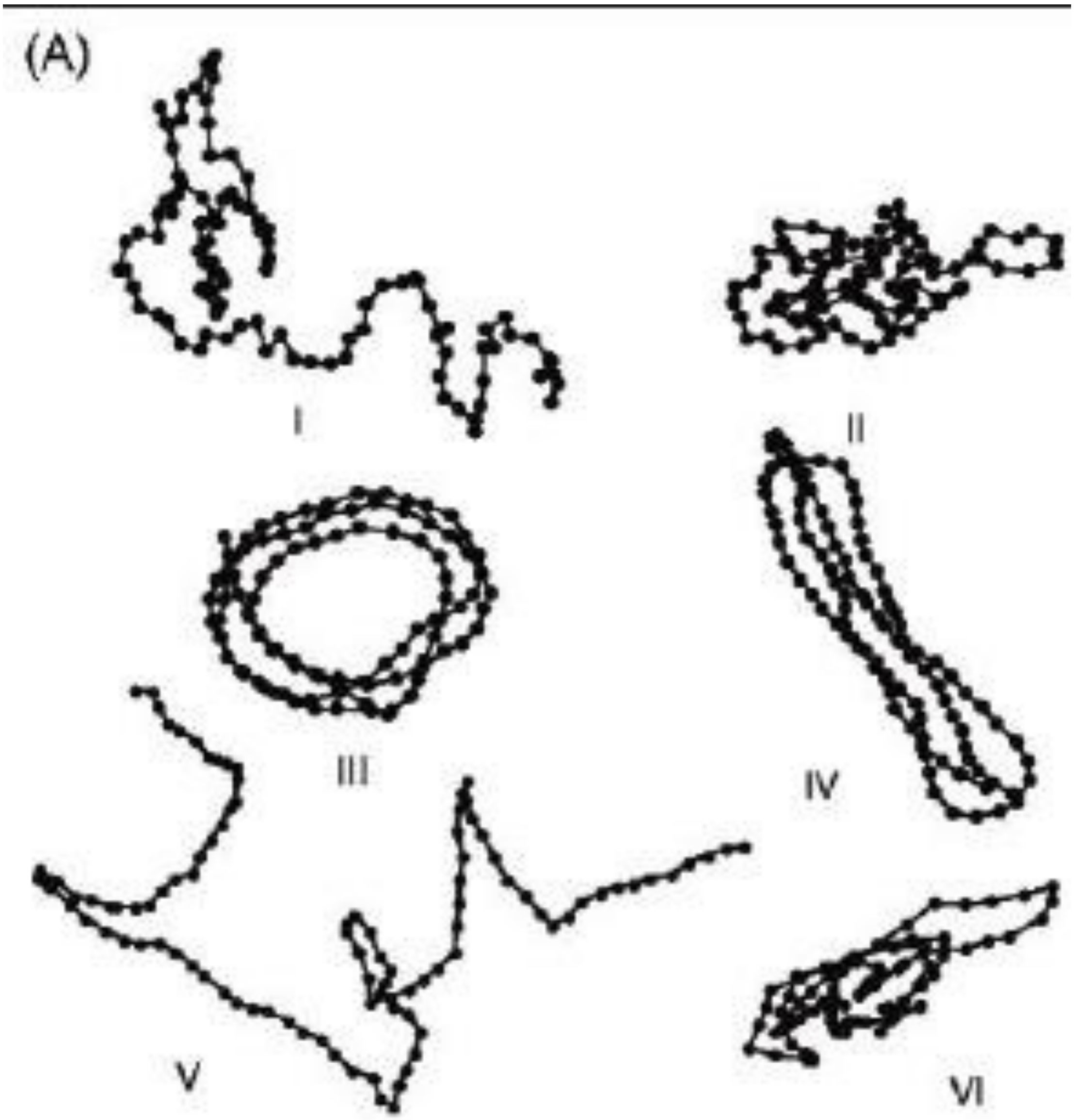

Figure 2. The typical conformations of polymer chains (I, random coil; II, molten globule; III, toroid; IV, rod; V, defect-coil; and VI, defect-cylinder) [3].

In this work, SMFD was successfully used to investigate distribution and orientation of dye molecules in polymer particles from one emulsion. With the information, the distribution and conformation of polymer chains were supposed. This study could be extended by investigation of other polymer particles from ionic polymerization or polycondensation via SMFD.

6.3 Dispersions of graphene nanosheets for polymer composites

The goal of this work was to disperse graphene sheets in organic solvents with low toxicity. PI-b-PMMA with conjugated bonds, similar to chemical structure of graphene, could stabilize graphene in dispersions.

This study consisted of three parts:

1. Preparation of graphene nanosheets.
2. Preparation of non-aqueous dispersions of graphene sheets by using PI-b-PMMA as stabilizer
3. Preparation of polymer composites with the dispersions of graphene nanosheets

Graphene nanosheets were prepared by thermal exfoliation of graphene oxide foam from freeze-drying, a method to produce porous material in biology. The graphene oxide foam had extremely loose structure without any aggregates. At 1000 °C the foam was exfoliated to graphene nanosheets with a thickness about 3 nm (the special surface of the nanosheets was about 700 m^2/g). This value was comparable with the best results via thermal exfoliation reported in the literature [4, 5]. To deeply understand the thermal exfoliation process of graphene oxide foam, the influence of temperature and heating rate were studied. It was found that with a heating rate up to10 °C/min and a temperate above 550 °C the obtained graphene nanosheets had highly surface area (about 700 m^2/g).

Non-aqueous dispersions of the graphene nanosheets were prepared by use of amphiphilic copolymer PI-b-PMMA as stabilizer. Organic solvents with low toxicity like THF and hexane were focused in this work. It was found that the dispersions in THF kept stabile for a few of months. The stability of the dispersions was tested by centrifugation at 1000 rpm for 30 min. The concentration of graphene nanosheets was still over 0.1 mg/ml after centrifugation. To understand the stabilizing mechanism, graphene nanosheets were dispersed in a PMMA solution in THF. The nanosheets could be not stabilized, meaning the PI block was anchored on the surface of the sheets, and PMMA block stretched into THF as steric hindrances in the dispersion.

The stable dispersion was continuously used to prepare polymer composites. Two conventional polymers PMMA and PS were chosen. In SEM images it was observed that graphene nanosheets were homogenously distributed in both matrices without any aggregates. At about 3 wt% of graphene nanosheets for PS and 4 wt% for PMMA, the composites showed a jump of electric conductivity for 10^5 S/cm, called as percolation threshold where graphene nanosheets formed a continuous conducting network in the matrix. The influence of concentration of nanosheets on electric, thermal and mechanical properties of the composites was also studied in this study. The electric conductivity was increased with increasing concentration. The decomposition temperature was shifted to higher temperature, when the concentration was increased. The mechanical strength was measured from room temperature to 200 ºC. It was found the tensile strength was not strong changed. It could be explained by the defect structure of graphene nanosheets through the oxidation process (preparation of graphene oxide).

In this study, PI-b-PMMA showed strong interaction with graphene nanosheets and successfully stabilized them in THF, an organic solvent with low toxicity. The modified graphene nanosheets had good compatibility with polyurethane and polystyrene matrices. Especially the electric property was strongly improved with low concentration. This work could be extended to disperse other carbon materials, like carbon black and nanotube in THF or other organic solvents with low toxicity. On the other hand, PMMA block could be changed with other block, so that the modified graphene nanosheets could have compatibility with other polymer matrices.

Reference

1. Müller, K., Nicht-waessrige emulsionspolymerisationen, in Chemie und Pharmazie der Johannes-Gutenberg Universitaet 2008: Mainz.
2. Naundorf, C., et al., Hard versus Soft Materials as Supports for Metallocene and Post-Metallocene Catalysts. Macromolecular Reaction Engineering, 2009. **3**(8): p. 456-466.
3. Barbara, P.F., et al., Single-molecule spectroscopy of conjugated polymers. Accounts of Chemical Research, 2005. **38**(7): p. 602-610.
4. Boehm, H.P., et al., Das Adsorptionsverhalten Sehr Dunner Kohlenstoff-Folien. Zeitschrift Fur Anorganische Und Allgemeine Chemie, 1962. **316**(3-4): p. 119-127.
5. Stankovich, S., et al., Synthesis of graphene-based nanosheets via chemical reduction of exfoliated graphite oxide. Carbon, 2007. **45**(7): p. 1558-1565.

Chapter 7. Experimental Part

7.1 Methods

Gel Permeation Chromatography (GPC)

Gel permeation chromatography experiments were performed by equipments MZ-Gel SDplus 10E6, 10E4 on 500 columns. In order to detect the signals, differential refraktometers and a UV-detector from company Waters, ERC, Rheodyne and Soma were used. Before the measurements, all of samples were cleared with a Teflonfilter with pore size 0.2 µm.

Scanning Electron Microscopy (SEM)

Scanning electron microscopy was performed on a Gemini-1530-Microscopy from company Zeiss. The acceleration voltages were between 0.75 and 3 kV.

Transmission Electron Microscopy (TEM)

Electron microscopy was performed with a Tecnai-F20-Microscopy from company FEI. The samples were diluted in THF and then applied to a 400 mesh carbon-coated copper grid and left to dry.

Atomic force microscopy (AFM)

Atomic force microscopy was performed by using NanoScope-3a-3D microscopy. The samples were dropped on the substrates and then dried in a fume hood. After that the substrates were dried in vacuum for 12 h.

Dynamic Light Scattering (DLS)

The particle sizes were measured by Malvern Zetasizer 3000 photocorrelation spectroscopy at a fixed scattering angle of 90°.

Nuclear Magnetic Resonance (NMR)

Proton nuclear magnetic resonance (^{1}H-NMR) spectra were recoded on a Bruker Avance 250 spectrometer at 250 MHz in deuterated solvents using TMS as internal standard.

Infrared spectroscopy (IR spectroscopy)

The FT-IR measurements were performed to check for the urethane and urea bonds in porous polyurethane particles in a Nicolet 730 FT-IR spectrophotometer using a signal reflection ATR-crystal from company Thermo-Spectra-Tech.

Differential Scanning Calorimeter (DSC)

DSC measurements were carried out with samples of about 10 mg on a Mettler Digital-Scanning-Calorimeter 300. The samples were protected with nitrogen. Cooling and heating rates were 1 and 10 ^{o}C/min.

Thermal gravimetric analysis (TGA)

Gravimetric measurements were performed with a Kern RH 120-3 gravimeter to measure the thermal stability of nanocomposites.

Ultrasonication

Emulsion or homogenization was performed with a Brandelin Sonorex RK255H - W640 sonifier.

Dialysis

Graphene oxide was dialyzed to remove the salt and acids until the PH value is between 6 and 7. The membranes were purchased from Millipore.

Plasma-etching

The plasma-etching was performed on an OXFORD PLASMALAB 80PLUS. The Camber temperature was set to 20 ^{o}C, the pressure 80 mTorr and the O_2 flow flowed at 30. The RF power was 1 W and ICP forward power was 100 W. The silicon substrates are 3 inch diameter and have a specific resistance bigger than 1 Ohm/cm.

Ultraviolet-Visible Spectroscopy (UV-Spectroscopy)

UV analyses were carried out with a Perkin Elmer UV/Vis spectrometer Lambda 16. The dispersions of graphene nanosheets in THF were checked by using wavelength between 300 nm to 800 nm.

X-ray Diffraction (XRD)

Wide-angle diffraction patterns of graphene oxide, graphene nanosheets and graphite were obtained at room temperature, using nick-filtered Cu Kα radiation. Slightly pressed flat samples were mounted perpendicularly to the primary X-ray beam. A flat-film camera with a sample-film distance of 90 nm was used to record the reflections. Optical density data were collected from the photographically obtained patterns using a linear scanning microdensitometer LS20.

Mechanical properties measurements

The dynamic mechanical properties of the nanocomposites were determined using a dynamic mechanical analyzer (RMS 800, Rheometric Scientific). The measurements were carried out with a bending mode at a heating rate of 1ºC/ min between 0 ºC to 100 ºC. The nanocomposites film, 5 mm wide and 23 mm long strips with thickness from 200 µm to 250 µm, were clamped between film fixtures of the RMS 800. For the measurement from 100 ºC to 200 ºC, the samples were pressed to tablets with diameter 6 mm and thickness 0.6 mm.

Figure 1. The equipment of RMS 800 from Rheometric Scientific.

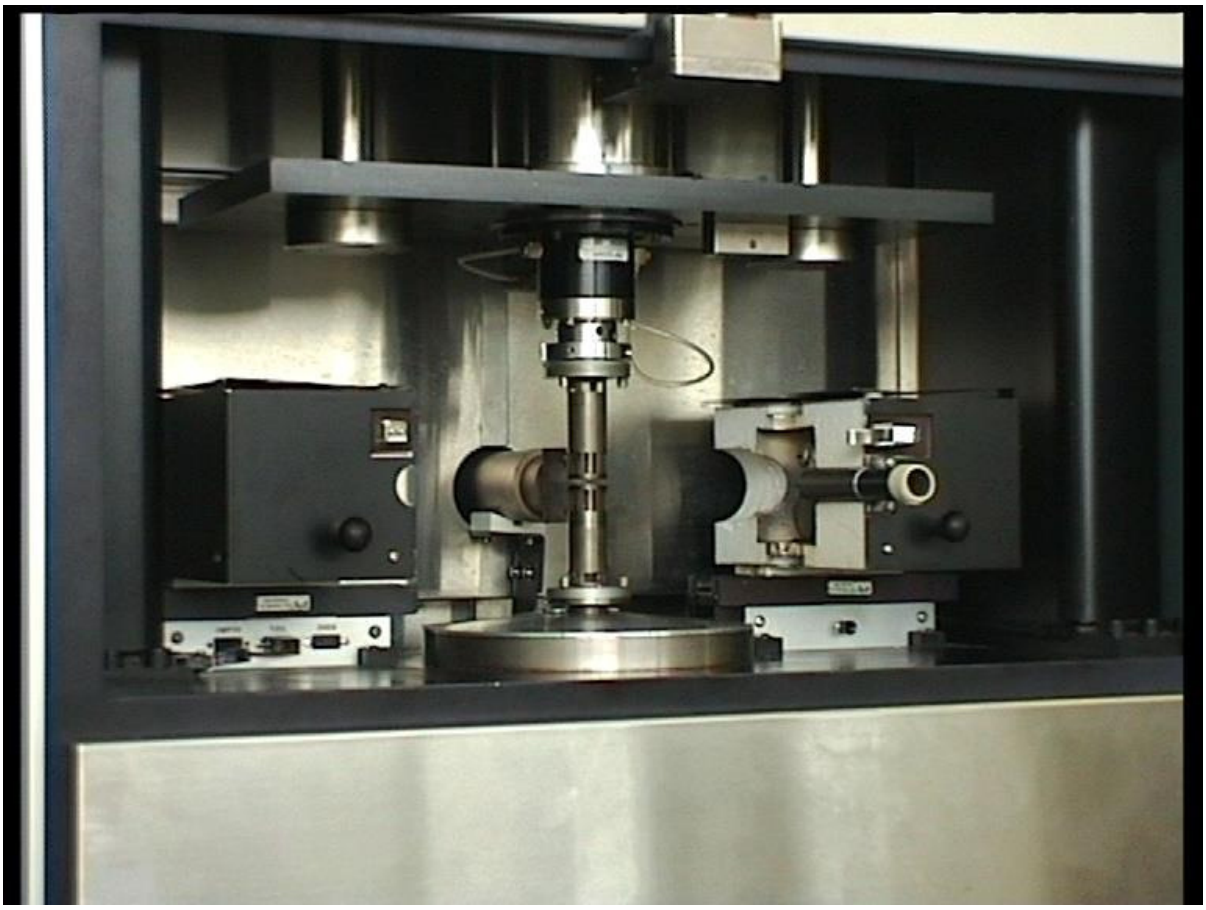

Figure 2. A near record of RMS 800 from Rheometric Scientific

Electric properties measurements

Measurements of frequency and temperature dependence of dielectric constant and electric conductivity of the graphene nanocomposites were done regarding a two-contact method with a Novocontrol (High Resolution Dielectric Analyzer). A round shape (d = 20 mm) sample was placed in the central part of the measurement cell.

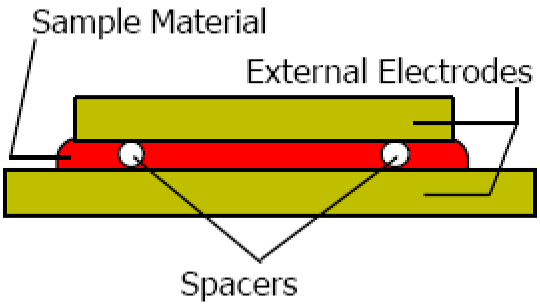

Figure 3. A two-contact method with a Novocontrol (High Resolution Dielectric Analyzer).

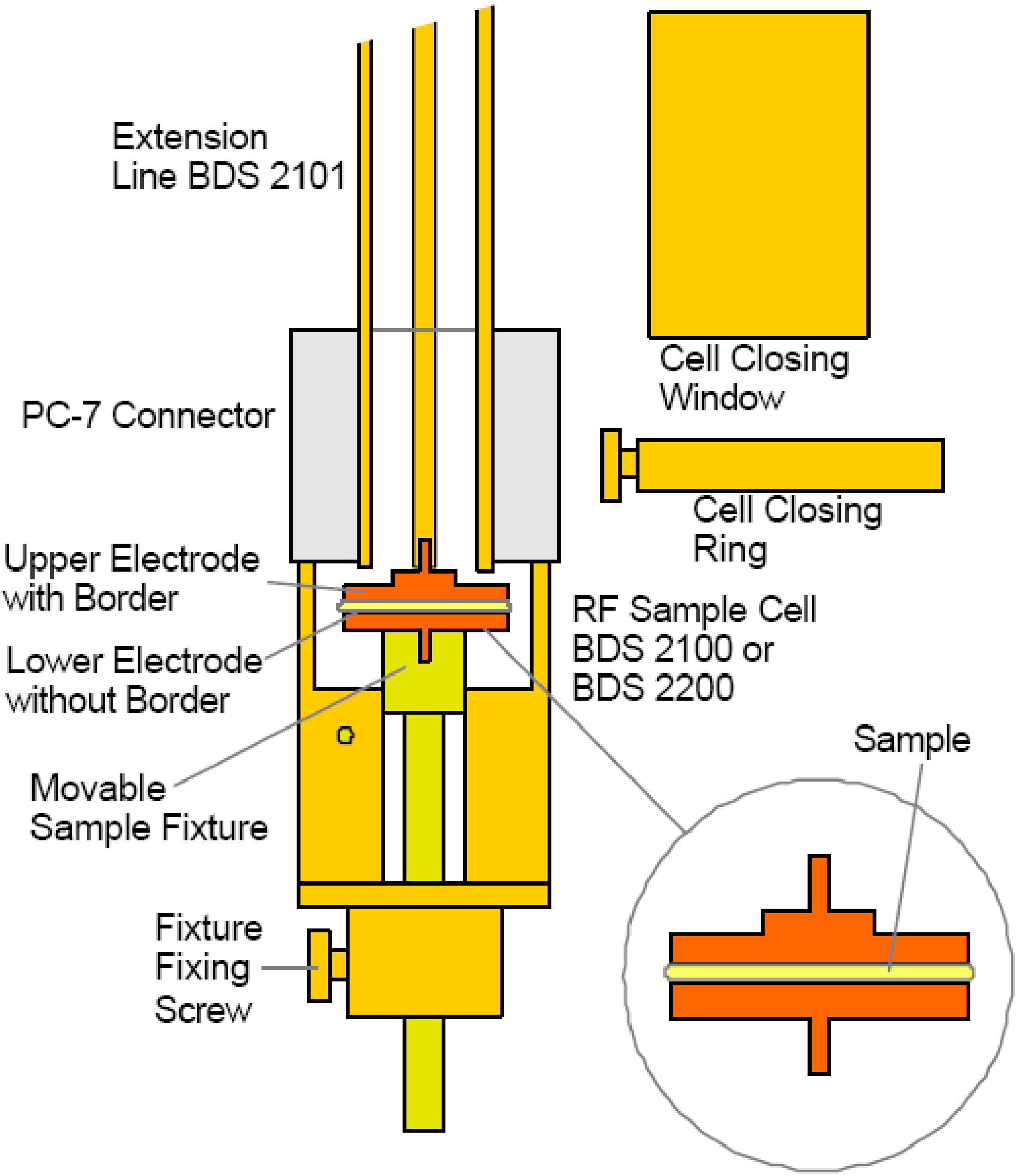

Figure 4. Mounting of Electrodes in the sample Cell

7.2 Synthesis of porous polyurethane particles

7.2.1 Preparation of stabile non-aqueous emulsion (Sec 3.2)

Materials

The monomers 4,4'-methylene diphenyl diisocyanate (MDI) 98% purity, 1,6-hexane diisocyanate (HMDI) 95% purity and 1,4-bis(hydroxymethyl) cyclohexane (BHC) 99% purity were purchased from Sigma-Aldrich and used as received. Emulsifier Polyisoprene-block-polymethylmethacrylate (PI-b-PMMA) copolymer was prepared using a sequential anionic polymerization technique. The recipe was described elsewhere [1]. Catalyst triethylene diamine (TEDA) was received from Sigma-Aldrich. Anhydrous solvents n-hexane (Acros Organics), Dimethylformamide (DMF) (Aros Organics) and Tetrahydrofuran (THF) (Aros Organics) were dried over molecular sieves (4 Å). All the chemicals were stored in glove box under nitrogen.

Preparation of a stable emulsion

Emulsifier PI-b-PMMA (250 mg) and continuous phase n-hexane (12 ml) were stirred magnetically at room temperature, until a stable dispersion was formed. A mixture consisting of diol BHC, catalyst TEDA (50 mg, 0.45 mmol) and DMF (0.5 g, 6.5 mmol) was used as dispersed phase and added dropwise to the n-hexane/copolymer dispersion. To form an emulsion, the mixture was stirred at room temperature for two hours and treated by ultrasound for 10 min using a Bandelin Sonorex RK255H ultrasonic bath, operating at 640 W. Subsequently, the mixture of MDI and HMDI in DMF (0.5 g, 6.5 mmol) was added dropwise to the emulsion. The polyaddition continuously ran for 8 h at 40 °C. Then the emulsion was place in a separating funnel with n-hexane in order to stop the polymerization. The collected particles were washed twice with n-hexane. The component for the polyaddition and the analytical data of the polyurethane particles were listed in Table 1.

Dispersion	MDI (mmol)	HMDI (mmol)	Diol (mmol)	Catalyst (mg)	Particle (nm)	Yield (%)
YZ003	0.5	2.5	3	10	200-400	93
YZ133	0.5	2.0	2.5	10	80	98
YZ135	0.5	0.5	1	10	50-150	95
YZ140	0.5	0.25	0.77	10	200	85

Table 1. Component for the polyaddition and analytical data of the polyurethane particles

7.2.2 Preparation of polyurethane porous particles via fission/fusion method (sec 3.3)

Materials

In this preparation, one more catalyst was used here, Bis[2-(N,N-dimethylamino)ethyl] ether (BDAEE), which was purchased from Sigma-Aldrich and used as received. The other chemicals were similar to above (sec 6.2.1).

Preparation of porous polyurethane particles

At first, two emulsions with water or diol as dispersed phase were prepared: Emulsifier PI-b-PMMA (250 mg) and continuous phase n-hexane (12 ml) were stirred magnetically at room temperature, until a stable dispersion was formed. A mixture consisting of diol BHC, catalyst TEDA (50 mg, 0.45 mmol) and DMF (0.5 g, 6.5 mmol) was used as dispersed phase and added dropwise to the n-hexane/copolymer dispersion. The emulsion was stirred at room temperature for two hours and treated by ultrasound for 10 min using a Bandelin Sonorex RK255H ultrasonic bath, operating at 640 W. A mixture consisting of water, catalyst BDAEE (50 mg, 0.31mmol) and DMF (0.5 g, 6.5 mmol) was used as dispersed phase and also added dropwise to another n-hexane/copolymer dispersion. Subsequently, the two dispersions were mixed together by stirring for two hours and treated by ultrasound for 10 min. Then, a mixture of MDI and HMDI in DMF (0.5 g, 6.5 mmol) was added dropwise to the mixed emulsion. The polyaddition ran for 8 h at 40 ºC. Then the emulsion was place in a separating funnel with n-hexane in order to stop the polymerization. The collected particles were washed twice with THF. The component for the polyaddition and the analytical data of the polyurethane particles were listed in Table 2.

Dispersion	Water (mmol)	Diol (mmol)	MDI (mmol)	HMDI (mmol)	Particle (µm)	Yield (%)	Porosity
YZ134	1	1	1	1	0.1	97	No
YZ136	3	1	2	2	2-2.5	92	Yes
YZ169	5	1	3	3	1.5-2	98	inside
YZ143	10	1	5.5	5.5	1-3	98	Yes
YZ144	20	1	10.5	10.5	2	95	Yes

Table 2. The component for the polyaddition and the analytical data of the polyurethane particles

7.2.3 Preparation of polyurethane porous particles via combination method (sec 3.4)

Materials

In this preparation, catalyst Bis[2-(N,N-dimethylamino)ethyl] ether (BDAEE) was purchased from Sigma-Aldrich and used as received. The other chemicals were similar to above (6.2.1).

Preparation of porous particles

At first, tow emulsions were prepared: emulsifier PI-b-PMMA (250 mg) and continuous phase n-hexane (12 ml) were stirred magnetically at room temperature, until a stable dispersion was formed. A mixture consisting of diol BHC, catalyst TEDA (50 mg, 0.45 mmol), catalyst BDAEE (50 mg, 0.31mmol) and DMF (0.5 g, 6.5 mmol) was used as dispersed phase and added dropwise to the n-hexane/copolymer dispersion to form an emulsion. A mixture consisting of MDI/HMDI (1:1) and DMF (0.5 g, 6.5 mmol) was used as dispersed phase and added dropwise to another n-hexane/copolymer dispersion to form an emulsion. The both emulsions were stirred for two hours and treated with ultrasound for 10 min. Then they were mixed together by treatment with ultrasound for 10 min using a Bandelin Sonorex RK255H ultrasonic bath, operating at 640 W. Subsequently, they were stirred for 8 h at 40 °C. Then the emulsion was place in a separating funnel with n-hexane in order to stop the polymerization. The collected particles were washed twice with THF. This dispersion stayed at room temperature for two days. The component for the polyaddition and the analytical data of the polyurethane particles were listed in Table 3.

Sample	MDI/HMDI (mmol)	Diol (mmol)	Particle (µm)	Yield (%)
YZ205	6	2.5	1	80
YZ235	5	2.5	1	92
YZ168	4	2.5	2.5	98
YZ197	3	2.5	2.0	91

Table 3. The component for the polyaddition and the analytical data of the polyurethane particles

7.2.4 Preparation of polyurea porous particles (sec 3.5)

Materials

In this preparation, catalyst Bis[2-(N,N-dimethylamino)ethyl] ether (BDAEE) was purchased from Sigma-Aldrich and used as received. The other chemicals were similar to above (6.2.1).

Preparation

At first tow emulsions were prepared: emulsifier PI-b-PMMA (250 mg) and continuous phase n-hexane (12 ml) were stirred magnetically at room temperature, until a stable white solution was formed. A mixture consisting of water, BDAEE (50 mg, 0.31mmol) and DMF (0.5 g, 6.5

mmol) was used as dispersed phase and added dropwise to the n-hexane/copolymer dispersion to form an emulsion. A mixture consisting of MDI/HMDI (1:1) and DMF (0.5 g, 6.5 mmol) was used as dispersed phase and also added dropwise to another n-hexane/copolymer dispersion to form an emulsion. The both emulsions were stirred for two hours at room temperature. Then they were mixed by treatment with ultrasound for 10 min using a Bandelin Sonorex RK255H ultrasonic bath, operating at 640 W. Subsequently, they were stirred for 8 h at 40 °C. Then the emulsion was place in a separating funnel with n-hexane in order to stop the polymerization. The collected particles were washed twice with THF. The component for the polyaddition and the analytical data of the polyurea particles were listed in Table 4.

Sample	MDI/HMDI (mmol)	Water (mmol)	Particle (nm)	Yield (%)
YZ98	1	1	200	98
YZ99	1.1	1	50-200	97

Table 4. The component for the polyaddition and the analytical data of the polyurea particles.

7.2.5 Polymer composites with polyurethane porous particles (sec 3.6)

Materials

The monomers für polyurethane matrix (polyol Desmophe 680 M = 770 g/mol) and (polyisocyanate N3390 M = 214 g/mol) were used as received from BASF. Polystyrene (molecular weight 18000 g/mol PD = 1.1) as matrix was purchased from Fluka. THF was used as received from Aros Organics. Porous polyurethane particles were from sample YZ168.

Preparation of polyurethane composites

Monomers Desmophe 680 and N3390 were mixed together in 1ml THF with a weight ratio 1:3.2 for 30 min. Porous particles were then added into the mixture. The amount of particles was 3.1 wt%, 5 wt% and 7.8 wt% of monomers weight. The dispersion was stirred for 8 h at room temperature and treated by ultrasound for 10 min in ice bath. Subsequently, it was poured into a mould which was continuously put in withdrawal in order to vapor THF without forming bubbles in the composites. After one day, the most of THF was removed and the mould was put in oven with vacuum for 8 h with 100 °C in order to polymerize the monomers polyol Desmophe 680 and polyisocyanate N3390.

Preparation of polystyrene composites

The polystyrene with molecular weight 18000 g/mol was mixed with porous particle in 1 ml THF. The weigh ratios of particles were 4.8 wt%, 7.8 wt% and 10 wt%. The dispersions were stirred for 8 h at room temperature and treated by ultrasound for 10 min in ice bath. They were poured into a mould which was continuously put in withdrawal in order to vapor THF without forming bubbles in the composites. After one day, the most of THF was removed and the mould was put in Vacuum for 8 h in order to remove the residual THF.

7.2.6 Porous particles used as catalyst carrier (sec 3.7)

Materials

Porous particles were from the sample YZ168. Anhydrous toluene was used as received from Aros Organics.

Preparation

Polyurethane porous particles were at first dried for 12 hours under reduced pressure. Once the sample was moved into a glove box, 300 mg of polyurethane porous particles were redispersed in 5 ml of toluene. The solution was mechanically stirred overnight to guaranty complete redispersion of the particles. A solution of MAO (3 ml, 1.5 M, 10 wt% in toluene) was added to the redispersed particles. A minimum of three hours under mechanical stirring was necessary to support MAO on the particles. The supernatant toluene containing was removed via syringe, and the particles were dried under reduced pressure for 24 hours. Immobilization of the catalyst on the porous particles was carried out as follows: inside of the glove box, 0.03 mmol of phenoxy-imine catalyst was dissolved in 5 ml of toluene. The catalyst solution was mixed with the MAO pre-activated porous particles, and then the solution was stirred for 3 hours. The supernatant solution was removed via syringe, and the remaining catalytically active porous particles were dried under reduced pressure for 24 hours and further moved into the glove box. The collected particles were then ready for their use towards ethylene polymerization. A previously heated (50 °C or 70 °C) and evacuated (1 hour) video microscopy reactor with a capacity up to 50 ml was transferred to the glove box. Onto a silver plate holder a small sample (about 2 mg) of supported particles was carefully put, the sample holder was incorporated into the video microscopy reactor. After sealing the reactor, the system was transferred into the ethylene gas line, which was attached to the video microscopy set up, equipped with a temperature controller. Once the desired polymerization temperature was reached, the flow of ethylene was set and the polymerization was allowed to begin. After one hour of polymerization, the reactor was opened to the atmosphere to release the ethylene gas and quench the catalyst. No further manipulation was necessary and the collected polymer was characterized by conventional techniques.

7.3 Synthesis of polymer particles loaded with PDI dye (sec 4.2 and 4.3)

Materials

The monomers 1,6-hexane diisocyanate (HMDI) 95% purity,
1,4-bis(hydroxymethyl)cyclohexane (BHC) 99% purity and methyl methacrylate (MMA) 99% purity were purchased from Sigma-Aldrich and used as received. MMA was distilled under reduced pressure prior to use. Emulsifier Polyisoprene-block-polymethylmethacrylate (PI-b-PMMA) copolymer was prepared by using a sequential anionic polymerization technique. The recipe was described elsewhere [1]. The perylene dye with hydroxyl groups and double bonds were prepared by Dr Lui. The recipe was described elsewhere [2] . Catalyst triethylene diamine (TEDA) was received from Sigma-Aldrich. 2,2´-azobis(4-methoxy-2,4-dimethylvaleronitrile) (V-70) was purchased from Wako Pure Chemical Industries. Anhydrous solvents n-hexane (Acros Organics) and DMF (Aros Organics) were dried over molecular sieves (4 Å). All the chemicals were stored in glove box under nitrogen.

Preparation of polyurethane particles loaded with PDI dye

At first two emulsions were prepared with diol or PDI dye as dispersed phases: Emulsifier PI-b-PMMA (250 mg) and continuous phase n-hexane (12 ml) were stirred magnetically at room temperature, until a stable dispersion was formed. A mixture consisting of BHC (72 mg, 0.5 mmol), catalyst TEDA (50 mg, 0.45 mmol) and DMF (0.5 g, 6.5 mmol) was used as dispersed phase and added dropwise to a n-hexane/copolymer dispersion. A mixture consisting of PDI with hydroxyl groups (the amount was calculated down), catalyst TEDA (50 mg, 0.45 mmol) and DMF (0.5 g, 6.5 mmol) was used as dispersed phase and also added dropwise to another n-hexane/copolymer dispersion. The two emulsions were mixed by stirring for 2 h and treated with ultrasound for 10 min, using a Bandelin Sonorex RK255H ultrasonic bath, operating at 640 W. A mixture of HMDI (84 mg, 0.5 mmol) and DMF (0.5 g, 6.5 mmol) was slowly added into the emulsion and stirred for 8 h at room temperature. Then the emulsion was place in a separating funnel with n-hexane in order to stop the polymerization. The collected particles were washed twice with n-hexane.

Preparation of PMMA particles loaded with PDI

At first two emulsions were prepared with diol or PDI dye as dispersed phases: Emulsifier PI-b-PMMA (250 mg) and continuous phase n-hexane (12 ml) were stirred magnetically at room temperature, until a stable dispersion was formed. A mixture consisting of MMA (50 mg, 0.5 mmol) and DMF (0.5 g, 6.5 mmol) was used as dispersed phase and added dropwise to an n-hexane/copolymer dispersion. A mixture consisting of PDI with double bounds (the amount was calculated following) and DMF (0.5 g, 6.5 mmol) was used as dispersed phase and also added dropwise to another n-hexane/copolymer dispersion. The two emulsions were mixed by stirring for 2 h and treated with ultrasound for 10 min using a Bandelin Sonorex RK255H ultrasonic bath, operating at 640 W. A mixture of V-70 (50 mg, 0.16 mmol) and DMF (0.5 g, 6.5 mmol) was added into the emulsion and stirred for 1 h at room temperature. After treatment by ultrasound for 10 min, the radical polymerization was carried out by stirring for 8 h at room temperature. Then the emulsion was place in a separating funnel with n-hexane in order to stop the polymerization. The collected particles were washed twice with n-hexane.

Calculation of the amount of PDI dye for 1 mmol polymer particles

At first the amount of particles was determined where the weight of 1 mmol particles and the density were assumed as pure particles without PDI dye.

$$N_{PMMA} = \frac{M_{PMMA}}{m_{PMMA}} = \frac{M_{PMMA}}{v_{PMMA} d_{PMMA}} = \frac{M_{PMMA}}{\frac{4}{3}\pi r_{PMMA}{}^{3} d_{PMMA}} = \frac{100\text{mg}}{\frac{4}{3} \times 3.14 \times (50 \times 10^{-9})^{3} \times 1.19\,\text{g}/\text{cm}^{3}} = 1.6 \times 10^{15}$$

$$m_{PDI} = \frac{N_{PMMA} \times 10}{6.02 \times 10^{23}} = 2.66 \times 10^{-8}\,\text{mol}$$

M_{PMMA} = 100 mg (1 mmol PMMA)

d_{PMMA} = 1.19 g/cm^3 (Density of PMMA)

r_{PMMA} = 100 nm (Diameter of PMMA particle)

n = 10 (Amount of PDI molecules in each particle

N_{PMMA} = Amount of PMMA particles in 100 mg

N_{PDI} = Amount of PDI molecules in N_{PMMA} PMMA particles

m_{PDI} = the mol amount of PDI

$$N_{PU} = \frac{M_{PU}}{m_{PU}} = \frac{M_{PU}}{v_{PU}\, d_{PU}} = \frac{M_{PU}}{\frac{4}{3}\pi r_{PU}{}^{3} d_{PU}} = \frac{312\text{mg}}{\frac{4}{3}\times 3.14\times(100\times10^{-9})^{3}\times 1.0\text{g}/\text{cm}^{3}} = 7.4\times10^{13}$$

$$m_{PDI} = \frac{N_{PU}\times 10}{6.02\times10^{23}} = 1.21\times10^{-9}\,\text{mol}$$

M_{PU} = 312mg (1 mmol PU)

d_{PU} = 1.0 g/cm^3 (Density of PU)

r_{PU} = 100 nm (Diameter of PU particle)

n = 10 (Amount of PDI molecules in each particle)

N_{PU} = Amount of polyurethane particles in 100 mg

N_{PDI} = Amount of PDI molecules in N_{PU} polyurethane particles

m_{PDI} = the mol amount of PDI

7.4 Preparation of graphene nanocomposites

7.4.1 Preparation of graphene oxide foam (sec 5.3.1)

Materials

Natural flake graphite (NFG) was used received from Sigma-Aldrich. Fuming nitric acid (>90%), sulfuric acid (95-98%), sodium nitrate (>99%) and potassium permanganate (>99%) and hydrogen peroxide solution (50%) were purchased from Sigma-Aldrich.

Preparation

Graphene oxide was prepared with Hummers method [3]. 10 g of flake graphite and 5 g of sodium nitrate were mixed in a 2-liter flask which was cooled to 0 ºC with a ice bath. 0.23 liter sulfuric acid was slowly added into the mixed in order to keep the temperature at 20ºC. While maintaining vigorous agitation, 300 g of potassium permanganate was added to the suspension. The ice bath was then removed and the temperature of the suspension reached to 35 ºC. As the reaction progressed, the mixture became pasty with brownish grey color. After three days, 0.5 liters of water was slowly stirred into the paste, causing violent effervescence and an increase in temperature to 100ºC. The obtained diluted brown suspension was then further diluted to approximately 5 liters with warm water and treated with hydrogen peroxide to reduce the residual permanganate and manganese dioxide to colorless soluble manganese sulfate, until the suspension turned bright yellow and no gas was bubbled. The suspension was centrifugated with speed 20000 rpm a few of times, till the PH value was 7. The obtained dark brown stable dispersion of graphene oxide in water was treated by ultrasound for 8 h in ice bath. The goal of this step was to obtain graphene oxide monolayer dispersion.

Subsequently, the aqueous suspension of graphene oxide was frozen into liquid nitrogen (-196 °C) and then was freeze-dried using a lyophilizer with a condenser temperature of -50 °C and inside pressure less than 20 Pa. After 4 days lyophilization process, low-density, porous graphene oxide brown foam was finally obtained. It was kept in a desiccator for one week in order to remove the residual water.

7.4.2 Thermal reduction of graphene oxide foam (sec 5.3.2)

The dried GO foam (10 mg) was put into a 50 mm long, 10 mm broad quartz ship. It was inserted into a tube furnace (GERO Hochtemperature Ofen 75242 from Germany Neuhausen) and was flushed with argon for 30 min. Then the furnace was heated to different temperatures (250 °C, 550 °C, 750 °C and 1000 °C) with different heating rates (1 °C/min, 5 °C/min, 10 °C/min, 20 °C/min and 30 °C/min).

7.4.3 Dispersion of graphene nanosheets with different surfactants (sec 5.4.1)

Materials

Water was distillated. Surfactant SDBS and SDS were purchased from Sigma-Aldrich. Lutensol AT50 is a poly(ethylene oxide) hexadecyl ether with an glycol block length of 50 units supported by BASF. THF (99%) and n-Hexane (99%) were used as received from Sigma-Aldrich. Graphene nanosheets were obtained by exfoliation at 1000 °C with heating rate 30 °C/min.

Preparation

Graphene nanosheets (exfoliated at 1000 °C with a heating rate 30 °C/min) with different surfactants were dispersed in suitable solvents. The dispersion was stirred for 8 h and treated by ultrasound for 8 h. The components of the dispersions were listed following.

Surfactant (1 mg)	Solvent (1 ml)	Graphene nanosheets
SDBS	Water	0.1mg
SDS	Water	0.1mg
Lutensol	THF	0.1 mg
PI-b-PMMA	THF	0.1 mg
PI-b-PMMA	n-Hexame	0.1 mg

Table 5. The components of the dispersions of graphene nanosheets with different surfactants.

7.4.4 Preparation of the dispersion of graphene nanosheets in THF (sec 5.4.2)

Materials

Graphene nanosheets were prepared by exfoliation at 1000 ºC with a heating rate 30 ºC /min. THF (99%) was used as received from Sigma-Aldrich.

Preparation

Graphene nanosheets (1 mg) (exfolicated at 1000 ºC with a heating rate 30 ºC/min) and 5 mg PI-b-PMMA was mixed in 1 ml THF. It was stirred at room temperature for 8 h and then treated by ultrasound for 8 h with ice bath. To measure the stability of the dispersions, they were centrifugated with different speed (1000 rpm, 2000 rpm, 3000 rpm, 4000 rpm and 5000 rpm) for 30 min. The obtained concentrations were listed following:

Centrifugation (rpm)	Concentration (mg/ml)
1000	0.10
2000	0.053
3000	0.025
4000	0.011
5000	0.0057

Table 6. The concentrations of graphene nanosheets in THF after treatment of centrifugation.

7.4.5 Dispersion of graphene nanosheets with organic solvents (sec 5.4.3)

Materials

THF, n-Hexane, NMP, DMF and toluene were used as received from Sigma-Aldrich. Graphene nanosheets were obtained by exfoliation at 1000 ºC with a heating rate 30 ºC/min.

Preparation

Graphene nanosheets (0.1 mg) (exfolicated at 1000 °C with a heating rate 30 °C/min) were added into different organic solvents (THF, n-Hexane, NMP, DMF and toluene) without using any surfactants. The mixture was stirred for 8 h and then treated by ultrasound for continuously 8 h.

7.4.6 Preparation of the polymer composites with graphene nanosheets (sec 5.5)

Materials

PMMA 18000 g/mol (PD 1.1), PS 25000 g/mol (PDI 1.1) and PI-b-PMMA were used as received from the polymer synthesis apartment in the institute. THF was used as received from Sigma-Aldrich. Graphene nanosheets were exfoliated at 1000 °C with a heating rate 30 °C.

Preparation

Graphene nanosheets and surfactant PI-b-PMMA with weight ratio (1:1) were mixed in 10 ml THF. The mixture was stirred at room temperature for 8 h and then treated by ultrasound for 8 h. PMMA or PS with different amount were added in the obtained stable dispersion and continuously stirred for 8h and treated by ultrasound for 8 h. The polymer composites dispersions were then precipitated in methanol. The obtained powder was dried in vacuum for 8h. In order to measure the electric, mechanical properties, the powder was pressed in a hydraulic hot press (Model 0230C-X1, PHI-Tulip) at 18 kN with a temperature of 200 °C. The obtained films had a thickness from 200 nm to 250 nm.

7.4.7 Calculation of percolation threshold and the critical exponent for PS (sec 5.5.2.1)

The DC conductivity of PS composites with different concentrations of graphene nanosheets was measured at frequency 1 Hz.

	Graphene nanosheets Wt%	Conductivity S/cm
1	6	2.50E-04
2	4.3	2.60E-05
3	3.1	2.00E-06
4	1	1.70E-11
5	0.68	2.00E-11
6	0.42	1.00E-11
7	0.34	1.20E-11
8	0.1	1.00E-11

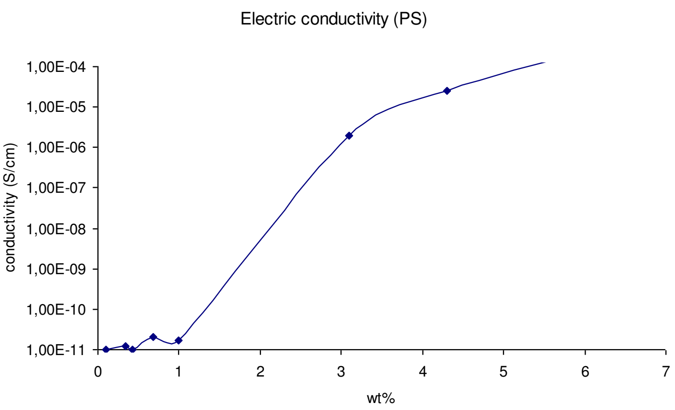

Figure 5. The direct current conductivity of the PS composites versus the weight concentration of graphene nanosheets

The percolation threshold P_c clearly occurs between 2.0 and 3 wt%. In order to get an estimate for P_c and the critical exponent s, the σ_{DC} data for P_c - P is fitted to Eq. (1).

$$\sigma_{DC} \approx (P_c - P)^{-s} \qquad (1)$$

This was done by variation of P_c in the interval from 2.1 to 3.0 in steps of 0.1. For each estimated value of P_c the value of s was determined from relation of σ_{DC} and P_c - P .In the table 6 it is shown calculated critical exponent s, when P_c varies from 2.1 wt% to 3.0 wt%.

$P_c = 3.0\%$

P (%)	$P_c - P$ (%)	Conductivity (S/cm)
1	2	1.70E-11
0.68	2.32	2.00E-11
0.42	2.52	1.00E-11
0.34	2.68	1.20E-11
0.1	2.9	1.00E-11

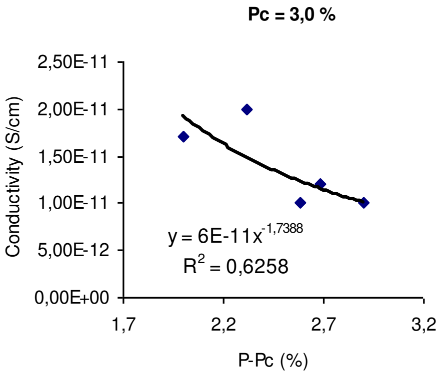

Figure 6. An example to calculate the critical exponent s with $P_c = 3.0\%$.

Nr	P_c (wt%)	critical exponent s	Determination (R^2)
1	2.1	1.07	0.6141
2	2.2	1.15	0.6166
3	2.3	1.21	0.6166
4	2.4	1.29	0.6185
5	2.5	1.36	0.6201
6	2.6	1.44	0.6215
7	2.7	1.51	0.6228
8	2.8	1.59	0.6239
9	2.9	1.66	0.6249
10	3.0	1.73	0.6258

Table 7. The calculated critical exponent s and the determination

The lowest value of the root mean square error was found for $P_c = 3.0$ wt% with the exponent s = 1.73. In order to get the critical exponent t; the σ_{DC} data for $P - P_c$ is fitted to Eq. (2),

$$\sigma_{DC} \approx (P - P_c)^t \qquad (2)$$

with $P_c = 3.0$ %. The calculated critical exponent t is 1.30.

Pc = 3.0%

P (%)	$P - P_c$ (%)	Conductivity (S/cm)
6	3	2.50E-4
4.4	1.4	2.60E-5
3.1	0.1	2.00E-6

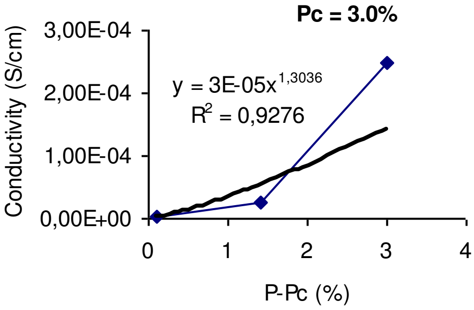

Figure 7. The calculation of the critical exponent t with $P_c = 3.0\%$

7.4.8 Calculation of percolation threshold and the critical exponent for PMMA (sec 5.5.2.1)

The values of the DC conductivity of PMMA composites with different weight concentrations of graphene nanosheets were measured.

	Graphene nanosheets Wt%	Conductivity S/cm
1	6,00	2,30E-04
2	5,20	1,80E-05
3	3,90	3,00E-10
4	3,20	1,10E-10
5	0,63	1,10E-11
6	0,50	1,30E-11
7	0,33	1,50E-11
8	0,22	1,50E-11

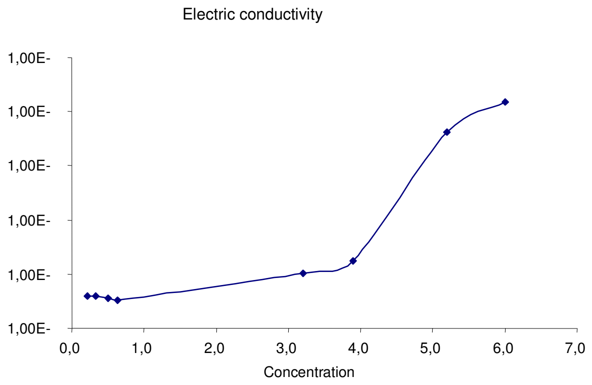

Figure 8. The direct current conductivity of the PMMA composites versus the weight concentration of graphene nanosheets

The percolation threshold P_c clearly occurs between 3.0 and 4 wt%. In order to get an estimate for P_c and the critical exponent s; the σ_{DC} data for P_c - P is fitted to Eq. (1).

$$\sigma_{DC} \approx (P_c - P)^{-s} \tag{1}$$

This was done by variation of P_c in the interval from 3.0 to 4.0 in steps of 0.1. For each value of P_c the value of s was determined from relation of σ_{DC} and P_c – P.

Nr	P (%)	P_c – P (%)	Conductivity (S/cm)
1	3.2	0.10	1.10E-10
2	0.63	2,67	1,10E-11
3	0.50	2,80	1.30E-11
4	0.33	2,97	1.50E-11
5	0.22	3,08	1.50E-11

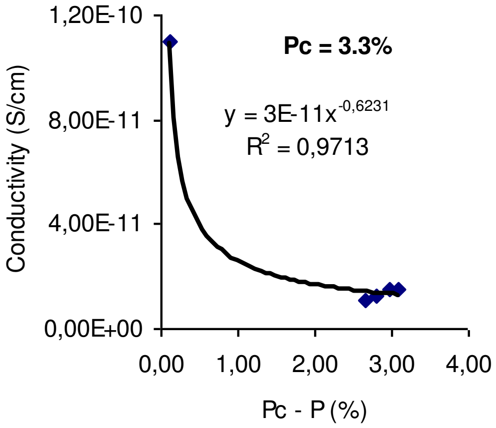

Figure 9. An example to calculate the critical exponent s with P_c = 3.3%.

Nr	P_c (%)	Critical exponent s	Determination (R^2)
1	3.3	0.623	0.971
2	3.4	0.774	0.969
3	3.5	0.896	0.967
4	3.6	1.006	0.966
5	3.7	1.108	0.964
6	3.8	1.205	0.963
7	3.9	1.298	0.962
8	4.0	1.388	0.961

Table 8. The calculated critical exponent s and the determination.

The lowest value of the root mean square error was found for P_c = 3.3 wt% with the exponent s = 0.623. In order to get the critical exponent t; the σ_{DC} data for $P - P_c$ is fitted to Eq. (2),

$$\sigma_{DC} \approx (P - P_c)^t \tag{2}$$

with P_c = 3.3 %. The calculated critical exponent t is 9.14

Nr	P (%)	$P-P_c$ (%)	Conductivity (S/cm)
1	6.0	2.7	2.30E-4
2	5.2	1.9	1.80E-5
3	3.9	0.6	3.00E-10

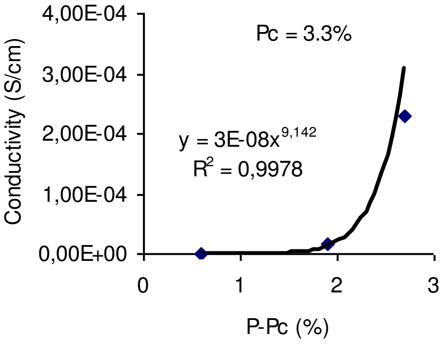

Figure 10. The calculation of the critical exponent t with P_c = 3.3%

Reference

1. Müller, K., Nicht-waessrige emulsionspolymerisationen, in Chemie und Pharmazie der Johannes-Gutenberg Universitaet 2008: Mainz.
2. Woell, D., et al., Radical polymerization tracked by single molecule spectroscopy. Angewandte Chemie-International Edition, 2008. **47**(4): p. 783-787.
3. Hummers, W., S, and R. Offeman, E,, Prepartion of Graphitic oxide. Contribution from the baroid division, National lead Company, 1957